Next Generation Automotive DeNO$_X$ Catalysts: Ceria What Else?

Wang, Yixiao

DOI
10.4233/uuid:72603e00-09dc-4a68-94ee-1f0878dedd4d

Publication date
2017

Document Version
Final published version

Citation (APA)
Wang, Y. (2017). *Next Generation Automotive DeNO$_X$ Catalysts: Ceria What Else?* [Dissertation (TU Delft), Delft University of Technology]. https://doi.org/10.4233/uuid:72603e00-09dc-4a68-94ee-1f0878dedd4d

Next Generation Automotive DeNO$_x$ Catalysts: Ceria What Else?

Next Generation Automotive DeNO$_x$ Catalysts: Ceria What Else?

Proefschrift

ter verkrijging van de graad van doctor

aan de Technische Universiteit Delft,

op gezag van de Rector Magnificus prof. ir. K.C.A.M. Luyben,

voorzitter van het College voor Promoties,

in het openbaar te verdedigen op

3 november 2017 om 12:30 uur

door

Yixiao WANG

Master of Science in Biomedical Engineering,
Xiamen University, Xiamen, China,

geboren te Fuzhou, China.

Dit proefschrift is goedgekeurd door de

promotor: prof. dr. F. Kapteijn
promotor: prof. dr. ir. M. Makkee

Samenstelling promotiecommissie:

Rector Magnificus,	voorzitter
prof. dr. F. Kapteijn,	Technische Universiteit Delft, promotor
prof. dr. ir. M. Makkee,	TU Delft / Politecnico di Torino, Italy, promotor

Onafhankelijke leden:

Dr. E. Redekop	University of Oslo, Norway
Prof. dr. H. Xu	FuDan University, China
Prof. dr. A. Trovarelli	University of Udine, Italy
Prof. dr. E. Tronconi	Polytechnic University of Milan, Italy
Prof. dr. F. M. Mulder	Technische Universiteit Delft
Prof. dr. ir. W. de Jong	Technische Universiteit Delft, reservelid

This research was supported by the China Scholarship Council (CSC).

Printed by: Gildeprint,The Netherlands

Cover design: Liang Dong

ISBN 978-94-6186-859-6

An electronic version of this dissertation is available at
http://repository.tudelft.nl/.

Science is a wonderful thing
if one does not have to earn one's living at it.

Albert Einstein

Contents

1

Introduction

Saving our planet, lifting people out of poverty, advancing economic growth... these are one and the same fight.
We must connect the dots between climate change, water scarcity, energy shortages, global health, food security and women's empowerment.
Solutions to one problem must be solutions for all.

Ban Ki-moon

1

This chapter gives an overview of automotive pollutant emissions reduction regulations, NO_x emission strategies and challenges, the objectives, and outline of this thesis.

1.1. CO_2 legislation

Atmospheric carbon dioxide (CO_2) grows rapidly and is accompanying to the economic growth [1]. Cars are responsible for around 12% of total EU emissions of CO_2 [2]. Therefore, EU legislation sets mandatory CO_2 emission reduction targets for new vehicles from 2013 onwards. The average emissions level of a new car sold in 2016 was 118.1 g/km CO_2, significantly below the 2015 target of 130 g/km. By 2021, phased in from 2020 onwards, the CO_2 emission has to be lower to 95 g/km for all average new cars of the company [2], which corresponds to a fuel consumption of around 3.8 L/100 km. All these CO_2 emission standards are given under the current approved NEDC driving cycle. With the introduction of the (more realistic real driving emissions) "WLTP" driving cycle (Worldwide harmonized Light vehicles Test Cycle), CO_2 emission levels of vehicles and the related pollutant emissions (mainly NO_x) will be significantly higher.

The legislation on CO_2 emission drives the development of increasingly more fuel efficient cars with lower fuel consumptions than those in conventional gasoline engines, *e.g.,* lean burn engines including lean-burn gasoline and diesel engine. The lean burn engine operates with excess oxygen and the presence of nitrogen at the high flame temperature will result in more NO_x formation in the combustion chamber than with stoichiometric combustion [3]. Due to legislation all cars could have $DeNO_x$ technologies on board, the conversion of NO_x under lean conditions is however much more coumbersome. Therefore, it will be anticipated that by the effective introduction of the new certification test such as WLTO or Real Driving Emissions the NO_x emission will increase. As a consequence, the automotive industry faces enormous challenges to compromise the balance between drivability (passengers' satisfaction), fuel efficiency (CO_2 emission), and pollutant emission legislation. Increasing fuel efficiency is a way to reduce fuel consumption of vehicles, which brings economic profits for car owners, decreases the CO_2 emission and increases energy sustainability. It should be noted that in the life time of car already 50% of the CO_2 emission is related to the production of the car. The most important way to reduce carbon dioxide emissions on the road is via the vehicle weight reduction by engine downsizing. Among others, engine downsizing can be enabled by advances in turbocharging and fuel injection. In order to deliver the same or even more required power as

engines with a large displacement for driving, engine downsizing (a smaller displacement) requires higher peak brake mean effective cylinder pressures (BMEPs) [4]. For diesel engines, aggressive downsizing tends to increase the specific load, which, in turn, increases the pollutants emission, *e.g.,* oxides of nitrogen (NO_x) [5]. In the automotive industry, the volume of after-treatment systems as rule of tumb are the same as the volume of the displacement in the engine. In other words, the smaller engines will decrease the relative contact time (or increase the gas hourly space velocity). Therefore, the introduction of CO_2 legislation requires an even more efficient after treatment system for the pollutants, *e.g.,* nitrogen oxides (NO_x), carbon monoxide (CO), Ozone (O_3), Particulate Matter (PM).

1.2. Automotive exhaust gas pollutants emission

1.2.1. Legislated pollutants and EU emission standards

Air pollution is a problem for both environment and society since it causes a multitude of adverse effects on human health, environment, and climate [6, 7]. The air pollutant emissions from the automotive contributed significantly to the overall air quality in Europe. Emissions of PM, NO_x, HCs, and CO are pollutants regulated by Euro emissions standards.

EU Emission standards specify the maximum amount pollutant that is allowed to emit from the exhaust gasses of a vehicle when it is tested under laboratory conditions or using a specific driving cycle. Table 1.1 shows the EU emission standard of the PM, NO_x, HCs, and CO for a passenger car. From Euro 3 to 6, diesel engines have a lower CO emission standards while a higher NO_x emission is allowed. Gasoline vehicle starts regulation on PM from Euro 5, indicating that the PM emission from the gasoline is an issue as well. From Euro 5 for a diesel engine, the PM emission standard remains the same value at 0.005 g/km. However, the emission standards on NO_x dropped from 0.5 (Euro 3) to 0.08 (Euro 6) g/km. In the future, the NO_x emission standard will become even more stringent.

Table 1.1: Euro emission standards for passenger cars in g/km [8].

Stage	Date	CO	HCs	HCs+NO_x	NO_x	PM
			Diesel			
Euro 1	1992.07	2.72	-	0.97	-	0.14
Euro 2	1996.01	1.0	-	0.7	-	0.08
Euro 3	2000.01	0.64	-	0.56	0.5	0.05
Euro 4	2005.01	0.50	-	0.30	0.25	0.025
Euro 5	2009.09b	0.50	-	0.23	0.18	0.005
Euro 6	2014.09	0.50	-	0.17	0.08	0.005
			Gasoline			
Euro 1	1992.07	2.7	-	0.97	-	-
Euro 2	1996.01	2.2	-	0.5	-	-
Euro 3	2000.01	2.3	0.20	-	0.15	-
Euro 4	2005.01	1.0	0.10	-	0.08	-
Euro 5	2009.09b	1.0	0.10	-	0.06	0.005
Euro 6	2014.09	1.0	0.10	-	0.06	0.005

1.2.2. Emission test cycles

Emission testing (verification) cycles are used to evaluate whether a type of vehicle meets the emission requirement set by the European Commission before it is allowed to be available in the market. For the light-duty vehicles, a combined chassis dynamometer test is used for emission testing and certification in Europe, including four ECE Urban Driving Cycles, simulating city driving in combination with one Extra Urban Driving Cycle (EUDC), simulating highway driving conditions [9]. This New European Driving Cycle (NEDC) was introduced in 2000 together with a cold-start test procedure [9]. This (currently approved) NEDC cycle is working under an extremely mild condition for engines, which is too unrealistic from the real driving. Therefore, a more realisticdriving cycle, Common Artemis Driving Cycles (CADC), is to replace the NEDC [10]. In order to lower the NO_x emission from the diesel car on the road, the RDE testing (analogous to the CADC) requirements will be introduced from September in 2017 [11].

- ECE cycle
  The ECE is an urban driving cycle characterising with a low vehicle speed, low engine load, and low exhaust gas temperature (Figure 1.1A).

- EUDC cycle
  The Extra Urban Driving Cycle has been added after the fourth ECE cycle to simulate a high-speed driving mode (Figure 1.1B). The maximum speed of the EUDC cycle is 120 km/h.

- NEDC cycle
  Before the emission test in EUDC cycle, the vehicle is allowed to soak for at least 6 hours at temperature of 20-30 °C, and 40 s idle period is allowed. In NEDC cycle, the cold start test is added into the EUDC cycle to eliminate this idling period. This modified cold-start procedure is referred to as the New European Driving Cycle (NEDC).

- CADC cycle
  The Common Artemis Driving Cycles (CADC) was developed based on the European real world driving behaviour. Artemis means Assessment and Reliability of Transport Emission Models and Inventory Systems. CADC cycle contains Urban, Rural road, and Motorway driving cycles, as shown in Figure 1.2 [9].

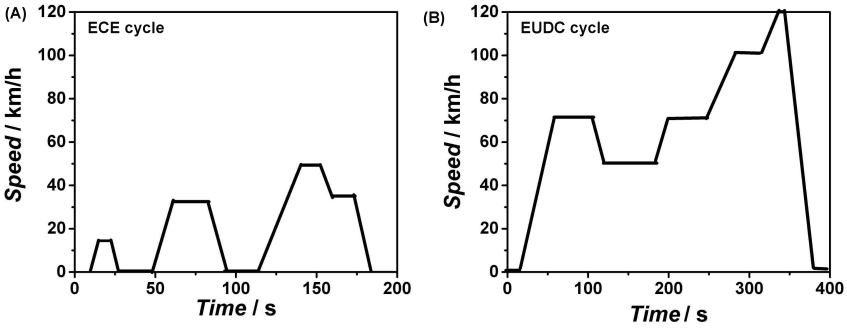

Figure 1.1: (A) ECE test cycle and (B) EUDC test cycle [9].

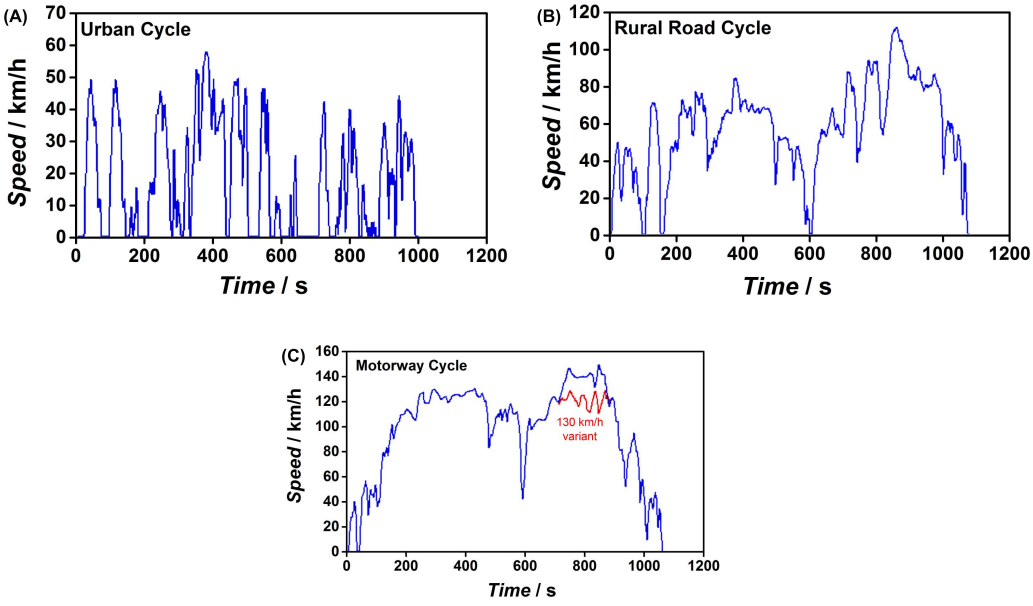

Figure 1.2: Artemis Driving Cycles: (A) urban cycle; (B) rural road cycle; and (C) motorway cycle [10].

Table 1.2: Air quality Guideline for Europe in 1987 first edition (WHO Regional Office for Europe).

	Time-weighted average	Average time
Nitrogen dioxide	400 µg/m^3	1 hour
	150 µg/m^3	24 hours
Carbon monoxide	100 µg/m^3	15 minutes
	30 µg/m^3	1 hour
	10 µg/m^3	8 hours
Ozone	150-200 µg/m^3	1 hour
	100-1210 µg/m^3	8 hours
sulphur dioxide and PM	125 µg/m^3	24 hours
	50 µg/m^3	1 year

Table 1.3: Air quality Guideline for Europe in 2015 (WHO Regional Office for Europe).

	Time-weighted average	Average time
Nitrogen dioxide	200 µg/m^3	1 hour
	40 µg/m^3	24 hours
Carbon monoxide	30 µg/m^3	1 hour
	10 µg/m^3	8 hours
Ozone	180 µg/m^3	1 hour
	120 µg/m^3	8 hours
PM_{10}	50 µg/m^3	24 hours
	40 µg/m^3	1 year
$PM_{2.5}$	25 µg/m^3	1 year

1.3. Air quality and NO_x in particular

Since the mid-1980s the WHO Regional Office for Europe has developed standards and goals for air quality management. As shown in Table 1.2 and 1.3, the Air quality standard for CO and O_3 hardly changed from 1987 till now. In the 2nd edition in the year 2000, a particulate matter (PM) limit was recommended to be provided separately from SO_2. Particularly, in the report of WHO Regional Office for Europe (1987), Table 1.2, the guideline for NO_2 1 h and 24 h mean concentration is 400 µg/m^3 and 150 µg/m^3, respectively. Moreover, this number dropped to 200 µg/m^3, and 40 µg/m^3, respectively, in the 2nd edition (2000) of WHO Regional Office for Europe and onwards. Nitrogen oxides (NO_x, including NO and NO_2) are a group of hazardous, toxic, and harmful gasses, which have an adverse effect on both environment and human health, *e.g.,* the cause of acid rain, photochemical smog, and affecting the human respiratory system.

As shown in Figure 1.3, NO_x is globally distributed over the world, especially in China, Europe, and USA [12]. A high concentration of NO_x is observed in the northeast of China, as indicated by dark red colour. However, even in Europe where the NO_x concentration is much lower than that in China, the level of NO_x concentration in most of the EU cities is still higher than those of the safety limit [13] as shown in Figure 1.4 presenting the NO_x concentration in the EU cities in 2014. Red and dark red dots indicate where the EU daily limit value (40 µg/m^3) is exceeded. Regarding the source of NO_x, around 40% is reported from the on road transport, as shown in Figure 1.5 [6, 14, 15]. Therefore, the regulation on NO_x emission is an efficient way to lower down the NO_x concentration in the air and improve the air quality.

European legislative authorities have addressed the NO_x emissions of passenger diesel vehicles by introducing NO_x emissions standards from Euro 3 in 2000 with the allowed level at 0.5 g/km (Table 1.1). NO_x emission regulation becomes more and more stringent from Euro 3 to Euro 6 (Table 1.1) [8]. The introduction of Euro 6 led to NO_x emission at the level of 80 mg/km. In the past 14 years, NO_x emission was aimed to be 80% lower. However, the real on-road emission levels were much higher than the actual allowed by the regulation [16–18]. As shown in Figure 1.6, on-road car emissions during Euro 3 (2000) were closer to 1000 mg/km. Although the

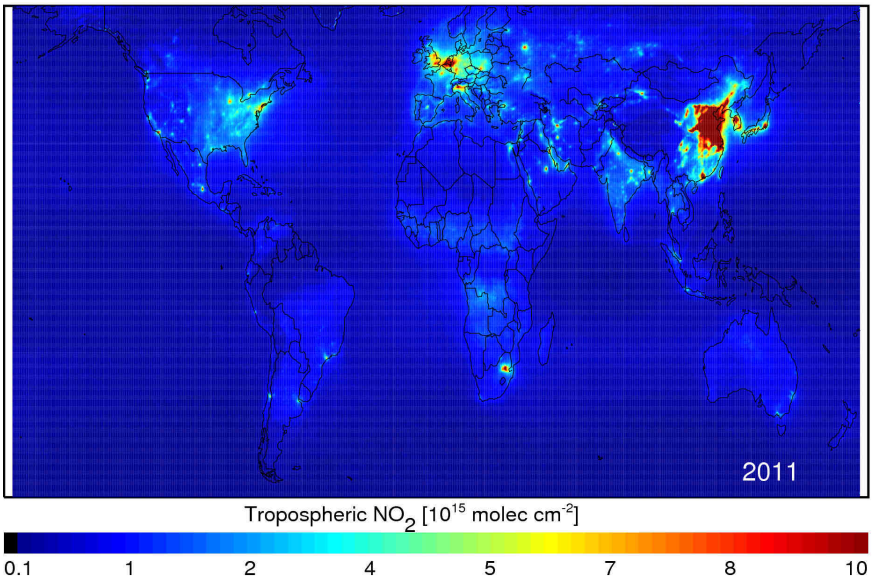

Figure 1.3: NO_2 pollution around the world in 2010 [12].

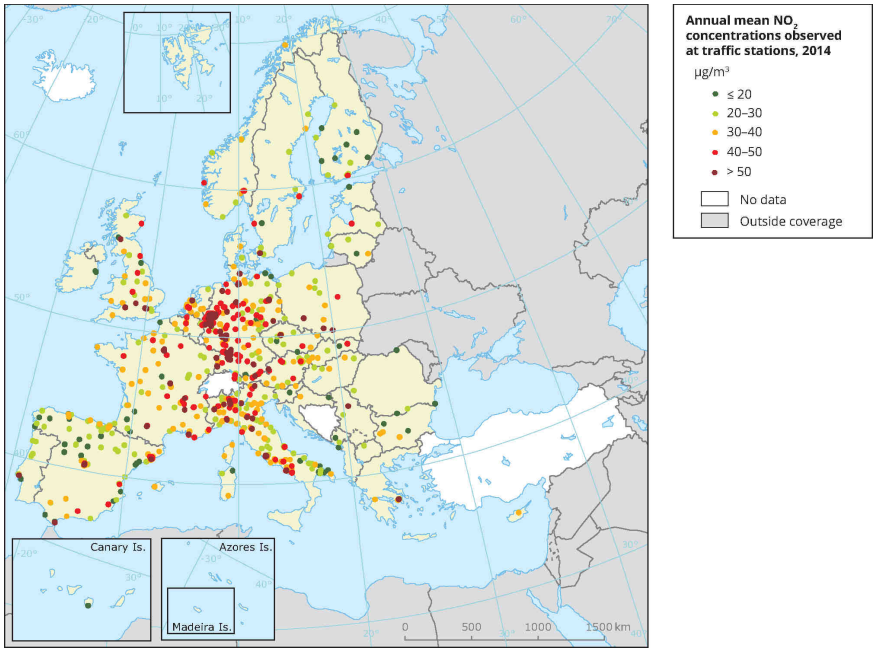

Figure 1.4: The annual mean NO_2 concentration observed in EU in 2014 [13].

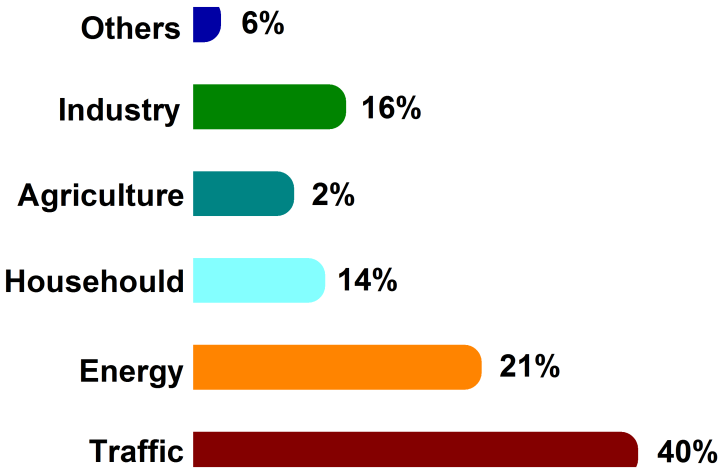

Figure 1.5: NO_x emission by sector in EU [14, 15].

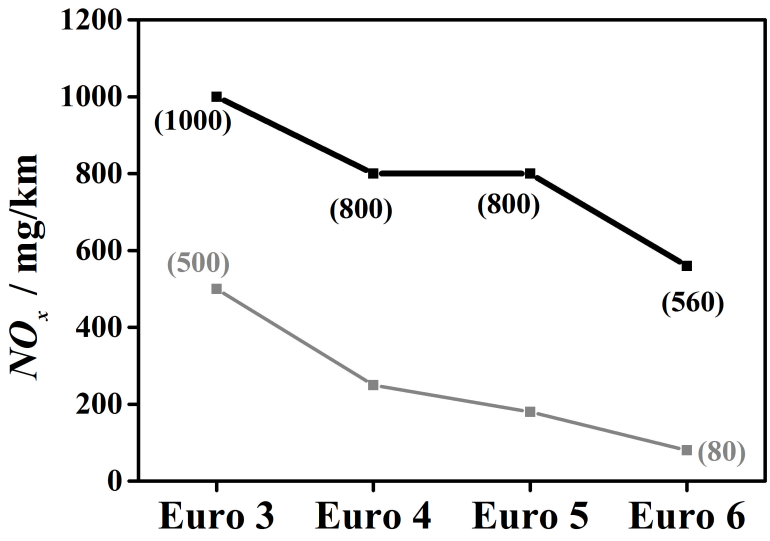

Figure 1.6: NO_xemission under real driving condition (black line)and NO_x emission standards for light-duty diesel vehicle (grey line), according to the Euro standards [8, 16].

Euro 4 emission standard (2005) set a limit of 250 mg/km for NO_x diesel emissions, followed by 180 mg/km in Euro 5 (2009). However, the on-road concentrations did not change at all from 2005 to 2009, which were in the range of 800 mg/km. The real NO_x emission in Euro 5 was more than four times higher than allowed. The real NO_x emission in Euro 5 was only 20% lower than the actual NO_x emission in Euro 3. Even in Euro 6, NO_x emissions were on average 400% higher than the Euro 6 limit (sometimes even more) if measured under real driving conditions. However, the vehicles that emitted more NO_x than allowed still received their type-approval and could be sold on the market because they needed only to meet the requirement under laboratory conditions only (NEDC testing protocole). Currently, the NO_x emission from a diesel car is only able to pass an current approved laboratory test. Therefore, on 28^{th} October 2015, Member States of the Europen Union agreed on the application of new real driving emissions (RDE) tests to determine whether a new car model is allowed to be introduced on the market from 1^{st} September 2017 [11]. In a first step, car manufacturers are allowed to emit 2.1 times higher NO_x emission (relatively to Euro 6) for the new models from September 2017 onwards. In a second phase, only 1.5 times higher NO_x emission (relatively to Euro 6) is allowed for all new models from January 2020 onwards.

1.4. Automotive NO_x emission strategies

1.4.1. Engine modification

1.4.1.1. Fuel injection strategy

Fuel injection delivers the fuel into the combustion chamber of the engine. However, fuel injection strategy has significant influences on the performance of engine and pollutant emissions. High fuel injection pressures and flexible injection rate shaping can effectively reduce the pollutant formation in the engine.

In a diesel engine, the use of high fuel injection pressures (2000 bar), combined with smaller injection holes with a diameter between 120 and 150 µm, can reduce PM emissions by the formation of smaller fuel droplets and a better air-fuel mixing. Conventional fuel injection system employed a sin-

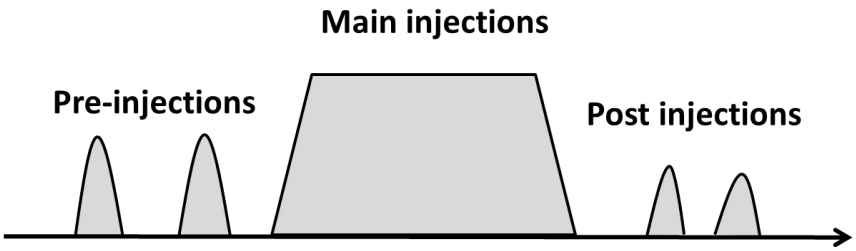

Figure 1.7: Multiple injection events [19].

gle injection for every engine stroke cycle, but in newer systems multiple injection events are applied (Figure 1.7).

For the pilot injection (pre-injection), a small amount of the fuel is injected before the main fuel injection, allowing for a smaller and more delayed main injection event and reduced NO_x emissions. Moreover, for post injections, a small amount of fuel is injected after the main injection, which provides hydrocarbon supply to the exhaust stream, allowing for more efficient exhaust pollutant control technologies (discussed below in section 1.4.2.2).

1.4.1.2. EGR: Exhaust Gas Recirculation

NO_x is formed during the engine combustion in a temperature above 1300 °C [20]. The main precursors for NO_x formation are N_2 and O_2 from the the intake air. A small fraction of N_2 and O_2 can dissociate atoms to form NO_x. The amount of NO_x formation is a function of combustion temperature. High compression ratios of diesel engines and excess of O_2 in the combustion chamber directly causes the higher NO_x emissions than those from a gasoline combustion chamber. Exhaust Gas Recirculation (EGR) is an effective in-cylinder method to reduce NO_x emissions from diesel engines by lowering the flame temperature and the oxygen concentration in the combustion chamber. Incorporated (even cooled) EGR into the diesel engine, some exhaust gas can be recycled to the combustion chamber. The recycled gas can act as a diluent to reduce the combustion temperatures and hence lower the NO_x emissions. However, application of EGR to reduce NO_x emissions (reduction of the maximum combustion temperature) will result in a less efficient combustion process and to a higher fuel consumption.

Overall, the engine modifications adapt the combustion process in the engine and will diminish the formation of hazardous emission, especially of NO_x and PM. However, the engine modification, which decreases NO_x, often increases the PM formation from the engine, and *vice versa*. This so-called NO_x-PM trade-off presents a critical challenge to diesel emission reduction strategies [21]. Euro 6 requires a significant advancement over Euro 5 on the NO_x emission limit, reducing it from 0.18 g/km to 0.08 g/km. The engine modification itself will be not sufficient to meet the Euro 6 and more stringent future requirements. The introduction of Euro 6 for the lower limit of NO_x requires after-treatment control technologies, such as Selective Catalytic Reduction (SCR), NO_x Storage Reduction (NSR), or other after-treatment.

1.4.2. Development of after-treatment technology

A three-way catalyst (TWC) mounted in a gasoline vehicle is capable to a simultaneous removal of NO_x, CO, and unburnt HCs for stoichiometric air-fuel supply. The main reactions are described as followed.

$$CO + NO \rightarrow CO_2 + N_2$$

$$CO + O_2 \rightarrow CO_2$$

$$HC + O_2 \rightarrow CO_2 + H_2O$$

However, it does not remove NO_x in the case of diesel and lean burn gasoline engines due to the excess of O_2 present in the exhaust gas. Therefore, other deNO_x systems need to be developed for diesel and lean-burn gasoline engines.

1.4.2.1. Selective catalytic reduction (SCR)

1.4.2.1.1 NO_x reduction with NH_3

Ammonia-SCR is a mature and widely commercialised technology for NO_x removal from stationary sources. From 2004, SCR technology is selected for the part of the heavy-duty vehicles in the EU, Japan, and the USA to meet the NO_x emission standards [22]. Instead of ammonia, an aqueous urea solution is used as reductant, which can be refilled at fuel stations. From 2015, all new model diesel passenger cars in Europe have to meet the Euro

6 legislation, which leads partially to the application of Urea-SCR in diesel passenger cars, in particular for an engine displacement capacity of 1.6L or more [23]. Passenger vehicles require their refilling of the AdBlue tank [23].

- Catalyst development

  Typically, V_2O_5 catalysts supported on TiO_2, with different promoters (WO_3 and MoO_3), are commercially employed in monolith type catalysts. However, the strong disadvantages of the vanadium-based catalysts include the toxicity of V_2O_5 and the narrow operation temperature window (300-400 °C) [24]. Therefore, much work focused on developing vanadium-free NH_3-SCR catalysts, with emphasis on a high deNO_x efficiency and N_2 selectivity, excellent hydrothermal stability, and insensitivity to co-existing poisoning components in the SCR (automotive exhaust) atmosphere such as H_2O, SO_2, or HCs.

  Alternative Mn-based catalyst has been developed on laboratary scale as an alternative to the vanadium catalyst [25, 26]. The Mn-based catalyst showed a broader operating temperature window (150-350 °C), but is sensitive to sulfur poisoning, although the addition of CeO_2 or Co to the Mn-based catalyst was found to improve the SO_2 resistance [27]. Additionally, many efforts have also focused on the development of zeolite based catalyst. Cu-ZSM-5 and Fe-ZSM-5 have been extensively studied. They showed excellent low-temperature NH_3-SCR activity and a broad operation temperature window, but a limited hydrothermal stability [28].

  Recently, a series of Cu-chabazite (Cu-CHA) catalysts containing eight-membered ring pores with a small pore size (0.38 × 0.38 nm) are reported and commecially approved, which showed a high NH_3-SCR activity, a very good N_2 selectivity and an excellent hydrothermal stability with great application potential in the deNO_x process of diesel engines [29, 30].

- Chemical reaction

  Firstly urea forms ammonia via a hydrolysis reaction, before the actual SCR reactions start. Then the ammonia will react with NO or NO_2 via several reactions steps. The overall reactions are described as follows [31]:

$$Standard\ SCR: 4NO + 4NH_3 + O_2 \rightarrow 4N_2 + 6H_2O \quad (NO/NH_3/O_2)$$

$$Fast\ SCR: NO_2 + NO + 2NH_3 \rightarrow 2N_2 + 6H_2O \quad (NO/NH_3/NO_2)$$

The high deNO$_x$ efficiency is related to the 'Fast SCR" (NO/NH$_3$/NO$_2$, due to the presence of NO$_2$) and the lower reduction rate to the "standard SCR" (NO/NH$_3$/O$_2$).

- Issues in Urea- SCR system
  Although NH$_3$ (or urea) was very efficient as a reducing agent, some problems still existed. The NH$_3$ adsorption on the catalyst, via the urea dosing system, is the first step achieving conversion of NO$_x$ to N$_2$. However, NH$_3$ can desorb from the catalyst and result in the release of unreacted NH$_3$ ('ammonia slip') [32, 33]. The challenge of Urea-SCR control strategy is to solve the trade-off NO$_x$ conversion against ammonia slip. Major factors affecting system performance are urea input (injection and hydrolysis) and NO$_x$ concentration in the feed gas. Therefore, Urea-SCR system will perform well if under controlled and very well defined conditions, *e.g.,* temperature and NO$_x$ concentration in the feed. Furthermore, an additional tank for storing urea makes the car bulky and heavier, resulting in additional fuel consumption and smaller car "free" space. For a truck, for 1000 L diesel fuel consumption at least 50 L of urea is required. For a passenger car, an urea tank of 10-15 L is required for an average 20.000 km interval service of the car. The actual urea consumption is closely related to the driven ambition. Additionally, the downsizing of the engine will increase the gas hourly space velocity through the catalyst bed and temperature of exhaust gas from the combustion engine (described in section 1.1). These have clearly affected the overall NO$_x$ conversion efficiency of Urea-SCR.

1.4.2.1.2 NO$_x$ reduction with hydrocarbons (HCs)

The unique advantage of HC-SCR is that the diesel fuel can be used as a reductant for NO$_x$ reduction, thus reducing the cost involved in infrastructure development for delivering of the urea reductants to the heavy-duty engine exhaust system. Therefore, HC-SCR of NO$_x$ will be a potential alternative to the NH$_3$/urea-SCR.

Many catalysts, such as zeolite, base oxide/metal, and noble metal catalysts have been found to be effective for the SCR of NO$_x$ with hydrocarbons (HC-SCR) in the presence of excess oxygen. Zeolite catalysts (Cu, Fe-ZSM-5) are effective for the NO$_x$ reduction, but the water tolerances are a large hurdles

to be taken (hydrothermal stability). The small pore chabazite shows an extremely high hydrothermal stability. However, the largest pore window in the chabazite framework is an 8-ring (3.8 Å × 3.8 Å), which strongly limits the diffusion of diesel fuel molecules (even isobutane as a model component) into the structure. Cu or Fe-chabazite hardly works in HC-SCR. Noble metal based catalysts, such as Pt/Al_2O_3 and Pd/Al_2O_3, exhibit a high deNO_x activity in a very narrow temperature range (200-300 °C), as shown in Figure 1.8 [34]. Metal oxide catalysts for the reduction of NO_x with hydrocarbons have received an extensive attention due to their high-temperature activity and hydrothermal stability. Up to now, Ag/Al_2O_3 is one of the most promising catalysts for the HC-SCR. However, the thermal stability strongly depends on the preparation method and reaction conditions [35]. Furthermore, the poor low-temperature activity (below 300 °C) and narrow temperature window are additional challenges for these Ag/Al_2O_3 catalysts. For aromatic hydrocarbons, typically present up to 15% in diesel fuel, exhibit very low activity for the NO_x reduction, which indicates that the issues of catalyst activity and deactivation by hydrocarbons poisoning still need to be solved for the commercial application of HC-SCR. It should be noted that HC-SCR will increase the overall fuel consumption and, as a consequence, increase the CO_2 emissions.

1.4.2.2. NO_x storage reduction (NSR)

NO_x Storage and Reduction (NSR) system, developed by Toyota researchers, is regarded as the leading technology to control NO_x emission under lean-burn conditions. The engine is continuously operating under the excess of oxygen (lean) conditions. Short hydrocarbon pulses are periodically injected into the engine to create short periods with reducing (rich) conditions. NSR catalysts comprise of precious metals, NO_x storage components, and support metal oxides. $Pt/BaO/Al_2O_3$ and $Rh/BaO/Al_2O_3$ are the most commonly applied NSR catalysts. Figure 1.9 schematically illustrates the generally accepted mechanisms of NO_x storage/reduction in the $Pt/BaO/Al_2O_3$ catalyst. Under lean conditions, NO_x is trapped in the storage components of the NSR catalyst and subsequently reduced by reductants (CO, H_2, hydrocarbons) under fuel rich conditions [36]. The following five steps can describe the NSR system operation during the lean-rich cycle:

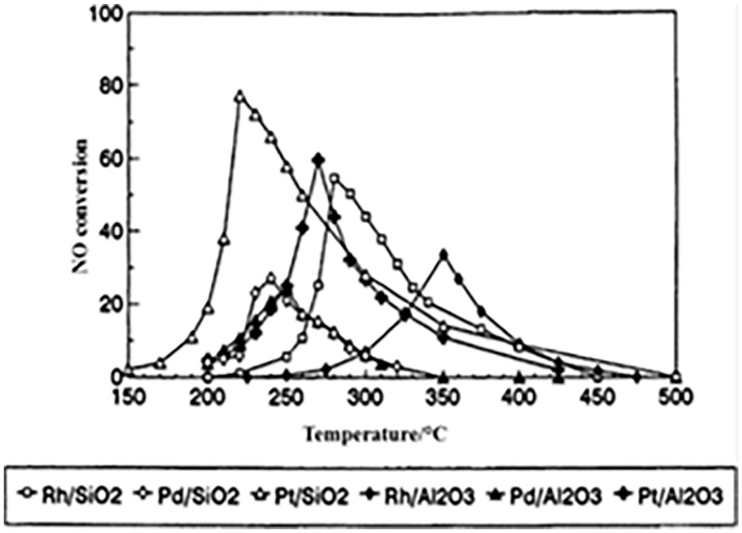

Figure 1.8: Reduction of NO by C_3H_6 under lean conditions *vs.* temperature on monometallic Pt, Rh, and Pd based catalysts (500 ppm NO, 1000 ppm C_3H_6 , and 5% O_2, gas hourly space velocity 60 000 L/L/h) [34].

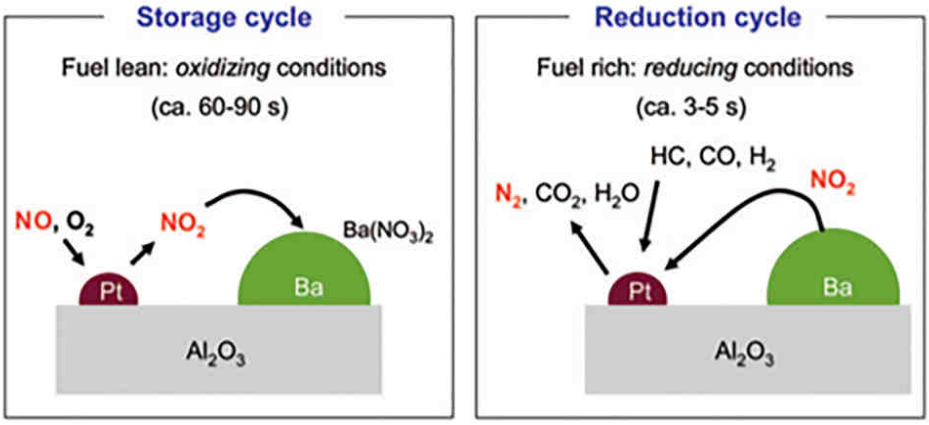

Figure 1.9: Illustration of the possible mechanism of the NOx storage/reduction [36].

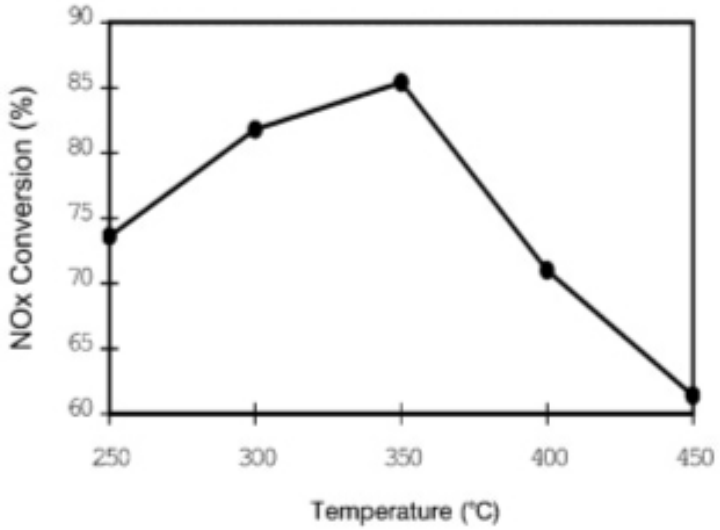

Figure 1.10: Effect of reaction temperature on NO_x conversion over $Pt/BaO/Al_2O_3$ with a 90 s lean phase (SN= 12.3) and a 30 s rich phase (SN= 0.86). Stoichiometry number (SN) = $2[O_2]+[NO]/[CO] +9[C_3H_6]$), GHSV=35.000 L/L/h [37].

- Oxidation of NO to NO_2 (lean period)
- Storage of NO or NO_2 in the form of nitrites or nitrates (lean period)
- Formation of reductants (HCs, CO, and H_2) during rich condition (rich period)
- Release some of NO_x from the stored nitrite or nitrate (rich period)
- Reduction of NO_x into N_2 (rich period)

One major challenge for the NSR system is that NO_x conversion decreases at high gas hourly space velocity (GHSV, short contact times) and high temperatures. Only a high activity can be maintained around 300-350 °C [37, 38], shown in Figure 1.10 at a moderate GHSV of 35.000 L/L/h. The lower NO_x conversion at high temperature is caused by the low NO_x trapping performance with increasing temperature. As shown in Figure 1.11 [39], the catalyst conversion performance severely decreased when the GHSV increased above 30.000 L/L/h. At higher space velocities due to kinetic limitation, the exhaust gasses passing through the catalyst will not have sufficient resi-

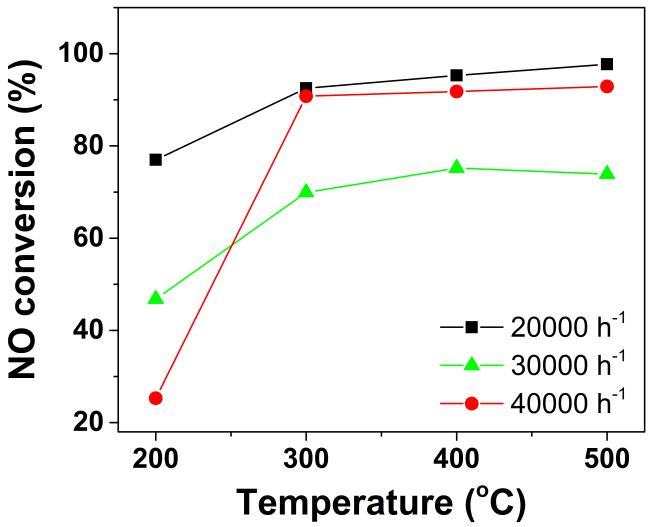

Figure 1.11: Influence of gas hourly space velocity on NSR activity (Catalyst: Pt/BaO/Al_2O_3 particles, alternative pulses of lean and rich were injected under 120 s/20 slean/rich cycles, lean: 500 ppm NO+7.5% O_2+10% CO_2+10% H_2O, rich: 500 ppm NO+7.5% CO +10% CO_2 +10% H_2O) [39].

dence (contact) time to store the NO_x and convert the stored NO_x with the help of reductants. Both will result in a declined conversion performance. Another partially unsolved problem of this NSR catalyst is its deactivation caused by SO_2/SO_3. The formation of stable barium or potassium sulfates and PtS (RhS) species are the main reason for these catalyst deactivations [40, 41].

1.4.2.3. Coupled NSR and SCR system

Recently, coupled NSR and SCR systems are introduced. Ammonia is produced during the regeneration step of the NSR catalyst and then stored on the downstream SCR catalyst. The stored ammonia will further react with NO_x passing through the NO_x-trap during the next lean period, shown in Figure 1.12 [42]. This system requires extensive and detailed chemical engineering knowledge. This coupled system aims to increase the overall NO_x reduction and maximise the N_2 selectivity while preventing ammonia slip. An upstream Diesel particulate filter (DPF) for diesel soot trapping is, however,

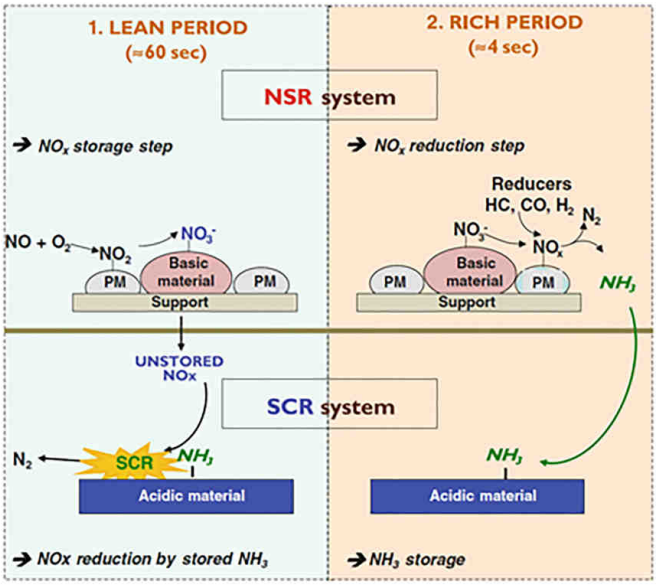

Figure 1.12: Schematic view of the combined NSR + SCR process [42].

required. The NSR-SCR system must be compatible with the DPF working mode. Filter regeneration (the exothermic oxidation of diesel to CO_2) induces severe isotherms (600-700 °C), which exposes NSR-SCR catalysts to a harsh (high temperature) environment. To maintain the durability of this coupled system, the catalysts must exhibit a high thermal stability.

It should be noted once more that the NSR and the NSR-SCR systems will increase the overall fuel efficiency of the cars, up to 2% are claimed, but in practise upto 10% are required.

1.4.2.4. Combined PM and NO_x system

1.4.2.4.1 NO_x reduction with soot

Soot (active carbon) has been used as a reducing agent and a catalyst support for the NO removal from exhaust gasses. However, the application of active carbon as a support is not practical due to its degradation during the oxidation reaction by the exhaust gas stream. Using carbon as a reductant offers obvious advantages, these include: (1) soot is present in the exhaust gas or produced from injected fuel and (2) its oxygen scavenging capability

[43, 44]. The NO reduction by activated carbons originating from different raw materials shows that the NO reduction begins in the temperature range from 250 to 400 °C and exhibits a sharp increase up to 100% conversion above 650 °C [45]. Alkali metals are effective catalysts for the gasification of carbon by H_2O, CO_2, and NO_x [46, 47]. Potassium is the most efficient catalyst: the presence in carbons is responsible for high NO removal at a temperature around 200 °C, and 100% NO reduction at 500 °C [48]. However, this system will be not applicable for the automotive NO_x abatement technologies due to the consumption of soot and/or active carbon during the NO_x reduction process. The refilling of active carbon in the catalyst bed of vehicle after-treatment system is inconvenient. This system will not work for NO_x abatement when no carbon is present.

1.4.2.4.2 Continuously Regenerating Trap (CRT)

Continuously Regenerating Trap (CRT) systems have been used to remove diesel soot, in which a diesel soot oxidation catalyst installed upstream of a wall-flow monolith diesel soot filter will oxidise NO into NO_2. Subsequently, NO_2 reacts with the deposited soot on the filter to form CO_2 and NO. The soot oxidation accelerated by the presence of NO_2 [49]. Simultaneously, only up to 10-15% of NO is converted into N_2 [43]. This method is regarded as a successful method to remove the soot, however, for NO_x reduction, this technology will be not able to meet any of the NO_x emission standards.

1.4.2.4.3 Diesel particulate-NO_x Reduction (DPNR)

Based on the CRT and the NO_x storage reduction technology, Toyota Company has developed the diesel particulate-NO_x Reduction (DPNR) system to remove simultaneously soot and NO_x. The DPNR system contains a cell wall of the diesel particulate filter (DPF) base, coating with NO_x storage and reduction catalyst in the internal pore surfaces. The structure of DPNR is illustrated in Figure 1.13 [50]. NO is oxidised to NO_2 and oxygen is converted to adsorbed oxygen atoms on the Pt-active sites under fuel lean conditions. Most of the NO_2 is converted further to nitrate species and nitrite species on the surface of the storage catalyst. The remaining NO_2 and the absorbed oxygen atoms can directly react with diesel soot. When the exhaust atmosphere becomes rich by fuel injection, nitrate species and nitrite species will

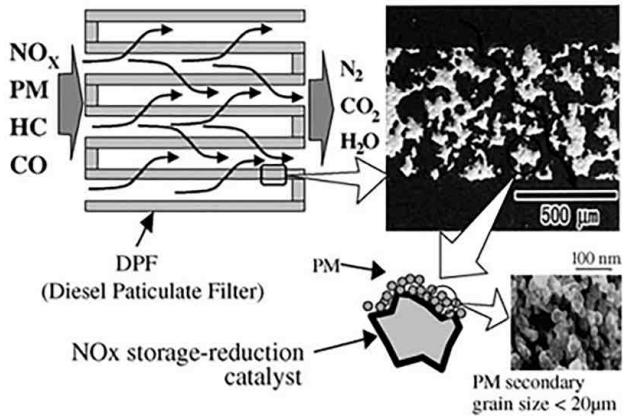

Figure 1.13: The structure of DPNR catalyst (cross-sectional view) [50].

decompose into NO_2, which is then further reduced to N_2 by soot, HCs, H_2, and CO over noble metal sites.

This DPNR system is working under fuel lean and fuel rich conditions. However, during the NO_x storage phase, the PM cannot be oxidised, which affect the efficiency of PM abatement. Moreover, during the fuel rich condition where both NO_x reduction and PM oxidation take place, some of the stored NO_x will be released.

1.4.2.5. Diesel NO_x after treatment by Adsorbed Intermediate Reductants (Di-Air)

Both HC-SCR and NSR systems have a narrow temperature window in which NO_x reduction occurs with an adequate activity. Additionally, the low NO_x storage rate and the relatively low operation temperatures, which are required to store NO_x in NSR systems, limits its application at high gas hourly space velocity (GHSV) condition and temperatures, characteristic for real driving emission performance test (included in future standardised emission tests). The Di-Air (Diesel NO_x after treatment by Adsorbed Intermediate Reductants) system was recently developed by Toyota [51, 52], as illustrated in Figure 1.14. Rather than using post-injection to create fuel rich conditions (NSR system) in the combustion chambers in the engine, the Di-Air system uses high-intensity and high frequency short time fuel injection in the ex-

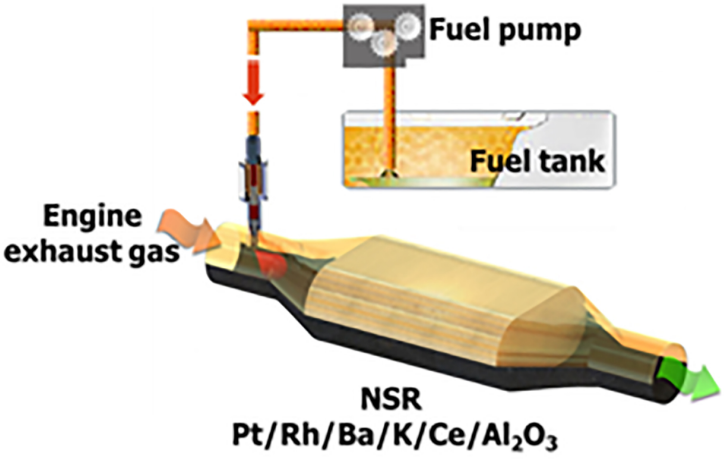

Figure 1.14: Engine exhaust layout of the Di-Air system.

haust pipe upstream of an NSR catalyst to increase the number of richness periods with a small fuel penalty of only 2%. Compared to the NSR system this Di-Air system was found to display a high NO_x reduction activity under overall lean conditions in the exhaust system (shown in Figure 1.15):

- At high gas hourly space velocity (GHSV)
- Over a very broad temperature range, up to 800 °C

As evident from Figure 1.16, small amplitude HC post-injections in the engine are not capable of achieving sufficiently high NO_x conversions, while short duration and high-intensity of HC injections in the exhaust pipe can achieve high NO_x conversions with the same amount of fuel injection. HCs are much more effective reductants than H_2 and CO, although the reason remained largely unclear. As claimed by the Toyota, the formation of intermediates containing C and N, such as iso-cyanates (R-NCO) and nitriles (R-CN) led to the high deNO_x activity under lean conditions. These iso-cyanates (R-NCO) and nitriles (R-CN) were generated from the reaction of HCs with surface adsorbed NO_x. These formed intermediates are thought to be responsible for prolonging the metallic state of noble metal NSR catalyst components under lean conditions and were more thermally stable than intermediates (-NCO and -CN) formed when CO was used as a reductant. Some of these hydrocarbons derived intermediates were presumed to convert to N_2 ei-

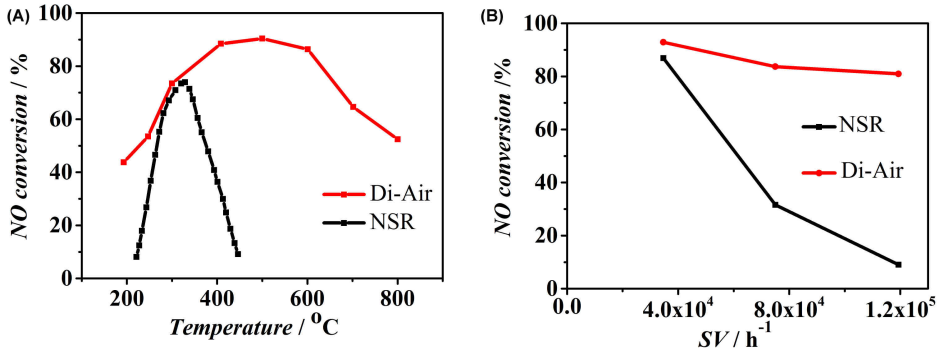

Figure 1.15: Comparison of NO_x conversion between conventional storage and reduction method (NSR) and the Di-Air method as a function of (A) temperature and (B) space velocity (*SV*) [51].

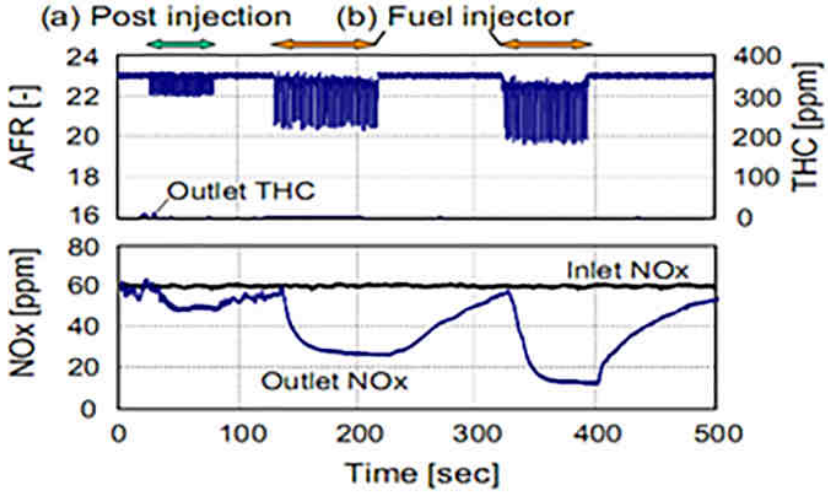

Figure 1.16: Changes in outlet NO_x concentration as a function of HC oscillation amplitude, while the amount of HCs is the same. AFR: air/fuel ratio. Reaction condition: GHSV = 75,000 L/L/h, "NSR" catalyst temperature = 550 °C, (a) = post injection, (b) = fuel injector, injection frequency f = 0.5 Hz [51].

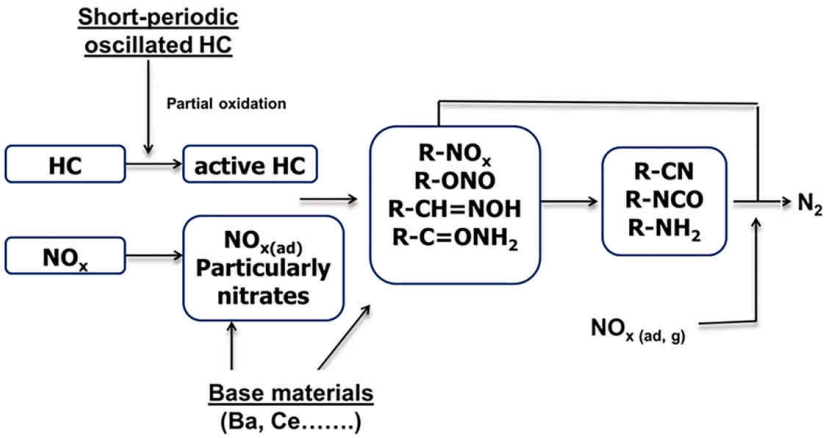

Figure 1.17: The proposed Di-Air reaction mechanism [51, 52].

ther independently or by reacting with close-by NO_x, while some were converted to -CN and -NCO by hydrolysis and could be selectively reduced to NO_x. Upon hydrolysis of these intermediates, many by-products can be expected, and some have been observed in another type of NO_x abatement technology at relatively high NO_x conversion [52, 53], like aldehydes (R-CHO), carboxylic acids (R-COOH), amines (R-NH_2), oximes (R-CNOH), and hydroxylamine (NH_2OH). The proposed Di-Air reaction mechanism is shown in Figure 1.17.

The specific function of HC as a reductant for the NO_x reduction reaction in the Di-Air system remained largely unclear, certainly when considering that an NSR catalyst contains many catalytic components, *e.g.,* Al, Ce, K, Ba, Rh and Pt, further research will be required to explain the reaction mechanism and role of these components.

1.5. Objectives of PhD thesis

Focusing on the Toyota Di-Air deNO_x system, this thesis is aimed to understand and improve this system further to reduce NO_x emissions from lean-burn gasoline and diesel vehicles and to be in compliance with the future stringent NO_x emission standards.

The thesis will emphasise on solving the following research questions:

Q1: What are the mechanistic aspects of the Di-Air process, and the role of each catalytic component (Pt, Rh, K, Ba, Ce, and Al_2O_3) and combinations thereof? Do their combinations have possible synergistic effects on NO_x reduction (conversion rate and temperature)? (Chapter 4 and 5)

Q2: What is the most powerful reductant produced by the fuel injection? Is the formation of "coke" beneficial for NO_x reduction? What is/are the intermediate product(s)? Is it "active coke," "active hydrocarbons," organonitrogen species, or hydrocarbon oxygenates? Or reduced (mixed) metal (oxides)? (Chapter 3)

Q3: What role does oxygen in the lean burn engine exhaust gas play in the deNO_x process? Is it beneficial for NO_x reduction or inhibiting this reaction? What is the performance of the different catalyst components in the presence or absence of oxygen? As the real exhaust contains 5-10% of CO_2 and H_2O, what are the effects of H_2O and CO_2? (Chapter 6 and 7)

1.6. Outline of the thesis

A brief introduction of NO_x abatement and the motivation for developing the new efficient DeNO_x system is presented in Chapter 1. The Temporal Analysis of Products (TAP) [54] technique is the main tool to study the reaction mechansim of the Di-Air system. Therefore, Chapter 2 describes the dedicated home-made instrument for this technique. In addition, the method of experiments data analysis is also included. In Chapter 3, the difference in reductant pre-treatment of ceria is discussed. Fuel pre-treatment will lead to a deeper reduction of ceria support. In additionally, the fuel pre-treatment will result in carbon deposition. These findings are significant to understand why fuel injection is needed for the Di-Air system, and why fuel injection is the most efficient reductant than other reductants, *e.g.,* CO and H_2. Chapter 4 covers the study of the NO reduction mechanism over the reduced ceria catalyst. This understanding is essential to explain the working principle of the Di-Air system. Chapter 5 discusses the role of the noble metals Pt, and Rh on ceria reduction and NO reduction. The competition between NO and an excess of O_2 (simulated exhaust conditions) is shown in Chapter 6, both for ceria, Rh/ceria and Pt/ceria. Chapter 7 further discusses the influence of

the mild oxidant CO_2 on the NO reduction. The competition of NO and (an excess of) CO_2, was further studied in a continuous flow reactor, showing that the presence of excess CO_2 hardly affected the NO reduction process into N_2.

The thesis concludes with a summary of the major results and presents an outlook for further study.

As several chapters have been published in international scientific journals some overlap in information is unavoidable, but they can be read independently.

References

[1] J. G. Canadell, C. Le Quéré, M. R. Raupach, C. B. Field, E. T. Buitenhuis, P. Ciais, T. J. Conway, N. P. Gillett, R. A. Houghton, and G. Marland, *Contributions to accelerating atmospheric CO_2 growth from economic activity, carbon intensity, and efficiency of natural sinks.* Proceedings of the National Academy of Sciences of the United States of America **104**, 18866 (2007).

[2] http://ec.europa.eu/clima/policies/transport/vehicles/cars_en, accessed 2017-05-11.

[3] M. Zheng, G. T. Reader, and J. Hawley, *Diesel engine exhaust gas recirculation—a review on advanced and novel concepts,* Energy Conversion and Management **45**, 883 (2004).

[4] T. V. Johnson, *Vehicular Emissions in Review,* SAE International Journal of Engines **SAE Number 2012-01-0368** (2012).

[5] R. Martinez-Botas, A. Pesiridis, and Y. Mingyang, *Overview of boosting options for future downsized engines,* Sci China Tech Sci **54**, 318 (2011).

[6] http://www.eea.europa.eu/publications/air-quality-in-europe-2015, accessed 2017-04-03.

[7] http://www.who.int/mediacentre/news/releases/2014/air-pollution/en/ (2014), accessed 2017-04-03.

[8] https://www.dieselnet.com/standards/eu (), accessed 2017-04-03.

[9] https://www.dieselnet.com/standards/cycles/eu-ld (), accessed 2017-04-03.

[10] https://www.dieselnet.com/standards/cycles/artemis.php (), accessed 2017-04-03.

[11] http://europa.eu/rapid/press-release_IP-15-5945_en.htm (), accessed 2017-04-03.

[12] https://eospso.gsfc.nasa.gov/sites/default/files/publications/NO$_2$GlobalLenticular_508.pdf, accessed 2017-04-03.

[13] http://www.eea.europa.eu/data-and-maps/figures/annual-mean-no2-concentrations-in-2014 (), accessed 2017-04-03.

[14] http://www.icopal-noxite.co.uk/nox-problem/nox-pollution.aspx, accessed 2017-04-03.

[15] https://www.eea.europa.eu/data-and-maps/indicators/main-anthropogenic-air-pollutant-emissions/assessment-3/emissions-of-the-main-air-pollutants-in-europe (), accessed 2017-04-03.

[16] D. C. Carslaw, S. D. Beevers, J. E. Tate, E. J. Westmoreland, and M. L. Williams, *Recent evidence concerning higher NO_x emissions from passenger cars and light duty vehicles,* Atmospheric Environment **45**, 7053 (2011).

[17] L. Yang, S. Zhang, Y. Wu, Q. Chen, T. Niu, X. Huang, S. Zhang, L. Zhang, Y. Zhou, and J. Hao, *Evaluating real-world CO_2 and NO_x emissions for public transit buses using a remote wireless on-board diagnostic (OBD) approach,* Environmental Pollution **218**, 453 (2016).

[18] M. Weiss, P. Bonnel, J. Kühlwein, A. Provenza, U. Lambrecht, S. Alessandrini, M. Carriero, R. Colombo, F. Forni, G. Lanappe, P. Le Lijour, U. Manfredi, F. Montigny, and M. Sculati, *Will Euro 6 reduce the NO_x emissions of new diesel cars? – Insights from on-road tests with Portable Emissions Measurement Systems (PEMS),* Atmospheric Environment **62**, 657 (2012).

[19] https://www.dieselnet.com/tech/diesel_fi.php (), accessed 2017-04-03.

[20] I. Zeldovich, G. Barenblatt, V. Librovich, and G. Makhviladze, *Mathematical theory of combustion and explosions* (Consultants Bureau,New York, NY, 1985).

[21] J. P. Neeft, M. Makkee, and J. A. Moulijn, *Diesel particulate emission control,* Fuel Processing Technology **47**, 1 (1996).

[22] K. Hirata, N. Masaki, H. Ueno, and H. Akagawa, *Development of Urea-SCR System for Heavy-Duty Commercial Vehicles,* SAE International Journal of Engines **SAE Number 2005-01-1860** (2005).

[23] http://en.greenchem-adblue.com/passenger-cars-vans/adblue-cars-and-light-commercial-vehicles, accessed 2017-04-03.

[24] J. Li, H. Chang, L. Ma, J. Hao, and R. T. Yang, *Low-temperature selective catalytic reduction of NO_x with NH_3 over metal oxide and zeolite catalysts—A review,* Catalysis Today **175**, 147 (2011).

[25] F. Kapteijn, A. D. Vanlangeveld, J. A. Moulijn, A. Andreini, M. A. Vuurman, A. M. Turek, J.-M. Jehng, and I. E. Wachs, *Alumina-supported manganese oxide catalysts: I. Characterization: effect of precursor and loading,* Journal of Catalysis **150**, 94 (1994).

[26] F. Kapteijn, L. Singoredjo, M. Vandriel, A. Andreini, J. A. Moulijn, G. Ramis, and G. Busca, *Alumina-supported manganese oxide catalysts: II. Surface characterization and adsorption of ammonia and nitric oxide,* Journal of Catalysis **150**, 105 (1994).

[27] L. Zhang, L. Shi, L. Huang, J. Zhang, R. Gao, and D. Zhang, *Rational Design of High-Performance DeNO$_x$ Catalysts Based on Mn$_x$Co$_{3-x}$O$_4$ Nanocages Derived from Metal–Organic Frameworks,* ACS Catalysis **4**, 1753 (2014).

[28] F. Liu, Y. Yu, and H. He, *Environmentally-benign catalysts for the selective catalytic reduction of NO$_x$ from diesel engines: structure–activity relationship and reaction mechanism aspects,* Chemical Communications **50**, 8445 (2014).

[29] J. H. Kwak, D. Tran, S. D. Burton, J. Szanyi, J. H. Lee, and C. H. Peden, *Effects of hydrothermal aging on NH$_3$-SCR reaction over Cu/zeolites,* Journal of Catalysis **287**, 203 (2012).

[30] D. W. Fickel, E. D'Addio, J. A. Lauterbach, and R. F. Lobo, *The ammonia selective catalytic reduction activity of copper-exchanged small-pore zeolites,* Applied Catalysis B: Environmental **102**, 441 (2011).

[31] E. Tronconi, I. Nova, C. Ciardelli, D. Chatterjee, and M. Weibel, *Redox features in the catalytic mechanism of the "standard" and "fast" NH$_3$-SCR of NO$_x$ over a V-based catalyst investigated by dynamic methods,* Journal of Catalysis **245**, 1 (2007).

[32] F. Willems, R. Cloudt, E. van den Eijnden, M. van Genderen, R. Verbeek, B. de Jager, W. Boomsma, and I. van den Heuvel, *Is Closed-Loop SCR Control Required to Meet Future Emission Targets?* (2007), 10.4271/2007-01-1574.

[33] M. van Nieuwstadt and D. Upadhyay, *Control of Urea SCR Systems for US Diesel Applications,* Oil & Gas Science and Technology – Revue d'IFP Energies nouvelles **66**, 655 (2011).

[34] R. Burch, *Selective reduction of nitrogen oxides by hydrocarbons under lean-burn conditions using supported platinum group metal catalysts,* Catalysis Today **26**, 185 (1995).

[35] N. Aoyama, K. Yoshida, A. Abe, and T. Miyadera, *Characterization of highly active silver catalyst for NO$_x$ reduction in lean-burning engine exhaust,* Catalysis Letters **43**, 249 (1997).

[36] G. Liu and P. Gao, *A review of NO$_x$ storage/reduction catalysts: mechanism, materials and degradation studies,* Catalysis Science & Technology **1**, 552 (2011).

[37] P. H. Han, Y. K. Lee, S. M. Han, and H. K. Rhee, *NO_x Storage and Reduction Catalysts for Automotive Lean-Burn Engines: Effect of Parameters and Storage Materials on NO_x Conversion,* Topics in Catalysis **16/17**, 165 (2001).

[38] J. Lee and H. H. Kung, *Effect of Pt dispersion on the reduction of NO by propene over alumina-supported Pt catalysts under lean-burn conditions,* Catalysis Letters **51**, 1 (1998).

[39] J. Wang, Y. Wang, S. Liu, J. Gao, J. Ma, and M. Shen, *The Study on the Capacity of NO_x Storage-Reduction Catalyst for Lean-Burn Engine,* (Springer, Berlin, Heidelberg, 2013) pp. 599–608.

[40] J. Breen, M. Marella, C. Pistarino, and J. Ross, *Sulfur-Tolerant NO_x Storage Traps: An Infrared and Thermodynamic Study of the Reactions of Alkali and Alkaline-Earth Metal Sulfates,* Catalysis Letters **80**, 123 (2002).

[41] E. Fridell, H. Persson, L. Olsson, B. Westerberg, A. Amberntsson, and M. Skoglundh, *Model Studies of NO_x Storage and Sulphur Deactivation of NO_x Storage Catalysts,* Topics in Catalysis **16/17**, 133 (2001).

[42] F. Can, X. Courtois, S. Royer, G. Blanchard, S. Rousseau, and D. Duprez, *An overview of the production and use of ammonia in NSR+SCR coupled system for NO_x reduction from lean exhaust gas,* Catalysis Today **197**, 144 (2012).

[43] M. J. Illán-Gómez, A. Linares-Solano, L. R. Radovic, and C. Salinas-Martínez de Lecea, *NO Reduction by Activated Carbons. 7. Some Mechanistic Aspects of Uncatalyzed and Catalyzed Reaction,* Energy & Fuels **10**, 158 (1996).

[44] M. Illán-Gómez, E. Raymundo-Piñero, A. García-García, A. Linares-Solano, and C. Salinas-Martínez de Lecea, *Catalytic NO_x reduction by carbon supporting metals,* Applied Catalysis B: Environmental **20**, 267 (1999).

[45] M. J. American Chemical Society., A. LINARES-SOLANO, C. SALINAS-MARTINEZ DE LECEA, and J. M. CALO, *Energy & fuels.* Energy & fuels **7**, 146 (1987).

[46] F. Kapteijn, A. J. C. Mierop, G. Abbel, and J. A. Moulijn, *Reduction of NO_x over alkali metal–carbon systems,* J. Chem. Soc., Chem. Commun. **16**, 1085 (1984).

[47] J. A. Moulijn, M. Cerfontain, and F. Kapteijn, *Mechanism of the potassium catalysed gasification of carbon in CO_2,* Fuel **63**, 1043 (1984).

[48] M. J. Illan-Gomez, A. Linares-Solano, L. R. Radovic, and C. Salinas-Martinez de Lecea, *NO Reduction by Activated Carbons. 2. Catalytic Effect of Potassium,* Energy & Fuels **9**, 97 (1995).

[49] K. Krishna, A. Bueno-López, M. Makkee, and J. Moulijn, *Potential rare earth modified CeO_2 catalysts for soot oxidation: I. Characterisation and catalytic activity with O_2,* Applied Catalysis B: Environmental **75**, 189 (2007).

[50] J. Suzuki and S. Matsumoto, *Development of Catalysts for Diesel Particulate NO_x Reduction,* Topics in Catalysis **28**, 171 (2004).

[51] Y. Bisaiji, K. Yoshida, M. Inoue, K. Umemoto, and T. Fukuma, *Development of Di-Air - A New Diesel deNO_x System by Adsorbed Intermediate Reductants,* SAE International Journal of Fuels and Lubricants **SAE Number 2011-01-2089** (2011).

[52] M. Inoue, Y. Bisaiji, K. Yoshida, N. Takagi, and T. Fukuma, *DeNO_x Performance and Reaction Mechanism of the Di-Air System,* Topics in Catalysis **56**, 3 (2013).

[53] K. Yoshida, Y. Nozaki, T. Mori, Y. Bisaiji, Y. Haba, K. Umemoto, and T. Fukuma, *Development of NSR and DiAir System to Achieve Clean Emissions under Transient Cycle,* SAE International Journal of Fuels and Lubricants **SAE Number 2011-01-2089**.

[54] J. T. Gleaves, J. R. Ebner, and T. C. Kuechler, *Temporal Analysis of Products (TAP)-A Unique Catalyst Evaluation System with Submillisecond Time Resolution,* Catalysis Reviews **30**, 49 (1988).

2

Temporal Analysis of Products

If you can't explain it simply,
you don't understand it well enough.

Albert Einstein

2

This chapter will give an overview of the Temporal Analysis of Products technology, the developed and home-built instrument, and its application to the project described in this thesis.

2.1. Introduction

2.1.1. What is TAP

Temporal Analysis of Products (TAP) is a vacuum pulse-response technique, developed by John T. Gleaves in 1988 [1]. By using a pulse valve small and narrow reactant gas pulses are introduced to a small finite volume (pre-volume) upstream of a packed catalyst bed. The introduced molecules, and eventually formed products upon interaction with the catalyst, diffuse through the packed catalyst bed in the Knudsen diffusion transport regime until they leave the packed bed, where they are recorded *versus* time (temporal response) by a mass spectrometer (MS). The TAP is working at an ultra- to high vacuum condition ($<10^{-8}$-10^{-9} mbar).

A typical TAP pulse-response concept is presented in Figure 2.1. The key components of a TAP setup include a fast gas pulse feed system, a reactor, a mass spectrometer, and a high-throughput (ultra-)high vacuum system. Upstream of the reactor the gas pulse from the gas feedline will be introdced, and downstream of the reactor is close to the MS that detects the eluting gas. The eluting gas leaving the reactor through is detected as a flux by the MS. The contribution of the local concentration in the vacuum chamber at the point of the MS can be neglected as: (1) the MS is located directly under the reactor exit; (2) the MS has a cross-beam ionisation chamber, which prevents molecules that have collided from the vacuum vessels wall to enter the ionisation chamber; and (3) the concentration at the MS is very low (maximum pressure in the order of 3.10^{-7} mbar after pulse introduction). For a typical experiment it has been calculated that at the worst 2.5% of the response is comprised of a contribution from the increased vacuum chamber concentration due to the reactor exit flux. During the experiments, the whole reactor is continuously evacuated.

In a typical TAP pulse experiment, the pulsed mixture contains reactant and an inert gas, which acts as an internal standard. Consequently, the flux of reactants, products, and inert gas are monitored by the MS.

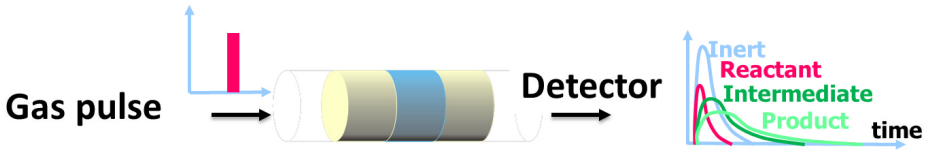

Figure 2.1: Schematic TAP pulse-response diagram.

2.1.2. Why TAP

The TAP technique has applications in many areas, *e.g.,* chemical kinetics and chemical engineering [2, 3] due to the following characteristics [1]: (1) Submillisecond time resolution. TAP provides sufficient time resolution for reactions thus offering two or more orders of magnitude better time resolution, as compared to other techniques [4, 5], *e.g.,* flow reactor studies with gas chromatography, Infrared and UV-Vis spectroscopic analyses. (2) Negligible change in the catalyst (oxidation state) upon a single pulse, *i.e.,* a single reactant pulse does not significantly influence the state of the catalyst. (3) Gas transport is well-defined and external mass-transfer limitations are implicitly handled by the Knudsen diffusion model. Knudsen diffusion governs gas transport through the catalyst bed and void volumes (unpacked channels). In the Knudsen diffusion regime molecules collide mainly with the catalyst or channel walls and the diffusivity in a packed bed is given by Equation 2.1 and 2.2 [6, 7]:

$$D_{kn} = \frac{\varepsilon_b}{\tau}\frac{2\bar{r}}{3}\sqrt{\frac{8RT}{\pi M}} \tag{2.1}$$

$$\bar{r} = \frac{2\varepsilon_b}{3(1-\varepsilon_b))}\gamma_p \tag{2.2}$$

With:

D_{kn}:	Knudsen diffusion coefficient
ε_b:	bed porosity
τ_b:	bed tortuosity
γ_p:	average particle radius
$\bar{r}$:	the average particle distance

The exit flux of an inert, non-interacting gas (Ar, Kr, or Ne, *etc.*) is purely

Figure 2.2: Photograph of the new TAP in Delft.

governed by a diffusional transport. The inert gas response can be regarded as a standard diffusion response curve for the packed bed, while a viscous flow contribution can be neglected [2]. In the case of a reaction or surface interaction, the exit flux will contain information about reactions, interactions (adsorption and desorption), and diffusion. Deviation from the standard diffusion response curve is an evidence of an additional gas-solid interaction or reaction, including the elementary steps of reactant adsorption, desorption, surface diffusion, surface reaction, and product desorption. TAP response data provide the identity, amount, and residence time of different species exiting from the TAP reactor, which makes it an ideal tool to investigate catalytic reaction mechanisms.

Inspired by the TAP system developed by John T. Gleaves, Delft University built a small new TAP instrument. Figure 2.2 shows the photograph of the new TAP machine in our lab.

2.1.3. Knudsen diffusion

Gas diffusion is a process where gas molecules randomly move from a region of high concentration (pressure) to a low concentration (pressure).

When the gas molecules collide with the walls of the reactor more frequently than with each other, this diffusion process is known as Knudsen diffusion. The diffusion is controlled by Knudsen diffusion, when the scale length of a system (diameter in the case of a circular channel, L) is comparable to, or smaller than the mean free path of the molecules (λ).

The Knudsen number (Kn), expressed as the mean free path divided by the scale length (Equation 2.3), provides a good measure of the relative importance of Knudsen diffusion.

$$Kn = \frac{\lambda}{L} \gg 1 \tag{2.3}$$

When Kn » 1, it indicates that Knudsen diffusion starts to become dominant.

When Kn > 1-10, collisions with reactor channel walls start to prevail over collisions with other molecules. As a consequence homogeneous reactions between molecules in the gas-phase can be considered non-exsistent in the Knudsen diffusion regime.

When Kn < 0.1, the transport of gas molecules is governed by a mix of molecular diffusion and viscous flow. In this (flow) regime, gas molecules frequently collide with each other, but less frequently with the channel walls. Molecules push each other forward. Therefore, the mean free path of the gas molecules is significantly shorter than the dimensions of the channel of reactor. This unwanted regime is poorly amenable for a good modeling description.

2.1.4. Typical TAP pulse experiments

2.1.4.1. Single-pulse TAP experiments

A single pulse TAP experiment can be considered as a state-defining experiment, since the catalyst surface state will hardly change. The number of catalyst surface atoms is typically 100,000 times that of the number of

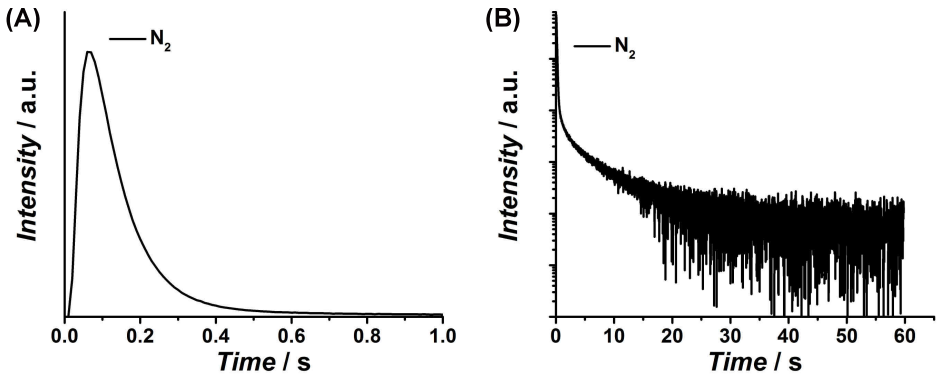

Figure 2.3: N_2 response upon a single NO pulse over H_2 pre-reduced Zr-La doped ceria at 500 °C. The given response is the average of 8 pulse responses with pulse size at $1.6 \cdot 10^{15}$

molecules in a pulse [1]. In that sense the single pulse experiment probes or characterises the catalyst state. This single-pulse TAP experiment is mostly used qualitatively. In practice the data cannot be quantified unless it is part of a multi-pulse sequence. Figure 2.3A and B shows a N_2 product response during a single NO reactant pulse over a H_2 reduced ceria at 500 °C for a 1 s and 60 s time sample period, respectively. In addition to, a relatively fast N_2 formation visible in Figure 2.3A, a much slower N_2 formation process can be identified from Figure 2.3B, as is evident from the slower decay of the N_2 signal over the period 5-30 s.

2.1.4.2. Multi-pulse TAP experiments

A multi-pulse TAP experiment involves injecting a series of reactant gas pulses over a catalyst sample, *i.e.,* a sequence of single pulse experiments. A multi-pulse experiment gradually alters the catalyst surface and/or bulk. For example, the reduction of ceria can be characterised by the total amount of H_2O formation in an H_2 multi-pulse experiment. Moreover, multi-pulse experiments are useful to probe the reactivity and selectivity of reactants for catalytic reactions as a function of catalyst oxidation state (Chapter 3).

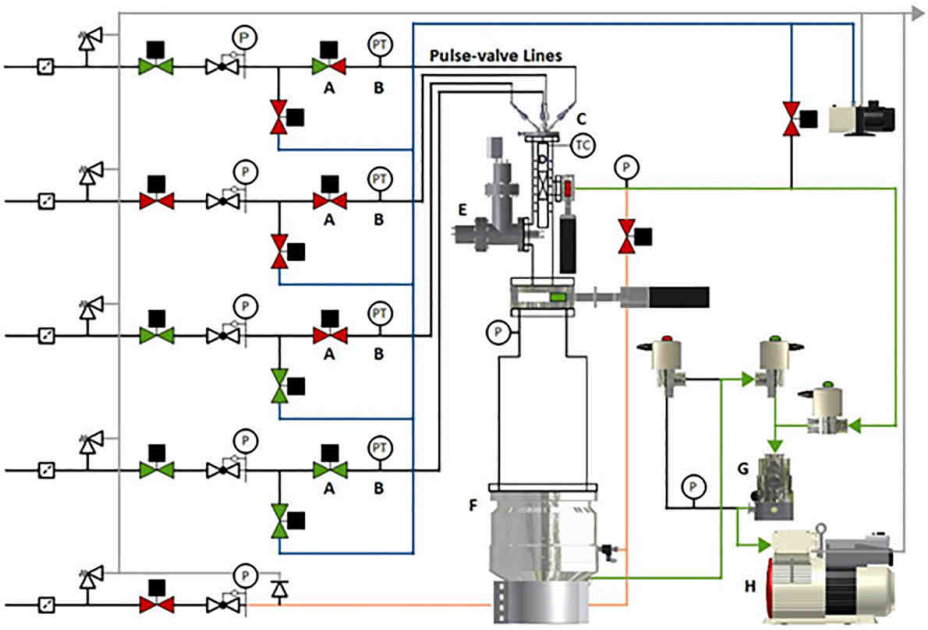

Figure 2.4: Schematic of TAP setup with main components indicated: A - dosing valve; B – pulse-valve line pressure and temperature sensors; C – pulse valves and pulse-valve manifold; D - reactor and oven; E - mass spectrometer; F – turbomolecular pump; G – turbomolecular drag pump; and H – backing pump.

2.1.4.3. Pump-probe TAP experiments

In a pump-probe experiment, two different reactants are sequentially pulsed from two pulse valves with a certain delay time (Δt) between the two pulses. The delay time between the two pulses can be varied from 0 to several seconds. In such a pump-probe experiment, information about the lifetime, reactivity and selectivity of 'invisible' adsorbed surface species can be obtained (Chapter 5).

2.2. Description of TAP system

The basic operation of our new TAP system is similar to that of the TAP system developed by John T. Gleaves. Our new TAP system consists of a

gas-supply system, heated reactor, detector, and a vacuum system. Figure 2.4 shows a schematic flow diagram of the new TAP setup in Delft. The main difference between our new TAP and that of Gleaves are:

- The use of turbo-molecular vacuum pumps (1800 L/s) instead of an oil diffusion pump (10000 L/s), and therefore, there is no need for a liquid nitrogen oil trap system (no oil contamination). The base pressure achieved by the vacuum system is in the range of 10^{-9}-10^{-10} mbar, which is even lower than that obtained by using an oil diffusion pump of a much higher capacity
- Higher measurement frequency. Sampling rates up to 500 kHz are possible to obtain clear response shapes. In a typical experiment, 10 kHz was applied, which already provides a clear response
- A smaller vacuum chamber in order to obtain lower based pressure
- Reactor is placed inside the vacuum chamber in order to minimise/avoid leakage

2.2.1. Gas supply

The four reactant feed gas lines are evacuated using a Pfeiffer Uno 2.5 rotary vane pump. A Pfeiffer DVI 005 M low leak rate ($< 1 \cdot 10^{9}$ mbar L/s) electromagnetically actuated dosing valve (A in Figure 2.4) is used to fill a pulse-valve line with reactant gas and seal-off its calibrated volume (13.6 mL). The pressure of a pulse-valve line is measured by a Pfeiffer CMR 271 high precision temperature controlled capacitive gauge (0-1100 mbar, B in Figure 2.4) and logged using the serial interface of its Pfeiffer TPG 256 A controller. The temperature of a pulse-valve line pressure gauge is measured by a type K thermocouple (B in Figure 2.4). The temperature data was logged using a National Instruments USB-9211A thermocouple ADC.

Four ultra-high speed pulse-valves, Parker Hannifin Series 9, are used to supply a pulse to the reactor. Theses pulse valves and the reactor are installed on a water-cooled custom conflat manifold (B in Figure 2.5). The pulse valve connection is sealed with a Viton O-ring. The pulse valves are activated by externally triggered Parker Hannifin Iota One pulse-valve drivers. The pulse valves have an opening delay of approximately 370 µs upon a 380 Vdc over-

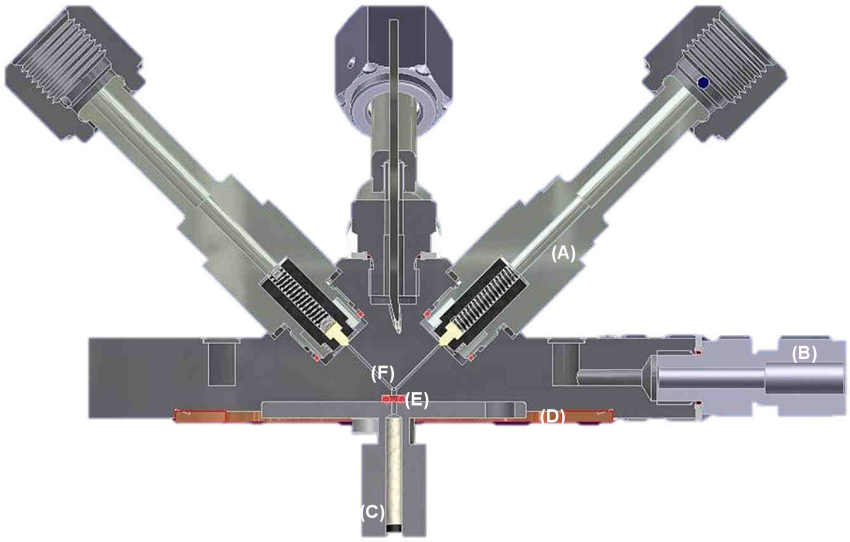

Figure 2.5: Drawing of the Valve Manifold. (A) Pulse Valve, (B) water cooling, (C) reactor, (D) copper seal, (E) O-ring, and (F) pre-volume.

driven voltage pulse, which is provided by the pulse valve driver when the voltage pulse duration is < 160 µs. The maximum pulse size is currently limited to $5 \cdot 10^{15}$ molecules under MS operation, as larger pulse sizes trigger the mass spectrometers ionisation filament protection circuit. The practical minimum pulse size is about $1 \cdot 10^{13}$, as smaller pulse sizes cannot be quantified accurately. The pulse-valve timing and triggering is processed by a National Instruments PCIe-6341 data acquisition card.

2.2.2. Reactor and oven

The stainless steel 304L reactor consists of two sections. The top section, which can be filled or left void (optional second grid) has a length of 3 mm and an internal diameter of 1 mm. The bottom section, which is meant to be packed, has a length of 27 mm and an internal diameter of 3 mm (C in Figure 2.5, Figure 2.6). The catalyst is sandwiched between two quartz particles (150-212 µm) yielding a total bed length of 27 or 30 mm and held in place by two or a stainless steel grid(s), for a void or filled first section, respectively (Figure 2.7). In the experiments performed for this thesis a filled top section

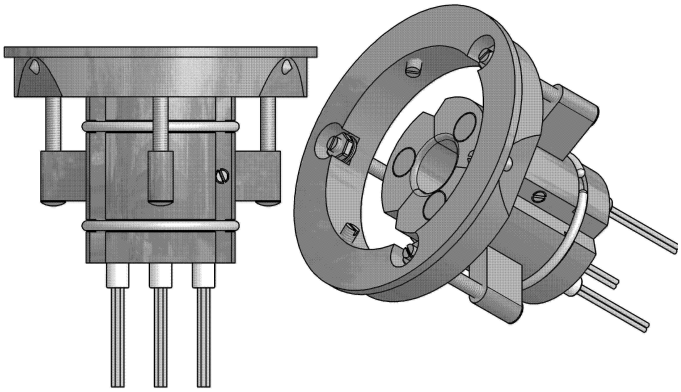

Figure 2.6: Drawing of the reactor heating system.

is always used. A stainless steel 304L extension tube mounted on top of the reactor fixes the (lower) grid and guides the reactor exit to within 7 mm of the mass spectrometer cross-beam ionisation entrance (Figure 2.7).

The reactor is coupled to the pulse-valve manifold and sealed by a Kalrez O-ring. The volume between the pulse-valve exit and the packed catalyst bed, called pre-volume, is around 12.09 µL for a packed top section or 14.45 µL for a void top section (F in Figure 2.5).

A three-segment stainless steel 304L oven surrounds the reactor (Figure 2.6), two snap rings press the oven segments against the reactor. Each oven segment is heated by a heating element (Watlow Firerod, 35 mm x 6.5 mm, 80 VAc, 50 W). The heating rod elements are connected in series and receive power from a Eurotherm TE10A (16 A, advanced single cycle) thyristor. The reactor temperature is currently limited to a maximum temperature of 600 °C (85-87% output power) due to an unfavourable magnetic pole configuration formed by the 3 oven segments, which causes segment repulsion and causes unstable temperatures at higher output power. The reactor temperature is measured by a type K thermocouple placed in the reactor wall at the height of the catalyst bed (Figure 2.6) and controlled by a Eurotherm 2216e single loop controller. The temperature of the reactor is logged using the oven temperature controller's serial interface.

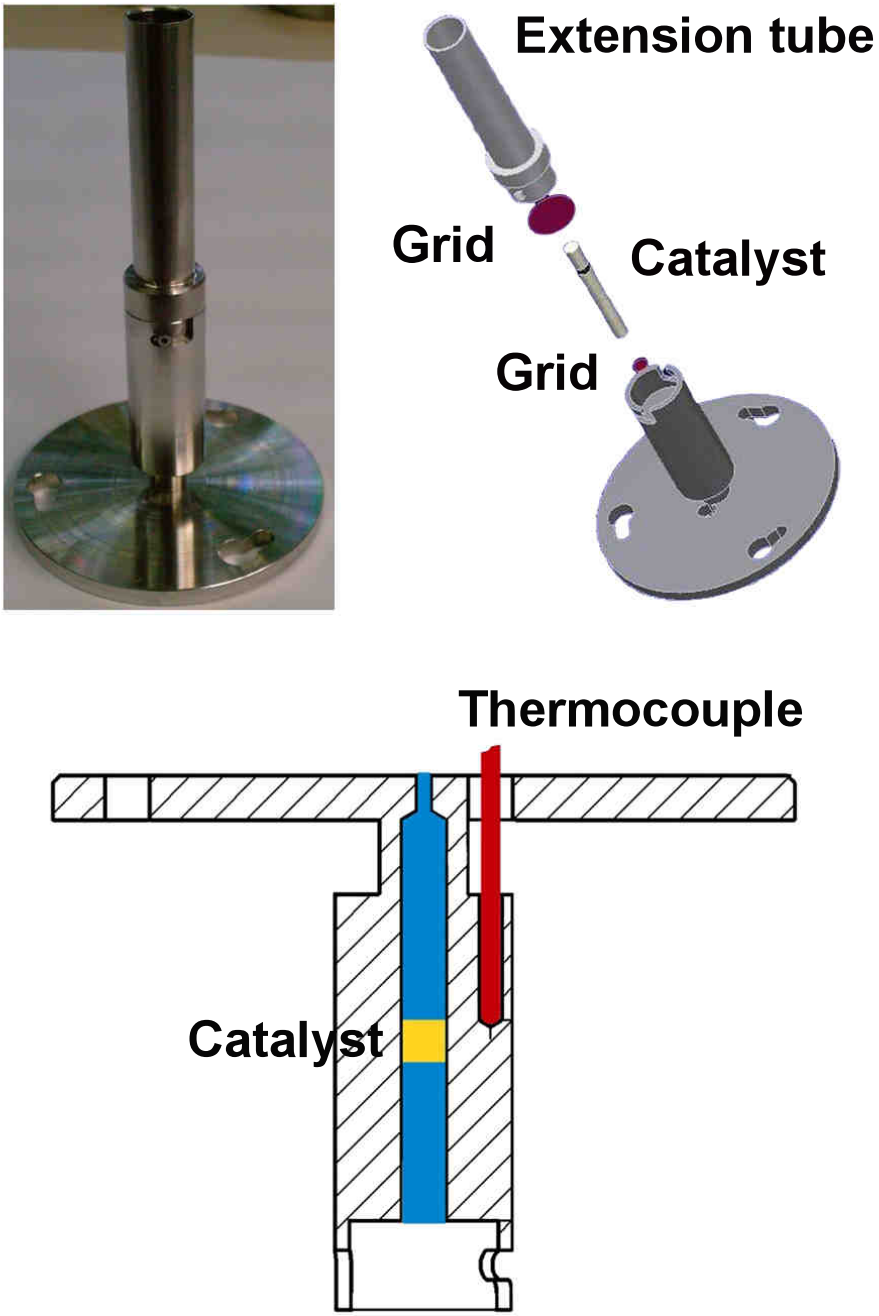

Figure 2.7: Photograph and drawing of the reactor.

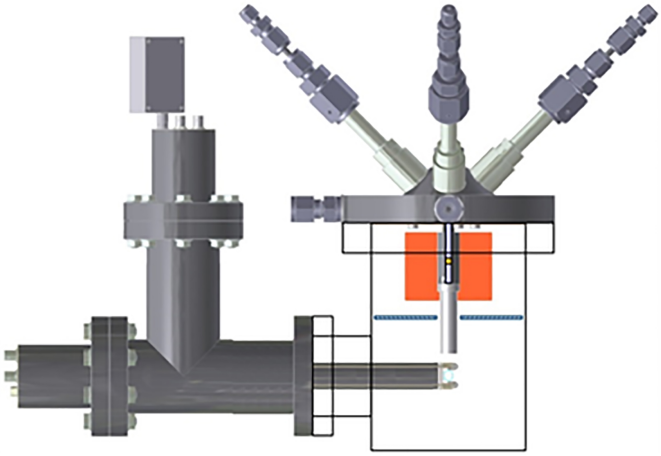

Figure 2.8: Crossbeam mass spectrometer in the TAP system.

2.2.3. Detector

A quadrupole mass spectrometer is used to measure the response of a specified mass. The used Pfeiffer QMG 422 Quadrupole mass spectrometer system consists of a QMA 125 mass analyser, QME 125 mass filter electronics (0-100 amu), QC 422 quadrupole controller, and an EP 422 electrometer. The QMA 125 mass analyser is composed of a crossbeam ionizer, two tungsten filaments and a discrete dynode secondary electron multiplier (E in Figure 2.4 and Figure 2.8). The EP 422 electrometer is employed at the lowest amplification setting, yielding an output signal rise time of 50 µs.

A Faraday shield (gauze) mounted beneath the oven and surrounding the reactor extension tube prevents electromagnetic interference from the oven heaters with the mass spectrometer. This yields response signals void of 50 Hz noise. The collected response signals contain only random noise, no noise related to a specific frequency could be identified. The response obtained upon a single pulse already has a good signal-to-noise ratio, 260 at the response signal maximum of 7.0 V at an average noise level of 0.027 V (Figure 2.9A). A clean noise free response is typically obtained after averaging 10 responses (Figure 2.9B). The mass spectrometers current amplifier (electrometer) has four physical gain levels, set by selecting feedback resistors (a higher feedback resistor value means a higher gain). The feedback

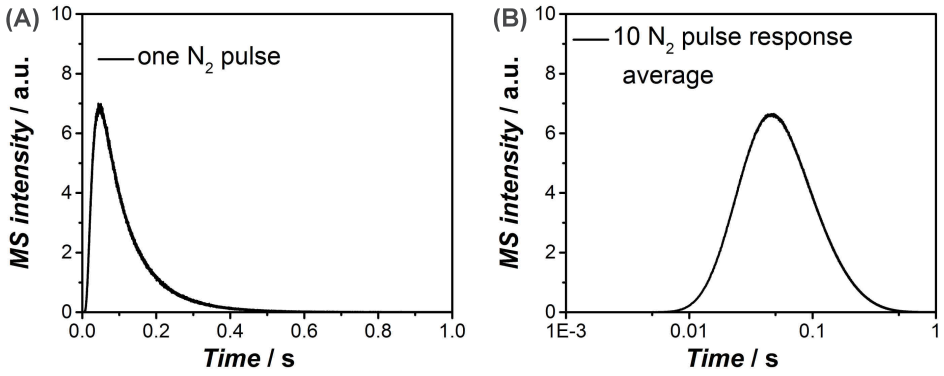

Figure 2.9: N_2 response upon a N_2 pulse over Pt/ceria at room temperature: (A) a single N_2 response signal(B) an averaged N_2 response signal obtained over 10 N_2 response signals. N_2 pulse size: $1.6 \cdot 10^{15}$ molecules/pulse, SEM voltage: 2800 V.

resistor, together with the operational amplifiers input capacitance and stray capacitance on the circuit board, form an input RC filter. This means that although the signal-to-noise ratio can considerably be improved by selecting a higher gain value, the amplifiers voltage output might not longer be able to follow the input SEM current signal (too large output signal rise time). For typical TAP experiments only the two lowest gain settings of the electrometer guarantee that undistorted response signals are obtained. All presented TAP results are obtained using the lowest gain setting of the electrometer. The mass spectrometer electrometer output signal data acquisition is processed by a National Instruments PCIe-6341 (500 kHz 16-bit ADC) data acquisition card.

2.2.4. Vacuum system

Ultra-high-vacuum (base pressure < $5 \cdot 10^{-10}$mbar) is generated by a Pfeiffer TPU 2301 P turbomolecular pump (1800 L/s N_2, F in Figure 2.4) and a Varian vacuum backing pump (H in Fifure 2.4). In order to enhance the pumping effectiveness of light gases, *e.g.,* H_2, a Pfeiffer TMH 071 P turbomolecular drag pump (60 L/s N_2, G in Figure 2.4) is switched in series with the main turbomolecular pump. The vacuum level is measured by a Pfeiffer PBR 260 automatically switching Bayard Alpert hot cathode ionisation or Pirani gauge and logged using the serial interface of its Pfeiffer TPG 256 A controller.

2.3. TAP experimental

Typically 10 to 20 mg of catalyst is sandwiched between two quartz particles (150-212 µm) beds, approximately 128 mg above and 90 mg below (Figure 2.6), yielding a total bed height of 30 mm. The packed bed is held in place by a stainless steel grid. The pre-volume between the four pulse-valve exits and the packed catalyst bed amounts to 12.09 µL.

All used gases contained either 20 vol.% Ar (33 vol.% Ar for H_2) or Ne (C_3H_6 and C_3H_8) as internal standard. For a reliable quantification, the use of an internal standard is required in order to compensate for drift in the mass spectrometer's secondary electron multiplier. All the $^{18}O_2$ experiments were performed without internal standard and are, therefore, not quantified.

In multi-pulse and co-pulse experiments a starting pulse size of approximately $1.6 \cdot 10^{15}$ molecules/pulse, excluding internal standard, was applied. The starting pressure in a closed off and calibrated volume (13.6 mL) of the pulse valve feed line was between 900 and 1000 mbar. For a multi-pulse experiment the collection time used to collect a single mass was 5.1 s, the pulse valve was triggered at 0.1 s. For a co-pulse experiment this collection time was 10.1 s, while the first pulse valve was triggered at 0.1 s and the second at 5.1 s. The sample frequency of the amplified MS signal was 10 KHz, using the lowest gain setting of the electrometer.

Typically in a TAP experiment, a sequence of several masses (*m/e*) is sampled alternatingly, *e.g.,* 5.1 s for the first mass in the sequence, followed by 5.1 s for the next mass in sequence until after the last mass in sequence this sequence is repeated. The number of masses, and hence the number ofpulses, required are determined by the used reactants, internal standard, the expected products and the interference of their ionisation fragments.

Before the start of an experiment, after loading the reactor at least 24 h is delayed, the background MS signal is recorded for 5.1 s per mass, while no pulses are introduced, for at least an hour for all masses to be sampled in the actual experiment (system baseline level). After an experiment (which might be an oxidation pulse train followed by an immediate reduction pulse train), all masses used in the actual experiment are sampled for 5.1 s per mass, while no pulses are introduced, until all background levels have decayed to stable levels, after this the background MS signal is recorded for 5.1 s per

mass, while no pulses are introduced, for at least an hour for all masses to be sampled in the actual experiment (system baseline level).

Besides the collection of the MS response data for all masses sampled, the following process variables are collected at 1 minute intervals:

- pressures and temperatures of the pulse valve feed lines
- pressure in the vacuum chamber
- reactor temperature
- oven heating output power

2.4. Quantification of TAP data

This section describes the quantification of a TAP multi-pulse experiment. In order to perform a meaningful quantification it is vital to have a stable catalyst, *e.g.,* no irreversible catalyst weight loss, no substantial irreversible loss of (specific) surface area and repeatable catalytic performance. Further prerequisites are a stable mass spectrometer with regards to ionisation yields and the amplification by means of the secondary electron multiplier.

The collected MS signal for all relevant masses is used to quantify the observed reaction products and unreacted reactants, while the recorded feed line pressure and temperature (used to correct the feed line pressure for temperature fluctuations) are used to obtain an equation that gives the pulse size of a known composition for any pulse in the multi-pulse experiment. During a multi-pulse experiment the pulse size decreases over the experiment, as the molecules are pulsed from a calibrated volume. As both the input and output molecules are quantified, a molar balance can be obtained. These molar balances for C, N and O species close within 15% for the quantified TAP experiments within this thesis.

2.4.1. MS signal integration

The quantification of weakly interacting species is fairly straight-forward, as a distinct response is observed, which after baseline correction can be numerically integrated over time. Reaction products and unreacted reactants

can, however, have a strong interaction with the catalyst, quartz bed, and reactor walls. No interaction have been found between neither quartz nor reactor in the performed experiments leading up to this thesis. Several components did, however, exhibit a strong interaction with the catalyst, *e.g.,* CO with oxidised and reduced La- and Zr- doped ceria. This interaction can be so strong, that the resulting response would have a width spanning several minutes. In these situations it is not practical to record the whole response, as experiments would simply take too long. Within the 5.1 s data collection time typically used for obtaining the response of one single mass, for a strongly interacting species no distinct response will be observed. Besides CO, also CO_2 and H_2O had no distinct response over the ceria-based catalysts. However, quantification is still possible when the increase in the baseline signal of these strongly interacting species (CO, CO_2, and H_2O) are considered.

A general procedure regarding the quantification of TAP response data is desired, as for example a TAP multi-pulse experiment can consist of 20.000 response data files or more. The quantification is, therefore, split in two parts, the integration of the 'visible' response (response signal area) and the integration of the slow desorbing molecules 'hidden' in the baseline level (baseline signal area). Hereafter the used terminology and procedures are explained. For that purpose an illustration multi-pulse experiment is shown in Figure 2.10. This illustration multi-pulse experiment, of which one response is shown in Figure 2.10A for a single arbitrary mass and the evolution of the baseline signal for that same arbitrary mass in Figure 2.10B, consists of the following stages:

- pulse number 0 – 2000, period in which the system baseline level is determined prior to the actual multi-pulse experiment, no pulses are given
- pulse number 2000 – 7000, period in which the actual multi-pulse experiment is performed
- pulse number 7000 – 10000, period in which molecules are allowed to desorb from the catalyst surface, no pulses are given
- pulse number 10000 – 12000, period in which the system baseline level is determined after the actual multi-pulse experiment, no pulses are given

It should be noted that upto 12000 pulses, the MS should be extreamely

stable in ordder to obtain quantification.

2.4.1.1. System baseline level

The system baseline level represents the (fictitious) MS signal for a certain mass that would have been obtained when no pulse experiment is performed, *i.e.,* the long-term background MS signal for that mass. These signals arise from molecules desorbing of vacuum vessel walls, *e.g.,* H_2O, which have not been pumped, back-diffusion through the vacuum pumps, and MS electrometer/current amplifier offset voltage. These signals, with the exception of the offset voltage, have the tendency to decay especially following a change of reactor contents or an increase in reactor temperature.

The system baseline level is collected for all masses used in the actual multi-pulse experiment over a period prior to (pulse number 0 – 2000, Figure 2.10B) and well after the experiment to allow for sufficient desorption time (pulse number 10000 – 12000, Figure 2.10B). The system baseline level, indicated by the red line in Figure 2.10B, during a multi-pulse experiment and the subsequent desorption period is interpolated using the following exponential function (Equation 2.4):

$$V_{SB,i}(t) = Ae^{-Bt} \tag{2.4}$$

where $V_{SB,i}$ (t) is the system baseline level at time t, and A and B are fitting parameters. The time, t, is considered to start at the begining of the system baseline level collection preceding the multi-experiment (pulse number 0, Figure 2.10B).

2.4.1.2. Experiment/desorption baseline level

The experiment baseline level ($V_{EBL,i}$) represents the increase in background level, mainly due to strong adsorption to the catalyst surface (CO, CO_2, and H_2O over ceria based catalysts), during a multi-pulse experiment (pulse number 2000 – 7000, Figure 2.10B). The desorption baseline level ($V_{DBL,i}$) represents the decline in background level immediately after the multi-pulse experiment (pulse number 7000 – 10000, Figure 2.10B), as strong adsorbed species desorb from the catalyst surface.

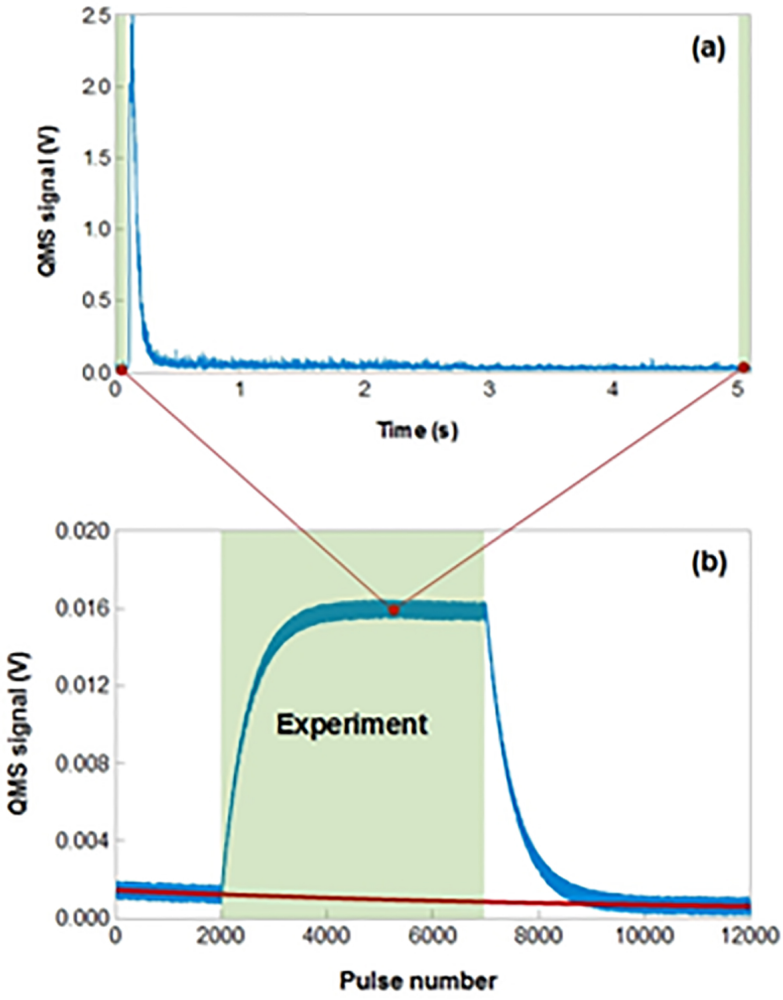

Figure 2.10: (a) a collected response shape, the green areas indicate the areas over which the experiment baseline is determined; (b) the experiment baseline evolution prior, during (green area) and after an experiment, the red line indicates the predicted system baseline level.

In general, a collection time of 5.1 s is used to collect a response for a certain mass, as the pulse is triggered at 0.1 s the experiment baseline level ($V_{EBL,i}$) can be determined from the average level over the period spanning from 0 - 0.1 and 5.0 - 5.1 s, indicated by the green areas in Figure 2.10A. The desorption baseline level ($V_{DBL,i}$) is determined in a similar way, although no pulse is given.

2.4.1.3. Response signal area

The response signal area ($A_{RSA,i}$) is determined by subtracting the experiment baseline level ($V_{EBL,i}$) or the desorption baseline level ($V_{DBL,i}$) for each data point in the range 0.1-5.0 s (Figure 2.10A), after which the resulting experiment/desorption baseline level corrected response signal is numerically integrated over that time range using the trapezium rule (Equation 2.5).

$$A_{RSA,i} = \int_{t=0.1}^{5.0} (V_{QMS,i}(t) - V_{EBL,i}(t))dt = \frac{1}{2f} \sum_{N=0}^{N-1} (V_{QMS,i}(t_{n+1}) - V_{EBL,i}(t_{n+1}) + V_{QMS,i}(t_n) - V_{EBL,i}(t_n)) \quad (2.5)$$

$A_{RSA,i}$: response signal area of component i (V s)
$V_{QMS,i}$: MS signal obtained for component i (V)
$V_{EBL,i}$: experiment baseline level of component i (V)
t: time (s)
f: sampling frequency (Hz)
N: number of samples in the 0.1 to 5.0 s interval

2.4.1.4. Baseline signal area

The baseline signal area ($A_{BSA,i}$) is determined by subtracting the system baseline level ($V_{SB,i}$) from the experiment baseline level ($V_{EBL,i}$) or the desorption baseline level ($V_{DBL,i}$) and multiplying the result by the total data collection time (Δt), defined as the collection start time of the current response minus the collection start time of the following response (Equation 2.6).

$$A_{BSA,i} = (V_{EBL,i}(t) - V_{SB,i}(t)) * \Delta t \quad (2.6)$$

$A_{BSA,i}$: baseline signal area of component i (V s)
$V_{EBL,i}$: experiment baseline level of component i (V)
$V_{SB,i}$: system baseline level of component i (V)
t: time (s)
Δt: the total data collection time (s)

2.4.1.5. Total signal area

The total signal area ($A_{TSA,i}$) is obtained by the summation of the response signal area ($A_{RSA,i}$) and baseline signal area ($A_{BSA,i}$) (Equation 2.7).

$$A_{TSA,i} = A_{RSA,i} + A_{BSA,i} \tag{2.7}$$

$A_{TSA,i}$: total signal area of component i (V s)
$A_{RSA,i}$: response signal area of component i (V s)
$A_{BSA,i}$: baseline signal area of component i (V s)

2.4.2. MS signal quantification and calibration

The obtained total signal areas ($A_{TSA,i}$) in the MS signal integration procedure, which are linearly proportional to the total number of molecules, of those masses that have passed through the ionisation volume of the MS, are firstly fragmentation corrected using the fragmentation factors found in the calibration procedure. These fragmentation factors are collected in a fragmentation matrix (F), horizontally this matrix (Table 2.1) indicates, for example, that CO_2 (*m/e* = 44) has a fragmentation with a magnitude of 0.209 times that of CO_2 (*m/e* = 44) at the mass of CO (*m/e* = 28). The 'unfragmented' total signal areas (A) are obtained via matrix inversion of the transposed fragmentation matrix (F) (Equation 2.8):

$$F^T \cdot A = A_{TSA} \Leftrightarrow A = (F^T)^{-1} \cdot A_{TSA} \tag{2.8}$$

F: the fragmentation matrix
A: a vector containing the 'unfragmented' total signal areas
$A_{TSA,i}$: a vector containing the (fragmented) total signal areas

In the cross beam ioniser of the MS positive ions are created upon interaction with electrons thermally ejected electrons from the filament. These positive ions are accelerated by an electric field towards the quadrupole rods, in

Table 2.1: Fragmentation matrix (F) for the components CO_2, CO and Ar

	CO_2	CO	Ar
CO_2 (*m/e*=44)	1.000	0.209	0.000
CO (*m/e*=28)	0.000	1	0.000
Ar (*m/e*=40)	0.000	0.000	1.000

which all masses except the selected one are rejected. The ions of the selected mass are bent by an electric field towards the secondary electron multiplier. The MS signal is the result of electrons freed from the surface of a discrete dynode of the secondary electron multiplier upon an ion collision. These freed electrons upon ion impact, free more electrons upon a collision with another discrete dynode (cascade). This cascade of electrons forms the current amplified and transformed to a voltage signal by the electrometer. This voltage signal is sampled by the analog to digital converter at discrete times only. Therefore, the integral of this signal over time (V s), an area, is linearly proportional to the total amount of ionised molecules (approximately 10% of the molecules passing through the ionisation volume) of the selected mass over the same time. For this reason an area, integrated voltage signal over time (V s), can be fragmentation corrected as it is linearly proportional to the amount molecules of the selected mass passing through the ionisation volume.

The 'unfragmented' total signal areas (A) are divided by the total signal area of the internal standard, yielding the relative signal areas (Arel). $A_{rel,i}$ represents the relative signal area of component i.

The response factor f_i for a component i, is calculated using the following equation, assuming a linear relation between the signal and the introduced amount of that component. Signal offsets are implicitly handled by the above described signal integration procedures, provided that a high enough secondary electron multiplier voltage (resolved system baseline signals) is used (Equation 2.9):

.

Table 2.2: Equimolecular response factor, f_i^0, for different components.

Gas	Concentration (vol%)	Relative Area, $A_{rel,i}$	f_i^0
H_2 in Ar	0.662	0.278	0.142
CO in Ar	0.801	3.881	0.964
CO_2 in Ar	0.797	3.853	0.981
NO in Ar	0.800	4.439	1.112
O_2 in Ar	0.797	3.048	0.776
C_3H_6 in Ne	0.788	16.959	4.563
C_3H_8 in Ne	0.787	36.171	9.790
N_2 in O_2 (Air)	0.788	4.767	1.279

$$f_i = \frac{A_i}{A_{std}} = \frac{s_i n_i}{s_{std} n_{std}} = \frac{s_i}{s_{std}} \frac{x_i}{(1 - x_i)} = f_i^0 \frac{x_i}{(1 - x_i)} \tag{2.9}$$

where:

s_i: the sensitivity factor for component i in V s molecule^{-1}
x_i: the molar fraction of component i
n_i: the number of molecules of component i pulsed
n_{std}: the number of molecules of internal standard pulsed
f_i^0: dimensionless equimolecular response factor.

This equimolecular response factor is determined by pulsing a mixture of a known composition, according to the following Equation 2.10:

$$f_i^0 = \frac{A_i}{A_s td} * \frac{x_i}{1 - x_i} \tag{2.10}$$

The equimolecular response factors, f_i^0 , for several components are shown in Table 2.2. In order to interconvert between equimolecular response factors obtained for different internal standards, the equimolecular response factors for one internal standard over the other are determined.

The detected amount of component i, S_i (n) in molecules, can then be calculated using the Equation 2.11:

$$S_i(n) = S(n)\frac{A_{rel,i}(1 - x_r)}{f_i^0} \tag{2.11}$$

where:

- S_i (n): number of molecules of component i contained in the pulse at pulse number n
- S(n): pulse size in molecules at pulse number n
- $A_{rel,i}$: relative signal area (measured signal in V s of component i divided by the internal standard signal in V s)
- x_r: molar fraction of the reactant in the reactant pulse
- f_i^0: unitless equimolecular response factor for component i

The number of molecules desorbed from the catalyst after the experiment is determined by subtracting the interpolated system baseline level from the measured post-experiment baseline level followed by fragmentation correction of their experiment baseline areas and quantified using their last known sensitivity factor (obtained from last experiment pulse sequences).

Calibration, in order to obtain the equimolecular response factors and ionisation fragmentation, is performed by pulsing a gas component over a quartz bed at ambient temperature, while recording the sequence of mass responses of the internal standard, the gas component and its known ionisation fragments. This sequence is repeated several times (normally 20.000 pulses) to improve the signal to noise level. The Ar to Ne internal standard conversion factor is determined by pulsing a known amount of Ar and Ne gas from 2 pulse-valve lines at ambient temperature. The H_2O signal was calibrated by pulsing H_2 over a quartz packed Pt sponge bed at 250 °C which was maintained in an oxidised state by an O_2 pulse prior to the H_2 pulse yielding 87% H_2 conversion.

The number of molecules desorbed from the catalyst after the experiment is determined by subtracting the predicted system baseline level from the measured post-experiment baseline level followed by fragmentation correction of their experiment baseline areas and quantified using their last known sensitivity factor (obtained from last experiment pulse sequences).

2.4.3. Pulse size quantification

To quantify the number of molecules in a pulse via the ideal gas law, corrections are made for the decreasing pressure in the pulse valve line during pulsing, and variations in ambient temperature. All data was normalised to 293 K. The logged pressure, P (Pa), in a pulse-valve line (B in Figure 2.4) is temperature corrected using the equation 2.12:

$$P^0 = T^0 \frac{P}{T} \tag{2.12}$$

where:

- P^0: temperature corrected pulse line pressure (Pa) at reference temperature T^0
- T^0: 293 K
- T: the logged pulse line gauge temperature (K)

The pulse size is proportional to the pressure in the pulse-valve line. Therefore, the temperature-corrected pressure as a function of the pulse number can be fitted using an exponential equation (Equation 2.13):

$$P^0(n) = Ae^{Bn} \tag{2.13}$$

where: n is the pulse number, and A and B fitting constants.

The pulse size, S (molecules) at pulse number n is determined using the Equation 2.14:

$$S(n) = \frac{N_A(P^0(n) - P^0(n+1))V_{line}}{RT^0} \tag{2.14}$$

where:

- N_A: Avogadro number
- V_{line}: calibrated pulse-line volume (m^3)
- R: gas constant

References

[1] J. T. Gleaves, J. R. Ebner, and T. C. Kuechler, *Temporal Analysis of Products (TAP)-A Unique Catalyst Evaluation System with Submillisecond Time Resolution,* Catalysis Reviews **30**, 49 (1988).

[2] J. T. Gleaves, G. Yablonsky, X. Zheng, R. Fushimi, and P. L. Mills, *Temporal analysis of products (TAP)—Recent advances in technology for kinetic analysis of multi-component catalysts,* Journal of Molecular Catalysis A: Chemical **315**, 108 (2010).

[3] S. O. Shekhtman, G. S. Yablonsky, J. T. Gleaves, and R. Fushimi, *"State defining" experiment in chemical kinetics—primary characterization of catalyst activity in a TAP experiment,* Chemical Engineering Science **58**, 4843 (2003).

[4] J. Happel, *Isotopic assessment of heterogeneous catalysis* (Elsevier, 2012).

[5] R. J. Berger, F. Kapteijn, J. A. Moulijn, G. B. Marin, J. De Wilde, M. Olea, D. Chen, A. Holmen, L. Lietti, E. Tronconi, and S. Yves, *Dynamic methods for catalytic kinetics,* Applied Catalysis A: General **342**, 3 (2008).

[6] D. G. Huizenga and D. M. Smith, *Knudsen diffusion in random assemblages of uniform spheres,* AIChE Journal **32**, 1 (1986).

[7] G. Yablonsky, M. Olea, and G. Marin, *Temporal analysis of products: basic principles, applications, and theory,* Journal of Catalysis **216**, 120 (2003).

3

Fundamental understanding of the Di-Air system I: The difference in reductant pre-treatment of ceria

Science is about knowing;
engineering is about doing.

Henry Petroski

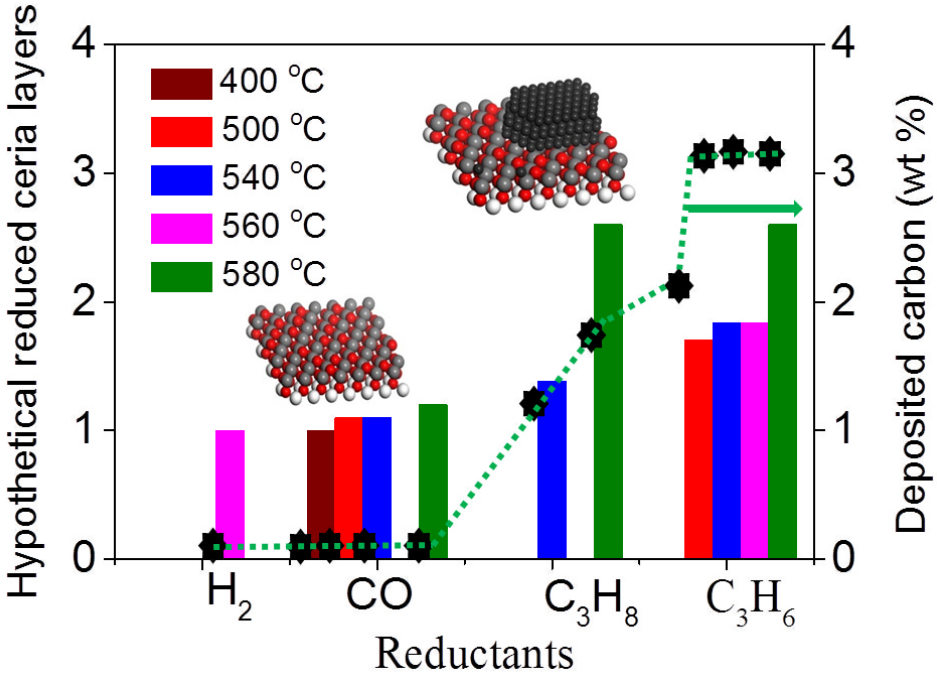
Hypothetical reduced ceria layers
Deposited carbon (wt %)
400 °C
500 °C
540 °C
560 °C
580 °C
0
1
2
3
4
H2
CO
C3H8
C3H6
Reductants

Toyota's Di-Air DeNO$_x$ system is a promising DeNO$_x$ system to meet NO$_x$ emission requiremens during the real driving. A fundamental understanding of why and how it works, however, largely lacks.

Ceria is one of the main ingredient in the Di-Air catalyst composition and will undergo oxidation-reduction cycles during operation due to pulsed fuel injection. In this Chapter, the reduction of ceria by reductants, e.g., CO, H_2, and hydrocarbons (C_3H_6 and C_3H_8), is investigated with the Temporal Analysis of Products (TAP) technique. The results show that the reduction by CO yields a faster catalyst reduction than by H_2, but in both cases the same final degree of ceria reduction is reached. Hydrocarbons generated an almost three times deeper degree of ceria reduction, and moreover resulted in carbonaceous deposits on the ceria surface. The total amount of converted NO over the C_3H_6 reduced sample is around ten times higher than over CO reduced ceria. The deeper degree of reduction and the deposition of carbon by hydrocarbon explain why hydrocarbons are the most powerful reductants in Toyota's Di-Air NO$_x$ abatement system.

This chapter is based on the following publication:
Y.Wang, M.Makkee, Applied Catalysis B; Environmental, doi: 10.1016/j.apcatb.2017.04.054

3.1. Introduction

In the European Union (EU) the regulated NO_x emissions have decreased over the past two decades. Nevertheless, 9% of EU-28 urban live in areas in which NO_x concentrations still exceed regulated NO_x standards in 2013, according to the Air quality for EU in 2014 [1]. In the European Union, around 40% of the NO_x emissions are from the traffic sector [2]. Due to the limited effectiveness of currently available NO_x emission abatement technologies, as of September 2017, 2.1 times the current Euro 6 NO_x emission standard (as measured with the conservative, less demanding ECE & EDCE test cycle) is allowed for in the newly established real driving emission (RDE) test [3]. In the future NO_x emission will become even more stringent, which clearly indicates that currently available technologies: Urea-SCR (Selective Catalytic Reduction) and Lean NO_x Traps (NSR - NO_x Storage & Reduction), still need significant improvements. Therefore, efficient exhaust emissions after-treatment technologies are highly demanded. Recently, Bisaiji *et al.,* (Toyota company) developed the Di-Air system (Diesel DeNO$_x$ System by Adsorbed Intermediate Reductants). Short rich and longer lean time intervals are created by high frequency direct injection of hydrocarbons (diesel fuel injection) into the exhaust upstream of a typical NSR catalyst (Pt/Rh/Ba/K/Ce/Al_2O_3) [4, 5]. The Di-Air system has shown promise to meet future NO_x emission standards under realistic driving test conditions.

In the Di-Air system, hydrocarbons are the most powerful reductants in the reduction of NO_x, as compared to other reductants, *e.g.,* CO and H_2 [5]. However, the working mechanism is still not clear. Before system optimisation with regard to catalyst formulation and fuel injection strategies, the principle and fundamental understanding of the Di-Air system are a prerequisite. Ceria is an essential catalyst ingredient in the Di-Air system, as it acts as an oxygen buffer. The ceria lattice oxygen can react with hydrocarbons, CO, and H_2 under rich conditions [6]. In our research, a commercially available Zr and La-doped ceria is used. The Zr-Ce solid solution, in which zirconium partially replaces cerium, provides a higher hydrothermal stability and a larger oxygen storage capacity [7], whereas lanthanum is present to increase the rate of oxygen bulk diffusion [8]. A reduced ceria can selectively convert NO into (di)nitrogen (N_2), even in the presence of an excess of oxygen [9, 10] (Chapter 4 and 6).

In this study, we mainly focus on the investigation of the reduction behaviour of the Zr and La-doped ceria catalyst, using H_2, CO, C_3H_6, and C_3H_8 as reductants. Temporal Analysis of Products (TAP) is used to ascertain the reaction between the reductants and the catalyst. Since a high frequency of hydrocarbon reductant injections is applied in the Di-Air system, these pulses will create a locally and temporally reducig environment. Therefore, all the experiments in this study are performed in the absence of gas-phase O_2. To demonstrate the effect of different reductants on NO reduction, NO pulsing is performed over the Zr-La doped ceria after pre-reduction treatment. The re-oxidation of the reduced ceria by NO is identical to the conversion of NO into N_2 over reduced ceria. These performed experiments will provide an insight in the product evolution as a function of the catalyst-reduction degree in an attempt to obtain a fundamental understanding of the Di-Air system.

3.2. Experimental

3.2.1. Catalyst and catalyst characterisation

The catalyst used is a commercial Zr-La doped ceria (BASF company, denoted further in this Chapter as 'ceria'), which serves as a core component in the Di-Air catalyst formulation. In brief, the typical fluorite structure of ceria was detected by Raman and XRD. The BET area was 65 ± 2 m^2/g. The crystal size of ceria determined by the Scherrer's equation and TEM analysis was on average 5 nm. The characterisation of this ceria is described in more detail in Chapter 4.

3.2.2. TAP multi-pulse experiments

The multi-pulse experiments were carried out in an in-house developed TAP (Temporal Analysis of Products) reactor. In all experiments a starting pulse size of approximately $1.6 \cdot 10^{15}$ molecules was used, the pulse size gradually decreases during an experiment as the reactant is pulsed from the closed and calibrated volume of the pulse-valve line. More details about TAP can be found in Chapter 2 [10, 11]. 21.2 mg was used in the TAP reactor. Prior to a ceria reduction, the catalyst was firstly re-oxidised at the same temperature at which the reduction was to be performed, using pulsing of 80 vol. % O_2

in Ar until a stable O_2/Ar signal ratio was obtained.

The reduction was carried out by pulsing reductant of either 80 vol.% C_3H_6 in Ne, or 80 vol.% C_3H_8 in Ne, or 80 vol. % CO in Ar, or 67 vol. % H_2 in Ar until a stable reactant and product to the internal standard (Ne or Ar) signal ratio was achieved, indicating that the ceria was equilibrated (reduced). NO multi-pulse experiments were performed using 80 vol.% NO in Ar.

The consumption of the oxygen species from the ceria during H_2, CO, C_3H_8, and C_3H_6 multi-pulse experiments was calculated using Equation 3.1:

$$n_{O,consumed} = n_{CO,in} - n_{H_2O,obs} + n_{CO,obs} + 2n_{CO_2,obs} \quad (3.1)$$

where n is the number of molecules or atoms of the specified species observed (obs), consumed, or introduced (in), based on the calibration of the MS signals (*m/e*) used and of the pulse size. For details on the quantification see Chapter 2.

The number of carbon species deposited on the doped ceria surface in the C_3H_6 multi-pulse experiments was calculated using Equation 3.2:

$$n_{C,deposited} = 3n_{C_3H_6,in} - 3n_{C_3H_6,obs} - n_{CO,obs} - n_{CO_2,obs} \quad (3.2)$$

Similarly, the number of carbon species deposited on the ceria surface in the C_3H_8 multi-pulse experiments was calculated using Equation 3.3:

$$n_{C,deposited} = 3n_{C_3H_8,in} - 3n_{C_3H_8,obs} - 3n_{C_3H_6,obs} - n_{CO,obs} - n_{CO_2,obs} \quad (3.3)$$

The number of carbon species during CO multi-pulse experiments on the ceria surface was calculated using Equation 3.4:

$$n_{C,deposited} = n_{CO,in} - n_{CO,obs} - n_{CO_2,obs} \quad (3.4)$$

The hypothetical ceria layers concept was used in order to obtain insight in the reductant reactivity as a function of the degree of ceria reduction (surface oxidation state). As the ceria (111) crystal plane is a stoichiometric O-Ce-O tri-layer stacked along the [111] direction, we regarded each O-Ce-O tri-layer as one hypothetical ceria layer. Assuming that Zr is identical to Ce, a maximum of 25% of the number of O ions in each crystal layer can be removed by reduction, the number of reducible oxygens in one hypothetical ceria layer. With a BET area of 65 m^2/g the number of reducible oxygens in one exposed surface layer is calculated to be $5.4 \cdot 10^{18}$ in 21.2 mg_{Cat}. Details can be found in Chapter 4 [10].

3.2.3. Operando Raman spectroscopy study

Operando Raman spectra (Renishaw, 2000) were recorded using a temperature controlled Raman cell (Linkam, THMS 600). Ten scans were collected for each spectrum in the 100-4000 cm^{-1} range using continuous grating mode with a resolution of 4 cm^{-1} and scan time of 10 s. The spectrometer was calibrated daily using a silicon standard with a strong absorption band at 520 cm^{-1}.

The samples were excited with 514 nm Ar line in the Raman cell, at 560 °C under atmosphere pressure. The spectra were recorded during the flow of C_3H_6 (1000 ppm in N_2, flow rate 200 mL/min).

3.3. Result

3.3.1. Reduction of ceria by CO

Figure 3.1 shows the result of the CO pulses experiment at 580 °C. During the initial period (pulse number 0-2000, Figure 3.1A), the CO was completely converted into CO_2. Pulse number 2000 corresponded to 0.4 hypothetical reduced ceria layers (Figure 3.1B). After this initial period, the CO conversion and CO_2 production progressively decreased, but never reached a zero conversion level during the duration of the experiment. In the CO oxidation process, only oxygen from the catalyst is consumed, as can be concluded from the oxygen balance (Table 3.2). No carbon deposits were observed on the catalyst within experimental error.

Similar results were obtained at 400-500 °C (Appendix A), but CO conversion did never reach full conversion in this temperature window. At 200 °C and lower, no significant CO oxidation activity was observed (not shown). The number of hypothetical reduced ceria layers (1.2 to 1.0) were relatively constant in the 400 to 580 °C temperature window (Table 3.2).

3.3.2. Reduction by H_2

Figure 3.2 shows the result of H_2 pulses experiment at 560 °C. For a very short period (pulse number 0-210, Figure 3.2A), hydrogen conversion was relatively high without a clear desorption of water. In contrast to the CO

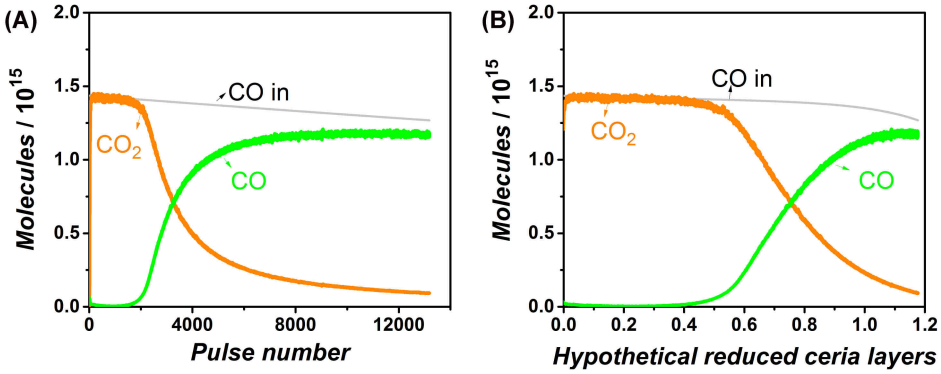

Figure 3.1: CO multi-pulse experiment over a pre-oxidised ceria at 580 °C, (A) with pulse number and (B) with hypothetical reduced ceria layers.

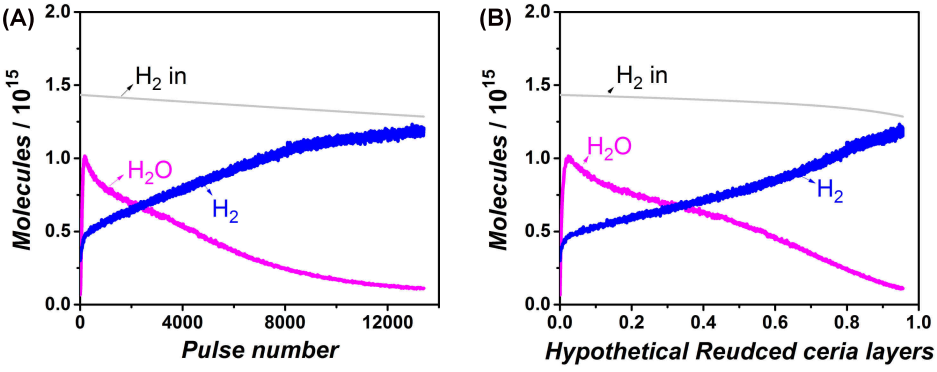

Figure 3.2: H_2 multi-pulse experiment over the pre-oxidised ceria at 560 °C, (A) with pulse number (B) with hypothetical reduced ceria layers.

Table 3.1: Definition of different stages during the C_3H_6 and C_3H_8 pulses in TAP.

Stage	Hydrocarbon Reactivity
I	Initial full conversion of hydrocarbon
II	Hydrocarbon conversion decline
III	Hydrocarbon conversion increase
IV	Period of constant hydrocarbon conversion
V	Hydrocarbon conversion decrease

experiment, the H_2 conversion was never complete. The H_2 conversion and H_2O production decreased progressively during the remainder of the experiment (pulse number 210 - end, Figure 3.2B). At the end of experiment, the number of extracted oxygen atoms, characterised as the number of hypothetical reduced ceria layers, corresponded with 1 reduced layer (Table 3.2).

3.3.3. Reduction by C_3H_6

Figure 3.3 shows the result of C_3H_6 pulses experiment at 580 °C. Different stages are used to define C_3H_6 reactivity profiles with pulse number, as shown in Table 3.1. The definition of different stages was also applied to C_3H_8 reactivity in Figure 3.5.

Figure 3.3A shows the product and reactants evolution *versus* pulse number during C_3H_6 pulses. In stage I (pulse number 0-80), a high activity was observed, where predominantly total oxidation products, *i.e.,* CO_2 and H_2O were formed. The H_2 formation was observed from the start of the experiment, while CO production was initially zero. Both H_2 and CO production increased during this stage I. After this short highly active stage I, C_3H_6 conversion rapidly declined in stage II (pulse number 80-500). In stage III and IV (pulse number 400-8000) predominantly partial oxidation took place and mainly CO and H_2 were observed. From pulse number 2800 to 8000 (stage III), C_3H_6 conversion increased to full conversion. H_2 was the major product

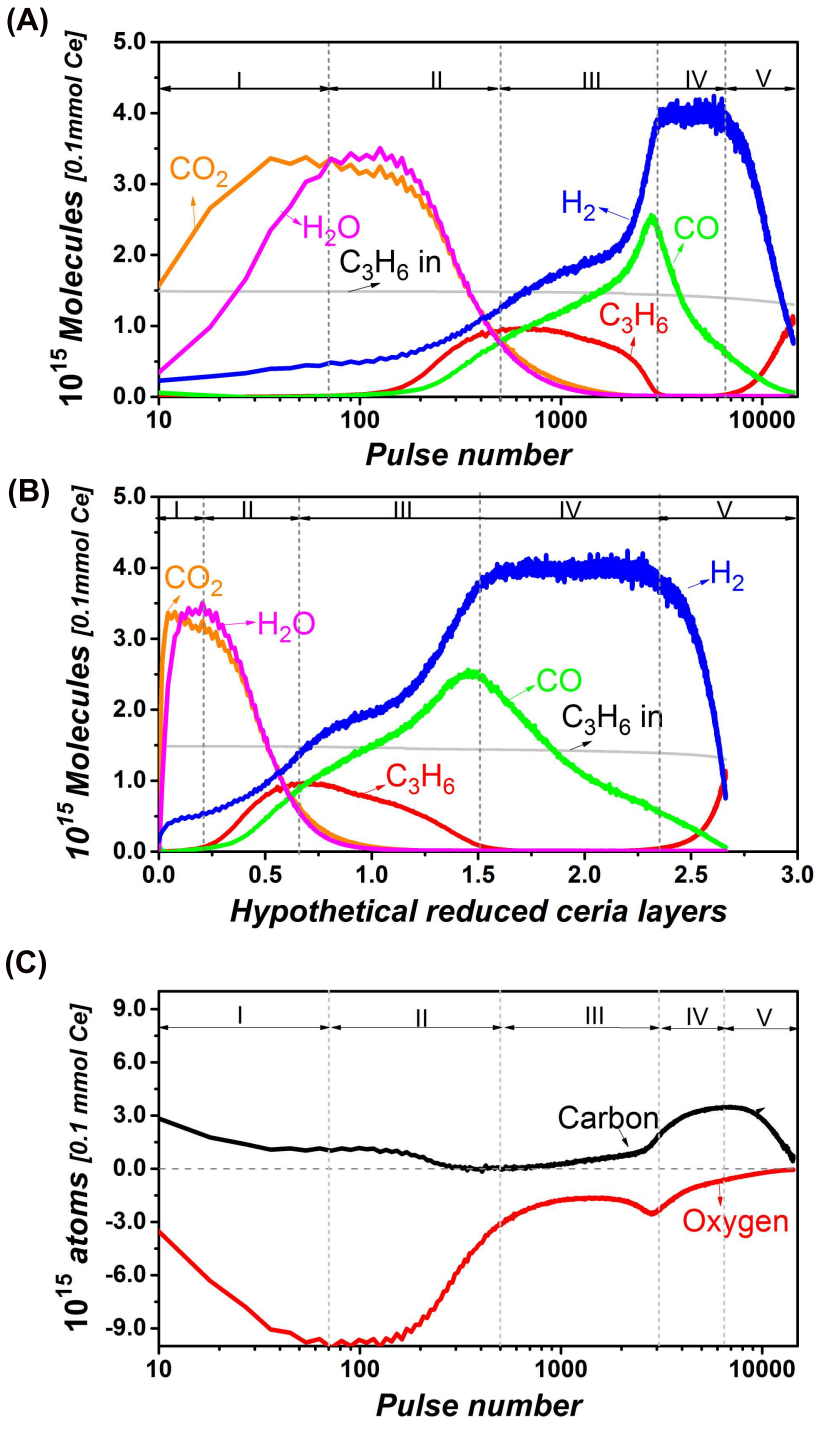

Figure 3.3: C_3H_6 multi-pulse experiment over a 21.2 mg (0.1 mmol) pre-oxidised ceria at 580 °C, (A) product and reactants evolution *versus* pulse number, (B) product and reactants evolution *versus* hypothetical reduced ceria layers, and (C) Carbon and oxygen balance *versus* pulse number.

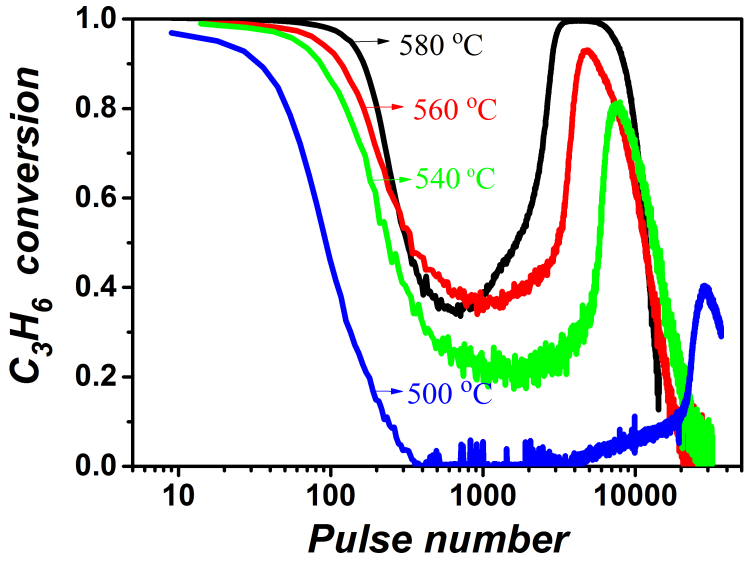

Figure 3.4: C_3H_6 conversion *versus* pulse number during C_3H_6 multi-pulse experiments over a pre-oxidised ceria at the indicated temperatures.

and the formation of CO declined with time in stage III. In stage V (pulse number 8000 - end), both C_3H_6 conversion and H_2 production declined. The H_2 production and C_3H_6 conversion remained persistent although at a low level and no CO was observed.

Some carbon (Figure 3.3C) started to deposit on the surface from stage II (determined from the carbon balance). Significant amounts of carbon depositions were observed when the CO formation started to decline, while H_2 formation persisted (stage IV). C_3H_6 shows full conversion during stage I and IV, corresponding to 0 to 0.25 and 1.5 to 2.7 hypothetical reduced ceria layers, respectively, as shown in Figure 3.3B.

The oxygen atom consumption and carbon atom deposition during the C_3H_6 multi-pulse experiment at 580 °C were calculated to be $1.5 \cdot 10^{19}$ oxygen atoms (2.6 hypothetical ceria layers) and $4.1 \cdot 10^{19}$ carbon atoms (2.9 wt.%), respectively, as shown in Table 3.2. Figure 3.4 shows the C_3H_6 conversion *versus* pulse number in a temperature window between 500 and 580 °C. Similar C_3H_6 reactivity profiles were observed, although the overall reactivity of C_3H_6 decreased, when reaction temperature declined. No significant

C_3H_6 activity and reduction of ceria were observed below 500 °C. Table 3.2 summarises the oxygen consumption (hypothetical reduced ceria layers) and carbon deposits for the 500 to 580 °C temperature window.

3.3.4. Reduction by C_3H_8

Figure 3.5 shows the result of C_3H_8 pulses experiment at 580 °C. As compared to C_3H_6, C_3H_8 in stage I did not have a full conversion. Figure 3.5A shows the product and reactant evolution *versus* pulse number during C_3H_6 pulses. In stage II (pulse number 80-1000), a short period of a higher activity (up to 40% conversion) was observed, where predominantly total oxidation products, *i.e.,* CO_2 and H_2O, were formed. The H_2 formation was observed from the start of the experiment, while CO production was initially zero, both H_2 and CO production increased during this stage II. The C_3H_8 conversion declined during stage II and increased during stage III (up to 60% conversion). In stage III and IV, partial oxidation took place and CO and H_2 were observed, while C_3H_6, the dehydrogenation product of C_3H_8, was only observed during stage III. The level of C_3H_8 conversion was substantially lower as compared to that of C_3H_6.

During the partial oxidation time interval (stage III, IV, and V), CO and H_2 were observed as the main products. The reaction rate increased with pulse number during stage III and IV. During stage III the C_3H_6 production, resulting from the dehydrogenation of C_3H_8, increased progressively but vanished towards the end of stage III. A maximum in CO production was observed when the activity for the dehydrogenation reaction vanished. In this the partial oxidation time interval, in contrast to the C_3H_6 multi-pulse experiment, the C_3H_8 conversion was never 100%. Initially, the C_3H_8 conversion was around 10% and reached a maximum conversion of 60% at the point of maximum CO production (Figure 3.6). Following the maximum in the CO production, the C_3H_8 conversion and H_2 production also reached their maximum level (stage IV, Figure 3.5). In stage V, the C_3H_8 conversion and CO and H_2 production declined. CO evolution stopped after pulse number 22000, while C_3H_8 conversion and H_2 production remained persistent at a low level. At a temperature of 500 °C and lower, the reactivity of C_3H_8 was negligible or none (not shown).

Table 3.2: Summary of the number of deposited carbon and extracted oxygen atoms in the ceria (21.2 mg) reduction experiments and the number of converted NO molecules during NO re-oxidation experiements.

Reduction by reactants	Deposited carbon		Extracted oxygen	
	Atoms	wt.%	Atoms	HRCL[1]
580 °C C_3H_6	$3.1 \cdot 10^{19}$	2.9	$1.5 \cdot 10^{19}$	2.6
560 °C C_3H_6	$3.4 \cdot 10^{19}$	3.2	$1.1 \cdot 10^{19}$	1.8
540 °C C_3H_6	$3.3 \cdot 10^{19}$	3.1	$1.1 \cdot 10^{19}$	1.8
500 °C C_3H_6	$1.9 \cdot 10^{19}$	1.8	$9.2 \cdot 10^{18}$	1.7
580 °C C_3H_8	$1.5 \cdot 10^{19}$	1.4	$1.5 \cdot 10^{19}$	2.6
540 °C C_3H_8	$1.1 \cdot 10^{19}$	1	$0.9 \cdot 10^{19}$	1.7
580 °C CO	-	-	$6.3 \cdot 10^{18}$	1.2
500 °C CO	-	-	$6.0 \cdot 10^{18}$	1.1
400 °C CO	-	-	$5.4 \cdot 10^{18}$	1.0
560 °C H_2	-	-	$5.2 \cdot 10^{18}$	1.0
Re-oxidation by NO at 540 °C			The number of converted NO	
Over CO pre-reduced at 540 °C			$6.8 \cdot 10^{18}$	
Over C_3H_8 pre-reduced at 540 °C			$2.9 \cdot 10^{19}$	
Over C_3H_86 pre-reduced at 540 °C			$7.6 \cdot 10^{19}$	

[1] hypothetical reduced ceria layer

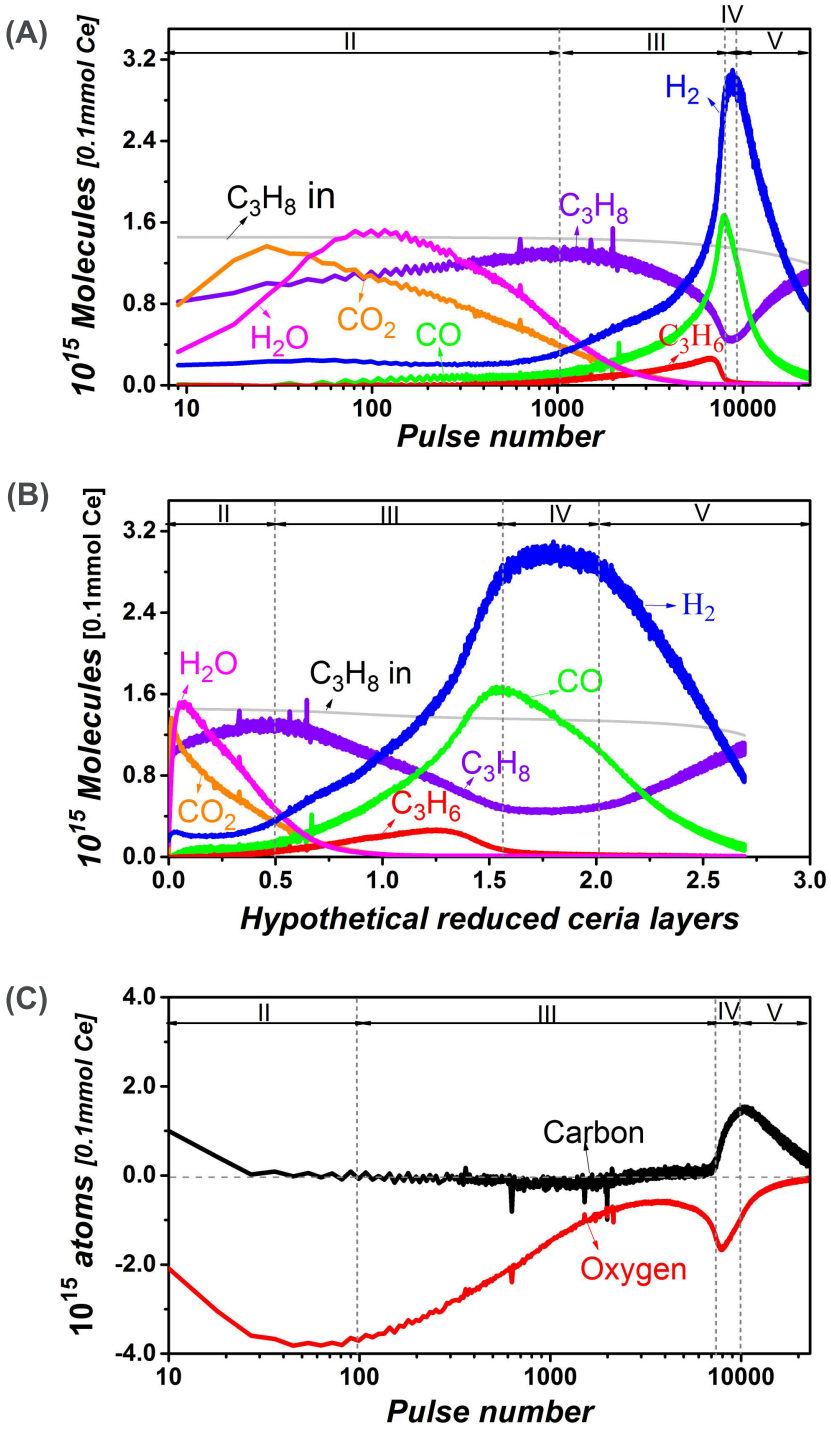

Figure 3.5: C_3H_8 multi-pulse experiment over a pre-oxidised ceria (21.2 mg,0.1 mmol) at 580 °C: (A) product and reactants evolution with (A) pulse number, (B) product and reactants evolution *versus* hypothetical reduced ceria layers.

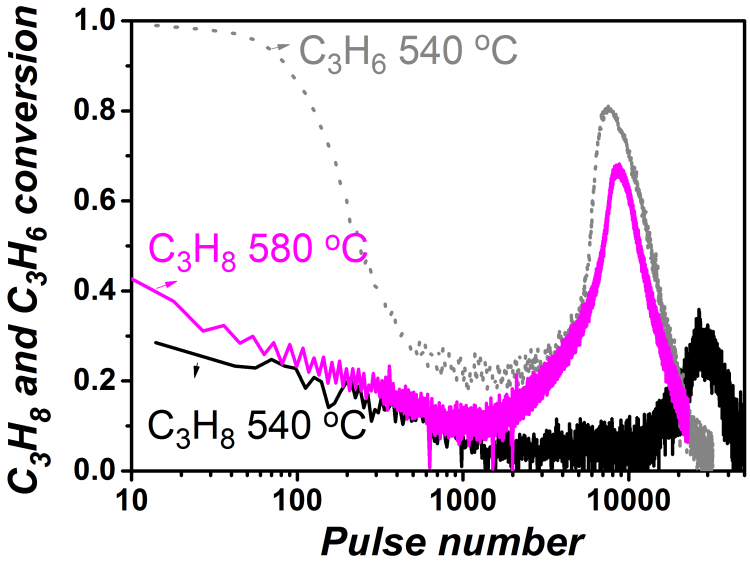

Figure 3.6: C_3H_8 and C_3H_6 conversion *versus* pulse number during C_3H_8 multi-pulse experiments over a pre-oxidised ceria at the indicated temperatures.

As shown in Table 3.2, the amounts of deposited carbon ranged from 1.4 to 0.9 wt.% for temperatures from 580 °C to 540 °C, which is less than that of propene. C_3H_8 was able to reduce the catalyst as far as 2.7 hypothetical reduced ceria layers, which was the same as that for C_3H_6 at 580 °C, but the required number of pulses, however, was around twice that of C_3H_6.

In Figure 3.6, the C_3H_8 conversion was plotted *versus* pulse number at 580 and 540 °C, respectively. In the initial total oxidation period, approximately 40% and 30% C_3H_8 conversion were achieved at 580 and 540 °C, respectively. The incremental C_3H_8 conversion in stage II and III was sensitive to the temperature, which shifted to higher pulse numbers with decreasing temperature and its maximum C_3H_8 conversion decreased from 65 to 30%, when the temperature decreased from 580 to 540 °C. Compared to C_3H_6 conversion at 540 °C, as indicated dotted grey line in Figure 3.6, C_3H_8 was less active and it took around two times pulses than that of C_3H_6 to reach the final state. As shown in Table 3.2, the amount of deposited carbon by C_3H_8 at 540 °C was around three times less than that for C_3H_6 at the same temperature, even the pulses of C_3H_8 is twice that of C_3H_6.

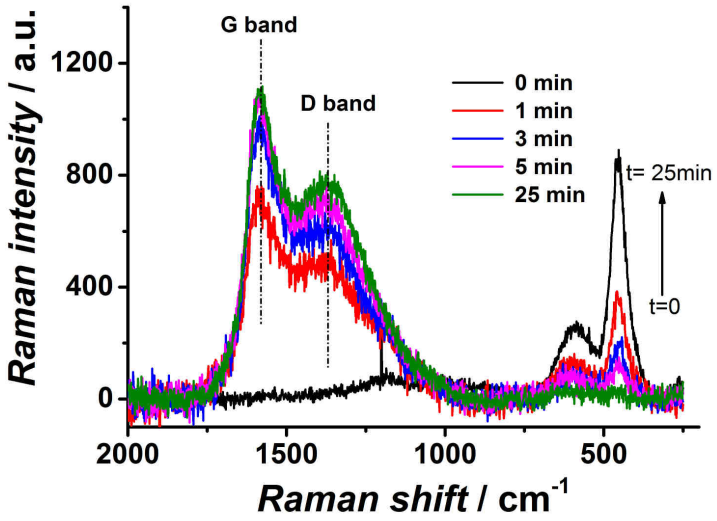

Figure 3.7: Raman spectra during C_3H_6 flow over ceria catalyst at 580 °C.

3.3.5. Operando Raman experiment of C_3H_6 flow over ceria

Operando Raman spectroscopy was used to characterise the deposited carbon formed over ceria during C_3H_6 flow at 580 °C. D-band and G-band of carbon were observed during the C_3H_6 flow as shown in Figure 3.7. The G-band corresponded to graphitic in-plane vibrations with E_{2g} symmetry. The D-band is generally assigned to the presence of defects in and disorder of carbon.

3.3.6. Re-oxidation of reduced ceria by NO

In order to investigate the effect of the reduction degree as well as the amount of deposited carbon on the NO reduction into (di)nitrogen (N_2) over (pre-reduced) ceria, NO was used in the re-oxidation ceria pre-reduced with CO, H_2 (not shown), C_3H_8, and C_3H_6 at 540 °C , as illustrated in Figure 3.8. For the CO (and H_2) pre-treated samples, full NO conversion was obtained till pulse number 2340, corresponding with around $6.8 \cdot 10^{18}$ NO molecules converted. For the propane pre-treated ceria, complete NO conversion maintained approximately till pulse number 1200. The total number of NO converted was around $2.9 \cdot 10^{19}$ molecules. For the C_3H_6 pre-treated ceria sample, however, NO shows full conversion up to pulse number 5600,

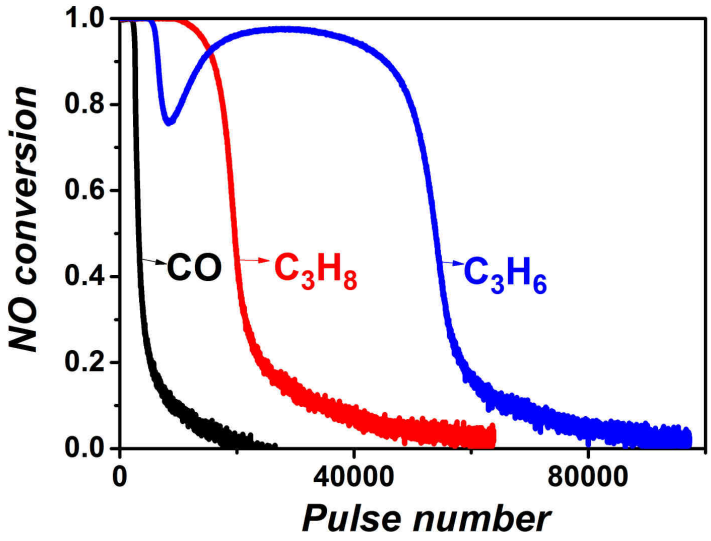

Figure 3.8: NO pulse convrsion over ceria pre-reduced at 540 °C by CO and hydrocarbons.

followed by a conversion decline to 76% at pulse number 9000. Subsequently, the NO conversion for the C_3H_6 increased to full conversion till pulse number 40000. NO conversion declined after pulse number 97300. The total amount of NO being converted was around $7.6 \cdot 10^{19}$ molecules.

3.4. Discussion

3.4.1. Reduction of ceria by CO and H_2

The CO multi-pulse experiments over ceria resulted in an overall catalyst reduction of around on average one hypothetical reduced ceria layer in the 400 to 580 °C temperature window (Table 3.2), indicating that a complete surface layer of ceria can be reduced by CO. The extraction of one oxygen resulted in the reduction of two Ce^{4+} ions into two Ce^{3+} ions. The oxidation of CO to CO_2 can be described as Equantion 3.5:

$$CO + 2Ce^{4+} + O^{2-} \rightarrow CO_2 + 2Ce^{3+} + \blacksquare \qquad (3.5)$$

(■ : oxygen vacancy)

The CO_2 production was due to the oxidation of CO by oxygen species (originating) from the ceria lattice since there was no gas-phase O_2 present during

the CO multi-pulse experiment. The full CO_2 conversion dropped at the point corresponding to 0.5 hypothetical reduced ceria layers Figure 3.1B, which indicated that the oxygen species generated from surface lattice oxygen had a high activity for the CO oxidation into CO_2. The observed decline in CO activity between 0.5 to 1 hypothetical reduced ceria layers Figure 3.1B implied that only surface oxygen participated in the CO oxidation.

Significant participation of the disproportionation of CO into carbon and CO_2 ($2CO \rightarrow C + CO_2$) can be excluded, because neigher hardly any deposited carbon was observed nor could be quantified through the calculated carbon balance (Figure 3.1A). The total reduction degree of ceria by CO was not significantly affected by temperatures in the range of 400-580 °C. The reactivity of CO, however, declined as the temperature decreased, since more CO pulses were needed in order to obtain the same reduction degree at the low temperatures of 400 °C, compared to 580 °C (Appendix A).

The limitation for the reduction of only one hypothetical reduced ceria layer by CO cannot be attributed to the oxygen diffusion since the reduction degree of ceria was not significantly influenced by a temperature between 400 and 580 °C. The role of ceria in the reduction of CO_2 to CO had been widely studied in the field of solar cells [12–14]. CO_2 can also re-oxidise reduced ceria, thereby forming CO. The coexistence of CO and CO_2 in the 0.5 to 1 hypothetical reduced ceria layer range suggested the presence of an equilibrium between CO, CO_2, Ce^{3+}, and Ce^{4+}, which may limit the obtainable degree of reduction for ceria during CO multi-pulse experiments (Figure 3.1B).

For the H_2 multi-pulse experiments, a high activity towards H_2 was observed from the start of the experiment (Figure 3.2) in the absence of any water desorption. This indicated that water or its precursor species were initially retained on the catalyst's surface. This activity towards H_2 activity dropped immediately after the initial pulses to a conversion of about two-third, further continuously declining until hardly any conversion was observed when one hypothetical reduced ceria layer was reached. Similar to the CO multi-pulse experiments, when the ceria surface became reduced, the reduced ceria tended to use water or an intermediate to re-oxidise itself [15]. The coexistence of H_2 and H_2O during a whole H_2 multi-pulse experiment suggested the presence of an equilibrium between H_2, H_2O, Ce^{3+}, and Ce^{4+},

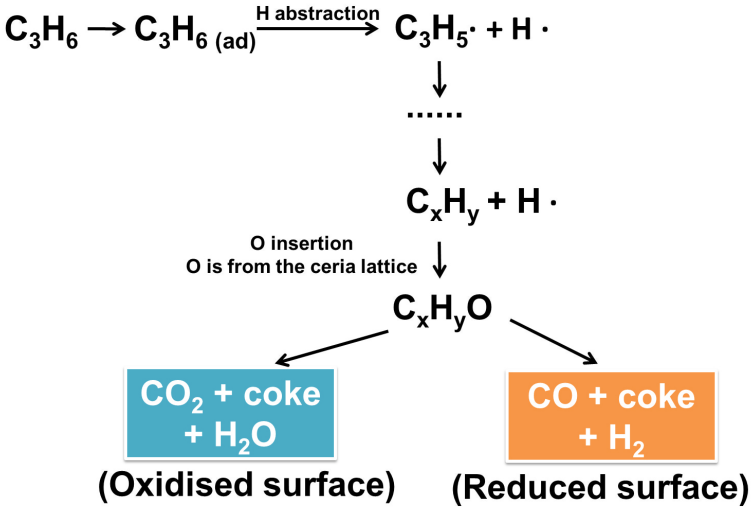

Figure 3.9: C_3H_6 activation steps for the formation of CO_2 and H_2O over oxidised ceria surface and the formation of CO and H_2 over reduced ceria surface.

which may limit a deeper reduction of ceria by H_2.

3.4.2. Reduction by hydrocarbons

3.4.2.1. Reduction by C_3H_6

The reduction of ceria by C_3H_6 led overall to 2.7 hypothetical reduced ceria layers at 580 °C (Table 3.2). Unlike CO and H_2 pre-treatment, the C_3H_6 interaction with the catalyst can be characterised by two types of reactions: complete C_3H_6 oxidation and subsequently C_3H_6 cracking/partial oxidation (Figure 3.3).

The initial high conversion to total oxidation products (stage I): CO_2 and H_2O, was most probably due to the high concentration of active surface oxygen species, which were formed through an oxygen activation chain as given in Equation 3.6 [16–18]:

$$O_{2(ad)} \overset{+e^{-1}}{\rightleftarrows} O_2^- \overset{+e^{-1}}{\rightleftarrows} O_2^{2-} \leftrightarrow 2O^- \overset{+2e^{-1}}{\rightleftarrows} 2O^{2-} \tag{3.6}$$

These active surface oxygen species reacted with C_3H_6 resulting mainly in

the formation of H_2O and CO_2 as described in Figure 3.9. The adsorbed C_3H_6 was activated by the active oxygen species from oxygen activation chain (equation 6), forming the $C_3H_5\cdot$ and $H\cdot$. Then $H\cdot$ will react with active oxygen species, forming $\cdot OH$. Another $H\cdot$ will be further abstracted from $C_3H_5\cdot$ and to form H_2O from $\cdot OH$. The remaining hydrocarbon fragment (C_xH_y) will react with active oxygen species, forming oxygen-containing hydrocarbon intermediates (C_xH_yO), and finally oxidation of some part of C_xH_yO to CO_2, the remained C_xH_yO will be deposited as "coke" as illustrated in Figure 3.9.

The C_3H_6 conversion dropped (stage II), accompanied by a decline in total oxidation products and the start of C_3H_6 cracking/partial oxidation reaction. The fall of C_3H_6 conversion during stage II was likely caused by the lower availability of the active surface oxygen species that were largely consumed during stage I. As described in Figure 3.9, the adsorbed C_3H_6 will be activated by the active oxygen species, forming the $C_3H_5\cdot$ and $H\cdot$. This $H\cdot$ will react with active oxygen species, forming $\cdot OH$. More H will be further abstracted from $C_3H_5\cdot$. However, on the reduced catalyst surface (less active surface oxygen), H surface species have more chance to associate to each other to form H_2. The remaining hydrocarbon fragment (C_xH_y) will react with active oxygen species, forming oxygen-containing hydrocarbon intermediates (C_xH_yO). Some part of C_xH_yO will be converted to CO, the remaining C_xH_yO will be deposited as coke. The Figure 3.9 was also applied to the C_3H_6 cracking reaction during the stage III. C_3H_6 conversion increased during stage III accompanied by an increased H_2 and CO formation, indicating mainly cracking/partial oxidation/dehydrogenation were taking place on the reduced ceria surface.

The CO formation arrived at a maximum at 1.5 hypothetical reduced ceria layers, while CO_2 and H_2O were not observed beyond 1 hypothetical reduced ceria layer. This observation indicated that for the formation of CO oxygen from the bulk of ceria was used, resulting in a deeper degree of catalyst reduction by C_3H_6, as compared to the CO and H_2 treatment. The CO formation declined after 1.5 hypothetical reduced ceria layers and ceased at 2.7 hypothetical reduced ceria layers. This will indicate that the deposited carbon oxidation to CO started to become limited when the catalyst reduced to 1.5 hypothetical reduced ceria layers. This can be explained by the scarcity

of active surface oxygen species either due to slow bulk oxygen diffusion or the activation of bulk oxygen to active oxygen species. The formation of CO implied the additional extraction of oxygen from ceria bulk, *i.e.,* a reduction of the ceria up to 2.7 hypothetical reduced ceria layers (stage V).

Also the increase of C_3H_6 conversion during stage III was likely due to the regeneration of active oxygen species from the bulk by diffusion to surface, which led to increased CO formation but to less carbon deposition as compared to stage II, based on the carbon balance calculations. The CO formation, however, declined beyond 1.5 hypothetical reduced ceria layers, while still a full C_3H_6 conversion and persistent H_2 formation was observed (stage IV). The full C_3H_6 conversion (C_3H_6 cracking) during stage IV cannot be ascribed to the increased active oxygen species availability. Otherwise, the CO formation rate would increase as well. Another type of species started to play a role in C_3H_6 cracking/partial oxidation (deeper dehydrogenation).

The total amount of carbon deposition till the point of 1.5 hypothetical reduced ceria layers was around $2 \cdot 10^{18}$ carbon atoms. Assuming that the carbon structure will be graphene-like structure, the coverage of ceria by carbon corresponded to roughly 4% of the available surface area (Detailed calculation is shown in Appendix A). Carbonaceous deposited (coke) that formed on the metal oxides can be regarded as the real catalyst site for (oxidative) dehydrogenation [19–22]. The formation of deposited carbon was observed from the operando Raman spectroscopy (Figure 3.7). The catalytic site on the coke will be the quinone/hydroquinone group on the surface of the coke [19–22], as evidence the formation of D-band and G-band (Figure 3.7). The full C_3H_6 conversion with persistent H_2 formation is attributed to the deposited carbon and will play a role in the deeper C_3H_6 dehydrogenation. The oxygen transport from ceria bulk will become the catalytically active site on the coke (C_xH_yO), and CO was formed by the oxidation of coke (C_xH_yO). When the number of available lattice oxygen declined, the CO formation declined as well. The deeper dehydrogenation of C_3H_6 will lead to more and more deposited carbon.

Till stage V, C_3H_6 conversion dropped, and simultaneously the H_2 formation declined as well from 2.2 hypothetical reduced ceria layers, indicating that the deeper dehydrogenation reaction largely slowed down. The slow-down of the bulk oxygen diffusion to surface when the ceria was 2.2 hypothetical

layers reduced caused the depletion of reducible oxygen on the ceria surface, which may explain the final lost in the C_3H_6 conversion and hardly any CO formation.

In addition, C_3H_6 conversion were persistent in a lower lever after 14000 C_3H_6 pulses, as shown in Figure 3.3. The total number of deposited carbon on the ceria surface after 14000 C_3H_6 pulses was around $3.1 \cdot 10^{19}$ carbon atoms (Figure 3.7), which accounted for about 2.9 wt.%. Assuming that the carbon structure will be single-sheet graphene-like and the ceria surface will be flat, the coverage of ceria by carbon will correspond to roughly 60% of the available surface area. There would be still about 40% of the surface area available. In reality, the catalyst particles are aggregated together, as evidenced by TEM (Figure 4.1 in Chapter 4). Therefore, the surface of ceria will be a network of pores. The carbon deposition may completely cover the surface, considering the some pores are blocked by the carbon particles. The blocking of the pores in combination with a slow-down of the oxygen diffusion from the bulk to the ceria surface and the deposited carbon may be main reasons for the final lost in the C_3H_6 conversion.

Similar C_3H_6 reactivity profiles were also observed in the 500 to 580 °C temperature window, although more pulses were needed. The maximum observed C_3H_6 conversion during the cracking reaction period (stage III) shifted to higher pulse numbers in the 580 to 500 °C temperature range, as shown in Figure 3.4. This observation indicated that more time (more pulses) was needed bulk oxygen diffusion and activation when temperature decreasing.

Such phenomenon also pointed out that the reactivity of C_3H_6 during stage III was likely controlled by the availability of active oxygen species on the surface regenerated by bulk oxygen diffusion. At 400 °C, only complete oxidation to CO_2 and H_2O was observed (no carbon deposition). No cracking reaction was observed was observed during the experiment time of 24 h C_3H_6 pulses.

The total amount of reducible oxygen during C_3H_6 oxidation was highly depended on temperature, as shown in Table 3.2. The number of oxygen atoms extracted in the C_3H_6 multi-pulse experiments declined from $1.5 \cdot 10^{19}$ to $0.9 \cdot 10^{19}$, *i.e.,* from 2.6 to 1.7 hypothetical reduced ceria layers when the

temperature decreased from 580 to 500 °C. The total amount of deposited carbon during the C_3H_6 multi-pulse experiment at 580 °C is twice that of the multi-pulse experiment at 500 °C. At 400 °C, carbon was hardly deposited, and no cracking/partial oxidation/dehydrogenation activities were observed.

3.4.2.2. Reduction by C_3H_8

C_3H_8 (Figure 3.5), shows the same trend as C_3H_6, although C_3H_8 conversion was lower than that of C_3H_6 during stage I and IV. This indicated that the reaction mechanisms were similar for both saturate and unsaturated hydrocarbons. C-H bond cleavage was easier for the unsaturated C_3H_6 as compared to the saturated C_3H_8 due to either the interaction with the surface through hydrogen bonding or Van der Waals forces for C_3H_8 and more strong electron-rich π orbital interactions on Lewis acid sites for C_3H_6 [23]. The lower reactivity, that C_3H_8 displayed towards oxygen species, did not affect the total amount of oxygen extracted during the whole C_3H_8 multi-pulse experiment, but affected strongly the amount of carbon deposited on the surface and the time to achieve the same degree of ceria reduction. Since the carbon deposition took predominantly place during stage IV, the lower C_3H_8 reactivity led to less carbon deposition. Comparing C_3H_6 and C_3H_8 pre-treatment at 580 °C, the amount of carbon deposited for the C_3H_6 pre-treatment was twice that for C_3H_8, as shown in Table 3.2.

The C-H bond cleavage is regarded as the first step in the activation of saturated hydrocarbons (C_3H_8). Due to the initial high concentration of active surface oxygen species in stage II, complete oxidation was observed with the formation of both H_2O and CO_2, similar as illustrated in Figure 3.9. The conversion of C_3H_8 decreased during stage II was due to the depletion of active oxygen species on the surface. A gradual increase in the amount of the C_3H_6 dehydrogenation product Figure 3.5 was observed from stage III, where the C_3H_8 conversion was enhanced. Similar to the C_3H_6 multi-pulse experiments (Figure 3.3), the C_3H_8 reactivity (Figure 3.5) increased during stage III was due to the reformation of surface active oxygen species by the diffusion of oxygen from the bulk of the ceria. Dehydrogenation of C_3H_8 to C_3H_6 was observed from initial of stage III and declined from the end of stage III. C_3H_6 evolution completely vanished from stage IV. The dehydrogenation selectivity of C_3H_8 to C_3H_6 in stage III can be explained by a

particular type of reformed active oxygen species, *e.g.,* O^-. C_3H_6 formation declined around 1.3 hypothetical reduced layers, indicating that these oxygen species, *e.g.,* O^- [24], were less present from 1.3 hypothetical reduced layers.

Similar as in the C_3H_6 multi-pulse experiments, the formation of CO during C_3H_8 multi-pulse experiment consumed oxygen from the catalyst bulk, *i.e.,* a deeper reduction. Deposited carbon started to play a role in C_3H_8 dehydrogenation during stage IV, where C_3H_8 conversion was around 60%.

The maximum conversion during the C_3H_8 cracking / partial oxidation / dehydrogenation reactions (stage III) shifted to a higher pulse number when the temperature was changed from 580 to 540 °C, as shown in Figure 3.6. Similarly to the observation in the C_3H_6 multi-pulse experiments, the reactivity of C_3H_8 during stage III was controlled by the availability of active oxygen species on the surface reformed by a temperature dependent oxygen diffusion. The observed C_3H_8 conversion drop can be explained with the same reasoning as discussed above for C_3H_6.

The total amount of reducible oxygen during C_3H_8 oxidation was significantly influenced by the temperature, as shown in Table 3.2. The number of oxygen atoms extracted in the C_3H_8 multi-pulse experiments declined from $1.5 \cdot 10^{19}$ to $0.9 \cdot 10^{19}$, *i.e.,* from 2.7 to 1.7 hypothetical reduced ceria layers as the temperatures were lowered from 580 to 540 °C.

3.4.3. Re-oxidation of reduced ceria with NO

The pre-treatment of ceria by CO, H_2, C_3H_8, and C_3H_6 at 540 °C led to a degree of catalyst reduction corresponding to 1, 1, 1.7, and 1.8 hypothetical reduced ceria layers, respectively. The pre-treatment with C_3H_6 and C_3H_8 additionally resulted in the deposition of $3.3 \cdot 10^{19}$ and $1.1 \cdot 10^{19}$ carbon atoms, respectively.

The differences observed in the reduction of NO into N_2 over ceria by using either CO, C_3H_8 or C_3H_6 pulses at 540 °C was shown in Figure 3.8. CO and H_2 pre-treatments shows only a short time interval, where NO was reduced into N_2. The reduction of NO to N_2 started with oxygen from NO filling an oxygen defect site, followed by N-O bond scission and the recombination, after surface diffusion and migration of N species into dinitrogen (N_2) [9, 10].

When all oxygen defects were refilled, the NO reduction was ended. Both C_3H_6 and C_3H_8 pre-treated reduced ceria were able to convert considerable more NO into N_2 (much longer time interval) as compared to CO and H_2 pre-reductions. The pre-treatment of C_3H_6 and C_3H_8 resulted in a deeper catalyst reduction and more deposited carbon. These carbon deposits acted as reductant buffer. The oxidation of deposited carbon by active oxygen species from ceria lattice recreated the oxygen defect sites that can be again used for additional NO conversion [10]. C_3H_6 pre-treatment provided higher capacity for NO reduction into N_2 than C_3H_8 pre-treatment due to a three times larger carbon deposition.

The CO and H_2 pre-treatments resulted only in the reduction of surface oxygen and hardly any or no deposited carbon. Therefore, CO and H_2 pre-treatments are less effecitve than a hydrocarbon pre-treatment. Deposited carbon, acting as a reductant buffer, extended the period in which NO can be reduced into N_2. C_3H_6 will be preferred over C_3H_8 due to its higher reactivity and increased carbon deposit formation.

3.5. Conclusions

- The degree of ceria reduction obtained by C_3H_6 and C_3H_8 reduction, corresponded with up to 2.7 hypothetical reduced ceria layers. As compared to H_2 and CO, at 580 °C the obtainable reduction degrees with these hydrocarbons were around 3 times higher (Table 3.2). Pre-treatment by C_3H_6 due to its higher reactivity, resulting in three times more carbon deposited, is prefered over that of C_3H_8.

- Hydrocarbon pre-treatment led to carbon deposits on the reduced ceria surface. These carbon deposits will, however, act as a reductant reservoir, leading to a higher number of NO converted molecules (selective re-oxidation of reduced ceria) into nitrogen [9, 10].

- The deeper degree of reduction of ceria during reduction by hydrocarbons will be due to the oxidation of deposited (hydro)carbon intermediated by additional lattice oxygen on the reduced ceria to CO. For H_2 and CO pre-treatment, the apparent existence of H_2, H_2O, Ce^{3+} and Ce^{4+} (or CO,

CO_2, Ce^{3+} and Ce^{4+}) equilibrium will limit the ceria reduction of to only one monolayer.

For practical application of ceria-based catalysts in Di-Air system, it might be beneficial to add promoters (for example noble metals) that allow these catalysts to convert hydrocarbons introduced by high frequent fuel injections at lower temperatures.

References

[1] http://www.eea.europa.eu/publications/air-quality-in-europe-2015, accessed 2017-04-03.

[2] http://www.theicct.org/real-world-exhaust-emissions-modern-diesel-cars, accessed 2017-04-03.

[3] http://europa.eu/rapid/press-release_IP-15-5945_en.htm, accessed 2017-04-03.

[4] Y. Bisaiji, K. Yoshida, M. Inoue, K. Umemoto, and T. Fukuma, *Development of Di-Air - A New Diesel deNO$_x$ System by Adsorbed Intermediate Reductants,* SAE International Journal of Fuels and Lubricants **SAE Number 2011-01-2089** (2011).

[5] M. Inoue, Y. Bisaiji, K. Yoshida, N. Takagi, and T. Fukuma, *DeNO$_x$ Performance and Reaction Mechanism of the Di-Air System,* Topics in Catalysis **56**, 3 (2013).

[6] H. YAO, *Ceria in automotive exhaust catalysts I. Oxygen storage,* Journal of Catalysis **86**, 254 (1984).

[7] A. Bueno-López, K. Krishna, M. Makkee, and J. Moulijn, *Enhanced soot oxidation by lattice oxygen via La^{3+}-doped CeO$_2$,* Journal of Catalysis **230**, 237 (2005).

[8] L. Katta, P. Sudarsanam, G. Thrimurthulu, and B. M. Reddy, *Doped nanosized ceria solid solutions for low temperature soot oxidation: zirconium versus lanthanum promoters,* Applied Catalysis B: Environmental **101**, 101 (2010).

[9] Y. Wang, J. P. de Boer, F. Kapteijn, and M. Makkee, *Fundamental Understanding of the Di-Air System: The Role of Ceria in NO$_x$ Abatement,* Topics in Catalysis **59**, 854 (2016).

[10] Y. Wang, J. Posthuma de Boer, F. Kapteijn, and M. Makkee, *Next Generation Automotive DeNO$_x$ Catalysts: Ceria What Else?* ChemCatChem **8**, 102 (2016).

[11] J. T. Gleaves, J. R. Ebner, and T. C. Kuechler, *Temporal Analysis of Products (TAP)-A Unique Catalyst Evaluation System with Submillisecond Time Resolution,* Catalysis Reviews **30**, 49 (1988).

[12] G. Centi and S. Perathoner, *Towards Solar Fuels from Water and CO$_2$,* ChemSusChem **3**, 195 (2010).

[13] K. Otsuka, Y. Wang, E. Sunada, and I. Yamanaka, *Direct Partial Oxidation of Methane to Synthesis Gas by Cerium Oxide,* Journal of Catalysis **175**, 152 (1998).

[14] T. Staudt, Y. Lykhach, N. Tsud, T. Skála, K. Prince, V. Matolín, and J. Libuda, *Ceria reoxidation by CO_2: A model study,* Journal of Catalysis **275**, 181 (2010).

[15] C. Padeste, N. W. Cant, and D. L. Trimm, *The influence of water on the reduction and reoxidation of ceria,* Catalysis Letters **18**, 305 (1993).

[16] Y. Zhao, X. Wu, J. Ma, S. He, and X. Ding, *Characterization and reactivity of oxygen-centred radicals over transition metal oxide clusters,* Physical Chemistry Chemical Physics **13**, 1925 (2011).

[17] M. S. Palmer, M. Neurock, and M. M. Olken, *Periodic Density Functional Theory Study of Methane Activation over La_2O_3: Activity of O_2^-, O^-, O_2^{2-}, Oxygen Point Defect, and Sr^{2+}-Doped Surface Sites,* Jouranl of the american chemical society **124**, 8452 (2002).

[18] B. M. And and A. V. Ramaswamy, *Defect-Site Promoted Surface Reorganization in Nanocrystalline Ceria for the Low-Temperature Activation of Ethylbenzene,* Journal of the american chemical society **129**, 3062 (2007).

[19] C. Nederlof, F. Kapteijn, and M. Makkee, *Catalysed ethylbenzene dehydrogenation in CO_2 or N_2-Carbon deposits as the active phase,* Applied Catalysis A: General **417**, 163 (2012).

[20] M. Pereira, J. Órfão, and J. Figueiredo, *Oxidative dehydrogenation of ethylbenzene on activated carbon catalysts. I. Influence of surface chemical groups,* Applied Catalysis A: General **184**, 153 (1999).

[21] L. E. Cadus, L. A. Arrua, O. F. Gorriz, and J. B. Rivarola, *Action of activated coke as a catalyst: Oxydehydrogenation of ethylbenzene to styrene,* Industrial & engineering chemistry research **27**, 2241 (1988).

[22] G. EMIG, *Action of zirconium phosphate as a catalyst for the oxydehydrogenation of ethylbenzene to styrene,* Journal of Catalysis **84**, 15 (1983).

[23] M. Zboray, A. T. Bell, and E. Iglesia, *Role of C–H Bond Strength in the Rate and Selectivity of Oxidative Dehydrogenation of Alkanes,* The Journal of Physical Chemistry C **113**, 12380 (2009).

[24] C. Li, Q. Xin, and X. Guo, *Surface oxygen species and their reactivities in the mild oxidation of ethylene on cerium oxide studied by FT-IR spectroscopy,* Catalysis Letters **12**, 297 (1992).

4

Fundamental understanding of the Di-Air system II: The role of ceria in NO reduction

Care and diligence bring luck.

Thomas Fuller

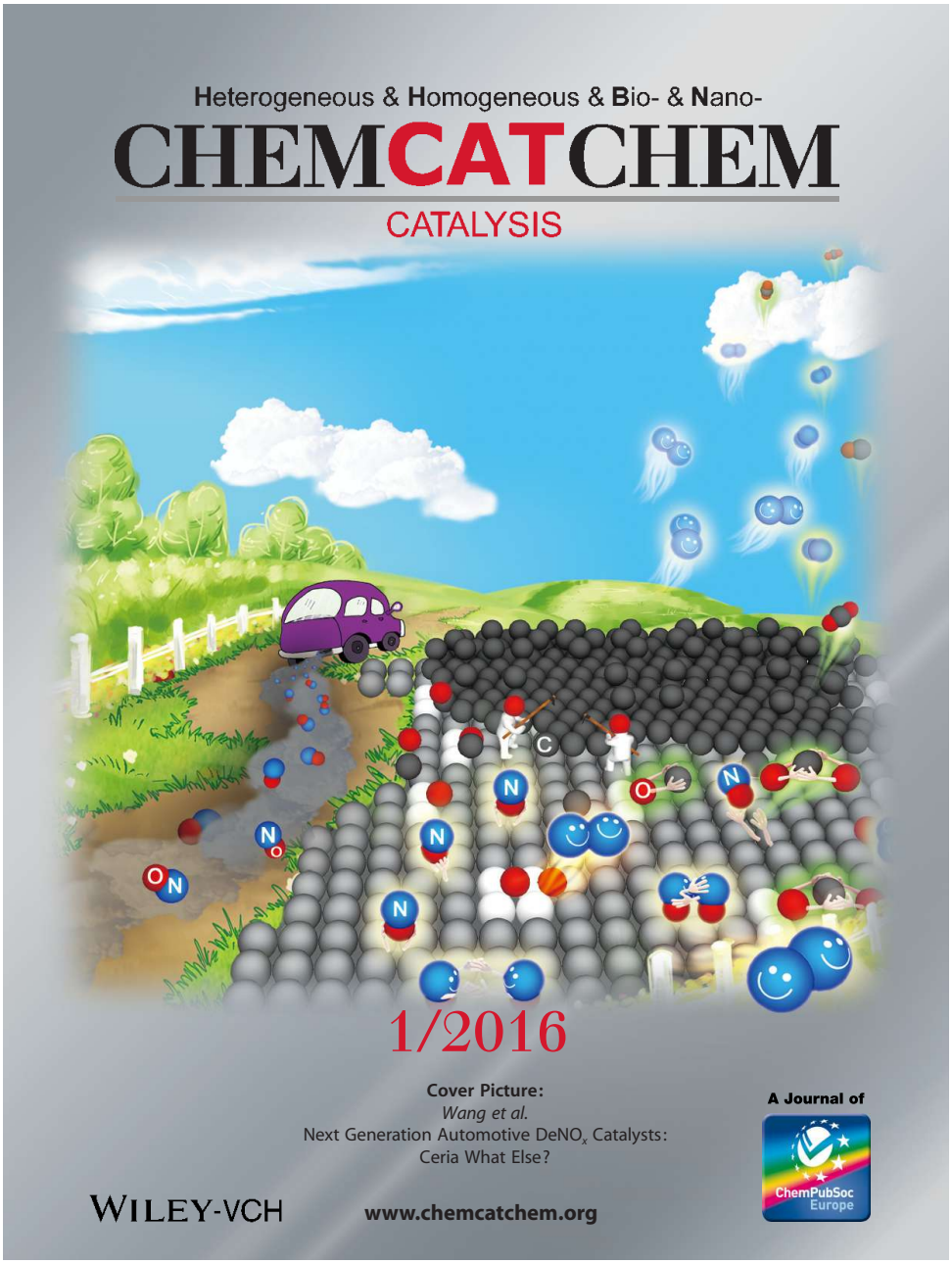
Heterogeneous & Homogeneous & Bio- & Nano-
CHEMCATCHEM
CATALYSIS
1/2016
Cover Picture:
Wang et al.
Next Generation Automotive DeNO$_x$ Catalysts:
Ceria What Else?
A Journal of
ChemPubSoc Europe
WILEY-VCH
www.chemcatchem.org

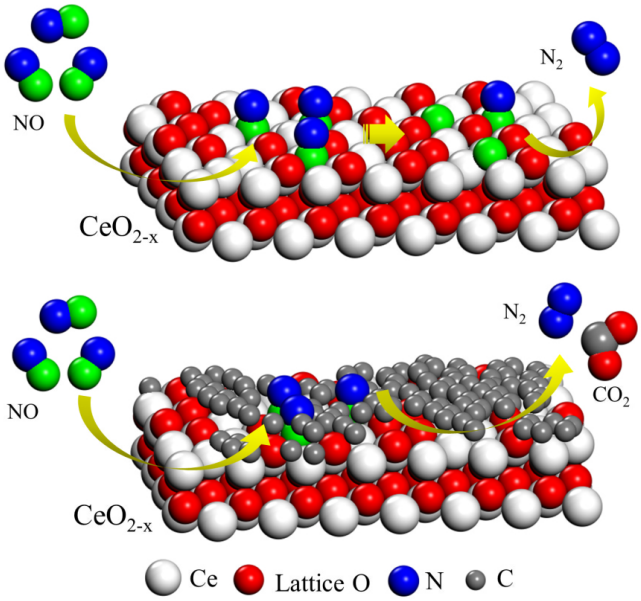

The temporal analysis of products (TAP) technique was used to study the NO reduction to N_2 over H_2- and C_3H_6-reduced La-Zr doped ceria at 560°C. (La-Zr doped) ceria is found to be capable of fuel oxidation and NO reduction. NO dissociates on oxygen anion vacancies, thereby refilling these vacancies with oxygen anions and forming N_2. The carbonaceous deposits formed upon catalyst reduction by C_3H_6, are oxidized by oxygen species originating from the ceria lattice. This recreates oxygen anion vacancies, which enables substantial additional NO reduction. These findings may open a new perspective on the understanding of $DeNO_x$ by hydrocarbons.

This chapter is based on the following publications:
Y.Wang, J.Posthuma de Boer, F.Kapteijn, M.Makkee, ChemCatChem 8,102(2016)
Y. Wang, J. P. de Boer, F. Kapteijn, and M. Makkee, Topics in Catalysis 59, 854 (2016)
M.Makkee,Y.Wang, SAE International Journal of Engine 10,4 (2017)

4.1. Introduction

NO_x abatement of the more fuel economic lean-burn engine remains a challenge. Future Euro 7 automotive legislation is anticipated to involve a further reduction of NO_x emissions compared to the current Euro 6 standards Figure 1.6 (Chapter 1). In addition, the more realistic Worldwide harmonized Light vehicles Test Procedures (WLTP) is expected to replace the outdated and unrealistic New European Driving Cycle (NEDC) of 1990. In order to comply with the anticipated Euro 7 standard, for a typical diesel exhaust composition, approximately 200 ppm NO has to be reduced to 10 ppm NO in competition with an excess of 5% O_2, 5% CO_2, and 5-10% H_2O. Extremely efficient exhaust emission after-treatment technologies will be required to meet future more stringent NO_x regulation. The Di-Air (Diesel NO_x after treatment by Adsorbed Intermediate Reductants) system, developed by Toyota, opts to meet these future NO_x-emission standards [1, 2].The scheme of the Di-Air system is shown in Figure 1.14 (Chapter 1).

Short fuel rich periods are created by the direct injection of fuel into the exhaust upstream of an NSR (NO_x storage reduction) catalyst (Pt/Rh/Ba/K/Ce/Al_2O_3) at temperatures above 350 °C. By using the same amount of fuel, high-intensity injections were shown to be more efficient in the reduction of NO_x as compared to low intensity or continuous fuel injection and/or post injection directly into the engine. How this system works remains a mystery. Currently, the DeNO_x mechanism remains controversial [3]. The reported key step is either: (a) the dissociative adsorption of NO on reduced catalytic sites [4], or (b) $NO_{2,ad}$, -NCO and -CN intermediate formation [5, 6]. In the Di-Air system, several catalyst components are involved, this makes the elucidation of which catalyst component(s) play(s) a major role in the reduction of NO_x a difficult task. What the role of each catalyst component is and why the Di-Air system can achieve its performance both remain unresolved.

In order to further develop and optimize this system, a detailed investigation with regard to the catalyst composition and final operation in practice is required. The Di-Air system has a complex reaction network with several interacting components and intermediates. The occurrence of mass-transport limitations and non-isothermal effects make meaningful bench-scale reactor tests and the data interpretation a non-trivial task. The dynamic nature of the Di-Air system makes it an ideal system to be explored by a pulse-

response technique, *e.g.,* Temporal Analysis of Products (TAP). TAP is a vacuum pulse-response technique developed to investigate gas-solid interactions with the aim to reveal the complex mechanism of catalytic reactions [7]. A more detailed description of the used TAP set-up, procedural details, can be found in Chapter 2.

A commercial Zr-La doped ceria catalyst (BASF Company) was used as a model for the ceria component. The enhanced thermal stability provided by Zr doping [8] is believed to be vital in obtaining consistent and reliable results. For undoped ceria, a significant decrease in the surface area was observed between 550 and 750 °C under air, vacuum or reducing enviro nments [9]. In separate experiments with undoped ceria, we observed sintering of the ceria as a function of time on stream. Furthermore, the addition of Zr is reported to increase the lattice oxygen mobility and reactivity [10]. The addition of La into the ceria structure is also believed to enhance lattice oxygen diffusion [11].

4.2. Experimental

4.2.1. Catalyst characterisation

4.2.1.1. N_2 adsorption

Tristar II 3020 Micromeritics was used to determine the textural properties like specific BET surface area and pore volume. The catalyst samples were degassed at 473 K for 16 h in a vacuum (0.05 mbar) before the nitrogen adsorption at liquid nitrogen temperature.

4.2.1.2. Inductively Coupled Plasma Optical Emission Spectroscopy (ICP-OES)

Approximately 50 mg of samples were destructed in 4.5 mL 30% HCl + 1.5 mL 65% HNO_3 using the microwave. The destruction time in the microwave was 120 min at max. power (90 W). After destruction, the samples were diluted to 50 mLwith Millipore-Q (purified demi) water. The samples were analysed with ICP-OES (PerkinElmer Optima 5300).

4.2.1.3. X-Ray photoelectron spectroscopy (XPS)

XPS measurements were recorded on a K-alpha Thermo Fisher Scientific spectrometer using monochromated Al Kα X-ray source. A flood gun was applied for charge compensation. Lorentz function was used to analyse the peak intensities. Binding energies were calibrated with C(1s) at 285 eV as a reference.

4.2.1.4. X-ray diffraction (XRD)

The Powder X-Ray diffraction (XRD) was recorded by a Bruker-AXS D5005 with a Co Kα source. The data was three times collected by varying the 2θ angle from 5° to 90° with a step size of 0.02.

4.2.1.5. Transmission electron microscope (TEM)

Transmission Electron Microscopy (TEM) images were recorded on a JEM-2100P electron microscope operating at 200 kV. Before being transferred into the TEM chamber, the samples dispersed in ethanol and deposited onto a carbon-coated copper grid, shortly dried in air and then quickly moved into the vacuum system of the microscope.

4.2.2. Catalytic testing

4.2.2.1. TAP pulses experiments

All experiments were performed with the same catalyst Zr-La doped ceria sample, of which 21.2 mg was packed between two quartz particle (150-212 µm) beds. In all experiments a starting pulse size of approximately $1.6.10^{15}$ molecules was used, the pulse size gradually decreases during an experiment as the reactant is pulsed from the closed and calibrated volume of the pulse-valve line. Prior to a ceria reduction, the catalyst was firstly re-oxidized at the same temperature at which the reduction was to be performed, using pulsing of 80 vol.% O_2 in Ar until a stable O_2/Ar signal ratio was obtained. The reduction of ceria was carried out by pulsing reductant quantities of 80 vol.% C_3H_6 in Ne, 80 vol.% CO in Ar or 67 vol.% H_2 in Ar until a stable reactant and product to internal standard signal ratio indicated that the catalyst was stablised. NO pulse experiments were performed using

Table 4.1: Bulk and surface composition of La-Zr-doped ceria

Metal atom fraction	Ce	La	Zr
Bulk	0.64	0.15	0.21
Surface	0.63	0.03-0.04	0.34

80 vol.% NO in Ar or ^{15}N (without internal standard) and were continued until the product distribution did not change any more. The reactor's inertness was confirmed by pulsing all employed reactants and major products over a quartz packed reactor at 580 °C, no detectable conversion into products, *e.g.,* N_2, CO, CO_2, H_2O, and H_2 was observed.

4.2.2.2. *Operando* Raman

Operando Raman spectra (Renishaw, 2000) were recorded using a temperature controlled *operando* Raman cell (Linkam, THMS 600). Ten scans were collected for each spectrum in the 100 - 4000 cm^{-1} range using a continuous grating mode with a resolution of 4 cm^{-1} and scan time of 10 s. The spectrometer was calibrated daily using a silicon standard with a strong band at 520 cm^{-1}. The ceria was firstly pre-treated by C_3H_6 (1000 ppm in N_2, flow rate 200 mL/min) for 2 h. N_2 was used to flush the cell for 20 min. Subsequently, NO (1000 ppm NO in N_2, the flow rate of 200 mL/min) was admitted to the cell.

4.2.2.3. Flow reactor

100 mg catalyst was placed in a 6 mm inner-diameter quartz reactor tube. A feed composition of NO (with He for balance) was used with a flow rate of 50 mL/min. The reactor effluent was online analyzed by quadrupole Mass Spectrometry (MS, Leiden probe microscopy, TPM T100 Gas Analyser).

Table 4.2: BET area and pore volume of ceria exposed to different conditions

Sample	BET (m^2/g)	Pore volume (mL/g)
Fresh sample	65	0.37
Aged sample[1]	65	0.38
Spent sample[2]	63	0.33

4.3. Result and discussion

4.3.1. Catalyst characterization

The bulk and surface composition of La-Zr-doped ceria (afterward note as doped ceria), determined by ICP-OES and XPS, respectively, shows that the surface contains hardly any La and enriches with Zr (Table 4.1) as compared to the bulk the surface. The doped ceria sample was thermally stable, as evidenced by the BET area (Table 4.2).

The TEM image (Figure 4.1A) indicated that the crystal size of this sample was approximately 5.0 ± 0.6 nm. The XRD pattern of the doped ceria sample (Figure 4.1B) showed the fluorite cubic structure (JCPD number: 43-1002), with dominant exposed (111) planes. The crystallite size of the doped ceria sample was calculated to be 5.0 ± 0.1 nm based on the Scherrer equation (Equation 4.1):

$$D = \frac{K\lambda}{\beta cos\theta} \tag{4.1}$$

With:

D: crystallite size
λ: X-ray wavelength 0.1789 nm
K: the particle shape factor 0.94
β: the full width at half height of the (111) reflection

The particle size calculated from Scherrer equation fitted well with the TEM result. A perfect ceria with (111) crystal plane exposure was created as

1 The aged sample is thermal treated in the static air environment at 650 °C for 24 h
2 The spent sample is obtained after several reaction cycles of C_3H_6 oxidation and NO reduction at 580 °C for 10 days

a model of Zr-La doped ceria, as shown in Figure 4.2. As the (111) crystal plane is a stoichiometric O-Ce-O tri-layer (0.316 nm) stacked along the [111] direction, assuming a perfect cubic crystal structure, the number of O-Ce-O tri-layer was determined to be 16 (111) layers in one single craystal, using the Equation 4.2:

$$n = \frac{crystalsize}{0.316\,\text{nm}} \tag{4.2}$$

The hypothetical ceria layers concept is introduced in order to obtain insight in the reactivity of the actual surface as a function of the degree of reduction (surface oxidation state). We regard one O-Ce-O tri-layer on the (BET) surface as one hypothetical ceria layer.

The total number of hexagonal surface units on the (BET) surface (Figure 4.2) is calculated to be $3.6 \cdot 10^{18}$ using the Equation 4.3:

$$N = \frac{S_{BET} \times W_{sample}}{S_{hexagonal\ unit}} \tag{4.3}$$

S_{BET}:	65 m^2/g
W_{sample}:	21.2 mg
$S_{hexagonal\ unit}$:	0.38 nm^2

The total number of O atoms in each hypothetical ceria layer can be calculated to be $2.2 \cdot 10^{19}$ using the Equation 4.4:

$$N_{Total\ O} = N \times n \tag{4.4}$$

where n represents the number of oxygen atoms in one hexagonal unit. The number of oxygen atoms in one hexagonal unit is 6.

Assuming that Zr and La are Ce, a maximum of 25% of the number of O ions in each crystal layer can be reduced, according to the Equation 4.5:

$$CeO_2 \leftrightarrow CeO_{1.5} + \frac{1}{2}O \tag{4.5}$$

The number of reducible oxygens in one hypothetical ceria layer is calculated to be $5.4 \cdot 10^{18}$ atoms.

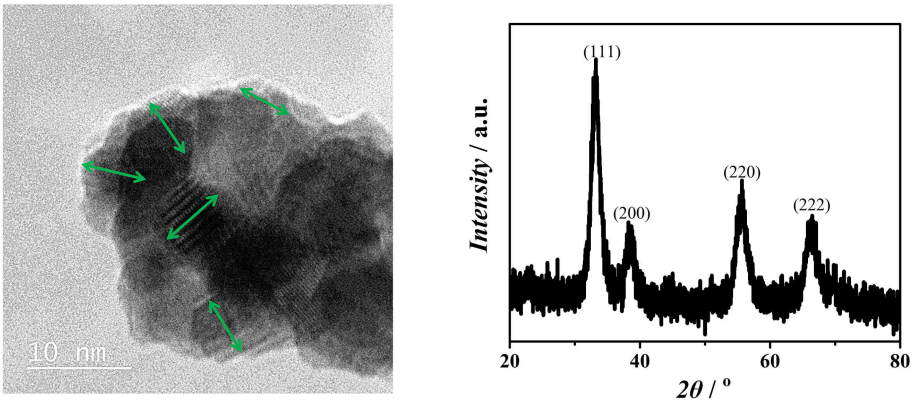

Figure 4.1: TEM image of Zr-La doped ceria, and (B) XRD pattern of a fresh Zr-La doped ceria.

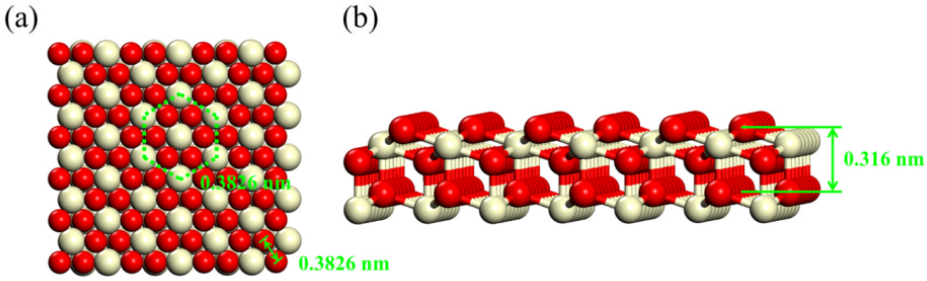

Figure 4.2: (a) top view of the (111) crystal plane, (b) side view of the (111) crystal plane (red: O, light yellow: Ce).

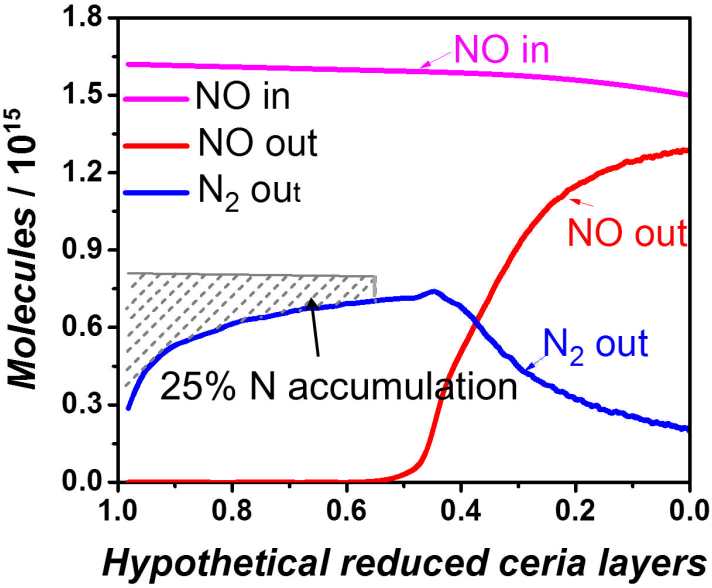

Figure 4.3: Reactant and product evolution during the NO pulse experiment over H_2 pre-reduced doped ceria at 560 °C.

Table 4.3: Summary of H_2 and hydrocarbon pre-treatment and NO re-oxidation.

Reduction stage	H_2 (560 °C)	C_3H_6 (560 °C)
Oxygen extraction(atoms)	$5.2 \cdot 10^{18}$	$1.1 \cdot 10^{19}$
Hypothetical reduced ceria layers	1	1.8
Carbon deposited (atoms, wt% on ceria)	-	$3 \cdot 10^{19}$ (3.3 wt%)
Re-oxidation stage	NO (560 °C)	NO (560 °C)
Oxygen accumulation(atoms)	$6 \cdot 10^{18}$	$1.1 \cdot 10^{19}$
Hypothetical reduced ceria layers after oxidation	0	0

4.3.2. Catalytic Testing

4.3.2.1. NO pulses over H_2 re-reduced doped ceria

Nover (pre- or re-) oxidized doped ceria did not show any reactivity. The product evolution observed for NO reduction over the H_2 reduced catalyst is shown in Figure 4.3. The pre-reduction by H_2 led to a (clean) reduced doped ceria from which $5.2 \cdot 10^{18}$ oxygen atoms were extracted, corresponding to 1 hypothetical reduced ceria layer. Subsequent NO pulses showed full NO conversion with N_2 as the only observed product for 1 to 0.5 hypothetical reduced ceria layers. At this stage, approximately 25% of the converted NO was not released as N_2 but had accumulated on the surface.

After that stage, an enhanced N_2 production was observed for each NO pulse. The N mass balance of the whole NO pulse experiment closed within 98%, indicating that all accumulated N was converted to N_2. There was no evidence of any N_2O or NO_2 formation. In total $6.0 \cdot 10^{18}$ oxygen atoms were incorporated into the catalyst, which is within experimental error (oxygen mass balance closed within 90%) equal to the number of oxygen atoms extracted during H_2 reduction (Table 4.3). This observation suggests that NO conversion is favored on a reduced surface, whereas an oxidized surface is hardly active.

An attractive mechanism to explain the current observations is the direct dissociation of adsorbed NO on oxygen anion vacancies, in which the O side of NO fills the oxygen anion vacancy, and the N species recombine to form N_2 [4, 12, 13].

4.3.2.2. NO pulses over C_3H_6 re-reduced doped ceria

In the Di-Air system, the high-frequency direct fuel injection upstream of the catalyst will create a local reducing enviro nment. In order to simulate such an enviro nment, C_3H_6 pulses were used to pre-reduce the catalyst. This C_3H_6 pulse experiment resulted in the extraction of $1.1 \cdot 10^{19}$ oxygen atoms, corresponding to 1.8 hypothetical reduced ceria layers. In addition, this C_3H_6 reduction led to the deposition of $3.4 \cdot 10^{19}$ carbon atoms (3.3 wt.% carbon). The results of the subsequent NO pulse experiment are shown in Figure 4.4.

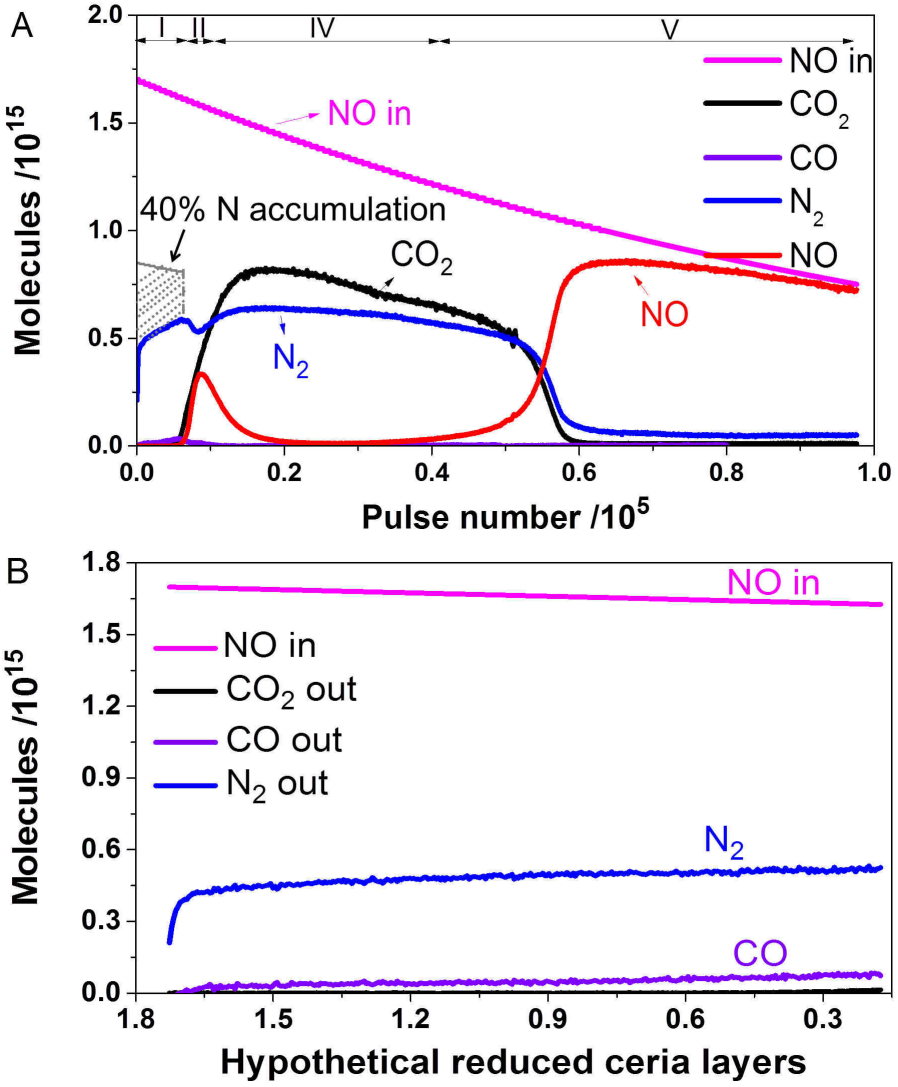

Figure 4.4: Reactant and product evolution during the NO pulse experiment over C_3H_6 pre-reduced Zr-La doped ceria at 560 °C (A) with pulse number; (B) with the number of hypothetical reduced ceria layers during stage I of (A).

In stage I of Figure 4.4A, corresponding with 1.8-0.5 hypothetical reduced ceria layers (Figure 4.4B), full NO conversion was observed with N_2 as the main observed product (hardly any CO formed). This finding was confirmed by an isotopic ^{15}N pulse experiment, in which $15N_2$ (mass 30) was observed as the major product with hardly any CO or CO_2 formation (Figure 4.5A). The oxygen balance indicated that $8.7 \cdot 10^{18}$ oxygen atoms accumulated during this stage, which is around 80% of the oxygen atoms extracted from the ceria lattice in the previous C_3H_6 pulse experiment. This indicates that at this point the catalyst had been largely re-oxidized by NO. Similar as in the H_2 pretreatment, not all converted NO emerged directly as N_2, approximately 40% of the N species had accumulated. In stage II, the evolution of CO_2 was observed. This evolution of CO_2 was closely followed by a temporary decrease in the NO conversion. The NO conversion increased again during stage III. In stage IV full NO conversion was observed, while N_2 and CO_2 were the only observed products, per 2 converted NO molecules approximately 1 CO_2 and 1 N_2 molecule was formed. In stage V, a progressive decrease in the NO conversion was observed, which dampened when it approached zero conversion. The N_2 and CO_2 production followed the same trend as the NO conversion. No or hardly any N_2O or NO_2 were formed and no traces of -CN or-CNO were observed.

In stage II, the evolution of CO_2 was observed. This evolution of CO_2 was closely followed by a temporary decrease in the NO conversion. The NO conversion increased again during stage III. In stage IV full NO conversion was observed, while N_2 and CO_2 were the only observed products, per 2 converted NO molecules approximately 1 CO_2 and 1 N_2 molecule was formed. In stage V, a progressive decrease in the NO conversion was observed, which levelling off upon approaching 0% conversion. The N_2 and CO_2 production followed the same trend as the NO conversion. No or hardly any N_2O or NO_2 were formed and no traces of -CN or-CNO were observed.

The observed accumulation of N species diminished with increasing pulse number. Up to stage IV, 13% of the N species had accumulated on the surface. The N mass balance of the whole NO pulse experiment closed within 94%, indicating that the N species arising from NO dissociation were almost entirely released as N_2. For the C_3H_6 reduction pre-treatment N accumulation was 1.6 times higher as compared to the H_2 reduction pre-

treatment. The accumulation of N may be related to that either (a) the recombination of N is affected by the presence of deposited carbon; or (b) more oxygen defect sites were present, e.g. ionic N species [13] are located in these oxygen defect sites. As this accumulation of N species was also evidenced in the NO pulse experiment over the H_2 reduced catalyst, it is unlikely that these accumulated N species were present in the form of -CNO or -CN as proposed by Toyota [1]. Detailed studies of the accumulated N species and their roles in the reduction of NO will be the subject of future articles (part of it will be discussed in Chapter 5).

The absence of oxidation products CO and CO_2 in stage I indicates that the carbonaceous residues, left on the surface after C_3H_6 pre-reduction, were not directly participating in the reduction of NO to N_2. NO dissociated on oxygen anion vacancies, as was also found for the H_2 reduction pre-treatment. NO dissociation resulted in a progressive re-oxidation of the catalyst with increasing NO pulse number (Figure 4.4B), thereby decreasing the number of oxygen anion defect sites. The start of CO_2 formation at the point at which the catalyst was largely re-oxidized suggests that at a specific catalyst oxidation state the La-Zr doped ceria catalyst becomes active in the oxidation of these deposited carbonaceous residues. The oxidation of these carbonaceous deposits creates two oxygen anion vacancies per formed CO_2 molecule, allowing the formation of one N_2 molecule from 2 NO molecules. This delayed CO_2 formation starts to counteract the depletion of oxygen anion vacancies that caused the temporary decline in NO conversion.

That oxygen species originating from lattice oxygen are responsible for the oxidation of carbon [14] was evidenced by an $^{18}O_2$ pulse experiment (Figure 4.5B), in which the initial exclusive formation of $C^{16}O$ and $C^{16}O_2$ indicated that gas-stage oxygen was not directly involved in the oxidation of these carbon deposits. In summary, NO re-oxidizes the catalyst and is not directly involved in the oxidation of carbonaceous deposits. The oxidation of carbonaceous deposits to CO_2 by oxygen species originating from lattice oxygen recreates oxygen anion defect centres responsible for additional NO dissociation. Therefore, these carbonaceous deposits can be seen as a delayed or stored reductant.

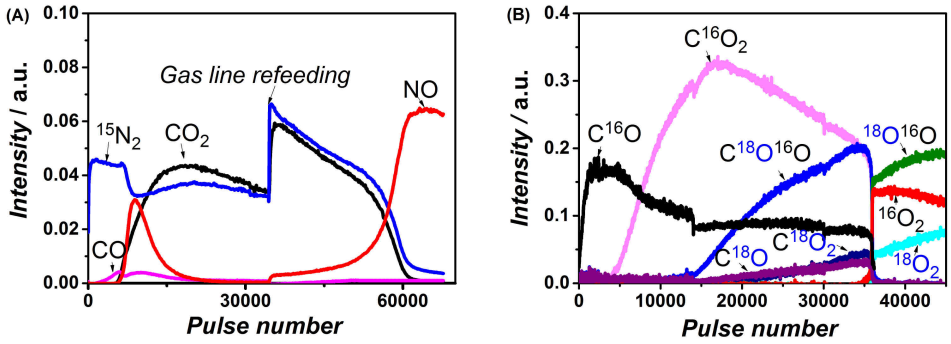

Figure 4.5: Reactant and product evolution upon pulsing (A) ^{15}N at 560 °C and (B) $^{18}O_2$ at 530 °C over Zr-La doped ceria pre-treated (21.2 mg) by C_3H_6 560 and 530 °C in TAP, respectively.

4.3.2.3. *Operando* Raman

As TAP is a vacuum technique, *operando* Raman (at atmospheric pressure) is applied to confirm the results obtained from TAP. NO reduction is performed over C_3H_6 pre-treated La-Zr doped ceria both at 560 °C and is shown in Figure 4.6. The band at 460 cm^{-1} is attributed to the symmetric stretch mode of the Ce-O_8 crystal unit, which is characteristic for the reduced fluorite ceria structure [15]. This peak disappears during the C_3H_6 pre-treatment, while under NO flow the increase in the intensity of the band at 460 cm^{-1} indicates that the pre-reduced La-Zr doped ceria catalyst is re-oxidised by NO. The bands at 1575 and 1350 cm^{-1} are assigned to G band and D band of carbon in the form of graphene or graphite [16]. The G band is usually assigned to zone centre phonons of E_{2g} symmetry of the perfect graphite structure, and the D peak is a breathing mode of A_{1g} symmetry, this mode is forbidden in a perfect graphite structure and only becomes active in the presence of structural defects and disorders [16]. The intensity of D band and G band of graphene/graphite remains constant during the first 270 min of NO/N_2 flow, indicating that the oxidation of carbon commences much later than the re-oxidation of the ceria. This observation also points out that the oxidation of carbon is via an oxygen species originating from the lattice and not from gas stage NO, in line with previous findings in the oxidation of soot on ceria-based catalysts [14].

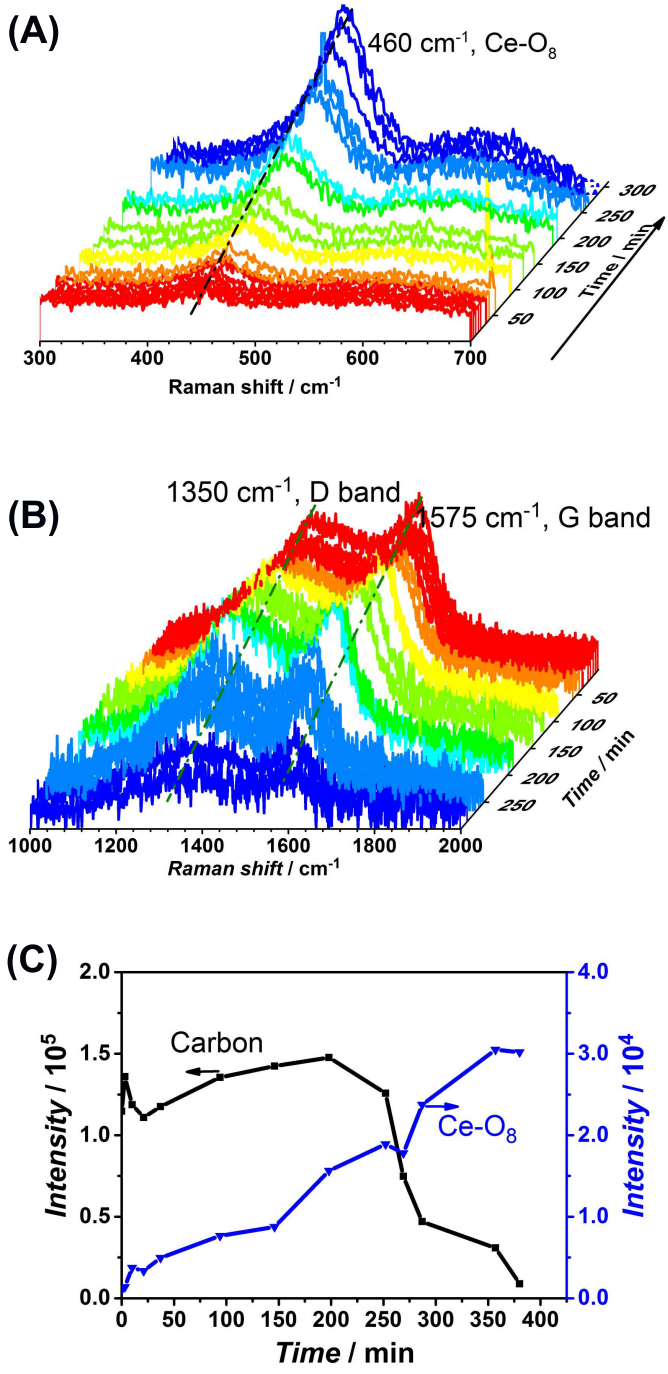

Figure 4.6: *Operando* Raman spectra of C_3H_6 reduced ceria upon exposure to NO (1000 ppm) at 560 °C, Raman spectra of the band at (A) 460 cm^{-1} and (B) 1575 and 1350 cm^{-1}; (C) Raman bands intensity of 460, 1575, and 1350 cm^{-1} responses *versus* time.

The inventors of the Di-Air system attributed the exceptional behaviour of their system to the formation of hydrocarbon -CN and -CNO type intermediates. In the current study, in which the presence of hydrocarbons and NO are decoupled, we found a similar behaviour for the hydrogen reduced and the hydrocarbon reduced (Zr-La doped) ceria. Hydrocarbon pre-reduced outperforms H_2 pre-reduced La-Zr doped ceria by a factor of 15, due to the deeper degree of reduction and the presence of carbon deposits. Also CO pre-reduced ceria was less effective by a factor of 13. We found no evidence that hydrocarbon residues or carbonaceous residues play a direct role in the NO conversion. However, these carbonaceous residues extend the effectiveness of the catalyst in the decomposition of NO under fuel lean conditions by recreating new oxygen anion vacancies. Toyota's observation, that large hydrocarbon pulses are beneficial [1, 2] can be explained by the formation of these carbon deposits, which are preferentially oxidized to CO_2 by oxygen species originating from lattice oxygen.

4.4. Conclusions

La-Zr doped ceria is a promising catalyst for a Di-Air system. Oxygen anion vacancies in La-Zr doped ceria are responsible for the decomposition of NO to N_2, thereby re-oxidizing these centers. The delayed oxidation of carbon deposits by oxygen species originating from lattice oxygen will in practice maintain a reduced surface state during fuel lean conditions. These carbon deposits can, therefore, be seen as a stored reductant with a delayed function. Our work, therefore, provides an alternative view on the role of hydrocarbons in the reduction of NO to N_2. Additional catalyst composition optimization may be considered in order to enhance the hydrocarbon activation capability at lower temperatures (< 500 °C).

References

[1] M. Inoue, Y. Bisaiji, K. Yoshida, N. Takagi, and T. Fukuma, *DeNO$_x$ Performance and Reaction Mechanism of the Di-Air System,* Topics in Catalysis **56**, 3 (2013).

[2] Y. Bisaiji, K. Yoshida, M. Inoue, K. Umemoto, and T. Fukuma, *Development of Di-Air - A New Diesel deNO$_x$ System by Adsorbed Intermediate Reductants,* SAE International Journal of Fuels and Lubricants **SAE Number 2011-01-2089** (2011).

[3] Y. Hu, K. Griffiths, and P. R. Norton, *Surface science studies of selective catalytic reduction of NO: Progress in the last ten years,* Surface Science **603**, 1740 (2009).

[4] M. Daturi, N. Bion, J. Saussey, J.-C. Lavalley, C. Hedouin, T. Seguelong, and G. Blanchard, *Evidence of a lacunar mechanism for deNO$_x$ activity in ceria-based catalysts,* Physical Chemistry Chemical Physics **3**, 252 (2001).

[5] M. Adamowska-Teyssier, A. Krztoń, P. D. Costa, and G. Djéga-Mariadassou, *SCR NO$_x$ mechanistic study with a mixture of hydrocarbons representative of the exhaust gas from coal combustion over Rh/$Ce_{0.62}Zr_{0.38}O_2$ catalyst,* Fuel **150**, 21 (2015).

[6] W. HECKER, *IInfrared observations of Rh-NCO and Si-NCO species formed during the reduction of NO by CO over silica-supported rhodium,* Journal of Catalysis **85**, 389 (1984).

[7] J. T. Gleaves, J. R. Ebner, and T. C. Kuechler, *Temporal Analysis of Products (TAP)-A Unique Catalyst Evaluation System with Submillisecond Time Resolution,* Catalysis Reviews **30**, 49 (1988).

[8] R. Si, Y. W. Zhang, L. M. Wang, S. J. Li, B. X. Lin, W. S. Chu, Z. Y. Wu, and C. H. Yan, *Enhanced Thermal Stability and Oxygen Storage Capacity for $Ce_xZr_{1-x}O_2$ (x = 0.4- 0.6) Solid Solutions by Hydrothermally Homogenous Doping of Trivalent Rare Earths,* The Journal of Physical Chemistry C **111**, 787 (2007).

[9] V. Perrichon, A. Laachir, S. Abouarnadasse, O. Touret, and G. Blanchard, *Thermal stability of a high surface area ceria under reducing atmosphere,* Applied Catalysis A: General **129**, 69 (1995).

[10] Z. Yang, T. K. Woo, and K. Hermansson, *Effects of Zr doping on stoichiometric and reduced ceria: A first-principles study,* The Journal of Chemical Physics **124**, 224704 (2006).

[11] L. Katta, P. Sudarsanam, G. Thrimurthulu, and B. M. Reddy, *Doped nanosized ceria solid solutions for low temperature soot oxidation: zirconium versus lanthanum promoters,* Applied Catalysis B: Environmental **101**, 101 (2010).

[12] Z. Yang, T. K. Woo, and K. Hermansson, *Adsorption of NO on unreduced and reduced CeO_2 surfaces: A plane-wave DFT study,* Surface Science **600**, 4953 (2006).

[13] S. Overbury, D. Mullins, D. Huntley, and L. Kundakovic, *Chemisorption and reaction of NO and N_2O on oxidized and reduced ceria surfaces Studied by soft x-Ray photoemission spectroscopy and desorption Spectroscopy,* Journal of Catalysis **186**, 296 (1999).

[14] A. Bueno-López, K. Krishna, M. Makkee, and J. Moulijn, *Enhanced soot oxidation by lattice oxygen via La^{3+}-doped CeO_2,* Journal of Catalysis **230**, 237 (2005).

[15] W. H. Weber, K. C. Hass, and J. R. McBride, *Raman study of CeO_2: Second-order scattering, lattice dynamics, and particle-size effects,* Physical Review B **48**, 178 (1993).

[16] A. C. Ferrari, J. C. Meyer, V. Scardaci, C. Casiraghi, M. Lazzeri, F. Mauri, S. Piscanec, D. Jiang, K. S. Novoselov, S. Roth, and A. K. Geim, *Raman Spectrum of Graphene and Graphene Layers,* Physical Review Letters **97**, 187401 (2006).

5

Evaluation the role of noble metals in NO_x reduction in the Di-Air $DeNO_x$ system

Success is no accident.
It is hard work, perseverance, learning, studying, sacrifice
and most of all,
love of what you are doing or learning to do.

Pele

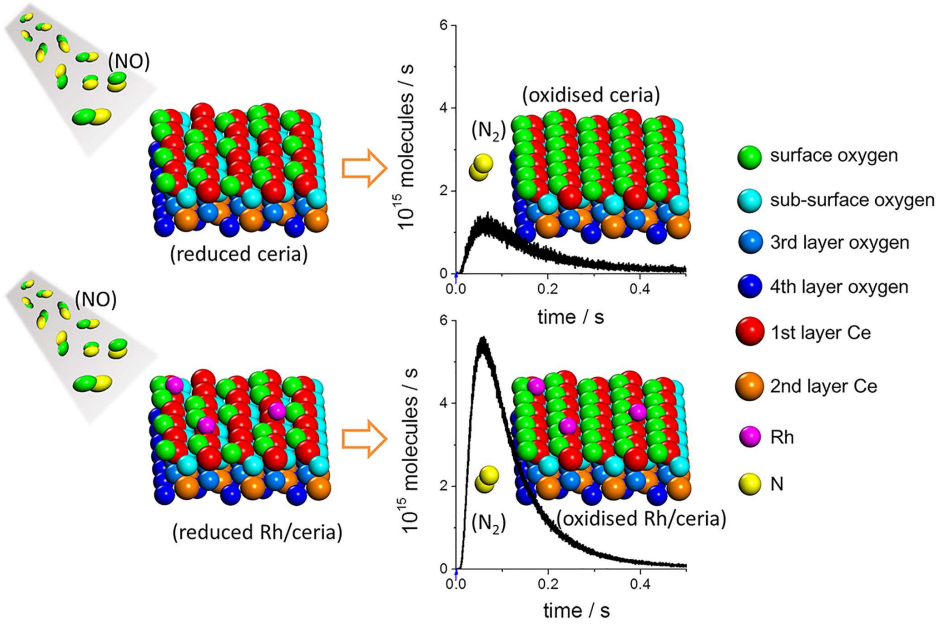
(NO)
(reduced ceria)
(oxidised ceria)
(N2)
10^15 molecules / s
time / s
(NO)
(reduced Rh/ceria)
(oxidised Rh/ceria)
(N2)
10^15 molecules / s
time / s
surface oxygen
sub-surface oxygen
3rd layer oxygen
4th layer oxygen
1st layer Ce
2nd layer Ce
Rh
N

Oxygen vacancies of reduced ceria are extremely selective sites in the catalytic conversion of NO into N_2 for the Di-Air deNO_x system, that will surpass by far commercially applied lean burn engine DeNO_x systems. The noble metals Pt and Rh promote the ceria reduction by hydrocarbons C_3H_6 and C_3H_8, at lower temperatures than without these metals. Rh was a more active promoter in ceria reduction and carbon deposition than Pt. During the NO reduction the pre-reduced ceria support becomes gradually oxidized and after filling 70-80% of the oxygen vacancies the NO starts to appear in the product mixture. In the presence of carbon deposit the lattice oxygen of the ceria reacts with the carbon keeping the ceria in a reduced form, sustaining the NO decomposition process as long as the carbon is present. The reduction of NO over pre-reduced noble metal/ceria showed a selective formation N_2, while N_2O and NO_2 formation were never observed. During the NO reduction process some unidentified N-species remain on the catalyst, the amount depending on the catalyst, but finally all nitrogen is released as N_2. More importantly, the presence of noble metal leads to a faster N_2 formation rate than over the bare ceria.

This chapter is based on the following publication:
Y.Wang, F. Kapteijn, and M.Makee, Evaluation the role of noble metals in NO_x reduction in the Di-Air DeNO_x system (underreview)

5.1. Introduction

Nitrogen oxides (NO_x) are harmful gasses which caused every year premature deaths of millions of people [1, 2]. Around 40% of the total NO_x released into the atmosphere originated from road transport [1, 3]. The actual average of NO_x emissions from the cars on the road is six to eight times more than the actual emission requirement [4]. Therefore, as of September 2017, the European Commission will proclaim that the real driving emission (RDE) will partially replace the current laboratory test in order to introduce new car models into the market [5]. However, up to 2.1 times higher NO_x emission (0.168 g/km), relatively to the current Euro 6 NO_x emission standard (0.08 g/km), is allowed under the RDE testing by September 2017 [5]. The fact that a higher NO_x emission by the new rule in 2017 is allowed indicating that currently available technologies: Urea- Selective Catalytic Reduction (SCR)[6–8], NO_x Storage and Reduction (NSR) [9–11] and combinations thereof still need to be significantly improved. In future, it can be anticipated that the NO_x emission will become even more stringent. Therefore, more efficient or alternative exhaust emissions after-treatment technologies will be required. Di-Air system [12], developed by Toyota Motor Company, showed promise to meet the future NO_x emission standards under real driving test conditions. The Di-Air system retains high NO_x conversion levels (above 80%) even up to 800 °C and high gas hourly space velocities (GHSV) up to 120.000 L/L/h . Short fuel rich and long fuel lean periods are created by the directly injecting hydrocarbons (HC's) at a high frequency downstream of the engine in the exhaust system upstream of a complex NSR catalyst ($Pt/Rh/Ba/K/Ce/Al_2O_3$) [12, 13]. Investigation on the role of each catalyst component is essential for understanding how the system works and its further improvement.

Ceria was a critical catalyst ingredient in the Di-Air system due to its redox properties and it can act as an oxygen buffer [14]. The lattice oxygen released during ceria reduction can react with hydrocarbon, CO, and H_2 under rich (fuel injection) conditions [15, 16]. HC's injection is essential to create a deep reduction of ceria and deposition of carbon on ceria [15]. Oxygen vacancies (reduced ceria) were found able to selectively convert NO into (di)nitrogen (N_2) [14], even in the presence of an excess of oxygen [17] and CO_2 (Chapter 7). The deposited carbon was oxidised by oxygen species

from the lattice oxygen of ceria under oxidative conditions, recreating new oxygen anion vacancies, thereby increasing substantially the NO reduction capacity.

The temperature required for the reduction of the applied unpromoted ceria composite by hydrocarbon (HCs), however, needed to exceed 500 °C for C_3H_6 and 540 °C for C_3H_8 used as reductant. The reactivity of oxygen in the ceria lattice is too low to activate the C_3H_6 and C_3H_8 at temperatures below 500 °C [15]. Considering automotive conditions, especially during the cold start, the reduction of ceria may be difficult. For practical application of ceria-based catalysts it may be beneficial to add promoters, *e.g.,* noble metals that could assist ceria reduction at lower temperatures. After hydrocarbon treatment of ceria at 300 °C Yao and Yao [16] found no oxygen storage capacity (OSC) and a limited capacity at 400 °C, meaning that HCs cannot reduce surface oxygen of ceria at temperatures below 300-350 °C. After addition of Pt, Pd, or Rh to ceria, however, a substantial OSC even at 300 °C was evidenced. Much research has been performed on $^{18}O/^{16}O$ isotope exchange, a common method used to study the adsorption/desorption properties of oxygen and the participation of lattice oxygen from ceria in oxidation reactions, either by using $^{18}O_2$ or $C^{18}O_2$ over the ceria and noble metal loaded ceria [18, 19]. The presence of noble metals was found to accelerate the exchange rate of oxygen from either $^{18}O_2$ or $C^{18}O_2$ in the lower temperature range as compared to bare ceria. Although improved oxygen exchange phenomena are no direct evidence for affecting reduction, it is an indication that the presence of noble metals may affect the reactivity of oxygen from the ceria lattice with HCs or carbonaceous deposits in the absence of gas-phase O_2.

The aim of this study is to investigate the role of noble metals on ceria for its reduction by HCs and performance in subsequent NO reduction. For this purpose, C_3H_6 and C_3H_8 were used as a model of fuel. Temporal Analysis of Products (TAP) was mainly used for the quantification of the degree of reduction of the ceria support and the NO reduction mechanism. Additionally, operando Raman spectroscopy performed in a fixed bed reactor was applied to support the TAP results.

A commercial Zr- and La-doped ceria is used as a model ceria system mainly for its high hydrothermal stability and enhanced oxygen lattice diffusion [14,

20, 21].

5.2. Experimental

5.2.1. Materials preparation

Pt/ceria and Rh/ceria, aimed at 0.5wt.% loading were prepared via an incipient wetness impregnation method on Zr-La doped ceria (a gift of Engelhard, now BASF, further denoted as ceria). The bulk atomic ratio of Ce, La and Zr is 0.64 : 0.15 : 0.21. Tetra-ammine platinum (II) nitrate and rhodium(III) nitrate hydrate purchased from Sigma-Aldrich, were used as precursors. Subsequently, the samples (thin layer in a crucible) were dried at 110 °C overnight and calcined at 550 °C for 5 h in a static air furnace.

5.2.2. Characterisation

5.2.2.1. N_2 adsorption

N_2 adsorption at 77 K (Tristar II 3020) Micromeritics was used to determine the textural properties like BET area and pore volume. The catalyst samples were pretreated by degassing at 473 K for 16 h in vacuum (0.05 mbar).

5.2.2.2. Inductively Coupled Plasma Optical Emission Spectroscopy (ICP-OES)

Approximately 50 mg of samples were digested in 4.5 mL 30% HCl + 1.5 mL 65% HNO_3 using microwave irradiation for 120 min at max. power (900 W). After the destruction, the samples were diluted to 50 mL with Millipore-Q (purified demi) water. The samples were analysed with ICP-OES (PerkinElmer Optima 5300).

5.2.2.3. X-Ray photoelectron spectroscopy (XPS)

XPS measurements were recorded on a K-alpha Thermo Fisher Scientific spectrometer using mono-chromated Al *Ka* X-ray source. A flood gun was applied for charge compensation. Lorentz function was used to analyse the peak intensities. Binding energies were calibrated with C(*1s*) at 285 eV as a reference.

5.2.2.4. X-ray diffraction (XRD)

The Powder X-Ray diffraction (XRD) was recorded by a Bruker-AXS D5005 with a Co *Ka* source. The data was collected three times by varying the 2θ angle from 5° to 90° with a step size of 0.02.

5.2.2.5. Transmission electron microscope (TEM)

Transmission Electron Microscopy (TEM) images were recorded on a JEM-2100P electron microscope operating at 200 kV. Prior to transfer the samples into the TEM analysis chamber, the samples were dispersed in ethanol and deposited onto a carbon-coated copper grid, shortly dried in air and, subsequently, inserted into the vacuum system of the microscope.

5.2.2.6. Raman microscopy

Raman spectra of samples were collected by a Renishaw in Via Reflex confocal Spectrometer. The excitation wavelength was 325 nm. The power of each laser line was kept at about 2.5 mW to prevent local heating. The resolution of the spectrometer was 1 cm^{-1}.

5.2.2.7. Temperature programmed reaction (TPR)

TPR (H_2) of all the samples were carried out in a fixed bed reactor system connected to a thermal conductivity detector (TCD) to monitor the consumption of hydrogen by the catalyst. Catalyst samples (200 mg) were packed between SiC layers (300 - 425 µm). The sample was then reduced in a 10% H_2/Ar flow of 30 mL_{STP}/min by increasing temperature from room temperature to 1000 °C with a heating rate of 5 °C/min. TCD was calibrated by using CuO as a reference. A permapure tubular drier was used to remove the water produced during the reduction step upstream of the TCD detector.

5.2.3. TAP pulse experiments between 450 °C to 500 °C

The pulse experiments were performed in an in-house developed and constructed TAP (Temporal Analysis of Products) reactor. Series of small gas pulses, typically in the order of $1 \cdot 10^{15}$ molecules, were introduced in a small volume upstream of the catalyst packed bed reactor. The produced pressure

gradient over the catalyst packed bed thereby causes the molecules to be transported through the packed bed to the ultra-low vacuum at the opposite side of the packed bed. Depending on the actual amount of molecules pulsed, the transport will be in the pure Knudsen diffusion regime. In other words, the molecules interact only with the 'walls' (catalyst surface and reactor walls) of the system and not with each other. Upon interaction with the catalyst, molecules can be converted into different products. The evolution of the reactant and product molecules is tracked (one mass *m/e* unit per pulse) with a high time resolution of 10 kHz using a quadrupole mass spectrometer. A careful calibration of the MS ensured a quantitative analysis, and overall mass balances could be closed within 5-15% accuracy. Details about TAP can be found elsewhere [14] and in Chapter 2.

5.2.3.1. Multi-pulse TAP experiment

10 mg Rh/ceria and Pt/ceria were used in the TAP reactor at 450 °C. In all experiments a starting pulse size of approximately $2 \cdot 10^{15}$ molecules was used (including reactants and internal standard gas), the pulse size gradually decreases during an experiment as the reactant was pulsed from a closed and calibrated volume of the pulse-valve line. Prior to a reduction, the catalyst was firstly (re-)oxidised at the same temperature at which the reduction was performed, using pulses of 80 vol.% O_2 in Ar until a stable O_2/Ar signal ratio downstream of the reactor was obtained. The reduction was carried out by injecting reductant pulses of either 80 vol.% C_3H_6 in Ne, 80 vol.% C_3H_8 in Ne, 80 vol.% CO in Ar, or 66.7 vol.% H_2 in Ar until a stable reactant and product to an internal standard signal ratio was obtained, indicating that the catalyst was 'equilibrated'. ^{15}NO and $^{18}O_2$ pulse experiments were performed using 80 vol.% ^{15}NO in Kr, and 5 vol.% $^{18}O_2$ in He, respectively.

The consumption of the oxygen species from the catalyst and the carbon species deposited during C_3H_8, and C_3H_6 multi-pulse experiments were calculated using the Equation 5.1and 5.2:

$$n_{O,consumed} = n_{H_2O,obs} + n_{CO,obs} + 2n_{CO_2,obs} \tag{5.1}$$

$$n_{C,deposited} = 3n_{C_3H_6,in(C_3H_8,in)} - 3n_{C_3H_6,obs(C_3H_8,obs)} - n_{CO,obs} - n_{CO_2,obs} \quad (5.2)$$

Where n is the number of molecules or atoms of the specified species observed (obs), consumed or introduced (in).

Similarly, the amount of oxygen accumulation and carbon consumption during ^{15}NO pulses experiments were calculated using the Equation 5.3, 5.5 and 5.4:

$$n_{O,accumulated} = n_{(NO,in)} - n_{CO,obs} - 2n_{CO_2,obs} - n_{N_2O,obs} - 2n_{NO_2,obs} \quad (5.3)$$

$$n_{c,consumed} = -n_{CO,obs} - n_{CO_2,obs} \quad (5.4)$$

$$n_{N,consumed} = n_{(NO,in)} - n_{NO,obs} - 2n_{N_2,obs} - 2n_{N_2O,obs} - n_{NO_2,obs} \quad (5.5)$$

5.2.3.2. Pump-probe TAP experiments

Pump-probe TAP experiments were performed using two pulse valves to consecutively inject ^{15}NO and ^{14}NO, respectively. Rh/ceria and ceria were used at 450 and 500 °C, respectively. Before the pump-probe experiment, multi-pulse experiments were conducted to reduce the catalysts by H_2, then ^{15}NO/Kr and ^{14}NO/Ar mixtures were subsequently injected in an alternating sequence, and the m/e intensity of $^{15}N_2$, $^{15}N^{14}N$,$^{14}N_2$,^{14}NO, and ^{15}NO were measured during each pulse for a time interval of 5 s. The injection time was t = 0 for ^{15}NO/Kr and t = 5 s for ^{14}NO/Ar.

5.2.3.3. Single pulse TAP experiments

Single pulse TAP experiments were performed to investigate the interaction of N_2 with the catalyst bed using one single pulse of N_2 over the catalyst. The study of N_2 interaction with oxidised catalyst was conducted by pulsing N_2 over a pre-oxidised catalyst at 450 °C. For the study over a reduced catalyst, 10000 pulses of H_2 were used to reduce the catalysts prior to the N_2 single pulse.

5.2.4. *Operando* Raman spectroscopy

The Raman spectroscopy measurements were performed under reaction conditions by using an AvaRaman-PRB-FC Raman probe. The catalyst sample (200 mg) was placed a 6 mm inner diameter quartz reactor tube and downstream equipped with a mass spectrometer (MS, Hiden Analytical, HPR-20 QIC) and infrared (IR) spectroscopy (Perkin–Elmer, Spectrum One), both for gas analysis. For the IR analysis a gas cell with KBr windows with a path length of ~5 cm was used. The spectra were recorded in a continuous mode using the Perkin-Elmer 'Time-Base' software between 4000 - 700 cm^{-1} wavenumbers with a spectral resolution of 8 cm^{-1} and an acquisition of 8 scans per spectrum, resulting in a time interval of 23 s between each displayed spectrum. Raman data were collected using a Kaiser Optical Systems RXN spectrometer with a diode laser operating at 532 nm and output power of 10 mW. AvaRaman-PRB-FC Raman probe was used to focus the laser beam to a spot and to collect the scattered radiation behaviour. A CCD camera was used to record the data using the Thermo Galactic Grams AI v. 7.0 software. Spectra were acquired using 2 scans at a resolution of 0.3 cm^{-1} in the range between 100 (detector cutoff) and 4350 cm^{-1}.

A feed composition of 0.2% NO (He balance) was used with a GHSV of 67.000 L/L/h. Prior to feeding NO, the catalyst was pre-treated by 1.25% C_3H_6 in He for 2 h and flushed with He (200 mL/min) for 30 min afterwards, both at 500 °C.

5.3. Result

5.3.1. Characterisation

5.3.1.1. Structure and chemical composition

Characterisation details of the ceria support were reported elsewhere [14, 22]. In brief, the typical fluorite structure of ceria was confirmed by Raman and XRD. The BET area was 65 ± 2 m^2/g. The crystal size of ceria determined by the Scherrer's equation and TEM measurements were on average 5.0 ± 0.6 nm.

The BET surface areas of Pt/ceria and Rh/ceria were similar to that of the support (65±2 m^2/g). Measured by the ICP-OES, the mass loadings of Pt

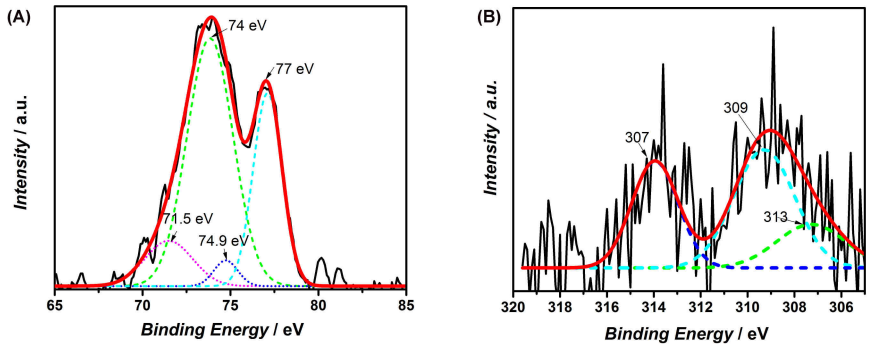

Figure 5.1: XPS of Pt (*4f*) and Rh (*3d*) core level region of (A) Pt/ceria and (B) Rh/ceria, respectively.

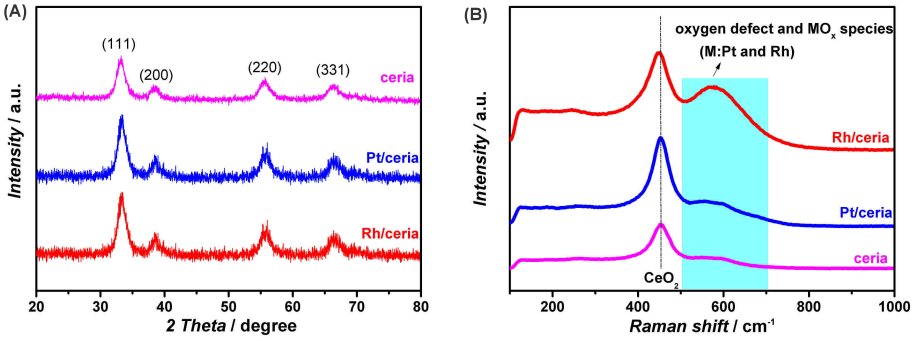

Figure 5.2: XRD pattern (A) and Raman spectra(B) of oxidised Pt/ceria, Rh/ceria, and ceria.

and Rh were determined to be 0.5 wt%. Figure 1A shows the XPS spectrum of Pt (*4f*). $4f_{7/2,5/2}$ peaks of PtO were observed at 71.5 and 74.9 eV with the spin-orbit splitting around 3.5 eV. $4f_{7/2,5/2}$ peaks of PtO_2 were found at 74 and 77.2 eV (Figure 5.1A). These binding energies for Pt were in good accordance with the literature values [23]. Figure 5.1B shows the XPS spectrum of Rh/ceria, corresponding to the electronic transitions Rh $3d_{3/2}$ and Rh $3d_{5/2}$, with binding energies at 313 eV and 306-310 eV [24]. 307 eV and 309 eV were assigned to be the presence of Rh^0 and Rh^{3+} of Rh $3d_{5/2}$, respectively [24, 25].

Figure 5.2A shows the XRD patterns of Pt/ceria, Rh/ceria, and the ceria support. The patterns of noble metal loaded samples show the fluorite cubic structure of CeO_2. Diffraction lines due to Rh and Pt metals or to any plat-

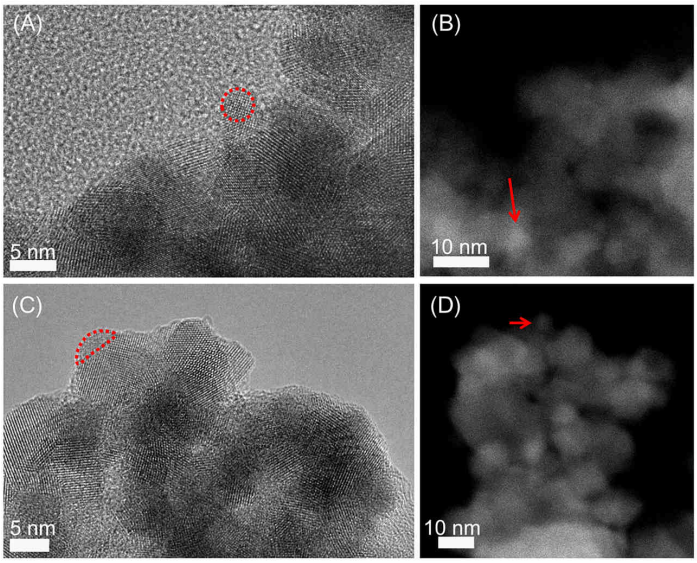

Figure 5.3: HR-TEM and STEM micrographs of oxidised Pt/CeO_2 (A and B) and Rh/CeO_2 (C and D), respectively.

inum oxides or rhodium oxides are not observed (below the detection of the XRD apparatus due to the low noble metal loading and the high noble metal dispersion of the ceria). The presence of a peak at around 460 cm^{-1} in the Raman spectra (Figure 5.2B) was due to the characteristic fluorite peak of ceria assigned to the F_{2g} mode. This peak presented a shoulder between 500 and 700 cm^{-1} including contributions of vacant sites of the ceria support and MO_x (PtO_x or RhO_x) species [24, 26, 27].

Figure 5.3 shows the TEM micrographs of Pt/ceria and Rh/ceria (TEM (Figure 5.3A and C) micrographs and STEM (Figure 5.3B and D) micrographs). Pt and Rh nanoparticles were circled in red in Figure 5.3A and C, respectively. The red arrows point the presence of Pt and Rh on ceria support in Figure 5.3B and D, respectively. However, the molar mass of noble metal and ceria, however, are very close and, therefore, their contrasts were low in the STEM micrograph (Figure 5.3B and D). In combination with the low mass loadings of Pt and Rh (0.5 wt.%), the noble metal particle size distributions could not be adequately obtained.

The reduction properties of Pt/ceria, Rh/ceria, and ceria were conducted

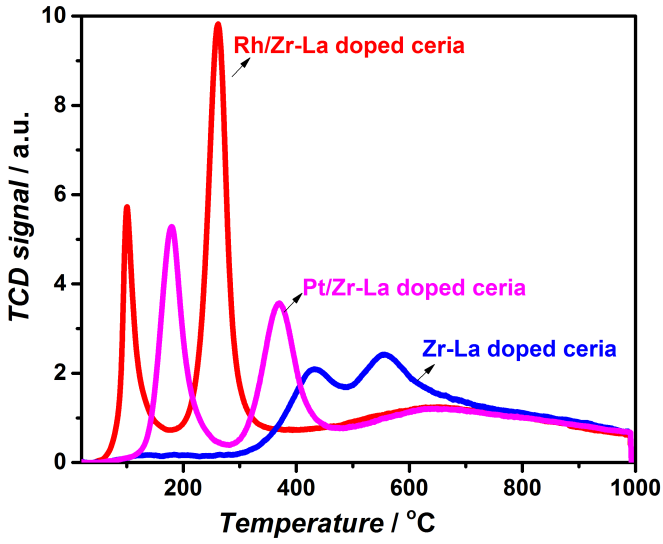

Figure 5.4: H_2-TPR profiles of ceria, Pt/ceria, and Rh/ceria.

by TPR(H_2), and the results are presented in Figure 5.4. Ceria shows two peaks centred at 430 and 550 °C. It is generally accepted that the low temperature (430 °C) process is attributed to the surface reduction and the high temperature (550 °C) accounted for the bulk reduction [16]. As compared to the ceria support, the surface and bulk reduction of noble metal loaded ceria significantly shifts to a lower temperature, the maxium reduction peak is given in Table 5.1. As shown in Table 5.1, the total H_2 consumption for ceria support, Pt/ceria, and Rh/ceria is 0.31, 0.36, and 0.43 mol H_2/mol Ce. However, hydrogen sonsumption cannot be related to the ceria reduction, due to that H_2 is incorporated into bulk CeO_2 above 200 °C [28].

5.3.2. Multi-pulses TAP experiments

5.3.2.1. Reduction of noble metal loaded ceria by reductants

The reduction of noble metal loaded ceria catalysts was investigated by using CO, H_2, C_3H_6, and C_3H_8 as reductant in TAP. As an example for a noble metal, Figure 5.5 shows the result of C_3H_6 pulses over the pre-oxidised Pt/ceria at 450 °C. Two types of C_3H_6 reactions were observed: complete C_3H_6 oxidation and C_3H_6 oxidative cracking/dehydrogenation, as described

Table 5.1: Summary of H_2-TPR (H_2 consumption unit: mol H_2/mol Ce).

	First peak		Second peak		Total H_2 consumption
	T/°C	H_2 consumption	T/°C	H_2 consumption	
Ceria	430	-	550	-	0.31
Pt/ceria	215	0.08	360	0.28	0.36
Rh/ceria	100	0.07	265	0.36	0.43

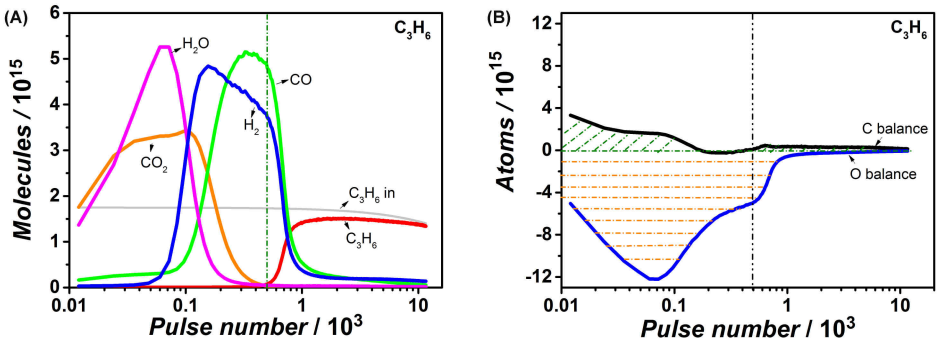

Figure 5.5: C_3H_6 pulses over a pre-oxidised 0.5 wt.%Pt/ceria at 450 °C, (A) product and reactant evolution, and (B) carbon and oxygen balance *versus* pulse number.

in the Equation 5.6 and 5.7, respectively. C_3H_6 experienced a full conversion till pulse number 500.

$$C_3H_6 \overset{\text{ceria}}{\rightleftarrows} CO_2 + H_2O \tag{5.6}$$

$$C_3H_6 \overset{\text{ceria}}{\rightleftarrows} CO + H_2 + C_{deposited} \tag{5.7}$$

During the complete C_3H_6 oxidation period (pulse number 0-50), the main oxidation products were CO_2 and H_2O. Moreover, a small amount of CO was observed. The H_2 formation considerably increased after pulse number 50, accompanied by a significant decline of the H_2O formation. CO formation increased after pulse number 90, where CO_2 formation significantly dropped with pulse number. During the pulse number from 50-1000 oxidative hydrocarbon cracking was the main reaction with the formation of CO and H_2. The oxygen and carbon balances at each C_3H_6 pulse are displayed in Figure 5.5B. The formation of CO_2, H_2O, and CO caused partial reduction of ceria from Ce^{4+} to Ce^{3+} (Table 5.2). Carbon deposition was observed during both the complete oxidation and cracking reactions. The pulses of C_3H_8 over Pt/ceria showed a similar product evolution as that for the C_3H_6 pulses, although the C_3H_8 showed full conversion till pulse number 150. Rh/ceria showed the same trends as Pt/ceria during the both C_3H_6 and C_3H_8 pulses at 450 °C, but carbon deposits for the Rh/ceria were significantly higher than that on Pt/ceria upon the C_3H_6 pulse exposure (Table 5.2).

Additionally, the pulse of CO over noble metal loaded ceria led to the CO_2 formation. Hardly any carbon was left over during the CO pulses. Moreover, the pulses of H_2 over the noble metal loaded ceria results in the formation of H_2O. The total amount of oxygen extraction during CO and H_2 exposures can be seen in Table 5.2.

5.3.2.2. NO reduction

The reduction of NO over H_2 reduced noble metals loaded ceria support was investigated in TAP by using ^{15}NO. Figure 5.6 shows the products and reactant evolution during the ^{15}NO pulses over H_2 reduced Pt/ceria and Rh/ceria at 450 °C. For the Pt/ceria (Figure 5.6A), the full ^{15}NO conversion

Table 5.2: Summary of oxygen extraction (O) and carbon deposition (C) using different reductants (unit: 10^{17} atoms / mg_{cat}) at 450 °C.

	Pt/ceria		Rh/ceria	
	O	C	O	C
H_2	2.1	-	2.2	-
CO	2.5	-	2.5	-
C_3H_6	6.3	2.8	8.2	8.0
C_3H_8	5.8	1.3	6.0	2.9

was observed with $^{15}N_2$ as the exclusive product from pulse number 0 to 700. Moreover, around 70% of oxygen vacancies were refilled by ^{15}NO before the breakthrough of ^{15}NO. There was no N_2O and NO_2 formation in that time frame. Similar to Pt/ceria, Rh showed full ^{15}NO conversion till pulse number 900, where 80% of oxygen vacancies were refilled by ^{15}NO (Figure 5.6B). $^{15}N_2$ was the exclusive product and no N_2O and NO_2 formation were observed. It is noted that some nitrogen temporarily accumulated on the samples.

The NO reduction into nitrogen over the hydrocarbons reduced noble metals loaded ceria support was investigated in TAP by using ^{15}NO, to distinguish its products from CO and N_2 (*m/e* = 28) and CO_2 from N_2O (*m/e* = 44). Figure 5.7 shows the products and reactant evolution and the carbon and oxygen balance during the ^{15}NO pulses over the C_3H_6 reduced Pt/ceria at 450 °C. As illustrated in Figure 5.7, stage I and II were used to distinguish the full ^{15}NO conversion time interval and the time intervals where NO started to breakthrough. Stage I was subdivided into stages Ia and Ib for the CO_2 formation during stage I. During stage Ia (from pulse number 0 to 1000, Figure 5.7A), full ^{15}NO conversion was observed with $^{15}N_2$ as the main product (negligible amount of CO formed). The evolution of CO_2 was observed from pulse number 1000 (stage Ib, Figure 5.7A). ^{15}NO showed

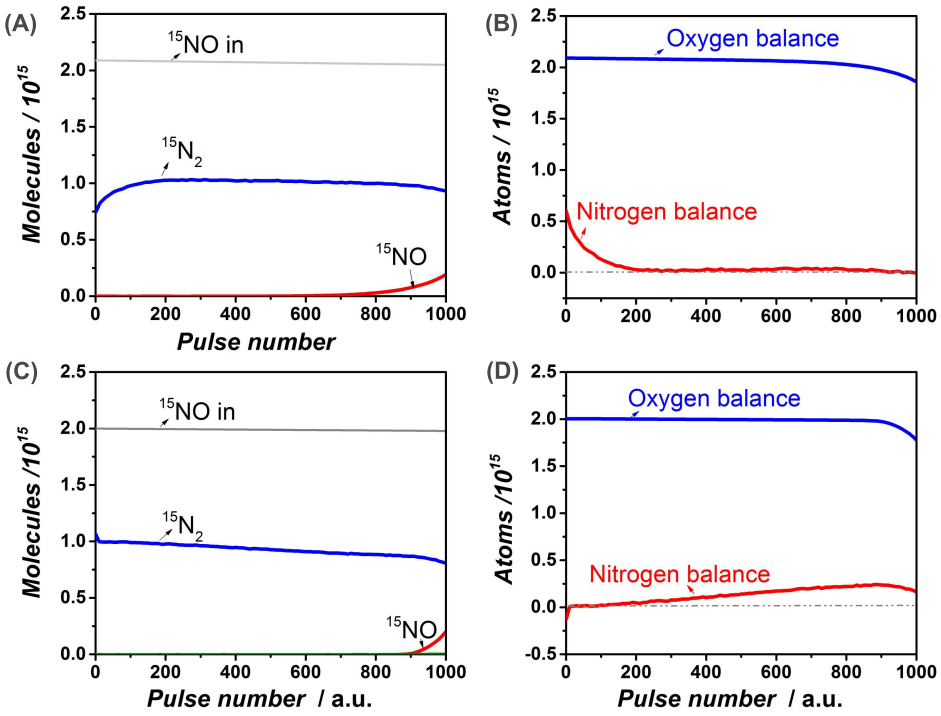

Figure 5.6: ^{15}NO pulse experiment over an H_2 reduced Pt/ceria (A and B) and Rh/ceria (C and D) at 450 °C, respectively.

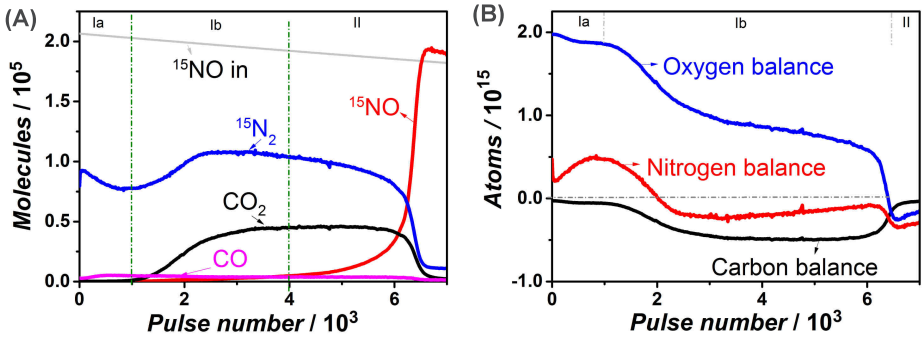

Figure 5.7: ^{15}NO pulse experiment over C_3H_6 reduced Pt/ceria at 450 °C, (A) products and reactant evolution and (B) carbon and oxygen balance versus pulse number.

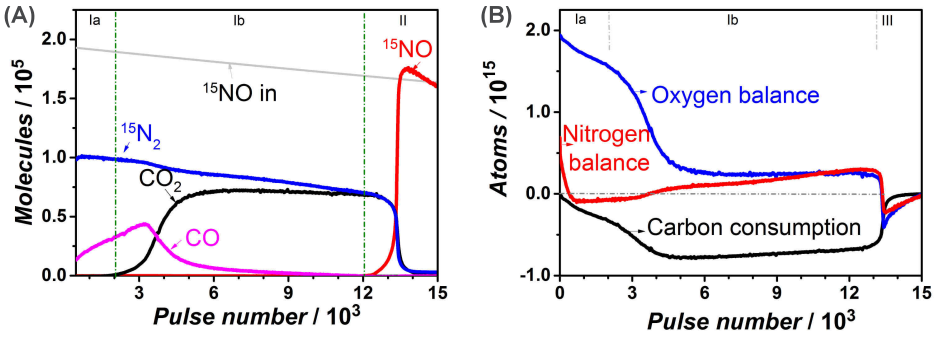

Figure 5.8: ^{15}NO pulse experiment over C_3H_6 reduced Rh/ceria at 450 °C, (A) products and reactant evolution, and (B) carbon and oxygen balance versus pulse number.

5

full conversion until pulse number 4000 (stage I, Figure 5.7A), where $^{15}N_2$ and CO_2 were the only products. From pulse number 4000 onwards (stage II, Figure 5.7A), a progressive decline to zero for the ^{15}NO conversion was observed. The $^{15}N_2$ and CO_2 production followed the same trend as that of the NO conversion. Neither $^{15}N_2O$ nor $^{15}NO_2$ were formed and no traces of cyanide or cyanate containing species were detected. The oxygen, carbon balances and nitrogen balance were plotted as shown in Figure 5.7B. During stage Ia (pulse number 0 to 1000, Figure 5.7B), oxygen incorporation into catalyst was observed with a negligible amount of carbon consumption. The majority of the carbon conversion was found from pulse number 1000 onwards (stage Ib), accompanied by an oxygen accumulation decline. Both oxygen accumulation and carbon consumption vanished after pulse number 6000. During stage I NO was fully converted, 80% of oxygen vacancies were refilled, and 50% of the deposited carbon was oxidised. 17% of ^{15}N was accumulated during the first 2000 ^{15}NO pulses, followed by the accumulated ^{15}N release during pulse number between 2000 and 6000. The N-balance closed to 90%.

The result of ^{15}NO pulses over a C_3H_6 reduced Rh/ceria (Figure 5.8) showed a similar trend as that over Pt/ceria. ^{15}NO started to breakthrough from pulse number 12000 onwards, which was 3 times larger than that over Pt/ceria. However, a small amount of CO evolution was observed during stage Ia of Rh/ceria NO conversion. During stage I (a full NO conversion period), 80% of oxygen vacancies were refilled and 90% of carbon deposits

were oxidised. Neither $^{15}N_2O$ nor $^{15}NO_2$ were formed and no traces of cyanide or cyanate containing species were detected during stage I and II. Hardly any ^{15}N accumulation before pulse number 5000. After that ^{15}N started to accumulate up to an N/O ratio of 1. Still a persistent $^{15}N_2$ formation was observed after ^{15}NO started to breakthrough until the carbon deposit had been consumed. The overall ^{15}N balance was closed to 90%.

5.3.2.3. $^{18}O_2$ pulses over C_3H_8 reduced Rh/ceria

Figure 5.9 shows the product evolution for the $^{18}O_2$ multi-pulse experiment over C_3H_8 reduced Rh/ceria at 450 °C. All introduced $^{18}O_2$ was completely converted until a steep oxygen breakthrough profile was observed from pulse number 30000 onwards. $C^{16}O$ evolved as the main product till pulse number 10000, where $C^{16}O_2$ started to evolve and gradually became the main product. After 13000 pulses $C^{18}O^{16}O$ was observed and a small amount of $C^{18}O_2$ was detected after pulse number 15000. After 28000 pulses $C^{16}O$, $C^{16}O_2$, $C^{18}O^{16}O$, $C^{18}O$, and $C^{18}O_2$ decreased to zero, where $^{18}O_2$, $^{16}O_2$, and $^{18}O^{16}O$ started to break through in a kind of exchange equilibrium. The observed $C^{18}O$ (*m/e* = 30) during pulse number 13000 to end of the pulse sequence was due to the fragmentation from $C^{18}O_2$ and $C^{18}O^{16}O$. A small amount of $C^{18}O$ was also observed before pulse number 13000, where the major product was $C^{16}O$. $^{16}O_2$ was the main product after the oxygen breakthrough.

5.3.3. Pump probe TAP experiments

In order to investigate the rate of N_2 formation from NO over H_2 reduced ceria and Rh/ceria, pump-probe TAP experiments were performed using alternating ^{15}NO and ^{14}NO pulses at 450 °C. The pulse size of ^{15}NO and ^{14}NO were both $1.5 \cdot 10^{15}$ molecules/pulse. Figure 5.10A and B shows the flux of $^{14}N_2$, $^{14}N^{15}N$, and $^{15}N_2$ at the exist of the reactor over a H_2 pre-reduced Rh/ceria. The pulse of ^{15}NO at t = 0 s in the first injection cycle led to the exclusive $^{15}N_2$ formation with a peak position at t = 0.056 s and peak height at $5.5 \cdot 10^{15}$ molecules/s. The total number of $^{15}N_2$ molecules formed during the time interval of 5 s was calculated to be $7 \cdot 10^{14}$ molecules. The pulse of ^{14}NO at t = 5 s in the 1st injection cycle resulted in the formation of a major product of $^{14}N_2$ with peak position at t = 5 + 0.056 s and $7 \cdot 10^{14}$ $^{14}N_2$

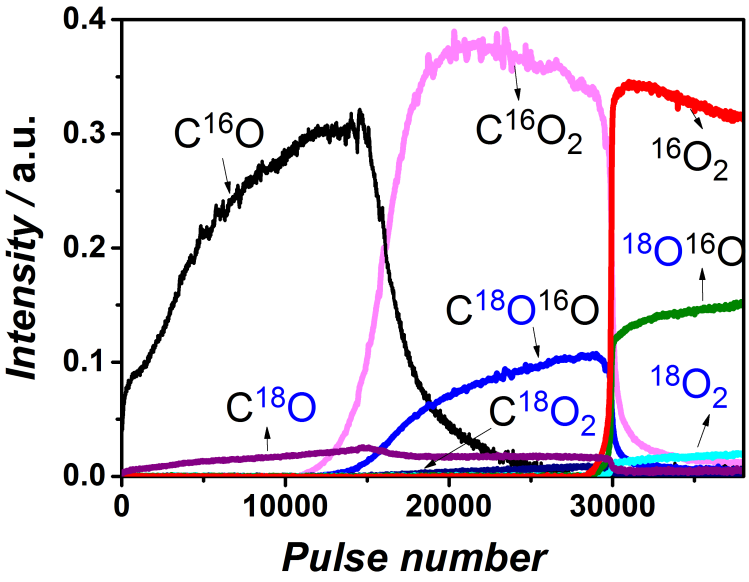

Figure 5.9: Product and reactant evolution versus pulse number during $^{18}O_2$ pulse experiment over C_3H_8 reduced Rh/ceria at 450 °C.

molecules formation during the time interval of 5 s. The peak height of $^{14}N_2$ was identical to the $^{15}N_2$ during the time period of 0-5 s. A small fraction of $^{14}N^{15}N$ molecules, around 2-3% of $^{14}N_2$, were observed from t = 5 to 10 s. After the first injection cycle, also a small fraction of $^{14}N^{15}N$ (2-3% of $^{15}N_2$) was observed during pulse of the ^{15}NO pulses, as indicated for the 70th injection cycle (Figure 5.10B).

Figure 5.10C and D shows the flux of $^{14}N_2$, $^{14}N^{15}N$, and $^{15}N_2$ during the ^{15}NO and ^{14}NO injections for the H_2 pre-reduced ceria at 500 °C. The pulse of ^{15}NO at t = 0 s during first injection cycle led to the exclusive $^{15}N_2$ formation. The total number of $^{15}N_2$ molecules formed during the time interval of 5 s was calculated to be $3.3 \cdot 10^{14}$ molecules. The maximum peak position of $^{15}N_2$ was at t = 0.063 s with peak height of $1.3 \cdot 10^{15}$ molecules/s. The pulse of ^{14}NO at t = 5 s during the 1st injection cycle led to the formation of both $^{14}N_2$ and $^{14}N^{15}N$. During the time from t = 5 to 10 s, the number of $^{14}N_2$ and $^{14}N^{15}N$ was calculated to be $3.7 \cdot 10^{14}$ and $2 \cdot 10^{14}$ molecules, respectively. $^{14}N^{15}N$ was also observed during the ^{15}NO pulses after the first injection cycle. Moreover, an increase in the intensity of $^{14}N_2$ and $^{14}N^{15}N$, and $^{15}N_2$ were observed during the 40th injection as compared to 1st in-

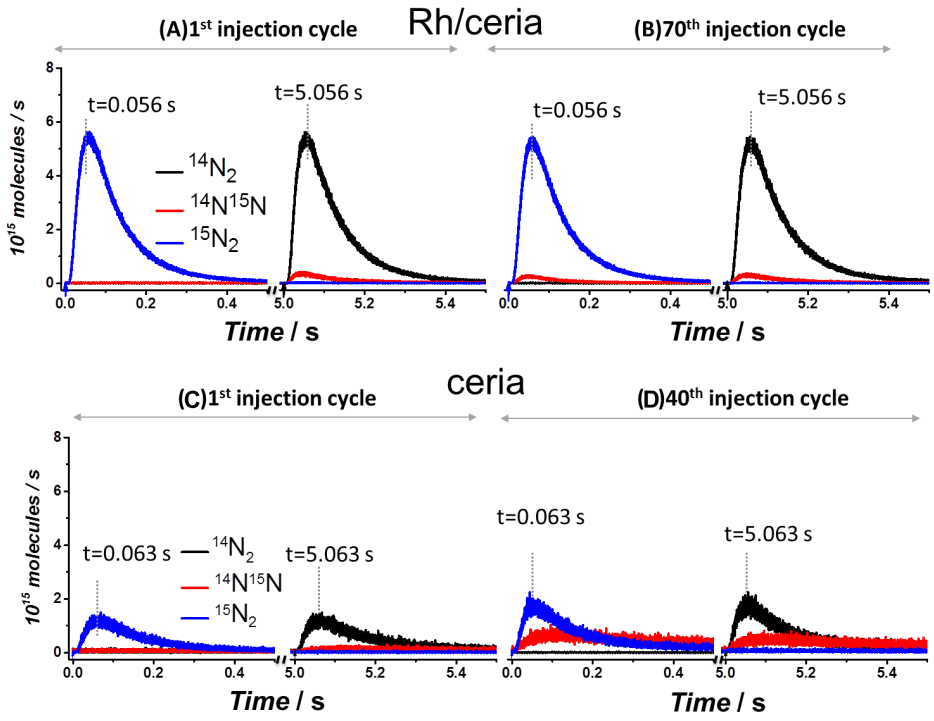

Figure 5.10: The flux of $^{14}N_2$, $^{14}N^{15}N$, and $^{15}N_2$ during the experiment of ^{15}NO and ^{14}NO alternate pulsing over the H_2 pre-reduced (A and B)Rh/ceria at 450 °C and (C and D) ceria at 500 °C, measured at the exist of the reactor. The blue arrow indicated the start of a pulse of ^{15}NO (t=0) and the black arrow for ^{14}NO (t=5 s). Pulse size: $1.5 \cdot 10^{15}$ molecules of ^{15}NO or ^{14}NO per pulse.

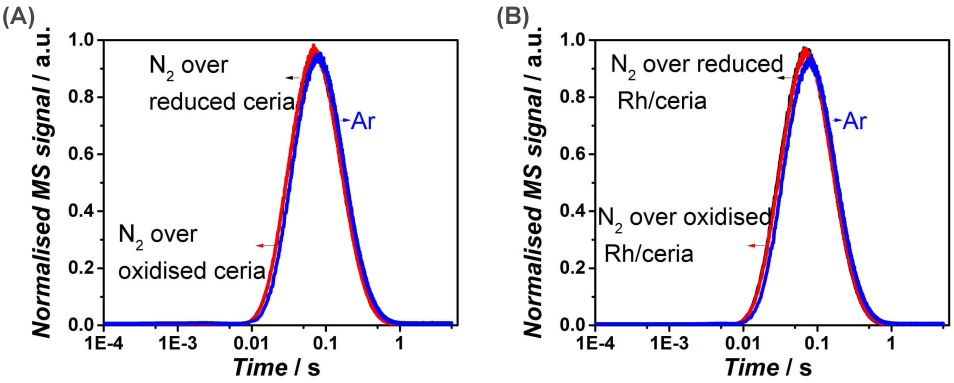

Figure 5.11: normalised N_2 and Ar MS signal during N_2 pulses over the ceria (A) and Rh/ceria (B).

jection cycle. During 40th injection cycle, $8.8 \cdot 10^{14}$ molecules of $^{15}N_2$ and $8 \cdot 10^{14}$ molecules of $^{14}N^{15}N$ were observed during ^{15}NO injection from t = 0 to t = 5 s, and $5.7 \cdot 10^{14}$ molecules of $^{14}N_2$ and $8 \cdot 10^{14}$ molecules of $^{14}N^{15}N$ were observed during ^{14}NO injection from t = 5 to 10 s.

5.3.4. N_2 pulses experiments over Rh/ceria and ceria

In order to explore the interaction of dinitrogen with ceria and Rh/ceria, $^{14}N_2$ pulses experiments were performed over different oxidation state of ceria and Rh/ceria. The Ar response was used as a standard reference response curve. Figure 5.11A shows the N_2 and Ar response shape over the ceria at 500 °C. The N_2 response showed peaks at t = 0.0672 s both over the oxidised and H_2 reduced ceria. Moreover, the Ar peak located at the time of t = 0.0803 s. Both Ar and H_2 showed the same response shape but with a shift of the peak position due to the difference in molar mass affecting the Knudsen diffusion coefficient [27]. Figure 5.11B shows the H_2 and Ar response shape over the Rh/ceria at 450 °C. The H_2 response showed a peak at t = 0.0674 s both over the oxidised and H_2 reduced ceria, while the Ar peak position was at t = 0.0805 s.

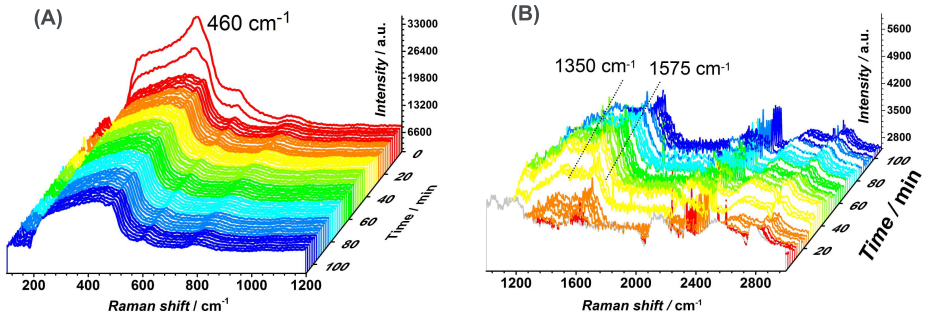

Figure 5.12: Raman spectra of the band at (A) 460 cm^{-1} and (B) 1575 and 1350 cm^{-1} during C_3H_6 exposure Rh/ceria at 500 °C.

5.3.5. *Operando* Raman study of NO reduction C_3H_6 oxidation and NO reduction over Rh/ceria

Figure 5.12 shows *operando* Raman spectra during 1.25% C_3H_6/He flow at 500 °C over Rh/ceria. The broad band from 100 to 500 cm^{-1} was attributed to the quartz tube. The sharp intensity centered at 460 cm^{-1} was attributed to the symmetric stretch mode of the Ce-O_8 crystal unit, which was characteristic for the fluorite ceria structure [29]. Its intensity started to drop after the first minute of C_3H_6 exposure and disappeared two minutes after C_3H_6 exposure. Subsequently, two bands at 1575 and 1350 cm^{-1} started to appear and grew during the prolonged C_3H_6 exposure. The bands at 1575 and 1350 cm^{-1} were assigned to the G band and D band of carbon [30]. The G band was usually assigned to zone center phonons of E_{2g} symmetry of the perfect graphite structure and the D peak was assigned to a breathing mode of A_{1g} symmetry, which is forbidden in a perfect graphite structure and only became active in the presence of structural defects and disorders.

Figure 5.13 shows operando Raman spectra for the NO reduction over C_3H_6 reduced Rh/ceria at 500 °C. As shown in the Figure 5.13A, the sharp feacture centered at 460 cm^{-1} was initially hardly visible and its intensity slightly increased during the first 20 min upon NO exposure. Moreover, it increased significantly after 60 min on NO stream. Subsequently, the intensities at 1575 and 1350 cm^{-1} strongly disappeared only after 90 min of NO exposure.

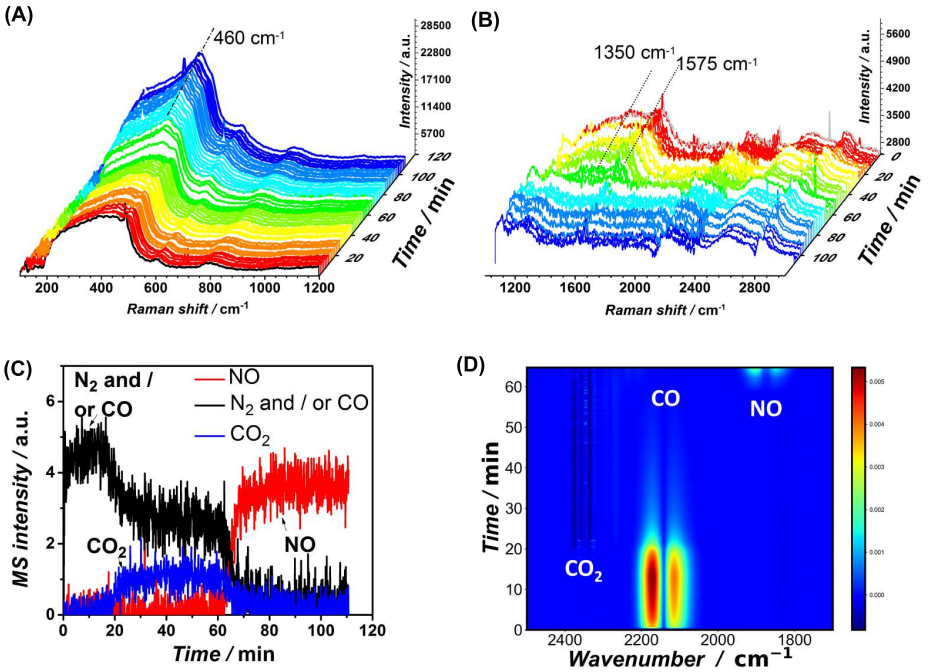

Figure 5.13: Raman spectra of the band at (A) 460 cm^{-1} and (B) 1575 and 1350 cm^{-1}, (C) MS and (D) FT-IR of NO exposure over a C_3H_6 reduced Rh/ceria at 500 °C.

During the *operando* Raman experiment, the gas evolution downstream the reactor was monitored with an MS and FT-IR spectrometer (Figure 5.13C and D, respectively). Full NO conversion was observed till 60 min. Only *m/e* = 28 was monitored, attributed from both N_2 and CO. The FT-IR data showed that CO was only formed in the initial stage of NO exposure, declining after 20 min. After 20 min, *m/e* = 44 assigned to CO_2 started to form. N_2O (detection limit < 1 ppm) was not observed in the FT-IR detector (Figure 5.13D). Therefore, the *m/e* = 44 was contributed to CO_2. Since the CO almost vanished around 30 min, the observed *m/e* = 28 response from 20 to 60 min was mainly attributed to N_2.

5.4. Discussion

5.4.1. Reduction of noble metal loaded ceria

Ceria is an important catalyst ingredient in the Di-Air system, since it is capable of fuel (HCs) oxidation and NO reduction. The oxygen from the ceria lattice can react with hydrocarbon, CO, and H_2, thus creating oxygen vacancies and reducing Ce^{4+} to Ce^{3+}. Oxygen vacancies in reduced ceria are the catalytic sites for selectively converting NO into (di)nitrogen (N_2), even in the presence of an excess O_2 and CO_2 (Chapter 7)[15]. However, the reduction of ceria with C_3H_6 and C_3H_8 required a temperature above 500 °C and 540 °C, respectively. Lowering the temperatures of ceria reduction by fuel is essential for an industrial application of this Di-Air $DeNO_x$ system.

The TPR(H_2) (Figure 5.4 and Table 5.1) shows that the noble metal loading onto the ceria support lowered the reduction temperature of the ceria support as compared to the ceria support. This shift in reduction temperature may be associated with the H_2 splitting on the noble metal and the existence of strong metal-support interaction, increasing the reactivity of lattice oxygen [31]. The high intensity in the range of 500 and 700 cm^{-1} on Rh/ceria from Raman spectroscopy (Figure 5.2B) indicated a stronger interaction between noble metal and ceria.

As shown in Figure 5.5, C_3H_6 and C_3H_8 experienced full conversion over Pt/ceria for a pulse number of 100 and 50, respectively. A complete oxidation to CO_2 and H_2O was observed during both C_3H_6 and C_3H_8 pulses, followed by a cracking reaction to CO, H_2, and carbon deposition. The total number of

oxygen extraction from Pt/ceria by C_3H_6 and C_3H_8 was around $6.3 \cdot 10^{17}$ and $5.8 \cdot 10^{17}$ oxygen atoms/mgcat (Table 2), respectively. Additionally, $2.8 \cdot 10^{17}$ and $1.3 \cdot 10^{17}$ carbon atoms/mgcat were deposited after using C_3H_6 and C_3H_8 as reductant, respectively. So C_3H_6 pulsing led to around 2 times higher carbon deposition than C_3H_8 pulsing. Apparently, the reduction by C_3H_6 or C_3H_8 of an oxidised noble metal loaded ceria followed a similar process, but resulted in different carbon deposits. Dehydrogenation and cracking of C_3H_6 was easier than that of C_3H_8 due to the strong electron-rich π-orbital interactions on Lewis acid sites [20], resulting in more carbonaceous deposit.

Pulsing C_3H_6 and C_3H_8 over Rh/ceria showed similar trends over Pt/ceria, which experienced both complete oxidation and cracking reaction. The total number of oxygen extraction from Rh/ceria by C_3H_6 and C_3H_8 were similar to that of Pt/ceria. However, the amounts of deposited carbon over Rh/ceria was around 3 times larger than on Pt/ceria when using C_3H_6 as a reductant. Furthermore, the operando Raman experiment of passing 1.25% C_3H_6/He gas stream over Rh/ceria at 500 °C (Figure 5.13) showed that the reduction of the ceria support occurs firstly, followed by the subsequent deposition of carbon.

The ceria support was not reactive for C_3H_8 and only slightly active for C_3H_6 at 450 °C. The addition of noble metals to the ceria support significantly enhanced the reactivities to C_3H_6 and C_3H_8, *i.e.,* the degree of ceria support reduction and the amounts of carbon deposition (Table 5.2). This agrees with the finding that noble metals were able to promote the oxygen mobility, surface migration, and reactivity, especially at the interface of noble metals and support [18].

5.4.2. Study of NO reduction

5.4.2.1. NO reduction routine and its selectivity to N_2

NO_2 and N_2O are common side products in the NO reduction technologies especially when using noble metal as an active ingredient in the catalyst composition [32–35]. Therefore, the study on NO reaction processes over noble metal/ceria is essential.

$^{15}N_2$ was the exclusive product of ^{15}NO reduction over the H_2 reduced

Pt/ceria and Rh/ceria (Figure 5.6). After around 70-80% of oxygen vacancies was refilled by oxygen from ^{15}NO, ^{15}NO started to break through, while no N_2O and NO_2 was formed. This was also observed for the ceria support [14]. The presence of Pt or Rh did not affect the NO reaction selectivity, *i.e.,* NO was selectively reduced into N_2. Moreover, when NO reduction was carried out over hydrocarbon reduced Pt/ceria and Rh/ceria then in the initial stage of ^{15}NO pulsing no oxygenate gas products were observed at 450◦C (Figure 5.7 for Pt/ceria). The absence of CO and CO_2 indicated that the carbonaceous residues, left on the surface after C_3H_6 pre-reduction, did not directly participate in the reduction of ^{15}NO into $^{15}N_2$. The formation $^{15}N_2$ indicated that ^{15}N-O was dissociated either on the reduced Pt or reduced ceria sites, with O filling the oxygen vacancies and ^{15}N species associated to form $^{15}N_2$. The absence of $^{15}N_2O$ indicated that ^{15}NO was selectively reduced into $^{15}N_2$ on the reduced Pt/ceria over the whole range of oxidation states of the catalyst. The ^{15}NO started to break through when 80% of the oxygen vacancies were refilled and 50% of deposited carbon was consumed (Figure 5.7B). The direct reaction between ^{15}NO and deposited carbon can be ruled out since there was no CO_2 formation before pulse number 1000. Approximately, the ratio between N_2 and CO_2 was around 2 during pulse number from 1000 to 4000, clearly demonstrated that the formation of one CO_2 allowed two NO to be reduced into one N_2. Around 17% of nitrogen species accumulated on the catalyst before pulse number 2000. However, the accumulated 13% of N was released as N_2 from pulse number 2000 to 6000. Therefore, the deposited carbon acted as a reductant buffer. Lattice oxygen of ceria was used for the oxidation of deposited carbon to CO and CO_2. $^{15}N_2O$ and $^{15}NO_2$ were never detectable. The direct reaction of ^{15}NO molecules to $^{15}NO_2$ over reduced Pt/ceria can be eliminated as well since carbon is an excellent reductant of NO_2 to NO [36, 37].

The overall performance of Rh/ceria (Figure 5.8) was similar. ^{15}NO started to break through much later than over Pt/ceria. The longer duration of the full ^{15}NO conversion was attributed to 3 times larger carbon deposition on Rh/ceria using C_3H_6 as a reductant. This clearly demonstrated that deposited carbon acted as reductant buffer for NO reduction. NO reduction to N_2 ended when there was no carbon left and the catalyst was (re)oxidised. A small amount of CO was observed before the evolution of CO_2 started during ^{15}NO over the C_3H_6 reduced Rh/ceria (phase I1, Figure 5.8A) in compari-

son with the case of Pt/ceria (Figure 5.7A). However, the major initial ^{15}NO oxidation activity resulted in filling the oxygen vacancies, as evidenced by the oxygen balance and carbon balance (Figure 5.8B). Regarding the N balance, hardly any ^{15}N accumulation before pulse number 5000. This was also demonstrated at the N_2 response shape I during NO pulses (Figure 5.10A and B), where 98% of injected NO was converted to N_2 in the time interval of 5 s. Upon further oxidation of the sample the N and O accumulation in a ratio of 1:1 suggested some NO adsorption until the carbon deposit was completely removed and NO broke through.

An experiment of $^{18}O_2$ pulses over the C_3H_8 reduced Rh/ceria at 450 °C (Figure 5.9) was performed to confirm that lattice oxygen was responsible for the oxidation of deposited carbon during stage Ib (Figures 5.7 and 5.8). The results showed hardly any $C^{18}O$ and $C^{18}O_2$ formation prior to pulse number 13000. $C^{18}O^{16}O$ started to evolve after pulse number 13000. The initial exclusive formation of unlabelled $C^{16}O$ and $C^{16}O_2$ indicated that gas-stage oxygen was not directly involved in the oxidation of the carbon deposit. Lattice oxygen was the main source for the oxidation of deposited carbon.

Operando Raman (at ambient pressure flow reactor) was applied to confirm further the results obtained from TAP (ultra-vacuum system, 10^{-9}-10^{-9} mbar) using Rh/ceria at 500 °C in flow reactor coupled with Raman probe, as shown in Figure 5.13. The band at 460 cm^{-1} (Figure 5.13A), attributed to the symmetric stretch mode of Ce-O_8 crystal unit in the oxidised catalyst [29], disappeared during the C_3H_6 reduction pre-treatment (Figure 5.12A), while it re-appeared and its intensity increased during the exposure to 0.2% NO/He. The changes of intensity at 460 cm^{-1} indicated that the reduced ceria was re-oxidised during 0.2% NO/He flow. The intensities at 1575 and 1350 cm^{-1}, assigned to G band and D band of carbon, remained almost constant during the first 20 min of 0.2% NO/He flows (Figure 5.13B), and afterwards, these two bands completely vanished. The operando Raman results confirmed the TAP's finding: NO mainly re-oxidised the reduced ceria, and after a sufficient degree of re-oxidation the deposited carbon started to react with the oxygen from the ceria lattice. Apparently in the flow set-up upon the C_3H_6 exposure firstly the catalyst was reduced and in second instance carbon was deposited. Upon NO exposure of the C_3H_6 pre-treated catalysts (ceria and Rh/ceria) initially the reduced catalyst was

oxidised and thereafter the carbon deposits were oxidised. This reduction-oxidation process could be completely repeated several times.

Like in the TAP reactor (Figure 5.8) CO formation was observed during the first 20 min, followed by the formation of CO_2 till 60 min (Figure 5.13C and D). N_2O and NO_2 formation was not observed. All results of this operando study (Figure 5.13) pointed out that NO was still selectively reduced into N_2 at these ambient pressure conditions. NO was dissociated on the active sites, being reduced ceria or reduced Rh sites, thereby filling the oxygen vacancies of ceria. In case of reaction on the noble metal the oxygen must have been transmitted to the ceria since this was eventually completely re-oxidised.

The investigation of NO reduction under both ultra-high vacuum TAP system and ambient pressure flow reactor pointed out that the presence of noble metal/ceria system can selectively reduce NO into N_2 [14, 15]. The conversion of NO into NO_2 was not observed on a reduced catalyst. Even NO_2 will be completely converted into N_2 when the catalyst was reduced [38]. Under all investigated (oxidative or reductive) circumstances no N_2O was detected (detection limit <1 ppm) on ceria and noble metal supported ceria. The presence of Rh and Pt on ceria can reduce the ceria at 450 °C C_3H_6 and C_3H_8, but unpromoted ceria was hardly reduced by C_3H_6 and C_3H_6 at 450 °C [22]. During NO reduction over the H_2 or C_3H_6 pre-reduced unpromoted ceria, up to 25% and 40% of N-species accumulation was observed, respectively. The Pt promoted ceria showed only 17% of N-species accumulation and Rh promoted ceria showed hardly (1%) N-species accumulation during the oxidation of the carbon deposit. The N/O atomic accumulation ratio in this period suggested the some kind of NO chemisorption took place (Figure 5.8B). The lower N-accumulation on Rh- and Pt/ceria indicated that these metals accelerate the N_2 release.

5.4.2.2. The effect of noble metal on N_2 formation rate

In the formation of N_2 the following steps can be distinguished: (1) NO adsorption, (2) NO dissociation, (3) N diffusion and association, and (4) N_2 desorption. Pump-probe TAP experiments with alternating ^{14}NO and ^{15}NO pulse were performed to explore this N_2 formation rate over ceria and Rh/ceria.

Over H_2 reduced ceria formation of only $^{15}N_2$ was observed during the first ^{15}NO pulse (Figure 5.10C). However, the $^{15}N_2$ response was much broader and lower in intensity than that for the H_2 reduced Rh/ceria (Figure 5.10A). The same holds for the $^{14}N_2$ response during the ^{14}NO injection. Both the $^{15}N_2$ and $^{15}N_2$ responses over the H_2 reduced ceria indicated a slow process of dinitrogen formation upon the NO pulses. This process of N_2 formation was so slow that some N-species were still sticking on the surface after the pulse detection time range (5 s). The observation of the mixed isotope $^{14}N^{15}N$ during the subsequent ^{15}NO injection suggested that stored ^{15}N, during the ^{15}NO injection, met ^{14}N created after the following ^{15}NO injection (Figure 5.10D), and recombined to $^{14}N^{15}N$, and vice versa for the reversed sequence. The formation of $^{14}N^{15}N$ further proved the accumulation of N (^{14}N and ^{15}N) species on the ceria surface that continue to slowly associate forming dinitrogen. The mixed isotope response is much broader and its maximum appeared also later than the dinitrogen stemming directly from the pulsed NO isotope, both evidencing a slower recombination process for these 'dwelling' nitrogen species.

Over the H_2 reduced Rh/ceria a smaller fraction of $^{14}N^{15}N$ was observed (Figure 5.10A and B). This suggested that more N accumulated on the H_2 reduced ceria than H_2 reduced Rh/ceria. The N-balance in Figure 5.6 also suggested that less N accumulated during the NO reduction to N_2. Almost all NO was converted and directly formed N_2 during the MS detection time range (5 s) over the H_2 reduced Rh/ceria before pulse number 200.

The N_2 formation includes NO adsorption, NO dissociation, N diffusion and association, and N_2 desorption. Regarding the NO adsorption, there was no ^{15}NO or ^{14}NO observed by the MS in the first ^{15}NO or ^{14}NO injection, *i.e.,* all the ^{15}NO or ^{14}NO molecules were completely and irreversibly adsorbed over both H_2 pre-reduced Rh/ceria and ceria. Therefore, the adsorption of ^{15}NO or ^{14}NO could not be the cause for the slow process of $^{15}N_2$ or $^{14}N_2$ formation over H_2 reduced ceria. The possibility of $^{15}N_2$ or $^{14}N_2$ desorption as a limiting step colud be ruled out by the experiments of pulsing N_2 over ceria and Rh/ceria in fully reduced or oxidized state as shown in Figure 5.11, where N_2 peak is at the same time position as the internal standard Ar response [39]. So once formed, the desorption of $^{15}N_2$,$^{14}N_2$ or $^{14}N^{15}N$ was not a limiting step. Then, either the NO dissociation or N diffusion and recombina-

tion, or a combination of these steps determine the slower $^{15}N_2$ formation process over the ceria. Lööf *et al.,* also observed an enhanced N_2 formation by addition of ceria to noble metal/Al_2O_3. Oxygen spillover from the noble metal to reduced ceria was attributed to the enhanced N_2 formation, which reduced the inhibition by the produced oxygen [40]. Mullins and Overbury also investigated the NO dissociation over reduced Rh/CeO_x and CeO_x using soft X-ray photoelectron spectroscopy (SXPS) [41]. They observed NO dissociation with no N_2 desorption at 175 °C over oxidised Rh/CeO_2, which suggested that the desorption of N_2 may be limited by the recombination of N on the surface. The faster N_2 formation over Rh/ceria than over ceria at least indicated that over Rh/ceria the N recombination was faster.

5.5. Conclusions

The addition of noble metals to ceria was essential for the selective NO reduction. The noble metals Pt and Rh promote the ceria reduction by hydrocarbons C_3H_6 and C_3H_8, at lower temperatures than without these metals. At 450 °C, Pt/ceria and Rh/ceria can be reduced by using C_3H_8 or C_3H_6 over Pt/ceria and Rh/ceria, while unpromoted ceria can hardly be reduced. Rh was a more active promoter in ceria reduction and carbon deposition than Pt. C_3H_8 or C_3H_6 lead to 3-4 times deeper reduction as comapred to the CO and H_2.

The reduction of NO over pre-reduced noble metal/ceria showed a selective formation N_2, while N_2O and NO_2 formation were never observed (detection limit 1 ppm). More importantly, the presence of noble metal leads to a faster N_2 formation rate than over the ceria. During the NO reduction the pre-reduced ceria support became gradually oxidized and after filling 70-80% of the oxygen vacancies the NO starts to appear in the product mixture. In the presence of carbon deposit the lattice oxygen of the ceria reacted with the carbon keeping the ceria in a reduced form, sustaining the NO decomposition process as long as the carbon is present. Gas-phase oxygen did not directly react with the carbon. During the NO reduction process some unidentified N-species remain on the catalyst, the amount depending on the catalyst, but finally all nitrogen is released as N_2.

References

[1] http://www.eea.europa.eu/publications/air-quality-in-europe-2015, accessed 2017-04-03.

[2] http://www.who.int/mediacentre/news/releases/2014/air-pollution/en/ (2014), accessed 2017-04-03.

[3] https://www.eea.europa.eu/data-and-maps/indicators/main-anthropogenic-air-pollutant-emissions/assessment-3/emissions-of-the-main-air-pollutants-in-europe, accessed 2017-04-03.

[4] D. C. Carslaw, S. D. Beevers, J. E. Tate, E. J. Westmoreland, and M. L. Williams, *Recent evidence concerning higher NO_x emissions from passenger cars and light duty vehicles,* Atmospheric Environment **45**, 7053 (2011).

[5] http://europa.eu/rapid/press-release_IP-15-5945_en.htm, accessed 2017-04-03.

[6] M. KOEBEL, M. ELSENER, and T. MARTI, *NO_x-Reduction in Diesel Exhaust Gas with Urea and Selective Catalytic Reduction,* Combustion Science and Technology **121**, 85 (1996).

[7] W. Miller, J. Klein, R. Mueller, W. Doelling, and J. Zuerbig, *The Development of Urea-SCR Technology for US Heavy Duty Trucks,* SAE International Journal of Engines , SAE Number 2000.

[8] H. T. Hug, A. Mayer, and A. Hartenstein, *Off-Highway Exhaust Gas After-Treatment:Combining Urea-SCR, Oxidation Catalysis and Traps,* SAE International Journal of Engines **SAE Number 930363**.

[9] S. Matsumoto, *Recent advances in automobile exhaust catalyst,* Catalysis Surveys from Japan **1**, 111 (1997).

[10] Y. Ikeda, K. Sobue, S. Tsuji, and S. Matsumoto, *Development of NO_x Storage-Reduction Three-way Catalyst for D-4 Engines,* SAE International Journal of Engines **SAE Number 1999-01-1279** (1999).

[11] M. Misono and T. Inui, *New catalytic technologies in Japan,* Catalysis Today **51**, 369 (1999).

[12] Y. Bisaiji, K. Yoshida, M. Inoue, K. Umemoto, and T. Fukuma, *Development of Di-Air - A New Diesel deNO_x System by Adsorbed Intermediate Reductants,* SAE International Journal of Fuels and Lubricants **SAE Number 2011-01-2089** (2011).

[13] M. Inoue, Y. Bisaiji, K. Yoshida, N. Takagi, and T. Fukuma, *DeNO$_x$ Performance and Reaction Mechanism of the Di-Air System,* Topics in Catalysis **56**, 3 (2013).

[14] Y. Wang, J. Posthuma de Boer, F. Kapteijn, and M. Makkee, *Next Generation Automotive DeNO$_x$ Catalysts: Ceria What Else?* ChemCatChem **8**, 102 (2016).

[15] Y. Wang and M. Makkee, *Fundamental understanding of the Di-Air system (an alternative NO$_x$ abatement technology). I: The difference in reductant pre-treatment of ceria,* Applied Catalysis B: Environmental (2017), 10.1016/j.apcatb.2017.04.054.

[16] H. YAO, *Ceria in automotive exhaust catalysts I. Oxygen storage,* Journal of Catalysis **86**, 254 (1984).

[17] M. Makkee, Y. Wang, R. Oord, D. van der Berg, and B. Weckhuysen, *Oxygen Vacancies in reduced Rh- and Pt-ceria for Highly Selective and Reactive Reduction of NO into N_2 in excess of O_2,* ChemCatChem (2017), 10.1002/cctc.201700578.

[18] A. Holmgren, D. Duprez, and B. Andersson, *A Model of Oxygen Transport in Pt/Ceria Catalysts from Isotope Exchange,* Journal of Catalysis **182**, 441 (1999).

[19] A. Bueno-López, K. Krishna, and M. Makkee, *Oxygen exchange mechanism between isotopic CO_2 and Pt/CeO_2,* Applied Catalysis A: General **342**, 144 (2008).

[20] V. Perrichon, A. Laachir, S. Abouarnadasse, O. Touret, and G. Blanchard, *Thermal stability of a high surface area ceria under reducing atmosphere,* Applied Catalysis A: General **129**, 69 (1995).

[21] L. Katta, P. Sudarsanam, G. Thrimurthulu, and B. M. Reddy, *Doped nanosized ceria solid solutions for low temperature soot oxidation: zirconium versus lanthanum promoters,* Applied Catalysis B: Environmental **101**, 101 (2010).

[22] Y. Wang, J. P. de Boer, F. Kapteijn, and M. Makkee, *Fundamental Understanding of the Di-Air System: The Role of Ceria in NO$_x$ Abatement,* Topics in Catalysis **59**, 854 (2016).

[23] S. Parres-Esclapez, I. Such-Basañez, M. Illán-Gómez, C. Salinas-Martínez de Lecea, and A. Bueno-López, *Study by isotopic gases and in situ spectroscopies (DRIFTS, XPS and Raman) of the N_2O decomposition mechanism on Rh/CeO_2 and Rh/γ-Al_2O_3 catalysts,* Journal of Catalysis **276**, 390 (2010).

[24] A. A. Hakeem, J. Rajendran, F. Kapteijn, and M. Makkee, *Effect of rhodium on the water–gas shift performance of Fe_2O_3/ZrO_2 and CeO_2/ZrO_2: Influence of rhodium precursor,* Catalysis Today **242**, 168 (2015).

[25] W. Lin, A. Herzing, C. Kiely, and I. E. Wachs, *Probing Metal–Support Interactions under Oxidizing and Reducing Conditions: In Situ Raman and Infrared Spectroscopic and Scanning Transmission Electron Microscopic–X-ray Energy-Dispersive Spectroscopic Investigation of Supported Platinum Catalysts,* The Journal of Physical Chemistry C **112**, 5942 (2008).

[26] L. Murrell, S. Tauster, and D. Anderson, *Laser Raman characterization of surface phase precious metal oxides formed on CeO_2,* (1991) pp. 275–289.

[27] G. Yablonsky, M. Olea, and G. Marin, *Temporal analysis of products: basic principles, applications, and theory,* Journal of Catalysis **216**, 120 (2003).

[28] J. Fierro, J. Soria, J. Sanz, and J. Rojo, *Induced changes in ceria by thermal treatments under vacuum or hydrogen,* Journal of solid state chemistry **66**, 154 (1987).

[29] W. H. Weber, K. C. Hass, and J. R. McBride, *Raman study of CeO_2: Second-order scattering, lattice dynamics, and particle-size effects,* Physical Review B **48**, 178 (1993).

[30] A. C. Ferrari, J. C. Meyer, V. Scardaci, C. Casiraghi, M. Lazzeri, F. Mauri, S. Piscanec, D. Jiang, K. S. Novoselov, S. Roth, and A. K. Geim, *Raman Spectrum of Graphene and Graphene Layers,* Physical Review Letters **97**, 187401 (2006).

[31] J. Fan, X. Wu, R. Ran, and D. Weng, *Influence of the oxidative/reductive treatments on the activity of $Pt/Ce_{0.67}Zr_{0.33}O_2$ catalyst,* Applied Surface Science **245**, 162 (2005).

[32] G. Ranga Rao, P. Fornasiero, R. Di Monte, J. Kašpar, G. Vlaic, G. Balducci, S. Meriani, G. Gubitosa, A. Cremona, and M. Graziani, *Reduction of NO over Partially Reduced Metal-Loaded CeO_2–ZrO_2 Solid Solutions,* Journal of Catalysis **162**, 1 (1996).

[33] Z. Wu, R. Jin, Y. Liu, and H. Wang, *Ceria modified MnO_x/TiO_2 as a superior catalyst for NO reduction with NH_3 at low-temperature,* (2008).

[34] I. Atribak, B. Azambre, A. Bueno López, and A. García-García, *Effect of NO_x adsorption/desorption over ceria-zirconia catalysts on the catalytic combustion of model soot,* Applied Catalysis B: Environmental **92**, 126 (2009).

[35] K. Krishna, A. Bueno-López, M. Makkee, and J. Moulijn, *Potential rare earth modified CeO_2 catalysts for soot oxidation: I. Characterisation and catalytic activity with O_2,* Applied Catalysis B: Environmental **75**, 189 (2007).

[36] G. Mul, W. Zhu, F. Kapteijn, and J. A. Moulijn, *The effect of NO_x and CO on the rate of transition metal oxide catalyzed carbon black oxidation: An exploratory study,* Applied Catalysis B: Environmental **17**, 205 (1998).

[37] M. V. Twigg, A. J. J. Wilkins, and N. S. Will, *Emission control,* (2001), US Patent 6,294,141.

[38] M. Nolan, S. C. Parker, and G. W. Watson, *Reduction of NO_2 on ceria surfaces,* The Journal of Physical Chemistry B **110**, 2256 (2006).

[39] J. T. Gleaves, G. Yablonsky, X. Zheng, R. Fushimi, and P. L. Mills, *Temporal analysis of products (TAP)—Recent advances in technology for kinetic analysis of multi-component catalysts,* Journal of Molecular Catalysis A: Chemical **315**, 108 (2010).

[40] P. Lööf, B. Kasemo, S. Andersson, and A. Frestad, *Influence of ceria on the interaction of CO and NO with highly dispersed Pt and Rh,* Journal of catalysis **130**, 181 (1991).

[41] D. Mullins and S. Overbury, *Coverage dependent dissociation of NO on Rh supported on cerium oxide thin films,* Surface science **511**, L293 (2002).

6

Oxygen Vacancies in Reduced Rh-and Pt-ceria for Highly Selective and Reactive Reduction of NO into N_2 in excess of O_2

A good decision is based on knowledge and not on numbers

Plato

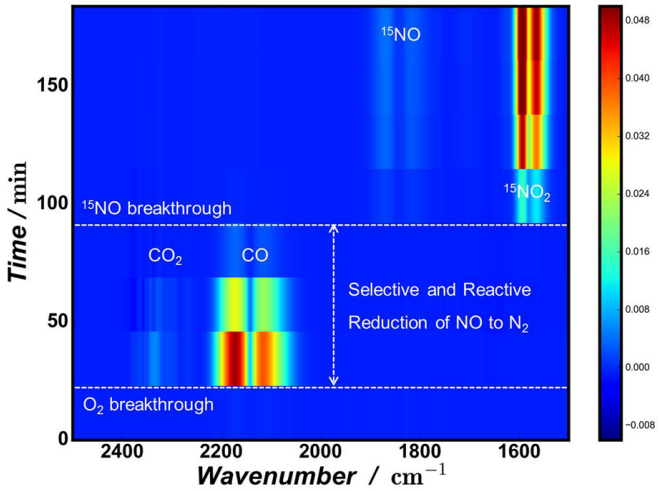

6

Commercial $DeNO_x$ catalysts exhibit a poor performance in the selective conversion NO into N_2, especially at high temperature and high gas hourly space velocities. In this study, oxygen vacancies of reduced ceria and Pt/ or Rh/ceria are found to be the efficient and selective catalytic sites for NO reduction into N_2. Even at low concentration of NO can compete with excess O_2 at high temperature of 600°C and high GHSV of 170.000 L/L/h, where SCR and NSR $DeNO_x$ system are not working properly. N_2O is not detected over the whole range of conditions, while NO_2 is only formed when the catalyst is oxidised, when both NO and O_2 start to breakthrough. For consideration of the fuel economy, the working temperature should be between 250 and 600°C. Above 600°C, most of the injected fuel was used for combustion with O_2. Below 250°C, ceria support will not be reduced by fuel and the oxidation rate of the deposited carbon by oxygen from the ceria lattice will be too low.

This chapter is based on the following publication:
Y.Wang, R.Oord, D.van den Berg, B. Weckhuysen, M.Makee. (2017). Oxygen Vacancies in Reduced Rh-and Pt-ceria for Highly Selective and Reactive Reduction of NO into N_2 in excess

6.1. Introduction

Nitrogen Oxides (NO_x) are a family of poisonous, highly reactive gasses, that have an adverse effect on our environment and human health. Each year around 2.6 million people' premature deaths are related to NO_x pollution, according to the World Health Organization [1]. The NO_x concentration in the air of most European countries is above the 40 µg/m^3, which is the safety limit value according to Air Quality Standards of European Emission [2]. Above 40% of the NO_x emissions are contributed by the on-road transportation [3]. The current Euro 6 emission standard has led to the development of highly efficient lean-burn turbo-charged diesel engines and catalytic deNO_x systems (Urea-Selective Catalytic reduction (SCR) and Lean NO_x Traps (NSR) or a combination thereof), aiming at ≤ 0.08 g/km NO_x emission. However, the real NO_x emission during the real driving is actually on average 6 times higher than the NO_x emission regulation standards [4]. This huge variation is among others, caused by the difference between the mild test conditions in the laboratory and the very dynamic acceleration and deceleration during the real driving. Therefore, from September 2017 the European Commission will partly replace the current laboratory test by the real driving emission (RDE) standard, aiming at 0.168 g/km NO_x emission, which is still even 2.1 times the current Euro 6 limit. In future, test conditions will be more stringent and with lower NO_x level. The current available technologies, including SCR [5–7], NSR [8–10], and combinations thereof, need to be significantly improved now and in the near future.

Recently, Bisaiji *et al.*(Toyota company) developed the Di-Air system in which short fuel-rich and long fuel-lean periods are created by the direct hydrocarbons (HC's) injection with a high frequency downstream of the engine in the exhaust system upstream of a complex NSR catalyst (Pt/Rh/Ba/K/Ce/Al_2O_3) [11]. The Di-Air system is a promising technology to meet the future NO_x emission standards under real driving test conditions (dynamic operations, high exhaust temperature, and high gas hourly space velocities (GHSV)) (Chapter 1).

However, detailed research is required to develop further and optimise this catalytic system before it can be commercialised at a large scale. Oxygen

of O_2. ChemCatChem, 9, 2935-2939

vacancies in reduced ceria have been found to act as the vital sites for NO reduction into N_2. Both these oxygen vacancies and deposited carbon created during the direct fuel injection in the exhaust can explain the high effectiveness of the Di-Air system [12]. However, the reactivity of NO towards oxygen vacancies could be an issue in a typical diesel gas exhaust stream, where approximately 200 ppm NO has to compete with 5% O_2, 5% CO_2, and 5-10% H_2O. In addition, NO_2 and N_2O, both to be avoided for environmental and human health reasons, are common side products in the NO reduction technologies especially when using noble metal as an active ingredient in the catalyst composition [13–16]. Therefore, the studies on reactivity and selectivity in NO reduction processes are essential. In order to investigate whether NO can be reduced into N_2 under real conditions, *i.e.,* trace amounts of NO in excess O_2 at high GHSV and high temperature, we have studied the selectivity and reactivity of NO reduction over ceria and noble metal loaded ceria in a fixed bed flow reactor.

6.2. Experimental

6.2.1. Catalyst preparation

Pt/Zr-La doped ceria and Rh/Zr-La doped ceria, aimed at 0.5 wt % noble metal loading, were prepared via incipient wetness impregnation method on Zr-La doped ceria (onwards denoted as 'ceria', a gift from Engelhard, now BASF). Tetra-ammine platinum (II) nitrate ($Pt(NH_3)_4(NO_3)_2$) and rhodium(III) nitrate hydrate ($Rh(NO_3)_3 \cdot xH_2O$,36% Rh laoding), both purchased from Sigma-Aldrich, were used as the precursor. Subsequently, the samples were dried at 110 °C overnight and calcined at 550 °C for 5 h both in a crucible in static air.

6.2.2. Catalyst characterisation

6.2.2.1. N_2 adsorption

Tristar II 3020 Micromeritics was used to determine the textural properties like BET area and pore volume [17]. The catalyst samples were degassed at 473 K for 16 h in a vacuum (0.05 mbar) before the nitrogen adsorption at liquid nitrogen temperature.

6.2.2.2. Inductively Coupled Plasma Optical Emission Spectroscopy (ICP-OES)

Approximately 50 mg of samples were destructed in 4.5 mL 30% HCl + 1.5 mL 65% HNO_3 using the microwave. The destruction time in the microwave was 120 min at max power (900 W). After destruction, the samples were diluted to 50 mL with Millipore-Q (purified demi) water. The samples were analysed with ICP-OES (PerkinElmer Optima 5300).

6.2.2.3. X-Ray photoelectron spectroscopy (XPS)

XPS measurements were recorded on a K-alpha Thermo Fisher Scientific spectrometer using monochromated Al *Ka* X-ray source. A flood gun was applied for charge compensation. A Lorentz function was used to analyse the peak intensities. Binding energies were calibrated with C(*1s*) at 285 eV as a reference.

6.2.2.4. X-ray diffraction (XRD)

The Powder X-Ray diffraction (XRD) was recorded by a Bruker-AXS D5005 with a Co *Ka* source. The data was three times collected by varying the 2θ angle from 5° to 90° with a step size of 0.02.

6.2.2.5. Transmission electron microscope (TEM)

Transmission Electron Microscopy (TEM) images were recorded on a JEM-2100P electron microscope operating at 200 kV. Before being transferred into the TEM chamber, the samples dispersed in ethanol and deposited onto a carbon-coated copper grid, shortly dried in air and then quickly moved into the vacuum system of the microscope.

6.2.2.6. Temperature Programmed Reduction (TPR)

TPR (H_2) of all the samples was carried out in fixed bed-reactor system connected to a thermal conductivity detector (TCD) to monitor the consumption of hydrogen by the catalyst. Samples of 200 mg catalyst were packed between SiC layers (300 - 425 µm). The samples were then reacted with the 10% H_2/Ar flow at a flow rate of 30 mL_{STP}/min, with temperature from

room temperature to 1000 °C at a heating rate of 5 °C/ min. The TCD was calibrated by using CuO as a reference. A Permapure tubular drier was used to remove the water produced during the reduction upstream of the TCD detector.

6.2.2.7. Thermogravimetric analysis (TGA)

The thermogravimetric analysis (TGA) in the synthetic air of the ceria and Pt/ceria samples on which carbon was deposited were carried out in a Mettler Toledo TGA/SDTA851e instrument. Ceria and Pt/ceria samples were pre-treated with 0.5% C_3H_6 (in He) at a reaction temperature of 600 °C for 2 h and cooled down to room temperature in the environment of 0.5% C_3H_6 in a flow reactor.

6.2.3. Catalytic Testing

A flow reactor was used to study the reactivity and selectivity of NO into N_2 in the presence of excess O_2. A series of experiments were performed by using ^{15}NO (and/or ^{14}NO) co-fed with an excess of O_2 over ceria, Pt/ceria, and Rh/ceria at 400 °C, 450 °C or 600 °C. To mimic the fuel injection in the Di-Air system, C_3H_6(1.25%) was used as a model fuel to pre-treat the catalyst at 400 °C, 450 °C, and 600 °C, respectively. ^{15}NO was used to distinguish $^{14}N_2$ and CO (both at *m/e* = 28) as well as CO_2 and $^{14}N_2O$ (both at *m/e* = 44).

In a typical experiemnt, 200 mg catalyst was loaded in a 6 mm inner-diameter quartz reactor tube. A feed composition of 0.2%, 0.01% or 0.05% of ^{14}NO (or ^{15}NO) in the presence of 5% O_2 (He balance) was used with gas hourly space velocities (GHSV) from 33.000 to 170.000 L/L/h. The exit gasses were online analysed by mass spectrometry (MS, Hiden Analytical, HPR-20 QIC) and Fourier Transform infrared (FT-IR) spectroscopy (Perkin–Elmer, Spectrum One).

A gas cell with KBr windows and a path length of ~5 cm^{-1} was used for the FT-IR analysis. The spectra were measured in a continuous mode using the Perkin-Elmer 'Time-Base' software between 4000-700 cm^{-1} wavenumbers with a spectral resolution of 8 cm^{-1} and an acquisition of 8 scans per spectrum, resulting in a time interval of 23 s between each spectrum.

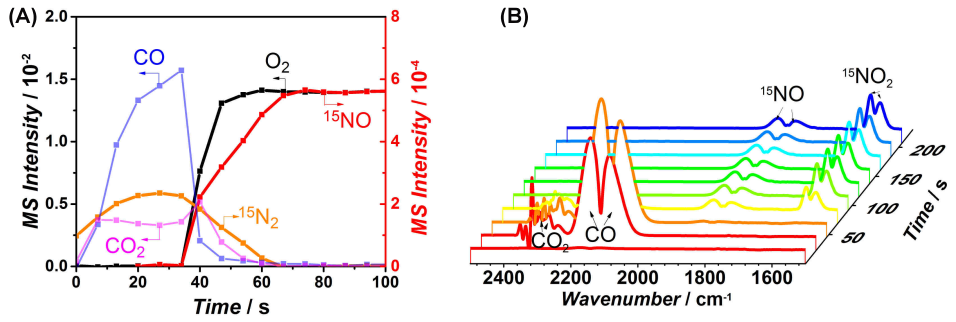

Figure 6.1: Gasses evolution during exposure of Rh/ceria C_3H_6 reduced at 600 °C to a 0.2% ^{15}NO + 5% O_2 containing He flow at a GHSV of 125.000 L/L/h at 600 °C. (A) MS signals and (B) FT-IR responses.

6.3. Result and discussion

6.3.1. Catalyst characterization

Detailed characterisations of ceria and Rh/ceria were reported in Chapter 4 and 5. Briefly, the crystal size of ceria with typical fluorite structure was on average 5 nm as determined by the Scherrer's equation and TEM micrograph analyses. The BET areas of Rh/ceria, Pt/ceria, and ceria were all 65 ± 2 m^2/g. For both the Pt/ceria and Rh/ceria, the noble metal loading was 0.5 wt %, as measured by ICP-AES.

6.3.2. Catalytic testing

6.3.2.1. NO reduction in the presence of O_2 at 600 °C

Figure 6.1A shows the ^{15}NO, O_2, and $^{15}N_2$ evolution at 600 °C under 0.2% ^{15}NO + 5% O_2 over C_3H_6 reduced Rh/ceria at a GHSV of 125.000 L/L/h. After switching to the reaction mixture, $^{15}N_2$ was observed until 70 s and no $^{15}N_2O$ or $^{15}NO_2$ were detected by MS during this time interval. ^{15}NO and O_2 started to break through from 35 s, followed by the formation of $^{15}NO_2$, detected by FT-IR (Figure 6.1B). The absence of $^{15}NO_2$ in the MS analysis is attributed to the instability of NO_2 and its easy decompositon into NO by high energy electrons in the mass spectrometer filament.

The formation of CO and CO_2, shown in Figure 6.1A, started to decline after

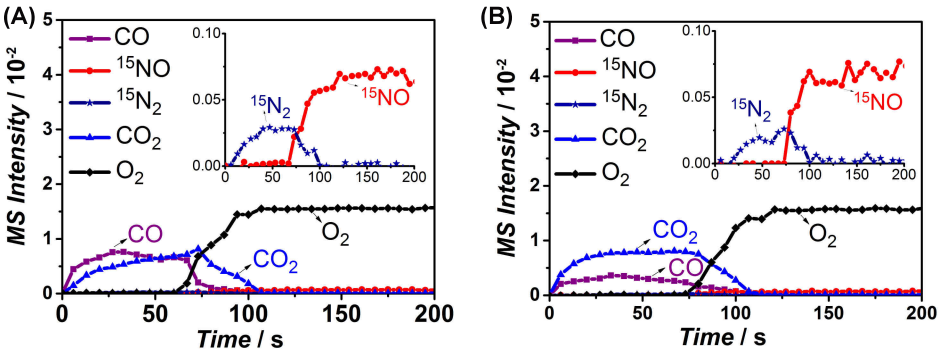

Figure 6.2: Reactant and product evolution upon 0.2% ^{15}NO + 5% O_2 in He exposure over at 600 °C C_3H_6 reduced Pt/ceria (A) and ceria (B) in a flow reactor with GHSV of 67.000 L/L/h at 600 °C. The insets of (A) and (B) present the $^{15}N_2$ and ^{15}NO evolutions *versus* time.

35 s and vanished after 70 s. The formation of CO and CO_2 was owing to the reaction of deposited carbon with oxygen from the ceria lattice [12], which re-created the oxygen vacancies and kept the ceria surface reduced. Therefore, the deposited carbon acted as buffer reductant. The decline in CO and CO_2 formation after 35 s indicated that the deposited carbon was almost entirely consumed and Rh/ceria started to be oxidised from 35 s onwards. The formation of $^{15}N_2$, as the exclusive N-containing product during the first 35 s, demonstrates the selective reduction of NO in the presence of excess O_2 in which Rh/ceria was in a largely reduced state at 600 °C. The simultaneous breakthrough of ^{15}NO and O_2 indicates that ^{15}NO and O_2 had the same reactivity towards oxygen vacancies at 600 °C. Hence, only 2% of the oxygen vacancies were filled by NO.

The ^{15}NO reduction in the presence of O_2 was also performed over Pt/ceria at 600 °C at GHSV of 67.000 L/L/h. The result was shown in Figure 6.2A. The ^{15}NO and O_2 started to breakthrough at the same time (t = 60 s). The inset of Figure 6.2A shows that $^{15}N_2$ was the exclusive product of ^{15}NO reduction during full ^{15}NO conversion time interval. The same selectivity and reactivity of NO and O_2 were also observed over C_3H_6 reduced ceria at 600 °C at GHSV of 67.000 L/L/h (Figure 6.2B). $^{15}N_2$ was also the exclusive product of ^{15}NO reduction during full ^{15}NO conversion time interval (Figure 6.2B inset).

Figure 6.3A shows the result of ^{15}NO reduction in the presence of O_2 over

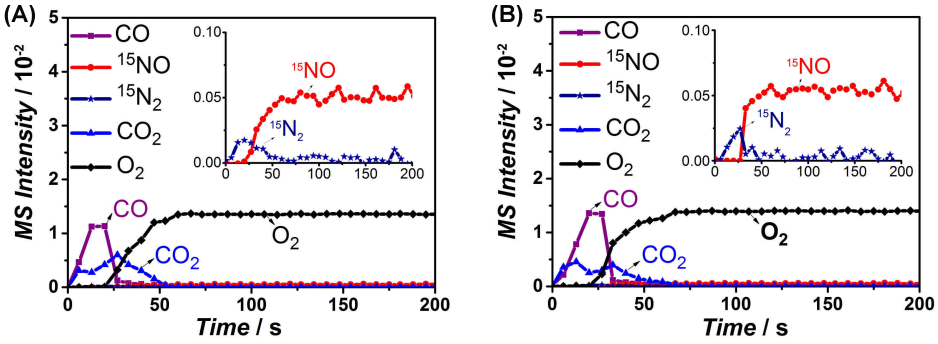

Figure 6.3: Reactant and product evolutions for 0.2% ^{15}NO + 5% O_2 exposure in He over at 600 °C C_3H_6 Pt/ceria (A) and ceria (B) GHSV of 170.000 L/L/h at 600 °C.

Pt/ceria at 600 °C at GHSV of 170.000 L/L/h, where SCR and NSR DeNO$_x$ systems are not working properly. The result for the reduced ceria shows that ^{15}NO and O_2 started to breakthrough at the same time (t = 20 s). The inset of Figure 6.3A shows that $^{15}N_2$ was still the exclusive product during the full ^{15}NO conversion time interval. Similar experiments over the reduced ceria shows the same breakthrough time for NO and O_2 (Figure 6.3B). The inset of Figure 6.3B shows $^{15}N_2$ was the exclusive product of ^{15}NO reduction. It can be concluded that even up to high GHSV 170.000 L/L/h, ^{15}NO was still selectively reduced into $^{15}N_2$ over both noble metal loaded ceria and ceria at high temeprature and gas hourly space velocities where SCR and NSR DeNO$_x$ system are not working.

Experiments using ^{14}NO were performed to further confirm the selectivity of NO, especially over noble metal loaded ceria. ^{14}NO with O_2 gas mixtures were used besides ^{15}NO with O_2 gas mixture to distinguish IR bands of CO (2174 and 2116 cm^{-1}) from those of $^{14}N_2O$ (2235 and 2208 cm^{-1}). The $^{15}N_2O$ bands were isotopically shifted to 2174 and 2116 cm^{-1} [18], the same as for CO. The results of 0.2% ^{14}NO + 5% O_2 over the ceria and Pt/ceria (Figure 6.4A and B) again shows no N_2O formation during the whole experiment and NO_2 was only formed, when NO and O_2 started to breakthrough and the ceria was fully re-oxidised. Therefore, it can be concluded that even in the presence of 25 times more O_2, the NO was selectively converted into N_2 on the reduced ceria surface at 600 °C. NO will be oxidised to NO_2 when the reduced ceria-based catalysts are 90% re-oxidised.

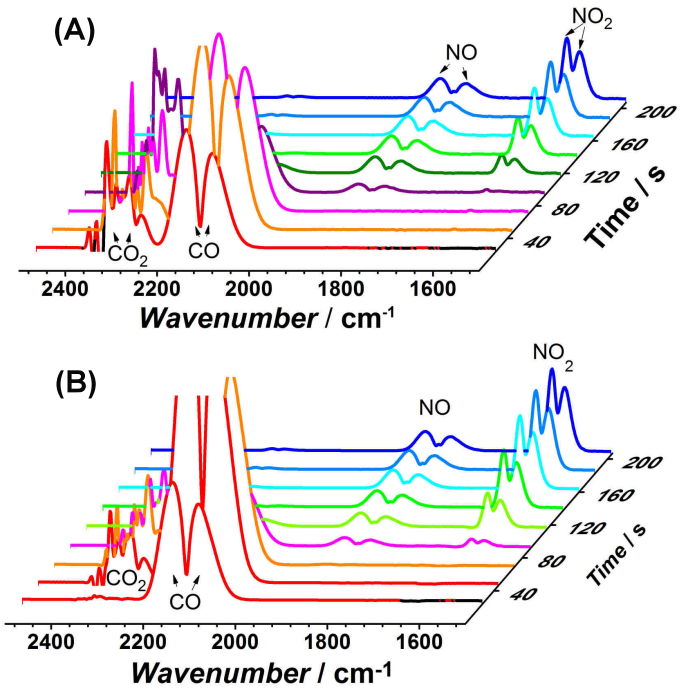

Figure 6.4: FT-IR of reactant and product evolutions for 0.2% NO + 5% O_2 exposure in He over at 600 °C C_3H_6 reduced ceria (A) and Pt/ceria (B); GHSV of 67.000 L/L/h at 600 °C downstream of flow reactor.

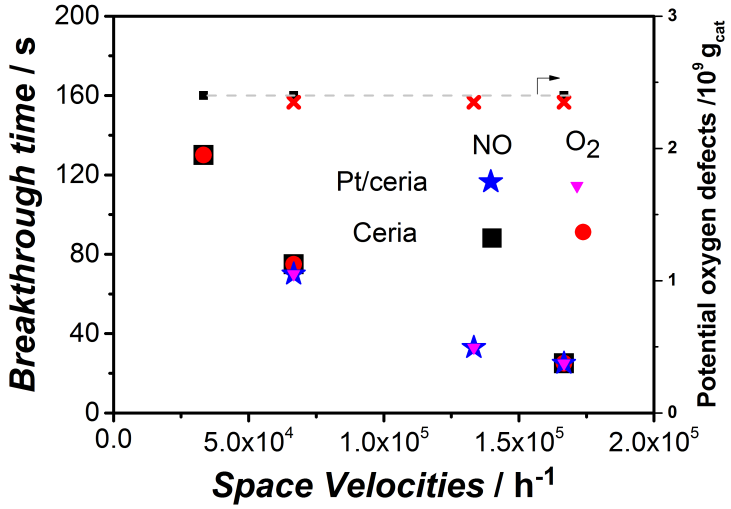

Figure 6.5: NO and O_2 breakthrough time during exposure of C_3H_6 reduced ceria and Pt/ceria to a gas flow with 0.2% NO + 5% O_2 in He at 600 °C as a function of the GHSV. Both ceria and Pt/ceria were pre-treated by 1.25% C_3H_6 in He at 600 °C.

Figure 6.5 shows the summaries of NO and O_2 breakthrough time during 0.2% NO + 5% O_2 flow over C_3H_6 reduced ceria and Pt/ceria at 600 °C for a GHSV between 33.000 L/L/h and 170.000 L/L/h. The results shows that NO and O_2 breakthrough time was an inversely proportional with GHSV. Since the reduction of ceria support was performed at the same conditions, the number of oxygen vacancies and deposited carbon were identical, *i.e.,* the same oxygen vacancies capacities based on assuming that all deposited carbon will be oxidised to CO_2. The NO and O_2 breakthrough time was largely depended on the space velocity, *i.e.,* the amount of NO and O_2 per time unit. The higher space velocities, the more NO and O_2 were fed per time unit, the earlier the breakthrough time of NO and O_2. The same was also observed for 0.2% NO + 5% O_2 exposure over C_3H_6 reduced Pt/ceria at 600 °C GHSVs ranging from 33.000 L/L/h to 170.000 L/L/h, where NO and O_2 breakthrough times was again inversely proportional to GHSV. Appanrently, even at GHSVof 170.000 L/L/h, the Di-Air system was not suffered for any kinetic limitation. For SCR and NSR, kinetic limitation will appear at GHSV of 50.000 L/L/h.

NO reactivity studies were further investigated over reduced ceria, Pt/ceria,

Table 6.1: The NO and O_2 breakthrough time using 0.05% + 5% O_2 over C_3H_6 reduced samples with GHSV of 67.000 L/L/h.

Catalyst	T/°C	Breakthrough time / s		t (NO) - t (O_2)
		t (NO)	t (O_2)	
Pt/ceria	600	60	60	0
Pt/ceria	400	215	5	210
Rh/ceria	600	65	65	0
Rh/ceria	400	253	10	245
Ceria	600	70	70	0

and Rh/ceria using NO concentrations 100 times lower than that of O_2. Table 6.1 summarises the NO and O_2 appearance times under 0.05% NO+5% O_2 over C_3H_6 reduced ceria-based catalysts at a GHSV of 67.000 L/L/h. As shown in Table 6.1, NO and O_2 had same breakthrough time for all catalyst at 600 °C. Therefore, the number of oxygen vacancies is fairly similar, and the reactvity of NO towards these oxygen vacancies at this tempearture is much higher than O_2 and still be reduced at low concentration in an excess of O_2.

6.3.2.2. NO reduction in the presence of O_2 at 450 °C

The reduction of ^{15}NO in the presence of O_2 was also performed at lower temperature at 400 °C and 450 °C. Figure 6.6A shows the ^{15}NO, O_2, and $^{15}N_2$ evolution at 450 °C during 0.2% ^{15}NO + 5% O_2 over C_3H_6 reduced Rh/ceria at GHSV of 67.000 L/L/h.

The selective reduction of ^{15}NO into $^{15}N_2$ was observed, where $^{15}N_2O$ was not observed (detection limit of 1 ppm) and $^{15}NO_2$ started to become detectable after ^{15}NO breakthrough (Figure 6.6B). ^{15}NO started to break through 50 s later than that of O_2. So, NO was more effective than O_2 in refilling the oxygen vacancies and the oxidation of the deposited carbon at 450 °C. 30% of oxygen vacancies had been filled by NO, where the concentration of

Table 6.2: Summary of H_2-TPR

	Surface reduction		Bulk reduction		Total reduction
	T/°C	H_2 (mmol/g_{cat})	T/°C	H_2 (mmol/g_{cat})	H_2 (mmol/g_{cat})
Ceria	430	-	550	-	1.2
Pt/ceria	215	0.3	360	1.2	1.5
Rh/ceria	100	0.3	265	1.4	1.7

oxygen from O_2 was 50 times higher than that of O_2.

NO reactivity studies were further investigated over reduced ceria, Pt/ceria, and Rh/ceria using NO concentrations 100 times lower than that of O_2 at 400 °C. Table 6.1 shows the NO and O_2 appearance time under 0.05% NO + 5% O_2 over C_3H_6 reduced ceria-based catalysts at a GHSV of 67.000 L/L/h. As shown in Table 6.1, O_2 appeared much earlier than NO over Pt/ceria and Rh/ceria at 400 °C. Clearly, NO can compete even at low concentration under an excess of O_2 for filling the oxygen vacancies. Around 30% of oxygen vacancies were refilled by NO.

Experiments using ^{14}NO were performed to further confirm the selectivity of NO over Rh/ ceria. Figure 6.7 shows the FT-IR spectra during 0.05% ^{14}NO + 5% O_2 exposure over C_3H_6 reduced Rh/ceria at 400 °C. The CO absorbance at 2174 and 2116 cm^{-1} was observed from the start and vanished after 90 s. In addition, a broad band at 2350 cm^{-1}, assigned to CO_2, appeared initially and vanished after 90 s. Absorbances at 1908 and 1850 cm^{-1} were observed from 255 s onwards, both assigned to ^{14}NO. During the whole time interval, no absorbance of $^{14}N_2O$ at 2235 cm^{-1} (detection limit of 1 ppm) was observed. The rise of 1601 and 1628 cm^{-1} bands after 285 s is attributed to the formation of $^{14}NO_2$. $^{14}NO_2$ was only observed when both ^{14}NO and O_2 had broken through. Oxidised ceria and Rh/ceria are well known catalysts to promote NO oxidation into NO_2 [13].

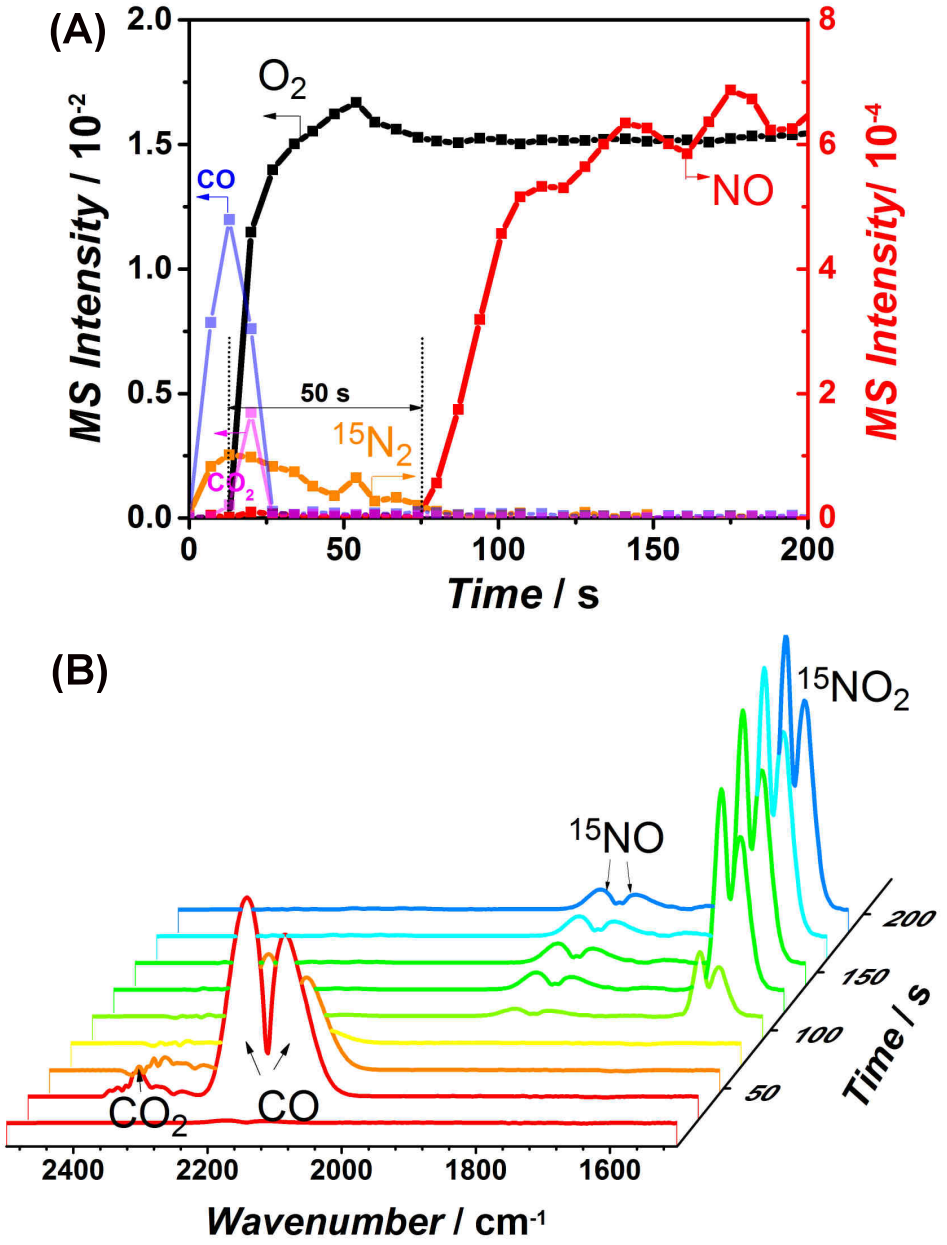

Figure 6.6: Gas evolution during exposure of Rh/ceria C_3H_6 reduced at 450 °C to a 0.2% ^{15}NO + 5% O_2 containing He flow at a GHSV of 125.000 L/L/h at 450 °C. (A) MS signals and (B) FT-IR responses.

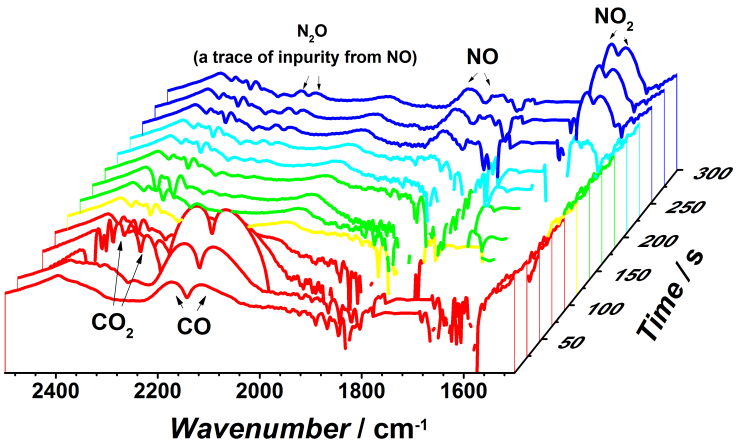

Figure 6.7: FT-IR of reactant and product evolutions for 0.05% NO + 5% O_2 exposure over at 400 °C C_3H_6 reduced Rh/ceria, GHSV of 67.000 L/L/h at 400 °C downstream of flow reactor.

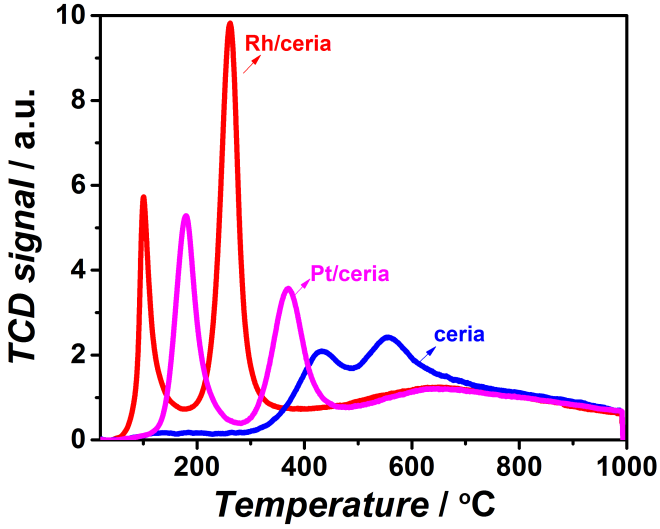

Figure 6.8: TPR(H_2) profiles for ceria (blue), Pt/ceria (magenta), and Rh/ceria (red).

6.3.2.3. Operational temperature window of Di-Air

In TPR with H_2 bare ceria support shows two reduction peaks centred at 430 and 550 °C. It is generally accepted that the low temperature (430 °C) reduction is attributed to the surface reduction and the high temperature (550 °C) accounts for the bulk reduction [19]. Compared to the bare support, surface and bulk reduction of noble metal loaded ceria shifted to lower temperature, as summarised in the Table 6.2. Therefore, as evidenced by TPR(H_2) (Figure 6.8, Table 6.2), the bulk oxygen reduction for noble metal loaded ceria was around 300 °C.

The ceria reduction by deposited carbon oxidation to CO and CO_2 by oxygen from ceria lattice provided new oxygen vacancies for NO reduction. Therefore, the oxidation of deposited carbon by ceria was essential for the rejuvenation of active catalyst sites (oxygen vacancies). TGA was applied to study the oxidation of deposited carbon in synthetic air. Ceria and Pt/ceria samples were firstly pre-reduced by using 0.5% C_3H_6 (in He) at a reaction temperature of 600 °C for 2 h and cooled down to room temperature in 0.5% C_3H_6 in He in a flow reactor. Around 10 mg of the samples were taken out for TGA analysis. The results in Figure 6.9 shows that the carbon oxidation effectively started from around 250 °C onwards over both ceria and Pt/ceria. Our previous experiments proved that oxygen from ceria lattice was used for the oxidation of deposited carbon over ceria and noble metal loaded ceria (Chapter 4 and 5) [12]. Therefore, the TGA results suggested that the reduction of ceria by the oxidation of deposited carbon started from 250 °C.

Therefore, as displayed in Figure 6.10, the operational temperature window for the Di-Air system will be from 250 to 600 °C. Below 250 °C, the reduction of ceria by fuel and oxidation of deposited carbon by oxygen from ceria will become the rate limiting steps. Above 600 °C, most of the deposited carbon will be primarily used for the reaction with O_2 and not for the NO reduction.

Due to the experimental limitations, dynamic injection of fuel onto the catalyst was not aimed for. In this study, C_3H_6 pre-treatment in 2 h was used to mimic the consequence of fuel injection, *e.g.,* ceria reduction and carbon deposition. In reality, the fuel, especially diesel will have a higher reactivity in ceria reduction and carbon deposition than the applied C_3H_6. Therefore, the reactivity of NO and O_2 can possibly be tuned over an even broader

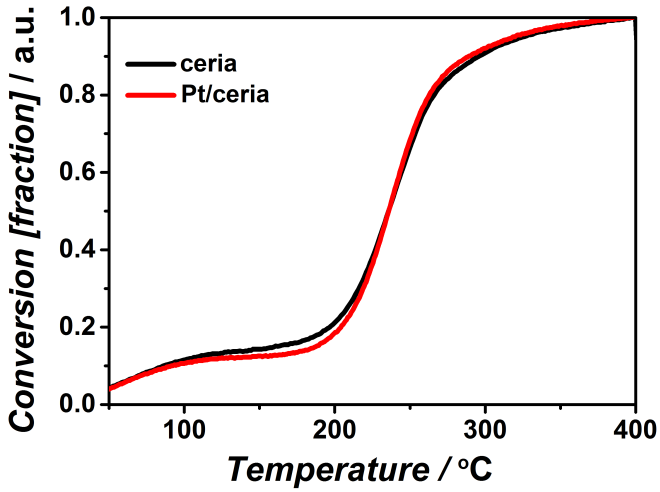

Figure 6.9: TGA profile in air of ceria (*black*) and Pt/ceria (*red*) pre-treated in a 0.5% C_3H_6 (in He) flow at 600 °C for 2 h. Heating rate 5 K/min.

temperature window.

The prominent advantage of the Di-Air system is maintaining a high NO conversion at high reaction temperatures ≥ 600 °C, and ≥ GHSV, 170.000 L/L/h, where NSR and SCR techniques are not effective at all [11]. The NSR system relies on the NO_x storage components, that can hardly work at 600 °C, causing the NSR system to fail in the high-temperature regime. NO_x storage will also fail when storage demands cannot be compensated at higher GHSV (above 40.000 L/L/h) due to kinetic limitation. The same GHSV kinetic limitations are applicable for SCR. The excellent performance of the Di-Air system at high reaction temperatures and high GHSV can be explained by the presence of oxygen vacancies and carbon deposits. The reduced ceria is extremely active and selective for NO conversion into N_2 even in excess oxygen. The existence of a reductant buffer (deposited carbon during fuel injection) extends the NO reduction capacity. Unlike the NSR system that relies on the capacity of and storage rate of NO_x storage materials, in the Di-Air system highly reactive oxygen vacancies and the reductant buffer (deposited carbon) can effectively be re-created by periodical fuel injection.

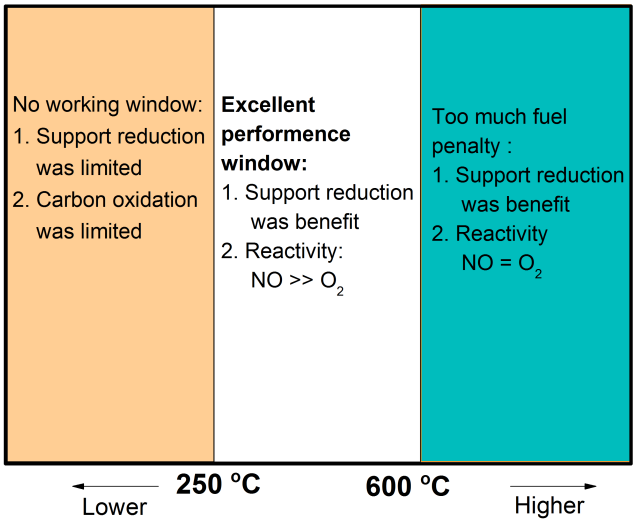

Figure 6.10: The Di-Air operational temperature window.

6.4. Conclusions

Noble metal supported ceria catalyst are promising starting materials for the development of the Di-Air system. The fuel injection direct onto the catalyst led to a reduced ceria and carbon deposition. Oxygen vacancies of reduced ceria and Pt/ or Rh/ceria are found to be the efficient and selective catalytic sites for NO reduction into N_2. Even at low concentration of NO can compete with excess O_2 at high temperature of 600 °C and high GHSV of 170.000 L/L/h. N_2O is not detected over the whole range of experimental conditions, while NO_2 is only formed when the catalyst is oxidised, where both NO and O_2 start to breakthrough. Oxygen vacancies indirect reduction with fuel and indirectly from the lattice oxygen reduction by deposited carbon are the active sites for the selective and reactive reduction of NO into N_2 in the presence of oxygen. For consideration of the fuel economy, the working temperature should be between 250 and 600 °C.

References

[1] http://www.who.int/mediacentre/news/releases/2014/air-pollution/en/ (2014), accessed 2017-04-03.

[2] http://www.eea.europa.eu/data-and-maps/figures/ annual-mean-no2-concentrations-in-2014 (), accessed 2017-04-03.

[3] http://www.eea.europa.eu/publications/air-quality-in-europe-2015, accessed 2017-04-03.

[4] http://europa.eu/rapid/press-release_IP-15-5945_en.htm (), accessed 2017-04-03.

[5] H. T. Hug, A. Mayer, and A. Hartenstein, *Off-Highway Exhaust Gas After-Treatment:Combining Urea-SCR, Oxidation Catalysis and Traps,* SAE International Journal of Engines **SAE Number 930363**.

[6] W. Miller, J. Klein, R. Mueller, W. Doelling, and J. Zuerbig, *The Development of Urea-SCR Technology for US Heavy Duty Trucks,* SAE International Journal of Engines , SAE Number 2000.

[7] M. KOEBEL, M. ELSENER, and T. MARTI, *NO_x-Reduction in Diesel Exhaust Gas with Urea and Selective Catalytic Reduction,* Combustion Science and Technology **121**, 85 (1996).

[8] M. Misono and T. Inui, *New catalytic technologies in Japan,* Catalysis Today **51**, 369 (1999).

[9] Y. Ikeda, K. Sobue, S. Tsuji, and S. Matsumoto, *Development of NO_x Storage-Reduction Three-way Catalyst for D-4 Engines,* SAE International Journal of Engines **SAE Number 1999-01-1279** (1999).

[10] S. Matsumoto, *Recent advances in automobile exhaust catalyst,* Catalysis Surveys from Japan **1**, 111 (1997).

[11] M. Inoue, Y. Bisaiji, K. Yoshida, N. Takagi, and T. Fukuma, *$DeNO_x$ Performance and Reaction Mechanism of the Di-Air System,* Topics in Catalysis **56**, 3 (2013).

[12] Y. Wang, J. Posthuma de Boer, F. Kapteijn, and M. Makkee, *Next Generation Automotive $DeNO_x$ Catalysts: Ceria What Else?* ChemCatChem **8**, 102 (2016).

[13] K. Krishna, A. Bueno-López, M. Makkee, and J. Moulijn, *Potential rare earth modified CeO_2 catalysts for soot oxidation: I. Characterisation and catalytic activity with O_2,* Applied Catalysis B: Environmental **75**, 189 (2007).

[14] G. Ranga Rao, P. Fornasiero, R. Di Monte, J. Kašpar, G. Vlaic, G. Balducci, S. Meriani, G. Gubitosa, A. Cremona, and M. Graziani, *Reduction of NO over Partially Reduced Metal-Loaded CeO_2–ZrO_2 Solid Solutions,* Journal of Catalysis **162**, 1 (1996).

[15] Z. Wu, R. Jin, Y. Liu, and H. Wang, *Ceria modified MnO_x/TiO_2 as a superior catalyst for NO reduction with NH_3 at low-temperature,* (2008).

[16] I. Atribak, B. Azambre, A. Bueno López, and A. García-García, *Effect of NO_x adsorption/desorption over ceria-zirconia catalysts on the catalytic combustion of model soot,* Applied Catalysis B: Environmental **92**, 126 (2009).

[17] M. F. De Lange, T. J. Vlugt, J. Gascon, and F. Kapteijn, *Adsorptive characterization of porous solids: Error analysis guides the way,* Microporous and Mesoporous Materials **200**, 199 (2014).

[18] T. Miller and V. Grassian, *A mechanistic study of nitrous oxide adsorption and decomposition on zirconia,* Catalysis Letters **46**, 213 (1997).

[19] H. YAO, *Ceria in automotive exhaust catalysts I. Oxygen storage,* Journal of Catalysis **86**, 254 (1984).

7

The influence of CO_2 on NO reduction to N_2 over reduced ceria - based catalyst

It's not what you look at that matters,
it's what you see.

Henry David Thoreau

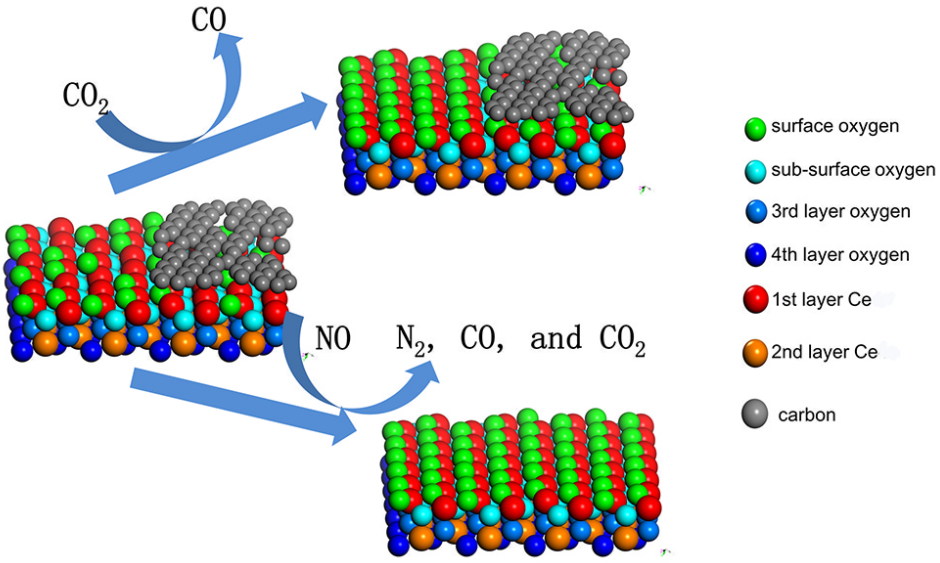
CO
CO_2
NO
N_2, CO, and CO_2
surface oxygen
sub-surface oxygen
3rd layer oxygen
4th layer oxygen
1st layer Ce
2nd layer Ce
carbon

Oxygen vacancies in reduced ceria are the catalytic sites for the NO reduction into N_2 in the Toyota Di-Air DeN abatement technology. Traces of NO (several hundred ppm*) have to compete with other oxidants present in excess, e.g., 5% CO_2 and 5% O_2, in an exhaust gas of a lean burn (diesel) engine. The reactivity of CO_2 and NO over a reduced ceria and noble metal loaded ceria has been investigated under ultra-high vacuum system in TAP and under atmosphere pressure in* operando *Raman and flow reactor. The results showed that CO_2 was a mild oxidant able to oxidize the oxygen vacancies but hardly oxidised deposited carbon over both ceria and noble metal loaded ceria. NO was a stronger oxidant and more efficient in refilling the oxygen vacancies and able to convert the deposited carbon, which acted as buffer reductant to extend the NO reduction time interval. NO was selectively and completely converted into N_2. The presence of excess CO_2 hardly affected the NO reduction process into N_2.*

This chapter is based on the following publication:
Y.Wang, M.Makee, (2018). The influence of CO_2 on NO reduction to N_2 over reduced ceria - based catalyst. Applied Catalysis B: Environmental, 221,196-205

7.1. Introduction

For diesel powered vehicles due to the more stringent NO_x emission standard and emission test certifications, more effective and advanced exhaust emission after-treatment technologies are required. The by EU commission in 2017 introduced realistic driving emission (RDE) significantly forces the improvement of the current $DeNO_x$ technologies, *i.e.,* NO_x Storage and Reduction (NSR) [1], Selective Catalytic Reduction (SCR) [2], and their combination thereof [3]. Recently, Bisaiji et al., (Toyota Company) developed a new emission control technology, the Di-Air system (Diesel $deNO_x$ System by Adsorbed Intermediate Reductants). In this system, short rich and lean periods are created by high frequency direct diesel fuel injection downstream of the engine into the exhaust upstream of a NSR catalyst (an unspecified complex mixture of $Pt/Rh/Ba/K/Ce/Al_2O_3$ coated onto a monolith) [4, 5]. These pulses will reduce the catalyst and create carbon deposits on the catalyst [6]. The Di-Air system promises to meet future emission standards under realistic driving test conditions. Oxygen vacancies of a reduced ceria have been identified to be the catalytic sites for the conversion of NO into N_2 [6]. Deposited carbon on the reduced ceria created during diesel fuel injection acts as a buffer reductant. The oxidation of deposited carbon via the ceria lattice oxygen species will recreate new oxygen vacancies in the ceria lattice. These recreated ceria oxygen vacancies provide additional NO conversion capacity [6].

In the exhaust gas of a lean burn engine, the concentration of O_2 and CO_2 (around 5%) are much higher than that of NO (in the order of hundred ppm). In a previous article we have demonstrated that even in the excess of oxygen NO is completely converted into N_2 (100% NO conversion with 30% efficiency with respect to oxygen at an O_2 to NO ratios of = 100) at 450 °C for bare ceria and noble metal loaded ceria [7]. CO_2 will also be capable to oxidize these sites of reduced ceria [8], which has been commonly reported in the field of solar fuel cells [9]. Metal and/or metal oxide interaction or boundary regions are reported to further assist in the CO_2 dissociation over the noble metal loaded ceria [10, 11]. Although the universal mechanism of CO_2 activation into CO and (atomic or molecular) oxygen is still unresolved [12, 13], the CO_2 activation via dissociation was extensively reported both by DFT modelling study and some experimental work. To best of our knowl-

edge, no work has been published on the efficiency and reactivity of CO_2 versus the number of oxygen vacancies in ceria. Especially, the relative reactivity of CO_2 versus NO will be crucial for the Di-Air system optimization. The oxidation of deposited carbon by CO_2 should be minimized in order to maximize the function of deposited carbon as buffer reductant for the NO reduction. Furthermore, the study of NO reactivity and selectivity in the presence of CO_2 are essential, as the common side products especially over noble metal catalysts, *e.g.,* N_2O and NO_2, have an even worse effect on our environment and human health.

Therefore, the Temporal Analysis Products (TAP, ultra-high vacuum) technique was applied to study the reactivity of CO_2 and NO versus the number of oxygen vacancies and deposited carbon over ceria and noble metal loaded ceria. *Operando* Raman (atmosphere pressure) and fixed bed flow reactor experiments were performed to confirm the TAP results. More importantly, the competition of small amount of NO with an excess of CO_2 was performed in a fixed-bed flow reactor in order to mimic of the selectivity and reactivity of NO reduction under more realistic conditions.

Commercially available Zr and La-doped ceria (a gift of BASF, further denoted as ceria) is used as a model of ceria due to its high hydrothermal stability [6, 14, 15]. The concept of the hypothetical ceria layer is introduced to describe the oxidation state of the catalyst. Each one O-Ce-O tri-layer is regarded as one hypothetical ceria layer. The number of reducible oxygen vacancies on one hypothetical reduced ceria layer was calculated to be $2.6 \cdot 10^{17}$ oxygen atoms/mg_{cat} for an agglomerate of ceria crystallites (5 nm) with a BET area of 65 m^2/g [6, 16].

7.2. Materials and methods

7.2.1. Materials preparation

0.5 wt.% Rh/ceria and Pd/ceria were prepared via an incipient wetness impregnation method on dried ceria. Rhodium(III) nitrate hydrate and Palladium(II) nitrate hydrate (purchased from Sigma Aldrich) were used as precursors in purified demi water. Subsequently, the samples were dried at 110 °C overnight and calcined at 550 °C for 5 h.

7.2.2. Characterisation

7.2.2.1. Inductively Coupled Plasma Optical Emission Spectroscopy (ICP-OES)

Approximately 50 mg catalyst was digested in 4.5 mL 30% HCl + 1.5 mL 65% HNO_3 in a microwave for 120 min. at max. power of 900 W. After destruction the samples were diluted to 50 mL with Millipore-Q (purified demi) water. The samples were analysed with ICP-OES (PerkinElmer Optima 5300).

7.2.2.2. N_2 adsorption

Tristar II 3020 Micromeritics was used to determine the textural properties like BET area and pore volume at -196 °C . The catalyst samples were degassed at 200 °C for 16 h in vacuum (0.05 mbar) prior to the nitrogen adsorption.

7.2.2.3. X-ray diffraction (XRD)

The powder X-ray diffraction (XRD) was recorded on a Bruker-AXS D5005 with a Co *Ka* source. The data was 3 times collected by varying the 2θ angle from 5° to 90° with a step size of 0.02.

7.2.2.4. Temperature Programmed Reaction (TPR)

TPR (temperature programmed reaction with hydrogen) for the ceria, Rh/ceria, and Pd/ceria were carried out in home-made fixed bed reactor system connected to a thermal conductivity detector (TCD) to monitor the consumption of hydrogen by the catalyst sample. 200 mg of sample was packed between SiC layers (300-425 µm). The sample was then reduced with H_2 (10%)/Ar flow with a flow rate of 30 mL_{STP}/min at a constant heating rate of 5 °C /min to 1000 °C . TCD was calibrated by using CuO as a reference. A Perma Pure tubular drier was used to remove the water produced during the reduction upstream of the TCD detector.

7.3. Catalytic testing

7.3.1. TAP experiments under ultra-high vacuum condition

The pulse experiments were carried out in an in-house developed TAP (Temporal Analysis of Products) reactor. Small gas pulses, typically in the order of $1 \cdot 10^{15}$ molecules, were introduced in a small volume (1 mL) upstream of the catalyst packed bed reactor. The produced pressure gradient over the catalyst packed bed thereby caused the molecules to be transported through the packed bed to the ultra-low vacuum at the opposite side of the reactor bed. Depending on the actual amount of molecules pulsed, the transport can be purely Knudsen diffusion. In other words, the molecules will only interact with the 'walls' (catalyst surface and reactor walls) of the system and not with each other. Upon interaction with the catalyst, the molecules can be converted into different products. The evolution of the reactant and product molecules is tracked (one mass at a time) in time with a high resolution of 10 kHz by means of a mass spectrometer. More details about TAP can be found in Chapter 2 [6].

21.2 mg of ceria, 10 mg of Rh/ceria, and 10 mg of Pd/ceria (100-250 µm) were used and loaded as a fixed-bed reactor in the TAP equipment. For all measurements, the gas pulses contained either 20 vol.% Ne or 20 vol.% Ar or 20 vol.% Kr as an internal standard. In all experiments, the catalyst was initially oxidised by admitting O_2/Ar pulses until the O_2 signal approached a stable level. Reductions of ceria or noble metal loaded ceria were subsequently performed using reductant pulses of either 80 vol.% C_3H_6 in Ne or 80 vol.% CO in Ar. The re-oxidation was conducted using oxidant pulses of either 80 vol.% CO_2 or 80 vol.% NO both in Ar, or 80 vol.% ^{15}NO both in Kr. In all experiments a starting pulse size of approximately $1.6 \cdot 10^{15}$ molecules was used, the pulse size gradually decreased during an experiment since the reactant was injected from the closed volume of a pulse-valve line.

The oxygen and carbon mass balances during the CO_2 or NO pulsing over the CO and C_3H_6 pre-reduced catalyst were calculated by Equation 7.1 and 7.2, respectively.

$$O_{balance} = NO_{in}(2 \times CO_{2in}) - 2CO_{2out} - CO_{out} - NO_{out} \qquad (7.1)$$

$$C_{balance} = CO_{2in} - CO_{2out} - CO_{out} \quad (7.2)$$

A positive Obalance meant that oxygen accumulates in/on the catalyst, while a negative Cbalance indicated the consumption of deposited carbon from the catalyst.

7.3.2. *Operando* Raman

Operando Raman spectra (Renishaw, 2000) were recorded using a temperature controlled *operando* Raman cell (Linkam, THMS 600). Ten scans were collected for each spectrum in the 100-4000 cm^{-1} range using continuous grating mode with a resolution of 4 cm^{-1} and scan time of 10 s. The excitation wavelength was 325 nm. The power of each laser line was kept at about 2.5 mW to prevent local heating effects. The spectrometer was daily calibrated using a silicon standard with a strong absorption band at 520 cm^{-1}. The (re-oxidised) ceria was pre-treated by C_3H_6 (1000 ppm in N_2, flow rate 200 mL/min) for 2 h. N_2 was used to flush the cell for 20 min. Subsequently, CO_2 (1000 ppm CO_2 in N_2, a flow rate of 200 mL/min) was admitted to the cell.

7.3.3. Flow reactor experiment under atmosphere pressure

The catalyst sample (200 mg) was placed in a 6 mm inner diameter quartz reactor tube and equipped downstream with mass spectrometry (MS, Hiden Analytical, HPR-20 QIC) and infrared (IR) spectroscopy (Perkin–Elmer, Spectrum One). For IR analysis a gas cell with KBr windows with an internal path length of ~5 cm was used. The spectra were recorded in a continuous mode using the Perkin-Elmer 'Time-Base' software between 4000-700 cm^{-1} wavenumbers with a spectral resolution of 8 cm^{-1} and an acquisition of 8 scans per spectrum, resulting in a time interval of 23 s between each displayed spectrum.

In all experiments, the catalyst was initially (re-)oxidised by O_2/He until the O_2 signal reached a stable level in MS. Reduction of catalyst was performed by flowing 1.25% C_3H_6 (He) for 2 h with a flow rate of 200 mL/min and subsequently flushed with He (200 mL/min) for 30 min at 450 °C. Feed compositions of either 0.2% NO/He or 0.2% CO_2/He or (0.2% NO + 5% CO_2)/He were used at a GHSV of 67.000 L/L/h .

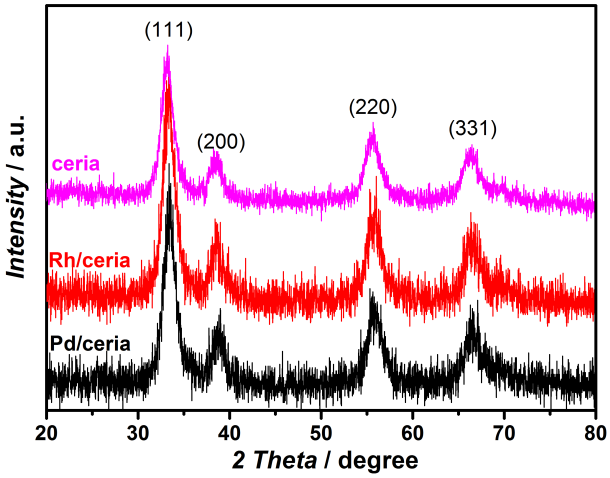

Figure 7.1: XRD pattern of ceria, Rh/ceria, and Pd/ceria.

7.4. Results and discussion

7.4.1. Characterisation

7.4.1.1. Structure and chemical composition

Characterisation details of the ceria support were reported in more detail elsewhere [6, 16]. In brief, typical fluorite structure of ceria was detected by Raman and XRD. A 5.0 nm crystal size of ceria was determined by the Scherrer's equation and confirmed by the analysis of the TEM micrographs. The bulk composition of ceria support was measured by ICP, which showed that the atomic ratio of Ce, Zr, and La was 0.64 : 0.15 : 0.21. The BET area of bare (fresh and spent) ceria was 65 m^2/g. The BET areas of Rh/ceria and Pd/ceria (fresh and spent) were similar to the bare ceria support (66 ± 2 m^2/g). The loadings of Rh and Pd were determined to be 0.5 wt.%, measured by ICP-OES (0.0486 $mmol/g_{cat}$ and 0.0470 $mmol/g_{cat}$ of Rh and Pd loading, respectively). Figure 7.1 shows the XRD patterns of ceria, Rh/ceria, and Pd/ceria. The patterns of both Rh/ceria and Pd/ceria showed a fluorite cubic structure of ceria. Diffraction lines due to Rh and Pd metals or any rhodium oxides and palladium oxides were not observed due to the low loading (0.5 wt.%) and high dispersion of these noble metals on the applied

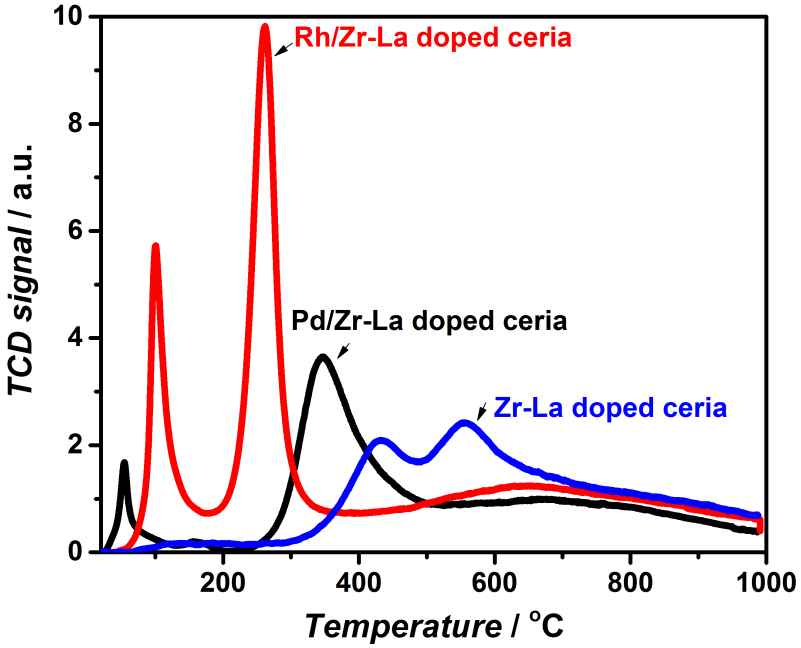

Figure 7.2: H_2-TPR profiles of ceria, Rh/ceria, and Pd/ceria.

ceria.

7.4.1.2. TPR(H_2)

The reduction properties of bare support and Rh- and Pd-loaded support were studied by TPR technique. The TPR(H_2) results are presented in Figure 7.2. The bare support showed two reduction steps centred at 430 and 550 °C. It was generally accepted that the low temperature (430 °C) process was attributed to the surface reduction, whereas the high temperature (550 °C) was accounted for the bulk reduction [17]. The total H_2 consumption was calculated to be 1.2 mmol/g_{cat}, corresponding to 2.7 ceria layer reduction. The H_2 consumption up to temperatures of 500 °C (surface reduction) was calculated to be 0.4 mmol/g_{cat}, corresponding to around 0.9 ceria layers reduction.

For Pd/ceria, the peak area at 50 °C with a H_2 consumption of 0.05 mmol/g_{cat} was contributed from the reduction of PdO to Pd. The amount of H_2 consumption is almost equal to the Pd loading on the ceria This was in agree-

Table 7.1: Summary of oxygen removal and deposited carbon (carbon atoms/mg_{cat}) by CO and C_3H_6 pre-treatment over ceria. Oxygen unit: oxygen atoms/mg_{cat}, Carbon unit: oxygen atoms/mg_{cat}

	T/°C	Oxygen removal		Deposited carbon
		Oxygen	Reduction layers	Carbon
CO	580	$3 \cdot 10^{17}$	1	-
	540	$3 \cdot 10^{17}$	1	-
C_3H_6	580	$7.1 \cdot 10^{17}$	2.8	$1.5 \cdot 10^{18}$
	560	$5.9 \cdot 10^{17}$	2.3	$1 \cdot 10^{18}$

ment with the literature [18]. The reduction peak area at 350 °C was related to the surface reduction of ceria support with H_2 consumption of 0.55 mmol/g_{cat}, corresponding to around 1.2 ceria layers reduction. The total H_2 consumption up to temperatures of 500 °C was calculated to be 1.3 mmol/g_{cat}, corresponding to 2.9 ceria layers reduction.

For Rh/ceria, the peak area with H_2 consumption of 0.3 mmol/g_{cat} at 100 °C which was larger than the amount needed for the reduction of Rh_2O_3 (or other type of RhO_x) to Rh (0.05 mmol/g_{cat} of Rh loading). Therefore, the hydrogen consumption was a combination reduction of Rh_2O_3 to Rh and a partial reduction of CeO_2 into Ce_2O_3. The total H_2 reduction was calculated up to a temperature of 350 °C to be 1.7 mmol/g_{cat}, corresponding to 3.8 layers ceria reduction.

7.4.2. Catalytic testing

7.4.2.1. Investigation of CO_2 and NO reactivity over reduced ceria support by TAP

To investigate the reactivity of CO_2 and NO towards the oxygen vacancies of ceria, CO and C_3H_6 were applied as reductants to pre-treat the catalyst samples. Table 7.1 summarises the result of CO and C_3H_6 pre-treatment

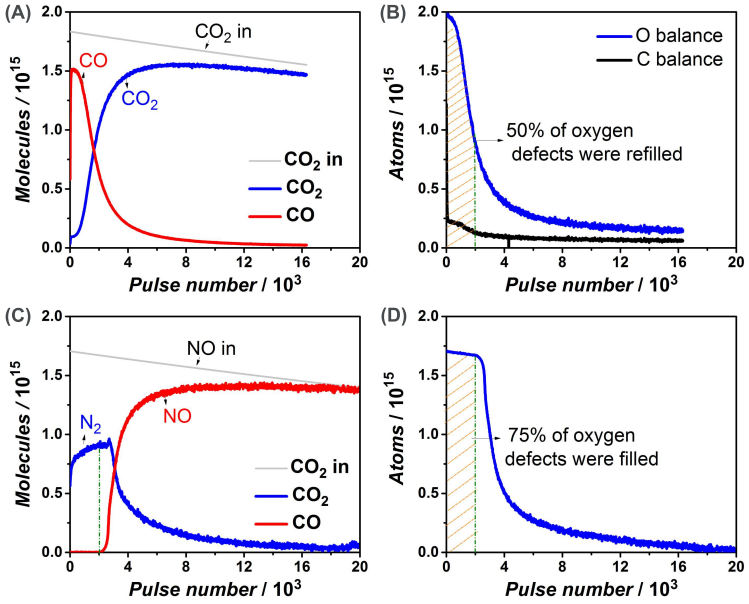

Figure 7.3: CO_2 pulse responses in TAP at 580 °C (A and B) and NO pulse responses at 540 °C (C and D) over CO reduced ceria at 580 °C and 540 °C , respectively.

over (re-oxidised) ceria [19]. All the CO_2 experiments were performed at 580 °C and the NO experiments were carried out at 540 °C and 560 °C .

The conversion of CO_2 over CO pre-reduced ceria at 580 °C was presented in Figure 7.3A and B. As shown in Figure 7.3A, the CO_2 conversion was almost 100% during the first several CO_2 pulses, accompanied by CO formation. Then the conversion quickly declined until to nearly zero conversion after 14000 CO_2 pulses. CO_2 was able to produce oxygen species and to re-oxidise reduced metal oxides [20], which made CO_2 a promising oxygen source or oxidant in partial oxidation reactions such as methane reforming [**?**] and oxidative dehydrogenation (ODH) of alkanes [21, 22]. Our TAP CO_2 pules experiment over CO reduced ceria (Figure 7.3A and B) showed that CO_2 molecules were able to convert to CO at 580 °C . The carbon balance during the CO_2 pulses (Figure 7.3B) showed a maximum 13% of carbon was left during the CO_2 pulse. Therefore, more than 85% of CO_2 was converted into CO with O filling into oxygen vacancies of ceria. This missing carbon could due to the slow desorption of CO and CO_2 from the ceria surface. It might be argued that the missing carbon can be formed as carbonate over

the ceria, since the exposure of ceria with CO_2 can cause the formation of carbonate over the ceria [23, 24]. However, over the reduced ceria surface, the formation of carbonate can be limited. A DFT calculation result had shown that CO_2 was favoured to chemisorb to the reduced ceria resulting in the formation of an activated mono-dentate carbonate species, which could further dissociate to form CO [25]. Regarding the activation of CO_2 over the reduced ceria, the assistance by hydroxyl groups could be largely eliminated, since CO_2 multi-pulse experiments were performed in ultra-high vacuum system. Oxygen anion vacancies and the associated electrons should be regarded as the active sites to activate CO_2 [25]. Therefore, the pathway of CO_2 activation via surface hydroxyl groups could be largely ruled out and had to proceed via a C=O bond activation. Charges had to be transferred from the reduced ceria to CO_2, resulting in the formation of CO_2^- anion radical species [26]. Overall, the CO_2 activation over oxygen anion vacancies resulted in that one of CO_2's O atoms was used to fill the oxygen anion defect site and, thereby, re-oxidising the reduced ceria in combination with the desorption of one CO molecule (Equation 7.3):

$$CO_2 + 2Ce^{3+} \leftrightarrow CO + 2Ce^{4+} + O^{2-} \tag{7.3}$$

Till 2000 pulses around half of the oxygen vacancies were filled. The NO pulses over the CO reduced ceria at 540 °C showed that NO was completely converted into N_2 during the first 2000 NO pulses, followed by a break-through of NO (Figure 7.3C). Around 75% of the oxygen vacancies were refilled when the NO conversion dropped down (Figure 7.3D). N_2 was the exclusive product during the NO reduction. N_2O and NO_2 were not observed.

The different observations between CO_2 and NO pulses indicated that the reaction rate of CO_2 for the re-oxidation process of ceria was slow, *i.e.,* CO_2 was not a very effective oxidant in refilling the oxygen vacancies. This could be either related to a slow desorption of CO or the negative driving force to the (quasi-) equilibrium between CO, CO_2, Ce^{3+}, and Ce^{4+}, according to Equation 7.3. The pulse of CO over the (pre-) oxidised ceria showed that CO could only reduce ceria up to 1 hypothetical ceria layer supported the existence of a (quasi-) equilibrium between CO, CO_2, Ce^{3+}, and Ce^{4+}. The inactivity of CO_2 could not be caused by the full coverage of CO on the surface according the carbon balance in Figure 7.3B.

In the Di-Air system, diesel fuel is used as reductant instead of CO and H_2. Therefore, the study on the performance in CO_2 over a fuel reduced ceria will be required. Propene was used to mimic diesel fuel used in the real practical operation. As displayed in Figure 7.4, stage I and stage II will be used to distinguish the full NO (CO_2) conversion (stage I) and NO (CO_2) started to breakthrough (stage II). The CO_2 conversion over C_3H_6 pre-reduced ceria is shown in Figure 7.4A and B. In contrast to the CO_2 conversion over a CO reduced ceria (Figure 7.3A and B), the CO_2 pulses over a C_3H_6 reduced ceria showed that CO_2 was completely converted till pulse number 6000 (stage I). CO was the only product. There is some more CO formation than was required for refilling the oxygen vacancies (Figure 7.4A). Apparently, some of the deposited carbon was consumed from the catalyst as indicated from the carbon balance in Figure 7.4B. According to the oxygen balance in Equation 7.1, oxygen vacancies in the ceria were refilled during the CO_2 pulses. As shown in Figure 7.4B, when CO_2 started to break through from pulse number 6000 onwards, the oxygen refilling rate declined. The CO_2 conversion dropped from 100% in stage I to around 20% in stage II. The quantity of oxygen accumulation during the stage I was around 50% of oxygen vacancies that created by the C_3H_6 pre-treatment. The total carbon consumption during stage I and stage II was around 2% of the deposited carbon formed during the C_3H_6 pre-treatment.

This full conversion time interval period (stage I, Figure 7.4A) was due to the deeper degree of ceria reduction (2.8 hypothetical reduced ceria layers). A higher degree of reduction of ceria drove the CO_2 conversion to CO (Equation 7.3). The formation of carbonate by CO_2 pulses could be eliminated here since carbon balance was negative, indicating that the CO_2 pulse will convert carbon deposits from the surface instead of carbon accumulation. The formation of CO during the CO_2 pulses will be a combination of CO_2 reduction and deposited carbon oxidation.

The majority of CO formation during stage I came from the reduction of CO_2 on the oxygen vacancies according to the carbon and oxygen balance in Figure 7.4B [20], as could be described by Equation 7.3. This observation confirmed the existence of a (quasi-) equilibrium between CO, CO_2, Ce^{3+}, and Ce^{4+}.

The oxidation of deposited carbon via lattice oxygen from ceria could be

described [6, 27], according to Equation 7.4:

$$C + 2Ce^{4+} + O^{2-} \leftrightarrow CO + 2Ce^{3+} \quad (7.4)$$

Therefore, the CO_2 pulses during the stage I where CO_2 was completely converted, led to oxygen accumulation in the ceria, thus re-filling the oxygen vacancies.

CO_2 started to break through from pulse number 6000 onwards, where 50% of oxygen vacancies in the one hypothetical mono-layer reduced ceria were present and 2% of deposited carbon was oxidised (Figure 7.4B). One might argue that gas phase CO_2 could react with surface deposited carbon, forming CO directly according to Equation 7.5:

$$CO_2 + C \leftrightarrow 2CO \quad (7.5)$$

This reaction will be very unlikely since then for each converted CO_2 molecule two CO molecules should be generated, which was not supported by the observation in Figure 7.4A. Also thermodynamically the gasification of carbon (stable graphite) to CO by CO_2 at this temperature is not favoured [28].

Figure 7.4C and D show the results of NO pulse over a C_3H_6 reduced ceria at 560 °C . The pulse of NO resulted in the formation of N_2 and CO, followed by the formation of N_2 and CO_2. NO was completely converted during the stage I and started to breakthrough from pulse number 30000 (stage II). The oxygen and carbon balances during the NO pulses were displayed in Figure 4D. The quantity of oxygen vacancies refilling during stage I was around 84%. The formation of CO and CO_2 during NO pulses indicated the conversion of deposited carbon from ceria surface. Total carbon conversion during the stage I was around 90% of deposited carbon. Apparently, NO conversion only dropped when most of the deposited carbon was consumed.

Oxygen anion defect centres in reduced ceria were responsible for the decomposition of NO into N_2, thereby re-oxidizing these defect centres. The oxidation of the carbon deposits by oxygen species originating from lattice oxygen will prolong a reduced ceria surface state. NO conversion time interval will, thereby, be extended due to the oxidation of deposited carbon by the ceria lattice oxygen, which will re-create oxygen vacancies in the ceria for additional NO reduction [6].

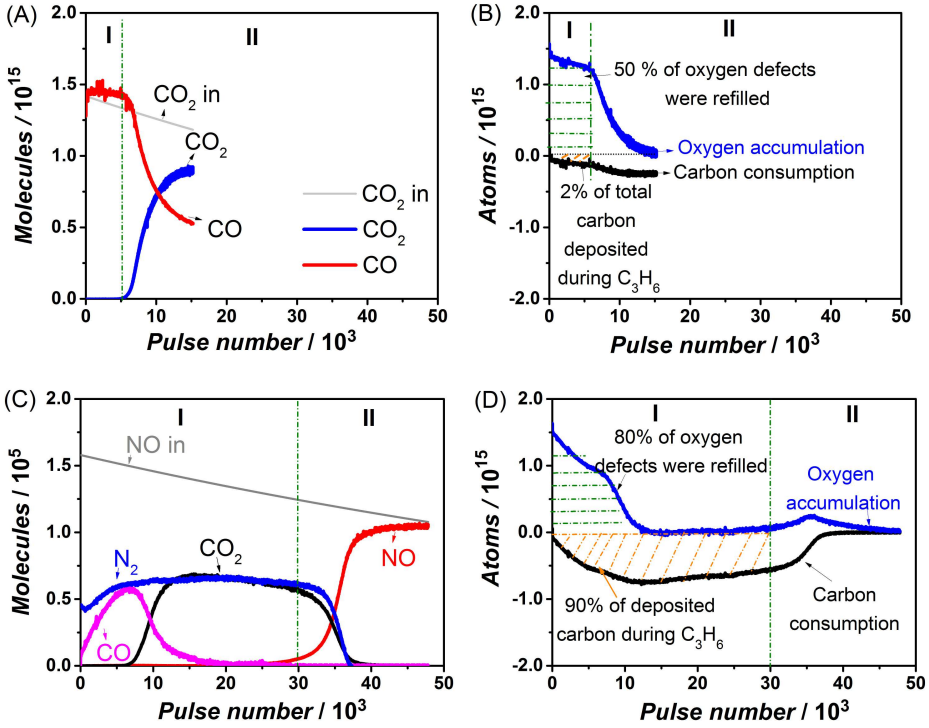

Figure 7.4: CO_2 pulse responses in TAP at 580 °C (A and B) and NO pulse responses at 540 °C (C and D) over CO reduced ceria at 580 °C and 540 °C , respectively.

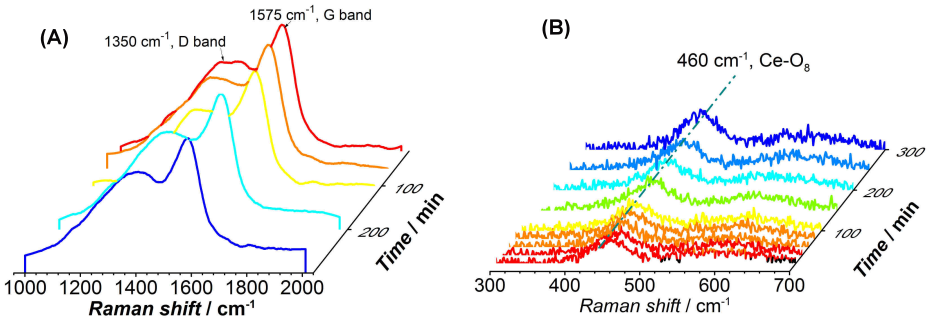

Figure 7.5: *Operando* Raman of CO_2 exposure over C_3H_6 reduced ceria at 560 °C : A) D band and G band of carbon; and B) Ce-O_8 band of ceria.

7.4.2.2. Investigation of CO_2 and NO reactivity over reduced ceria support by *operando* Raman

Operando Raman was applied to investigate the NO and CO_2 reaction reactivity over reduced ceria under atmosphere pressure. The band at 460 cm^{-1} was attributed to the symmetric stretch mode of Ce-O_8 crystal unit (F_{2g} mode), which was characteristic for a reduced fluorite ceria structure [29]. As shown in the Figure 7.5A, band at 460 cm^{-1} disappeared after the C_3H_6 pre-treatment and this band intensity re-appeared and its intensity increased during CO_2 exposure, indicating that pre-reduced ceria was re-oxidised by CO_2. The bands at 1575 and 1350 cm^{-1} were assigned to G band and D band of carbon in either graphene or graphite form, respectively. The G band was usually assigned to zone centre phonons of E_{2g} symmetry of the perfect graphite structure, and the D peak was a breathing mode of A_{1g} symmetry. This mode was forbidden for a perfect graphite structure and only became active in the presence of structural vacancies and disorders [30]. The intensity of D band and G band of graphene/graphite hardly changed during CO_2 exposure for C_3H_6 reduced ceria (Figure 7.5A), while the band at 460 cm^{-1} to some extent increased (Figure 7.5B), indicating that CO_2 was only able to re-fill oxygen vacancies.

In order to make a comparison between NO and CO_2 reactivity under atmosphere pressure, *operando* Raman spectroscopy was recorded during the NO flow over C_3H_6 reduced ceria at 560 °C. In contrast to the CO_2 experiment, the band at 460 cm^{-1} significantly increased during the NO exposure

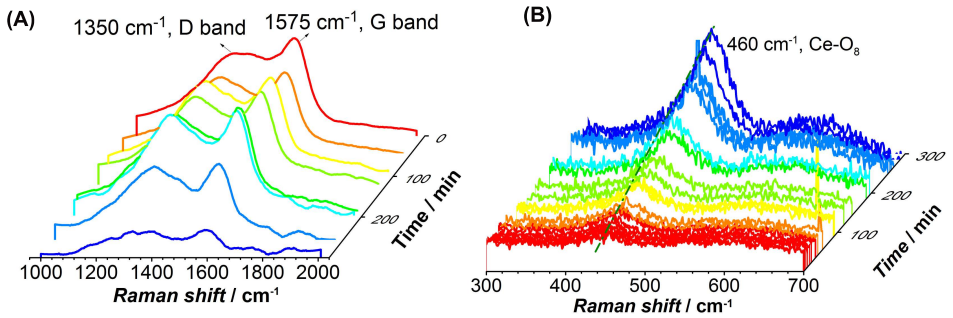

Figure 7.6: *Operando* Raman of NO exposure over C_3H_6 reduced ceria at 560 °C :A) D band and G band; and B) Ce-O_8 band.

(Figure 7.6B), indicating (re-)filling of oxygen vacancies by NO. The band at 1575 cm^{-1} and 1350 cm^{-1} also started to significantly decrease after 200 min (Figure 7.6A), indicating the oxidation of the deposited carbon).

7.4.2.3. Investigation of CO_2 and NO reactivity over reduced noble metal loaded ceria by TAP

The presence of noble metals on CeO_2 systems will promote the migration/exchange of oxygen species between isotopic $C^{18}O_2$ and Pt/$Ce^{16}O_2$ [10]. The presence of Pt accelerated the exchange rate between 200 and 400 °C , mainly favouring the exchange of one of the oxygen atoms of $C^{18}O_2$ molecule [10]. The loading of noble metal over ceria might have an influence in either in assisting or inhibiting CO_2 reduction reactivity versus NO. Additionally, loadings of either Rh on Pd on ceria were able to promote the reduction of ceria surface and bulk to lower temperature by hydrogen, as evidenced by TPR in Figure 7.2. However, the reduction of bare ceria required the temperatures exceeded 500 °C for C_3H_6 and 540 °C for C_3H_8 [19]. Here, to investigate the reactivity of CO_2 and NO towards the oxygen vacancies of noble metal loaded ceria, C_3H_6 was used as reductant to pre-treat the noble metal loaded ceria samples. Table 7.2 summarises the result of CO and C_3H_6 pre-treatment over Rh/ceria and Pd/ceria.

The results of CO_2 pulses over C_3H_6 reduced Rh/Ceria are shown in Figure 7.7A and B. CO_2 was completely converted during stage I (pulse number 0-2000, Figure 7.7A), more CO formation than the quantity of pulsed CO_2

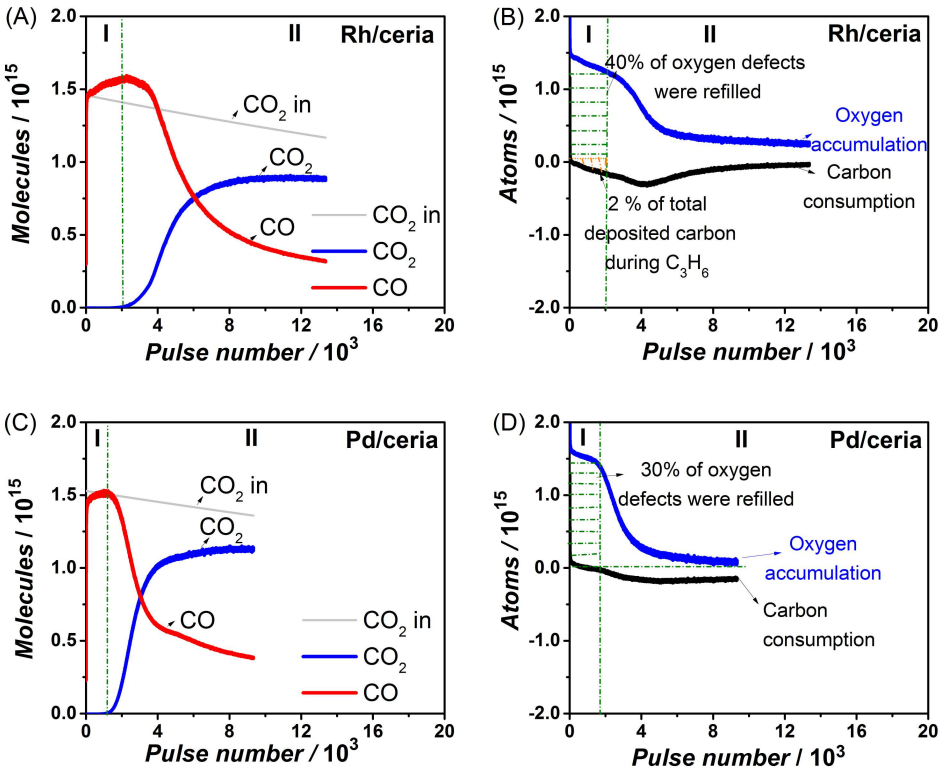

Figure 7.7: CO_2 pulse over at 450 °C C_3H_6 reduced Rh/ceria (A and B) and Pd/ceria (C and D). (A) and (C) gas evolution during the CO_2 pulses, and (B) and (D) oxygen and carbon balances.

Table 7.2: Summary of oxygen removal (oxygen atoms/mg_{cat})and deposited carbon (carbon atoms/mg_{cat}) by C_3H_6 pre-treatment over Rh/ceria and Pd/ceria.

Catalyst	T/°C	Oxygen removal		Deposited carbon
		Oxygen	Ceria reduction layers	
Rh/ceria	450	$8.2 \cdot 10^{17}$	3	$8.7 \cdot 10^{17}$
Pd/ceria	450	$7.3 \cdot 10^{17}$	2.8	$4.4 \cdot 10^{17}$

molecules was observed. CO_2 started to break through from pulse number 2000. According to Equation 7.1 and 7.2, the oxygen balance and carbon balance were plotted, as shown in Figure 7.7B. The oxygen balance showed that the quantity of oxygen accumulation during stage I was around 40% of oxygen vacancies that were created by the C_3H_6 pre-treatment. The oxygen accumulation dropped at the same point as the CO_2 reactivity dropped. The carbon balance indicated that around 2% of deposited carbon was oxidised. Initially the oxygen from the pulsed CO_2 was used for refilling the oxygen vacancies and those re-oxidised ceria vacancies were immediately partially used for the oxidation of the deposited carbon. After this initial stage the CO_2 conversion dropped when still a large amount of deposited carbon on the Rh/ceria sample was present. The re-oxidation rate of the remaining oxygen vacancies was inhibited.

Similar to the experiment over Rh/Ceria, the experiment of CO_2 pulses over C_3H_6 reduced Pd/Ceria at 450 °C was performed (Figure 7.7C and D). The CO_2 conversion was complete during stage I (0-1200 pulse number) and dropped during the stage II. The oxygen balance (Figure 7.7D) indicated that around of 30% of the oxygen vacancies had been refilled by CO_2 and only 1% of the deposited carbon was converted during stage I. In stage II the remaining deposited carbon inhibited the re-oxidation of the oxygen vacancies and subsequently also the conversion of the deposited carbon.

In order to make a comparison between CO_2 and NO reactivity over the noble metal loaded ceria, NO pulse experiments were also performed over Rh/ceria and Pd/ceria with the same pre-treatment as CO_2 pulse experi-

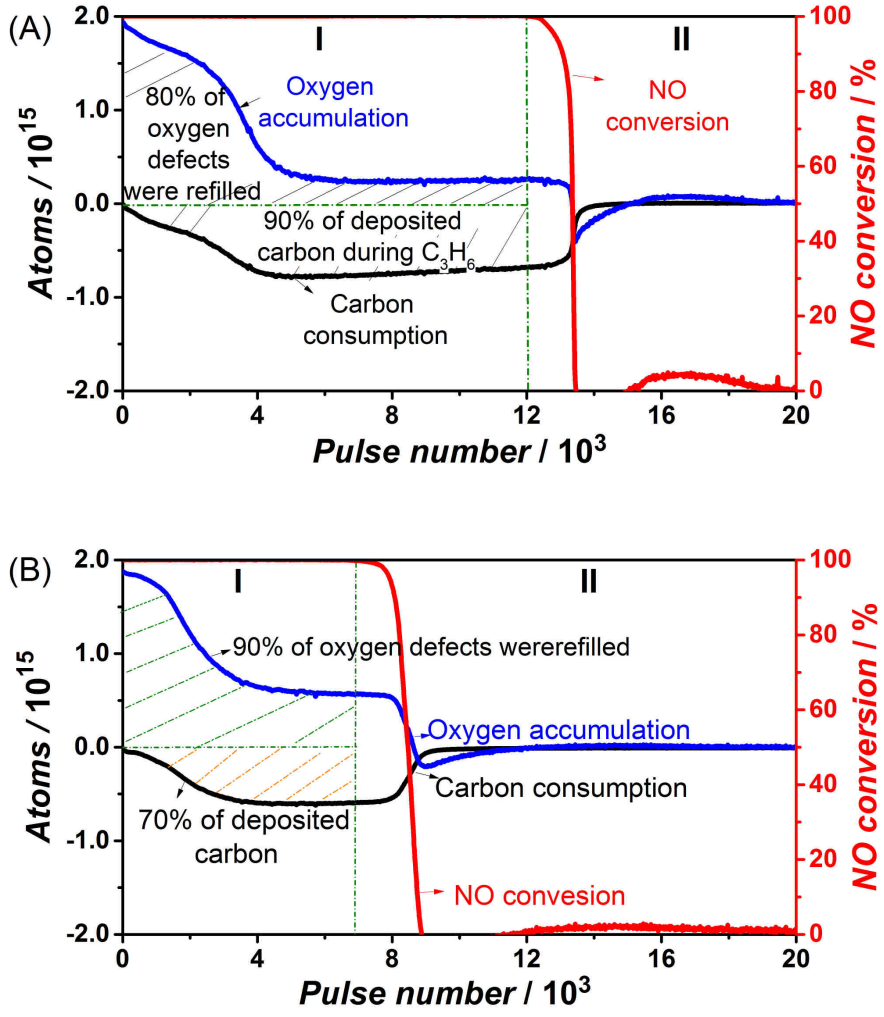

Figure 7.8: CO_2 pulse over at 450 °C C_3H_6 reduced Rh/ceria (A and B) and Pd/ceria (C and D). (A) and (C) gas evolution during the CO_2 pulses, and (B) and (D) oxygen and carbon balances.

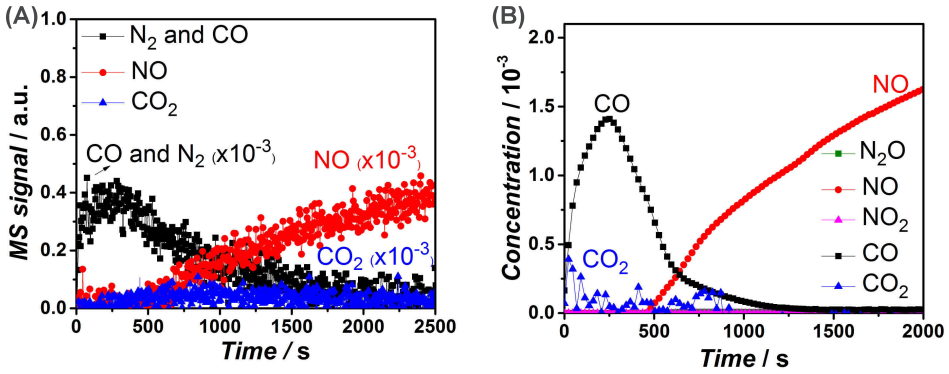

Figure 7.9: Reduction of NO over C_3H_6 pre-reduced Rh/ceria in a flow reactor at 450 oC.

ments in order to obtain the same reduction degree of ceria and the same amount of deposited carbon.

The pulse of NO over a C_3H_6 reduced Rh/Ceria at 450 °C showed that NO showed full conversion at a time interval of 12000 pulses (stage I, Figure 7.8A), followed by NO conversion dropped to zero during stage II. The oxygen balance indicated the refilling of oxygen vacancies in the Rh/ceria sample and during stage I approximately 80% of oxygen vacancies were refilled. At the same time the carbon balance indicated that 90% of the total deposited carbon was oxidised to either CO or CO_2 (Figure 7.8A).

Similarly to Rh/ceria, the NO pulse experiment over the C_3H_6 reduced Pd/Ceria at 450 °C showed that NO showed full conversion at a time interval of 7000 pulses (stage I, Figure 7.8B). During stage I, around 90% of oxygen vacancies were refilled and around 70% of deposited carbon was oxidised.

7.4.2.4. Investigation of CO_2 and NO reactivity over reduced Rh/ceria support by flow reactor

Similar to TAP experiments, C_3H_6 (1.25%) in helium was used as the reductant to pre-treat the Rh/ceria for 2 h in the flow reactor at 450 °C for the experiments of NO reduction in the presence of an excess of CO_2. The pre-treatment of C_3H_6 led to $8.2 \cdot 10^{17}$ carbon atoms/mgcat deposition and around 3 layers of ceria reduction.

Figure 7.9 shows the results of the exposure of 0.2% NO in He over the

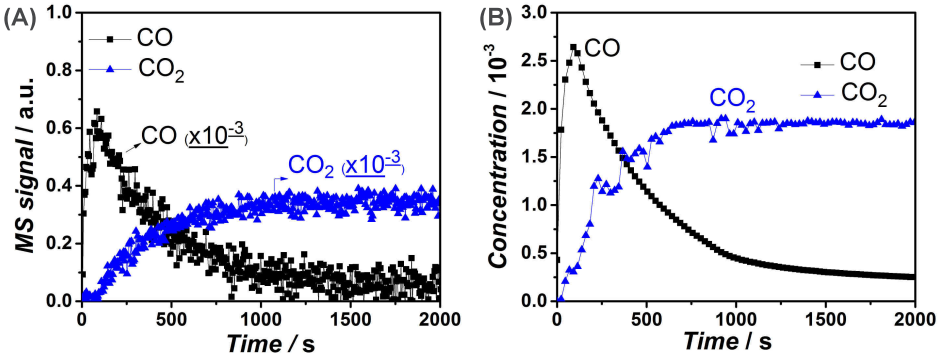

Figure 7.10: Reduction of CO_2 over C_3H_6 pre-reduced Rh/ceria in a flow reactor at 450 oC.

C_3H_6 reduced Rh/ceria at 450 oC with GHSV of 67.000 L/L/h. Figure 7.9A showed the MS response of gasses from the exit of the reactor. *m/e* = 28 was observed, attributed to the formation of N_2 and CO. NO was not observed during the first 450 s, followed by a signal increased gradually in the MS response. A low intensity of *m/e* = 44 was observed, attributed to the formation of CO_2. FT-IR results confirmed the formation of CO and CO_2 and excluded the formation of N_2O and NO_2, as shown in Figure 7.9B. The formation of only N_2 during the NO reduction was also reported by using ^{15}NO, as reported in our previous work [7]. The reduced ceria was fully re-oxidised and the total quantity of CO and CO_2 formed during the NO exposure was calculated to be $8 \cdot 10^{17}$ molecules, which was almost equal to the carbon deposition by C_3H_6 pre-treatment. The result of NO reduction in the flow reactor under atmosphere pressure in Figure 7.9 is consistent with the result from TAP. NO can selectively be reduced to N_2 and deposited carbon can be oxidised during the NO exposure at the applied conditions.

Figure 7.10 shows the results of the exposure of 0.2% CO_2 in He over the C_3H_6 reduced Rh/ceria at 450 °C with GHSV of 67.000 L/L/h. *m/e* = 28 and *m/e* = 44 were observed in the MS response (Figure 7.10A), attributed to CO and CO_2, respectively. CO_2 immediately broke through during the CO_2 feeding.

The FT-IR was also used to further quantify CO and CO_2 from the exit of reactor (Figure 7.10B). The reduced ceria was fully re-oxidised and the amount of carbon consumption was calculated to be $8.2 \cdot 10^{16}$ carbon atoms/mgcat,

which was around 10% of the total deposited carbon. The result of Figure 7.10 confirms that from TAP experiments, *i.e.,* CO_2 is a mild oxidant and the deposited carbon can hardly be oxidised (gasified) during the CO_2 exposure.

For a typical diesel exhaust composition, approximately several hundred ppm NO had to compete with an excess of 5% O_2, 5% CO_2, and 5-10% H_2O in order to meet the future automotive legislation emission standards. Although the results from TAP experiments showed that NO was able to be reduced on oxygen vacancies into N_2, it was still a question whether NO was able to reduce into N_2 in the presence of excess CO_2. Therefore, 0.2% of NO was used to compete with 5% CO_2 over C_3H_6 reduced Rh/ceria at 450 °C. As shown in Figure 7.11A, NO started to breakthrough at the time of t = 410 s *m/e* = 28 was observed, related to the formation of N_2 and CO. *m/e* = 44 immediately appeared during the CO_2 exposure and stabilized around 5%. There was no N_2O and NO_2 formation as confirmed by FT-IR (Figure 7.11B). Both N_2 and CO were observed with no detection of N_2O and NO_2 (detection limit 1 ppm), indicating that NO was completely selectively reduced to N_2 in a CO_2 excess. The total quantity of converted NO and CO_2 was calculated to be $1.1 \cdot 10^{18}$ NO molecules/mgcat and $5 \cdot 10^{17}$ CO_2 molecules/mg_{cat}, respectively. Although the CO_2 concentration was 25 times larger than that of NO, the number of converted NO molecules was around 2.2 times more than that of converted CO_2. More importantly, the reduction of CO_2 mainly occurred during the first 80 s, and CO_2 was hardly reactive during time from 80 s to 410 s, where still full NO conversion was observed. The carbon balance of Figure 7.11B was plotted in Figure 7.11C. The amount of carbon consumption during the first 80 s was calculated to be $8.8 \cdot 10^{16}$, which was around 10% of total deposited carbon. Therefore, the majority of the deposited carbon was consumed by the NO reduction to N_2. The reduction of CO_2 to CO occurred mainly over the reduced sites of ceria, refilling the oxygen vacancies. Once the oxygen vacancies were refilled the CO_2 conversion was almost completely stopped.

7.4.3. CO_2 versus the NO reactivity evaluation

Although CO_2 was able to fill the oxygen vacancies in the CO pre-reduced ceria, the effectiveness of the CO_2 re-oxidation was low since the CO_2 conversion dramatically declined after only a few CO_2 pulses as shown in Figure

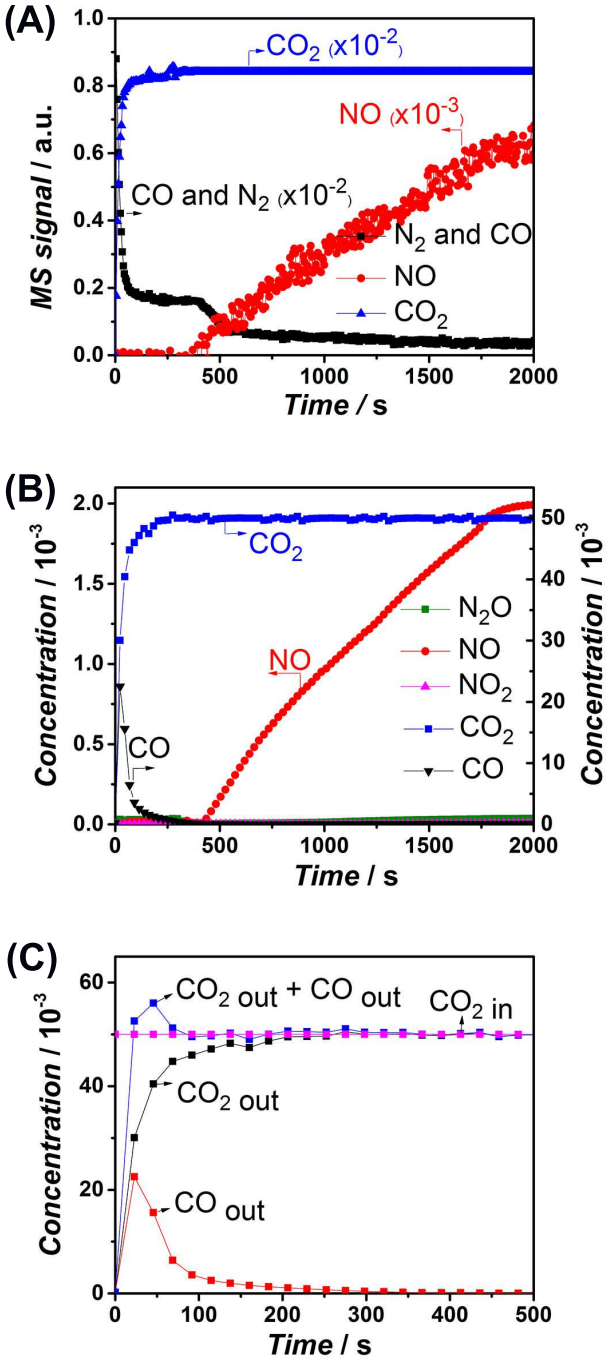

Figure 7.11: Reduction of NO in the presence of excess CO_2 over C_3H_6 pre-reduced Rh/ceria in a flow reactor at 450 °C.

7.3A and B. Up to 2000 CO_2 pulses, only 50% of oxygen vacancies were refilled. Regarding the C_3H_6 pre-reduced ceria, it can be concluded that the CO_2 was mainly used for the re-filling oxygen vacancies. CO_2 pulses will hardly consume any deposited carbon (Figure 7.4A and B). The *operando* Raman experiments under atmosphere pressure (Figure 7.6A and B) also pointed out that CO_2 is a mild oxidant in oxidising the reduced ceria and it hardly oxidised the deposited carbon. Even with noble metal loading, both the TAP multi-pulse experiment (Figure 7.7) and the flow reator (Figure 7.10) at atmospheric pressure suggest that CO_2 still hardly oxidised the deposited carbon. Further, from the perspective of thermodynamics, the gasification of carbon (stable graphite) to CO by CO_2 at this temperature is not favoured [28].

In contrast, NO pulses over C_3H_6 reduced ceria sample showed that NO was completely reduced into N_2 (stage I, Figure 7.4C), where 84% of oxygen vacancies were refilled and 90% of the deposited carbon was oxidised (Figure 7.4D). The TAP multi-pulse experiments suggested that NO was the more efficient oxidant for refilling oxygen vacancies and oxidation of deposited carbon (through the lattice), as compared to CO_2. Again, the flow reactor experiments under atmospheric conditions also confirmed that the NO can be reduced to N_2 and oxidise the deposited carbon.

Moreover, the CO_2 and NO competition experiment over the C_3H_6 pre-reduced Rh/ceria in the flow reactor indicated that NO is the much more powerful oxidant in competing for the oxygen vacancies (Figure 7.11). Around 90% of deposited carbon was consumed by NO. NO is selectively reduced to N_2 in the absence and presence of CO_2.

In the Di-Air system, total reduction capacity, including the oxygen vacancies of ceria and the deposited carbon, determined the quantity of NO molecules conversion in to N_2. And fuel injection is used to create the oxygen defect capacity. The low reactivity of CO_2 towards oxygen vacancies and deposited carbon over both reduce ceria and noble metal ceria implies that the most of the fuel will be used for reduction NO, not converting CO_2.

7.5. Conclusions

- CO_2 is a mild oxidant in the oxidation of oxygen vacancies of ceria due to the existence of a (quasi-) equilibrium between CO, CO_2, Ce^{3+}, and Ce^{4+}. The deposited carbon, generated during C_3H_6 (fuel) pre-treatment, will hardly be converted during CO_2 exposure.

- The loading of noble metals, Rh and Pd on the ceria hardly changed the reactivity of CO_2 in the oxidation of oxygen vacancies and deposited carbon.

- Compared to CO_2, NO was a much stronger oxidant. The deposited carbon can be fully oxidised (gasified) during the NO exposure.
- Traces of NO were able to compete with an excess of CO_2 for oxygen vacancies over Rh/ceria. The presence of CO_2 in the exhaust gas streams of lean burn engines will not significantly affect the NO reduction efficiency.

References

[1] Y. Ikeda, K. Sobue, S. Tsuji, and S. Matsumoto, *Development of NO_x Storage-Reduction Three-way Catalyst for D-4 Engines,* SAE International Journal of Engines **SAE Number 1999-01-1279** (1999).

[2] K. Hirata, N. Masaki, H. Ueno, and H. Akagawa, *Development of Urea-SCR System for Heavy-Duty Commercial Vehicles,* SAE International Journal of Engines **SAE Number 2005-01-1860** (2005).

[3] F. Can, X. Courtois, S. Royer, G. Blanchard, S. Rousseau, and D. Duprez, *An overview of the production and use of ammonia in NSR+SCR coupled system for NO_x reduction from lean exhaust gas,* Catalysis Today **197**, 144 (2012).

[4] Y. Bisaiji, K. Yoshida, M. Inoue, K. Umemoto, and T. Fukuma, *Development of Di-Air - A New Diesel deNO_x System by Adsorbed Intermediate Reductants,* SAE International Journal of Fuels and Lubricants **SAE Number 2011-01-2089** (2011).

[5] M. Inoue, Y. Bisaiji, K. Yoshida, N. Takagi, and T. Fukuma, *DeNO_x Performance and Reaction Mechanism of the Di-Air System,* Topics in Catalysis **56**, 3 (2013).

[6] Y. Wang, J. Posthuma de Boer, F. Kapteijn, and M. Makkee, *Next Generation Automotive DeNO_x Catalysts: Ceria What Else?* ChemCatChem **8**, 102 (2016).

[7] M. Makkee, Y. Wang, R. Oord, D. van der Berg, and B. Weckhuysen, *Oxygen Vacancies in reduced Rh-and Pt-ceria for Highly Selective and Reactive Reduction of NO into N_2 in excess of O_2,* ChemCatChem (2017).

[8] S. Sharma, S. Hilaire, J. Vohs, R. Gorte, and H.-W. Jen, *Evidence for Oxidation of Ceria by CO_2,* Journal of Catalysis **190**, 199 (2000).

[9] W. C. Chueh, C. Falter, M. Abbott, D. Scipio, P. Furler, S. M. Haile, and A. Steinfeld, *High-Flux Solar-Driven Thermochemical Dissociation of CO_2 and H_2O Using Nonstoichiometric Ceria,* Science **330** (2010).

[10] A. Bueno-López, K. Krishna, and M. Makkee, *Oxygen exchange mechanism between isotopic CO_2 and Pt/CeO_2,* Applied Catalysis A: General **342**, 144 (2008).

[11] O. Demoulin, M. Navez, J.-L. Mugabo, and P. Ruiz, *The oxidizing role of CO_2 at mild temperature on ceria-based catalysts,* Applied Catalysis B: Environmental **70**, 284 (2007).

[12] M. C. J. Bradford and M. A. Vannice, *CO_2 Reforming of CH_4,* Catalysis Reviews **41**, 1 (1999).

[13] L. G. Appel, J. G. Eon, and M. Schmal, *The CO_2–CeO_2 interaction and its role in the CeO_2 reactivity,* Catalysis Letters **56**, 199 (1998).

[14] L. Katta, P. Sudarsanam, G. Thrimurthulu, and B. M. Reddy, *Doped nanosized ceria solid solutions for low temperature soot oxidation: zirconium versus lanthanum promoters,* Applied Catalysis B: Environmental **101**, 101 (2010).

[15] V. Perrichon, A. Laachir, S. Abouarnadasse, O. Touret, and G. Blanchard, *Thermal stability of a high surface area ceria under reducing atmosphere,* Applied Catalysis A: General **129**, 69 (1995).

[16] Y. Wang, J. P. de Boer, F. Kapteijn, and M. Makkee, *Fundamental Understanding of the Di-Air System: The Role of Ceria in NO_x Abatement,* Topics in Catalysis **59**, 854 (2016).

[17] H. YAO, *Ceria in automotive exhaust catalysts I. Oxygen storage,* Journal of Catalysis **86**, 254 (1984).

[18] H. Zhu, Z. Qin, W. Shan, W. Shen, and J. Wang, *Pd/CeO_2-TiO_2 catalyst for CO oxidation at low temperature: a TPR study with H_2 and CO as reducing agents,* Journal of Catalysis **225**, 267 (2004).

[19] Y. Wang and M. Makkee, *Fundamental understanding of the Di-Air system (an alternative NO_x abatement technology). I: The difference in reductant pre-treatment of ceria,* Applied Catalysis B: Environmental (2017), 10.1016/j.apcatb.2017.04.054.

[20] T. Staudt, Y. Lykhach, N. Tsud, T. Skála, K. Prince, V. Matolín, and J. Libuda, *Ceria reoxidation by CO_2: A model study,* Journal of Catalysis **275**, 181 (2010).

[21] K. Chen, A. T. Bell, and E. Iglesia, *The Relationship between the Electronic and Redox Properties of Dispersed Metal Oxides and Their Turnover Rates in Oxidative Dehydrogenation Reactions,* Journal of Catalysis **209**, 35 (2002).

[22] C. Nederlof, F. Kapteijn, and M. Makkee, *Catalysed ethylbenzene dehydrogenation in CO_2 or N_2-Carbon deposits as the active phase,* Applied Catalysis A: General **417**, 163 (2012).

[23] G. N. Vayssilov, M. Mihaylov, P. S. Petkov, K. I. Hadjiivanov, and K. M. Neyman, *Reassignment of the vibrational spectra of carbonates, formates, and related surface species on ceria: a combined density functional and infrared spectroscopy investigation,* The Journal of Physical Chemistry C **115**, 23435 (2011).

[24] C. Binet, M. Daturi, and J. C. Lavalley, *IR study of polycrystalline ceria properties in oxidised and reduced states,* Catalysis Today **50**, 207 (1999).

[25] Z. Cheng, B. J. Sherman, and C. S. Lo, *Carbon dioxide activation and dissociation on ceria (110): A density functional theory study,* The Journal of Chemical Physics **138**, 014702 (2013).

[26] R. N. Compton, P. W. Reinhardt, and C. D. Cooper, *Collisional ionization of Na, K, and Cs by CO_2, COS, and CS_2: Molecular electron affinities,* The Journal of Chemical Physics **63**, 3821 (1975).

[27] A. Bueno - López, K. Krishna, M. Makkee, and J. A. Moulijn, *Active oxygen from CeO_2 and its role in catalysed soot oxidation,* Catalysis Letters **99**, 203 (2005).

[28] F. Kapteijn and J. Moulijn, *Kinetics of catalysed and uncatalysed coal gasification,* in *Carbon and Coal Gasification* (Springer, 1986) pp. 291–360.

[29] W. H. Weber, K. C. Hass, and J. R. McBride, *Raman study of CeO_2: Second-order scattering, lattice dynamics, and particle-size effects,* Physical Review B **48**, 178 (1993).

[30] A. C. Ferrari and J. Robertson, *Interpretation of Raman spectra of disordered and amorphous carbon,* Physical Review B **61**, 14095 (2000).

Summary and Outlook

Nitrogen oxides (NO_x, including NO and NO_2) are a group of hazardous, toxic and harmful gasses, which have an adverse effect on both environment and human health, *e.g.,* acid rain, photochemical smog, and affecting the human respiratory system. The NO_x concentration in most of the EU cities exceeds the EU annual limit value (40 µg/m^3). Around 40% of the emitted NO_x is attributed to transport related emissions. In currently applicable Euro 6, the real NO_x emission from a diesel car is on average 400% than the Euro 6 regulation limit allows if measured under more realistic driving conditions. Although NSR and SCR DeNO_x systems have been broadly investigated and commercially applied with the aim to reduce NO_x emissions from lean burn engines, some common problems still exist, *e.g.,* a narrow temperature window and a low gas hourly space velocity (up to 50.000 L/L/h) in order to convert the NO_x selectively into N_2. Due to the in practice high NO_x emission from September 2017 additional legislation will be in force to arrive at a more realistic determination of the highly dynamic NO_x emission by among others the introduction of the real driving emission (RDE) test in the certification procedure. The Di-Air (Diesel NO_x after treatment by Adsorbed Intermediate Reductants) system was developed by Toyota (2011-2012) and is still under development. This Di-Air system showed promise by yielding a high NO_x conversion, especially at high temperature (up to 600 °C) and high gas hourly space velocity (up to 125.000 L/L/h). This system opts to meet the future stringent NO_x reduction requirements under RDE test conditions (Chapter 1).

However, little is known about this system. The Di-Air system operates with high frequent injection of fuel pulses, this means that the catalyst operates under transient conditions. This is an open opportunity for an investigation by a transient research technique, like Temporal Analysis of Products (TAP). In Chapter 2 this nano-pulse reactor system is described and the qualities of this home-built system are demonstrated. Especially important, with regard to this thesis, are the quantitative capabilities of this machine. Depending on the complexity of the mass fragmentation of the molecules under investigation, mass balances typically close from 85% to 100%.

The principle and fundamental understanding of the Di-Air system is a prerequisite for the optimisation and application of this system. Moreover, the first step towards resolving the reaction mechanism is to understand the

role of each catalyst component in their claimed complex catalyst formulation (Rh, Pt, K, Ba, Ce on an alumina support) in the reaction network for NO reduction into nitrogen. Therefore, the research leading up to this thesis started by investigating the specific role each Di-Air catalyst component plays. The role of the main Di-Air catalyst components is summarised as follows:

- Al_2O_3
  C_3H_6, C_3H_8, CO, CO_2, H_2, and NO molecules were found to have a very limited interaction with the Al_2O_3 surface, *i.e.,* adsorption and desorption. No reactions were found to take place in the temperature range between RT - 600 °C (not in this thesis).

- Ceria
  Ceria was found to be capable of both fuel oxidation and NO conversion to either N_2 or NO_2.

  Oxidised ceria showed high activity in the oxidation of CO, H_2, and hydrocarbons in the absence of gas-phase oxygen. The obtainable ceria reduction degree was around 3 times higher when hydrocarbons (C_3H_6 and C_3H_8) were used as a reductant at 580 °C, as compared to H_2 and CO. Hydrocarbons led to the formation of carbon deposits on the reduced ceria surface. The higher reduction degree of ceria obtained by C_3H_6 and C_3H_8 above 500 °C can explain Toyota's observation that fuel injection led to higher NO_x conversion and efficiency than that of CO and H_2 at high temperature (Chapter 3).

  Oxidised ceria showed hardly any activity in the reduction of NO to N_2. H_2 or CO or hydrocarbon pre-reduced ceria were found to be very active in the selective reduction of NO to N_2. Oxygen anion vacancies in ceria are responsible for the decomposition of NO to N_2, thereby re-oxidising these defect centres. The delayed oxidation of carbon deposits by oxygen species originating from lattice oxygen will in practice maintain a reduced surface state during lean fuel conditions. These carbon deposits can, therefore, be seen as a stored reductant with a delayed function (Chapter 4).

- Noble metal (Rh, Pt, and Pd)

  Noble metals on ceria enhance the rate and degree of ceria reduction by

hydrocarbon based fuels. Rh is the most active among the investigated noble metals. With regard to NO reduction, the noble metals accelerate the selective reduction of NO into N_2, since less N accumulation on the catalyst was observed in comparison with NO reduction over bare ceria. The formation of both N_2O and NO_2 was excluded over reduced noble metal/ceria (Chapter 5).

- Alkali and alkaline earth metals (K and Ba):

  The addition of potassium to Rh/ceria resulted in a decrease in NO decomposition activity over time, *i.e.,* decrease with an increase in the number of oxidation-reduction cycles. Potassium can adsorb NO_x, but it requires a high temperature to desorb (700 °C), which in turn (NO_x adsorption) inhibits the reduction of the ceria support by the fuel. Therefore, the addition of potassium and/or barium onto ceria can have a short term benefit for the first few cycles. However, on the long term, the addition of potassium and barium will have adverse effects (not in this thesis).

Other oxidants, *e.g.,* O_2, CO_2, and H_2O, will also react with reduced ceria. The competition for oxygen vacancies between NO and other oxidants may be of critical importance. Therefore, the activity and selectivity of NO reduction in the presence of an excess of O_2 and CO_2 was investigated. It was found that small (trace) amounts of NO can decisively compete for oxygen vacancies, leading to the formation of N_2, with excess O_2 over both reduced ceria and noble metal loaded reduced ceria. Oxygen vacancies in ceria (directly) and deposited carbon (indirectly) are responsible for the high activity and selectivity over a broad temperature window (250 - 600 °C) and up to high GHSV (up to 170.000 L/L/h). No N_2O was observed, and NO_2 was only observed when NO and O_2 broke through when ceria is fully re-oxidised (Chapter 6). CO_2 was found to be a mild oxidant, able to oxidise oxygen vacancies, but was found to be largely incapable to oxidise the deposited carbon formed upon C_3H_6 pre-treatment in order to reduce ceria. In the competition for oxygen defect sites, the high NO decomposition activity and selectivity observed in (an excess) CO_2 indicated a strong preference for NO over CO_2. The presence of excess CO_2 hardly affected NO reduction into N_2 (Chapter 7).

The research in this thesis demonstrates that the Di-Air system is a promis-

ing system for highly efficient catalytic conversion of NO into N_2. Oxygen vacancies of ceria play a key role in the selective conversion of NO into N_2. Ceria is a promising base/starting material for an optimised catalyst formulation for the Di-Air system. Noble metals (especially Rh) and perhaps other metals are indispensable in order to lower fuel oxidation temperatures. NO_x storage components such as potassium and barium are not contributing positively to the performance of a Di-Air catalyst.

In this thesis, C_3H_6 or C_3H_8 were used to mimic fuel. Instead of high-frequency fuel injection upstream of the catalyst bed, a continuous flow of C_3H_6 or C_3H_8 is used to simulate fuel injection. Therefore, more research is needed with regard to an optimal fuel injection strategy.

Ceria is the core component in the Di-Air catalyst composition. The redox property of ceria ($Ce^{4+} \leftrightarrow Ce^{3+}$) is essential for NO_x reduction in the Di-Air system. However, the long-term usage of the catalyst in automotive and truck applications (at least 5 years in Europe and up to 12 years in for example the USA) requires a highly stable structure. Doping of ceria by Zr in the form of a Zr-Ce solid solution is commonly reported to stabilise the ceria structure. However, the redox behaviour of ceria is related to both the composition and the structure of the solid solution. Trovarelli *et al.* reported that the content of doped ZrO_2 should not exceed 50% in the Zr-Ce solid solution [1]. The inclusion of yttrium (Y), lanthanum (La) or gadolinium (Ga) ions in the $Ce_{1-x}Zr_xO_2$ lattice can enhance oxygen anion diffusion, thereby decreasing its reduction temperature. The induced decrease in reduction temperature by these tri-valent dopants might enhance the reactivity of ceria towards hydrocarbons, especially at lower temperatures, thereby alleviating the need for noble metals. Therefore, a test series in which different dopants in various Zr-Ce solutions are screened is recommended for the final application of the Di-Air system. Other reducible rare earth oxide-based solid solutions, *e.g.,* PrO_2 and TbO_2, might also be considered as (research) alternatives for ceria in the Di-Air system. Although the abundance of Pr and Tb, 1.3 and 0.1 ppm, respectively, versus 8.9 ppm for Ce, does not contribute to the use of abundant elements in catalysis. The study of these materials might, however, yield a better understanding of the relation between the reducibility of the material and its catalytic properties. PrO_2-based solid solutions, *e.g.,* Zr-Pr or Y-Pr, have shown a better redox

performance as compared to CeO_2-based solid solutions [2], which may be beneficial for fuel activation and subsequent creation of oxygen vacancies at a lower temperature.

In this thesis, a simple incipient wetness method was used to load 0.5 wt.% noble metal (Rh) on ceria in order to demonstrate the role of Rh in the Di-Air system. The loading of noble metal onto ceria significantly decreased the hydrocarbon activation temperature (Chapter 5). The Rh loading and the dispersion and the (hydro-thermal) stability on ceria should be optimised before final application in the Di-Air system.

High temperature has an adverse effect on noble metal stability when supported on oxides. High temperature may cause sintering of the noble metal particles, resulting in loss of specific surface area and hence a loss in activity. In automotive exhaust gas abatement, the vapour-phase transport of PtO_2 to the downstream SCR catalyst is regarded as a leading cause of Diesel Oxidation Catalyst (DOC) catalyst degradation [3]. Surface oxygen vacancies on ceria have been proposed to act as a trap for noble metals and, therefore, protect against sintering through strong chemical bond formation [4, 5]. This work may also be a good basis/starting point to develop highly dispersed and stable Rh/ceria catalysts.

Going back to the automotive $DeNO_x$ system. In Europe, 40% of the NO_x emissions find their origin in transportation. Although the application of electrical cars in cities can reduce NO_x pollution in cities to some extent, the overall pollution produced by the electrical cars, *e.g.,* the production of electricity, the pollution by making the battery and the disposal of the battery, etc., is more than that of fuel cars. More importantly, the higher cost associated with electric cars and the limited progress in battery technology and the uncertainty in live time, thereof (at least 12 -15 years should be required) impedes their popularity amongst potential users. Urea (ammonia)-SCR technology has proven its potential already in numerous passenger cars, which are compliant with the current Euro 6 legislation. However, refill costs and the necessity for refills within a service interval is a drawback. More importantly, 'NH_3' slip will remain a problem, since it is a challenge to obtain the right amount of urea at the right time in the extremely dynamic transient. The NO_x concentration in the exhaust gas depends on the current dynamic driving behaviour. In addition, the trend of downsizing engines will also

challenge the requirements on the SCR technology, by increasing the gas hourly space velocity and the temperature. With regard to the NSR system, the large issue is the narrow temperature window, the low allowable gas hourly space velocity, and the formation of undesired products, NO_2 and N_2O. The use of K and Ba components as NO_x adsorbents may give rise to problems when they cannot be regenerated very easily (high temperature and strong reducing environment) in the driving behaviour of the vehicle. Furthermore, K and Ba in the catalyst formulation have the tendency to form N_2O (nitrous oxide) under defined driving conditions. N_2O is a very strong greenhouse gas (600 times of that of CO_2) and contributes to the depletion of the ozone layer.

This thesis demonstrates that the Di-Air system is a promising system to meet more stringent NO_x abatement requirements under realistic test conditions (RDE test). The deposited carbon from the fuel injection acts as a reductant buffer, which makes this $DeNO_x$ system more dynamic as compared to the NSR and SCR system. However, the implementation of this system in the current market requires the installation of the fuel injection valve downstream of the engine and upstream of the catalyst/monolith, This redesign of the engine system, catalyst formulation and system optimisation (motor management system, coupled with a guaranteed performance over the life time of the car, *etc.*) are an enormous challenge. More work is really needed for a successful application of the Di-Air system and we are just at the beginning.

Samenvatting en Vooruitzicht

Stikstofoxiden (NO_x, voornamelijk alleen NO en NO_2) zijn een verzameling schadelijke en toxische gassen, die een negatieve invloed hebben op zowel het milieu als de gezondheid van de mens, zoals zure regen, smog, en in het bijzonder op het ademhalingssysteem. De NO_x concentratie in de meeste EU steden overschrijdt de jaarlijkse EU limiet (40 µg/m^3). Ongeveer 40% van de uitgestoten hoeveelheid NO_x is aan de transportsector gerelateerd. In de praktijk zijn de NO_x emissies van diesels ruim 400% hoger dan de Euro 6 norm. Alhoewel de NSR en SCR DeNO_x systemen uitgebreid zijn onderzocht en commercieel worden toegepast om de NO_x uitstoot te reduceren, blijven een aantal wetenschappelijke uitdagingen bestaan, zoals het beperkte temperatuurbereik van 150 tot 350 °C en een beperkte contactsnelheid (GHSV (gas hourly space velocity) tot 50,000 L/L/h) om NO_x selectief in N_2 te kunnen omzetten. Door de in praktijk hoge NO_x emissies, is vanaf september 2017 additionele wetgeving van kracht om de zeer dynamische NOx emissie te verminderen door onder andere de introductie van praktijk e rijemissie ('real driving emission' (RDE)) in de certificeringsprocedure op te nemen. In 2011-2012 is het Toyota Di-Air ('Diesel NO_x aftertreatment by Adsorbed Intermediate Reductants') systeem in ontwikkeling genomen in de ontwikkeling de Dit Di-Air systeem oogt veelbelovend, daar het hoge NOx omzetting bij hoge temperatuur (tot 600 °C) en zeer korte contacttijden (GHSV tot 125,000 L/L/h). Dit systeem opteert om aan de huidige en toekomstige strenge NO_x reductievereisten onder RDE test condities te voldoen (Hoofdstuk 1).

Over dit systeem is echter weinig bekend. De werking van het Di-Air is gebaseerd op frequente brandstofinjectiepulsen in de uitlaat vòòr het nabehandelingssysteem voor schonere uitlaatgassen. Dit houdt in dat de katalysator in het nabehandelingssysteem onder wisselende omstandigheden opereert. Dit is een open uitnodiging voor een onderzoek met een transiënte onderzoekstechniek als de 'Temporal Analysis of Products' (TAP). In Hoofdstuk 2 wordt dit nano-puls reactor systeem beschreven en worden de kwaliteiten van dit in eigen huis gebouwd systeem gedemonstreerd, waarbij voor mijn onderzoek de kwantitatieve prestaties van dit apparaat essentieel zijn. Afhankelijk van de analyse complexiteit door de fragmentatie van de onderzochte moleculen in de massaspectrometer sluiten alle massabalansen in het algemeen tussen de 85% en 100%.

Fundamentele kennis van dit Di-Air systeem is de voorwaarde voor de optimalisatie en toepassing van deze technologie. De eerste stap naar het ontrafelen van het reactiemechanisme is het begrijpen van de rol die elke katalysatorcomponent in de door Toyota geclaimde complexe katalysatorcompositie (Rh, Pt, K, Ba, Ce gedragen op een alumina support) in het NO-reductie reactienetwerk. De rol van de belangrijkste Di-Air katalysatorcomponenten kan als volgt worden samengevat.

- Al_2O_3
  C_3H_6, C_3H_8, CO, CO_2, H_2, en NO moleculen vertoonden een zeer bescheiden interactie met het Al_2O_3 oppervlak, *i.e.,* adsorptie en desorptie. Er konden geen reacties tussen deze moleculen en het alumina worden vastgesteld in het temperatuursinterval van kamertemperatuur tot 600 °C (niet in dit proefschrift).

- Ceriumoxide

  Ceriumoxide is in staat om zowel brandstof (koolwaterstoffen) te oxideren tot H_2O en CO_2, als NO om te zetten naar N_2 of NO_2.

  Geoxideerd ceriumoxide vertoonde een hoge activiteit in de oxidatie van CO, H_2, en koolwaterstoffen in de afwezigheid van zuurstof. De reductiegraad van ceriumoxide is ongeveer 3 maal hoger, als koolwaterstoffen (C_3H_6 en C_3H_8) werden gebruikt als reductor in plaats van H_2 en CO. Het gebruik van koolwaterstoffen leidt tevens tot de vorming van koolstofafzettingen op het gereduceerde ceriumoxide-oppervlak. De hogere reductiegraad van ceriumoxide, verkregen door het gebruik van C_3H_6 en C_3H_8 boven 500 °C, kan Toyota's waarneming verklaren, dat (koolwaterstof) brandstofinjecties tot een hogere NO_x conversie en efficiency leidde in vergelijking tot CO en H_2 (Hoofdstuk 3).

  Geoxideerd ceriumoxide vertoonde geen enkele activiteit in de reductie van NO naar N_2. Voor H_2, CO of koolwaterstof voor-gereduceerd ceriumoxide blijkt dat deze zeer actief was in de reductie van NO naar N_2. Zuurstofanionroostergaten in ceriumoxide zijn verantwoordelijk voor de omzetting van NO naar N_2, waarbij deze roostergaten worden opgevuld. De oxidatie van de koolstofafzettingen door het zuurstof uit het ceriumoxide rooster, zal er voor zorgen dat het ceriumoxide gereduceerd zal blijven. Deze koolstofafzettingen kunnen dan als een opgeslagen reductor

met een uitgestelde werking beschouwd worden (Hoofdstuk 4).

- Edelmetaal (Rh, Pt en Pd)

  Edelmetalen op het ceriumoxide-oppervlak verhogen de snelheid van de reductie en de reductiegraad van het ceriumoxide als koolwaterstof voor de reductie wordt gebruikt. Rh is het meest actief in de groep van de onderzochte edelmetalen. Wat betreft de NO-reductie, versnellen de edelmetalen de selectieve reductie van NO naar N_2 en vindt er aanzienlijk minder N ophoping op de katalysator plaats in vergelijking met de NO reductie over puur ceriumoxide. De vorming van zowel N_2O als NO_2 worden over gereduceerd edelmetaal/ceriumoxide uitgesloten (Hoofdstuk 5).

- Alkali- en aardalkali-metalen (K en Ba):

  De toevoeging van kalium aan Rh/ceriumoxide resulteerde in een verlaging van de NO omzetting in de tijd. Kalium kan NO_x adsorberen, maar een hoge temperatuur van boven de 700 °C is noodzakelijk voor de desorptie ervan. Dit heeft tot gevolg dat de reductie van het op het kalium geadsorbeerde NO_x beperkt wordt. Daardoor heeft de toevoeging van kalium en/of barium alleen in de eerste cyclus effect. De toevoeging van kalium en barium aan de rhodium-ceriumoxide katalysator resulteert in een gedeeltelijke omzetting van NO naar N_2O (lachgas) over de gereduceerde katalysator. Lachgas heeft een zeer sterk broeikaseffect (300 x sterker dan CO_2 (niet beschreven in dit proefschrift)).

Andere oxidatiemiddelen, zoals O_2, CO_2, en H_2O, zullen eveneens met gereduceerd ceriumoxide reageren. De competitie om zuurstofroostergaten tussen NO en andere oxidatiemiddelen kan cruciaal zijn. Om deze reden werd de activiteit en selectiviteit van NO-reductie onderzocht in een overmaat O_2 en CO_2. Hieruit bleek dat zeer kleine (spoor) hoeveelheden NO in een overmaat zuurstof en CO_2 de competitie om deze zuurstofroostergaten aan kan onder vorming van N_2 Dit geldt zowel voor gereduceerd ceriumoxide als voor met edelmetaal beladen gereduceerd ceriumoxide. Zuurstofroostergaten in ceriumoxide (direct) en de koolstofafzetting (indirect) zijn verantwoordelijk voor de hoge activiteit en selectiviteit over een zeer breed temperatuurinterval (250 - 600 °C) en tot hoge gasdebieten (GHSV tot 170.000 L/L/h). N_2O werd niet waargenomen en NO_2 werd alleen waargenomen wanneer NO en O_2 doorbraken en het ceriumoxide volledig was geoxideerd. (Hoofdstuk 6).

CO_2 bleek een mildere oxidatiemiddel te zijn. Het was in staat zuurstofroostergaten te oxideren, maar was niet in staat om de koolstofafzettingen te oxideren. De aanwezigheid van een overmaat CO_2 had nauwelijks invloed op de reductie van NO naar N_2 (Hoofdstuk 7).

Het onderzoek in dit proefschrift laat duidelijk zien dat het Di-Air systeem een zeer veelbelovend is voor de zeer efficiënte katalytische omzetting van NO naar N_2 in oxiderend milieu. Zuurstofroostergaten in het ceriumoxide spelen een sleutelrol in de selectieve omzetting van NO naar N_2. Ceriumoxide vormt een veelbelovende basis voor een geoptimaliseerde katalysator voor het Di-Air systeem. Edelmetalen (met name Rh), en wellicht andere metalen, zijn onmisbaar om een lager en dus breder temperatuurinterval te realiseren voor de NO reductie. Toevoeging van NO_x opslagcomponenten, zoals kalium en barium, leveren een negatieve bijdrage aan de prestatie van de Di-Air katalysator.

In dit proefschrift worden C_3H_6 of C_3H_8 gebruikt om de dieselbrandstof na te bootsen. In plaats van hoog frequente brandstofinjectie stroomopwaarts van de katalysator, wordt er een continue C_3H_6 of C_3H_8 stroom toegepast om de brandstofinjectie te simuleren. Door deze aanpak is verder onderzoek nodig om een optimale brandstofinjectiestrategie te kunnen vaststellen.

Ceriumoxide is het hoofdbestanddeel van de Di-Air katalysator. De redox eigenschap van ceriumoxide ($Ce^{4+} \leftrightarrow Ce^{4+}$) is essentieel voor de NO_x reductie in het Di-Air systeem. De lange wettelijke levensduur van de katalysator in transporttoepassingen (ten minste 5 jaar in Europa en tot 12 jaar in bijvoorbeeld de VS) vereist een zeer stabiele structuur. Het doteren van ceriumoxide met Zr in de vorm van een Zr-Ce mengkristal ter stabilisatie van de ceriumoxidestructuur wordt algemeen gerapporteerd. Echter, het redoxgedrag van ceriumoxide is gerelateerd aan zowel de samenstelling als de structuur van het mengkristal. Trovarelli *et al.,* rapporteerde dat de ZrO_2 hoeveelheid niet de 50% mag overstijgen in het Zr-Ce mengkristal [1]. De inclusie van yttrium (Y), lanthaan (La) of gadolinium (Ga) ionen in het $Ce_{1-x}Zr_xO_2$ kristalrooster kan de zuurstofaniondiffusie verhogen, waardoor de reductietemperatuur van het mengkristal afneemt. De geïnduceerde afname van de reductietemperatuur door deze trivalente doteringselementen kan de reactiviteit van ceriumoxide naar koolwaterstoffen verhogen met name bij lagere temperatuur, waardoor mogelijk de noodzaak voor het ge-

bruik van edelmetalen verdwijnt. Om deze reden wordt een vervolgonderzoek, waarin verschillende doteringselementen in verscheidene Zr-Ce mengkristallen worden onderzocht, aanbevolen voorafgaand aan de daadwerkelijke toepassing van het Di-Air systeem. Andere op reduceerbare zeldzame aardmetalen gebaseerde mengkristallen, *e.g.,* PrO_2 and TbO_2, kunnen als (onderzoeks)alternatieven voor ceriumoxide in het Di-Air systeem worden overwogen, alhoewel de beschikbaarheid van Pr en Tb, 1.3 en 0.1 ppm, respectievelijk tegen de 8.9 ppm voor Ce, niet bijdraagt aan de doelstelling om alleen goed beschikbare elementen voor katalyse te gebruiken. Een studie naar deze materialen zou echter wel tot een beter inzicht in de relatie tussen de reduceerbaarheid van het materiaal en de katalytische eigenschappen kunnen leiden. Op PrO_2 gebaseerde mengkristallen, *e.g.,* Zr-Pr of Y-Pr, laten betere redoxprestaties in vergelijking met op CeO_2 gebaseerde mengkristallen zien [2], wat een positieve uitwerking kan hebben op de brandstofreactiviteit en de daarop volgende vorming van zuurstofroostergaten bij een lagere temperatuur.

In dit proefschrift wordt een simpele porievolume impregnatie methode gebruikt om 0.5 wt.% edelmetaal (Rh) op ceriumoxide aan te brengen om het effect van Rh in het Di-Air systeem te demonstreren. Het aanbrengen van het edelmetaal op ceriumoxide resulteerde in een significante afname van de koolwaterstofactivatietemperatuur (Hoofdstuk 5). De hoeveelheid Rh, de dispersie en (hydro-thermische) stabiliteit op ceriumoxide zouden moeten worden geoptimaliseerd voor de daadwerkelijke applicatie van het Di-Air systeem.

Extreem hoge temperaturen hebben een negatieve impact op de stabiliteit van edelmetalen gedragen op oxiden. Het kan het sinteren (samenklonteren) van de edelmetaaldeeltjes veroorzaken, wat resulteert in een verlies van specifiek oppervlak en daardoor een verlies aan activiteit. In het reinigen van dieseluitlaatgas wordt het transport door de gasfase van het vluchtige PtO_2 naar de stroomafwaarts gelegen SCR katalysator beschouwd als een hoofdoorzaak voor de degradatie van de oxidatiekatalysator ('Diesel Oxidation Catalyst' (DOC)) [3]. Zuurstofroostergaten aan het oppervlak van ceriumoxide zijn voorgesteld als zijnde gaten voor edelmetalen en zouden om deze reden bescherming bieden tegen het sinteren van edelmetalen door de vorming van een sterke chemische binding [4, 5]. Voor een vervolgstudie

kan dit uitgangspunt een goed startpunt zijn voor het ontwikkelen van zeer disperse en stabiele Rh/ceriumoxide katalysatoren.

Terugkerend naar het DeNO$_x$ systeem voor de transportsector. In Europa is deze verantwoordelijk voor 40% van de NO$_x$ uitstoot. Alhoewel de toepassing van elektrische auto's in steden deNO$_x$ vervuiling in die steden tot op zekere hoogte kan reduceren, dan kan de algehele vervuiling veroorzaakt door deze elektrische auto's, *e.g.,* de productie van elektriciteit, de vervuiling veroorzaakt tijdens de productie van de batterijen en de verwerking van afgedankte baterijen, *etc.,* groter zijn dan de vervuiling veroorzaakt door auto's rijdend op fossiele brandstoffen. Nog belangrijker zijn de hogere kosten gerelateerd aan elektrische auto's, de bescheiden vooruitgang die is geboekt op het gebied van de batterijtechnologie en de onzekerheid omtrent de levensduur daarvan (ten minste 12-15 jaar is vereist) welke de populariteit onder potentiële gebruikers dempen. Ureum (ammonia-) SCR technologie heeft haar potentieel inmiddels bewezen in talloze auto's en vrachtwagen l, die voldoen aan de huidige Euro 6 norm. Echter, de bijvulkosten van ureum en de noodzaak van het bijvullen tussen de onderhoudsbeurten zijn een nadeel. Tevens is het van belang dat het doorslippen van 'NH_3' een serieus emissieprobleem blijft en het is een uitdaging om precies de juiste hoeveelheid ureum op precies het juiste moment tijdens het extreem dynamische rijgedrag te doseren. De NO$_x$ concentratie in de uitlaat is sterk afhankelijk van het dynamische rijgedrag van de autonome bestuurder. Bovendien zal de huidige motor-verkleiningstrend (meer vermogen uit een kleiner motorvolume) het nodige vergen van de SCR technologie door de toename van een veel hogere gasdoorvoersnelheid en temperatuur van het uitlaatsysteem. Ten aanzien van het NSR (NO$_x$ Storage and Reduction) systeem zijn de problemen het krappe temperatuurwerkingsinterval, de relatief lage gasdoorvoersnelheid en de vorming van ongewenste bijproducten zoals NO_2 en N_2O. Het gebruik van K en Ba componenten als NO$_x$ adsorbentia kan tot problemen in het rijgedrag op de weg leiden, indien deze niet makkelijk zijn te regenereren (hoge temperatuur en een sterk reducerende atmosfeer). Daar komt nog bij dat deze K en Ba katalysatorcomponenten onder bepaalde rijcondities de neiging hebben om N_2O (lachgas) te vormen. N_2O is een sterk broeikasgas (300 keer sterker dan CO_2) en draagt bij aan de aantasting van de ozonlaag.

Dit proefschrift laat zien dat het Di-Air systeem een veelbelovende kandidaat is om aan de verscherpte NO_x emissievereisten onder realistische testcondities (RDE test) te voldoen. Het door de brandstofinjecties op de katalysator afgezette koolstof functioneert als een reductorbuffer, waardoor dit $DeNO_x$ systeem veel dynamischer is in vergelijking met de NSR en SCR systemen. Echter, de implementatie van dit systeem in de huidige markt vereist de installatie van een brandstofinjectieklep na de motor en vòòr de (Di-Air) katalysator. Het vereiste herontwerp van het motor en uitlaatsysteem, de optimalisatie van de katalysatorsamenstelling en de gehele systeemoptimalisatie (motor management systeem gekoppeld aan de gegarandeerde prestatie over de levensduur van de auto, *etc.*) zijn enorme uitdagingen. Meer onderzoek is vereist voordat een succesvolle toepassing van het Di-Air systeem kan worden gerealiseerd.

We staan nog maar aan het begin.

Bibliografie

[1] A. Trovarelli, F. Zamar, J. Llorca, C. De Leitenburg, G. Dolcetti, and J. T. Kiss, *Nanophase fluorite-structured CeO_2-ZrO_2 catalysts prepared by high-energy mechanical milling,* Journal of Catalysis **169**, 490 (1997).

[2] C. Narula, L. Haack, W. Chun, H.-W. Jen, and G. Graham, *Single-Phase PrO_y-ZrO_2 Materials and Their Oxygen Storage Capacity: A Comparison with Single-Phase CeO_2-ZrO_2, PrO_y-CeO_2, and Pr_y-CeO_2-ZrO_2 Materials,* The Journal of Physical Chemistry B **103**, 3634 (1999).

[3] G. Cavataio, H.-W. Jen, J. W. Girard, D. Dobson, J. R. Warner, and C. K. Lambert, *Impact and prevention of ultra-low contamination of platinum group metals on SCR catalysts due to DOC design,* SAE International Journal of Fuels and Lubricants **2**, 204 (2009).

[4] N. Ta, J. Liu, S. Chenna, P. A. Crozier, Y. Li, A. Chen, and W. Shen, *Stabilized gold nanoparticles on ceria nanorods by strong interfacial anchoring,* Journal of the American Chemical Society **134**, 20585 (2012).

[5] J. A. Farmer and C. T. Campbell, *Ceria maintains smaller metal catalyst particles by strong metal-support bonding,* Science **329**, 933 (2010).

A

Fundamental understanding of the Di-Air system I: The difference in reductant pre-treatment of ceria

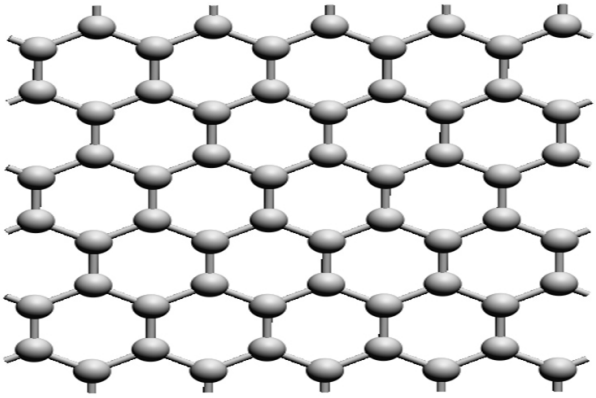

Figuur A.1: An atomic-scale hexagonal lattice of graphene structure.

Tabel A.1: The parameters of hexagonal lattice of graphene and the ceria catalyst.

Items	Parameters
C-C length	0.142 nm
Hexagonal unit area	0.524 nm^2
Carbon atoms in one hexagonal unit	2
BET area of ceria	65 m^2/g
Sample weight	21.2 mg
Sample BET area	1.378 m^2

The deposited carbon during the C_3H_6 or C_3H_8 pre-treatment is assumed as graphene structure, as showed as in Figure A1. The parameters of hexagonal lattice of graphene and the ceria catalyst is shown in Table A.1.

In case of $2 \cdot 10^{18}$ carbon atoms deposited, the number of hexagonal unit (N) is calculated to be $1 \cdot 10^{18}$ using Equation A.1:

$$N = \frac{The number of deposited carbon atoms}{The number of carbon atoms in one hexagonal unit} \quad \text{(A.1)}$$

The total area of deposited carbon S is calculated to be 0.0524 m^2 using the EquationA.2:

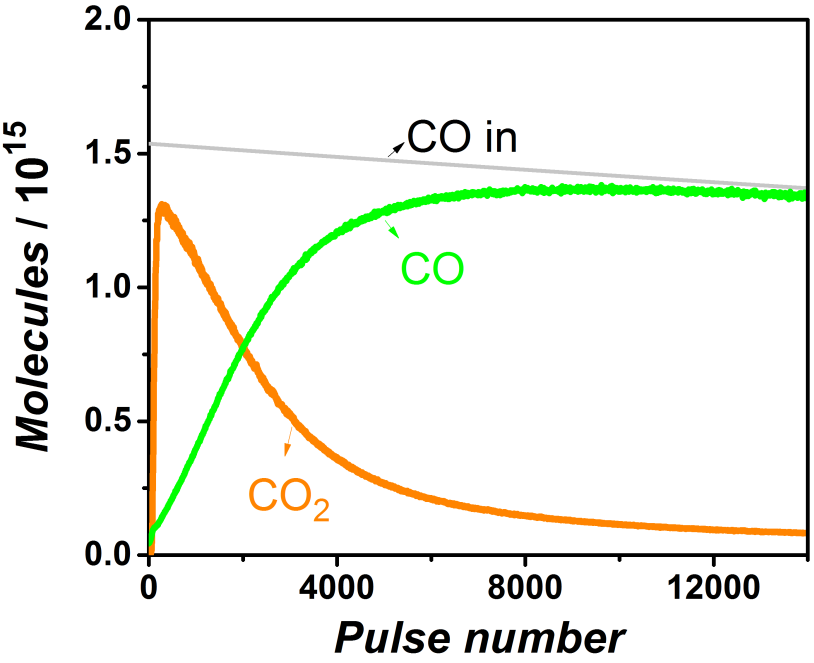

Figuur A.2: CO multi-pulse experiment over a pre-oxidised ceria at 580 °C.

$$S = N \times Hexagonalunitarea \tag{A.2}$$

The surface coverage of deposited carbon (θ) is calculated to be 4% using Equation A.3:

$$\theta = \frac{S}{SampleBETarea} \tag{A.3}$$

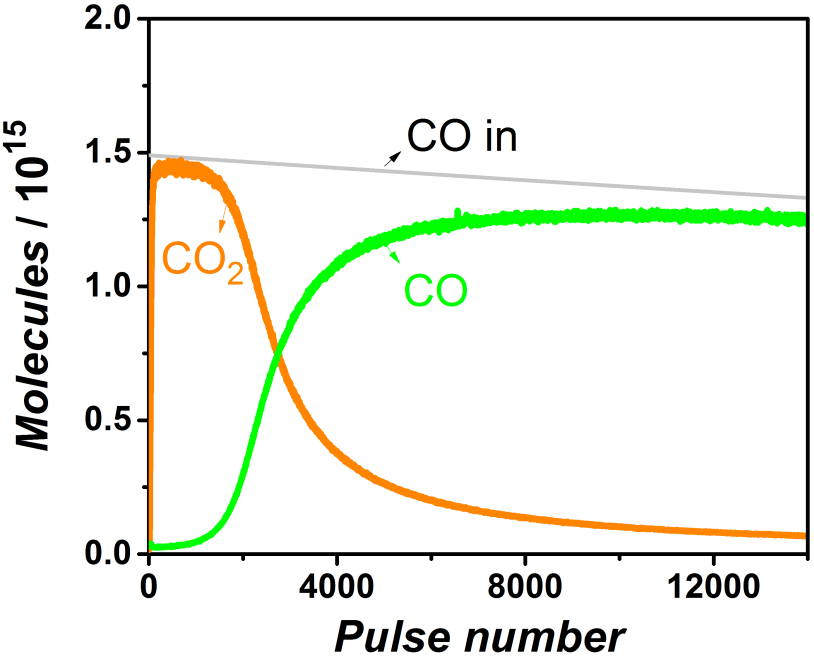

Figuur A.3: CO multi-pulse experiment over a pre-oxidised ceria at 500 °C.

List of Presentations

Oral Presentations at International Conferences:

- **Wang, Y.,** Posthuma de Boer, J., Kapteijn, F., and Makkee, M. The Role of Ceria in NO_x Reduction By Hydrocarbons and the Possible Reaction Pathway. 24^{th} North American Catalysis Society Meeting (NAM), Pittsburgh, PA, USA, 2015.
- **Wang, Y.,** Posthuma de Boer, J., Kapteijn, F., and Makkee, M. Fundamental understanding of the Di-Air system, the role of Ceria in the NO_x abatement. 10^{th} International Congress on Catalysis and Automotive Pollution Control (CAPoC), Brussels, Belgium, 2015. **Keynote speaker**
- **Wang, Y.,** Kapteijn, F., and Makkee, M. Next Generation Automotive $DeNO_x$ Catalysts: Ceria what else? 17^{th} Netherlands' Catalysis and Chemistry Conference (NCCC), Noordwijkerhout, The Netherlands, 2016.
- **Wang, Y.,** Kapteijn, F., and Makkee, M. Next Generation Automotive $DeNO_x$ Catalysts: Ceria what else? 16^{th} International Congress on Catalysis (ICC), Beijing, China, 2016. **Young Acientist Award**
- **Wang, Y.,** Kapteijn, F., and Makkee, M. The role of ceria in NO_x reduction by hydrocarbons and the possible reaction pathway in Toyota's Di-Air system. 9^{th} International Conference on Environmental Catalysis (ICEC), Newcastle, Australia, 2016.
- **Wang, Y.,** Kapteijn, F., and Makkee, M. Oxygen Vacancies of ceria for Highly Selective and Reactive Reduction of NO into N_2. 18^{th} Netherlands' Catalysis and Chemistry Conference (NCCC), Noordwijkerhout, The Netherlands, 2017.
- **Wang, Y.,** Kapteijn, F., and Makkee, M. Oxygen Vacancies of ceria for

Highly Selective and Reactive Reduction of NO into N_2. 25^{th} North American Catalysis Society Meeting (NAM), Denver, CO, USA, 2017.

- **Wang, Y.,** Posthuma de Boer, J., Kapteijn, F., and Makkee, M. Understanding Toyota's "Di-Air"technology for NO_x abatement. 1^{st} Temporal Analysis of Products (TAP) workshop, Denver, CO, USA,2017.
- Posthuma de Boer, J., **Wang, Y.,** Kapteijn, F., and Makkee, M. Novel concepts in TAP design. 1^{st} Temporal Analysis of Products (TAP) workshop, Denver, CO, USA,2017.
- Makkee, M., and **Wang, Y.** NO_x abatement via the Toyota Di-Air Technology, Global Automotive Management Council, Frankfurt, Germany, 2017. **Invited speaker**

Poster Presentations at International Conferences:

- **Wang, Y.,** Kapteijn, F., and Makkee, M. Oxygen Vacancies of ceria for Highly Selective and Reactive Reduction of NO into N_2. 18^{th} Netherlands' Catalysis and Chemistry Conference (NCCC), Noordwijkerhout, The Netherlands, 2017.
- **Wang, Y.,** Kapteijn, F., and Makkee, M. Oxygen Vacancies of ceria for Highly Selective and Reactive Reduction of NO into N_2. 25^{th} North American Catalysis Society Meeting (NAM), Denver, CO, USA, 2017.

List of Publications

Publications reated to this thesis:

- **Wang, Y.,** Posthuma de Boer, J., Kapteijn, F., and Makkee, M. (2016). Next Generation Automotive DeNO Catalysts: Ceria What Else?. ChemCatChem, 8(1), 102-105. (Inside cover)
- **Wang, Y.,** de Boer, J. P., Kapteijn, F., and Makkee, M. (2016). Fundamental Understanding of the Di-Air System: The Role of Ceria in NO_x Abatement. Topics in Catalysis, 59(10-12), 854-860.
- **Wang, Y.,** and Makkee, M. (2017). Fundamental understanding of the Di-Air system (an alternative NO_x abatement technology). I: The difference in reductant pre-treatment of ceria. Applied Catalysis B: Environmental. (doi: 10.1016/j.apcatb.2017.04.054)
- **Wang, Y.,** and Makkee, M. (2018). The influence of CO_2 on NO reduction to N_2 over reduced ceria - based catalyst, Applied Catalysis B: Environmental. (221),196-205
- **Wang, Y.,** Oord, R., van der Berg, D., Weckhuysen,B., and Makkee, M., (2017). Oxygen Vacancies in reduced Rh- and Pt-ceria for Highly Selective and Reactive Reduction of NO into N_2 in excess of O_2,ChemCatChem. (9) 2935-2939)
- Makkee, M., and **Wang, Y.** (2017). Reaction Mechanism Study of the Di-Air System and Selectivity and Reactivity of NO Reduction in Excess O_2. SAE International Journal of Engines, 10(2017-01-0910).
- **Wang, Y.,** , Kapteijn, F., and Makkee, M., Evaluation the role of noble metals in NO reduction in the Di-Air DeNO$_x$ system (submitted)
- **Wang, Y.,** and Makkee, M., The role of potassium in NO reduction in the Di-Air DeNO$_x$ system (in preparation)

- **Wang, Y.,** and Makkee, M., The investigation of N_2O and NO_2 reduction over ceria(in preparation)
- **Wang, Y.,** and Makkee, M., Mechanism study of N_2O decomposition over ceria catalyst by the TAP (in preparation)

Other publications:

- **Wang, Y.,** Hou, Z., Shen, L., Guo, H., Wang, G., Li, Y., and Jiang, Q. (2012). Synthesis of dumbbell-like ZnO microcrystals via a simple solution route. Nanoscale Research Letters, 7(1), 507.
- **Wang, Y.,** Hou, Z., Guo, H., Shen, L., Wang, G., Cui, F., and Zhang, Q. (2013). Preparation of ZnO nanorods via aqueous solution process and their PL properties. Materials Letters, 91, 107-110.
- Hou, Z., Zhou, C., Luo, Y., Zhan, C., **Wang, Y.,** Xie, L., and Zhang, Q. (2011). PLA nanoparticles loaded with an active lactone form of hydroxycamptothecin: development, optimization, and in vitro–in vivo evaluation in mice bearing H22 solid tumor. Drug Development Research, 72(4), 337-345.
- Hou, Z., Li, Y., Huang, Y., Zhou, C., Lin, J., **Wang, Y.,** and Zhang, Q. (2012). Phytosomes loaded with mitomycin C– soybean phosphatidylcholine complex developed for drug delivery. Molecular Pharmaceutics, 10(1), 90-101.
- Shen, L. H., Bao, J. F., Wang, D., **Wang, Y.,** Chen, Z. W., Ren, L., and Yang, A. Q. (2013). One-step synthesis of monodisperse, water-soluble ultra-small Fe_3O_4 nanoparticles for potential bio-application. Nanoscale, 5(5), 2133- 2141.
- Shen, L., Zhou, J., **Wang, Y.,** Kang, N., Ke, X., Bi, S., and Ren, L. (2015). Efficient Encapsulation of Fe_3O_4 Nanoparticles into Genetically Engineered Hepatitis B Core Virus-Like Particles Through a Specific Interaction for Potential Bioapplications. Small, 11(9-10), 1190-1196.

Acknowledgements

Finally, I am at the page where I can say the words: "thank you", to all of you. First of all thank you for opening my book.

Firstly, I want to thank my daily supervisor and promotor, prof.dr.ir. Michiel Makkee. Michiel, it is an honour to be your 24^{th} Ph.D. student. I appreciate all your contributions, in time, ideas, and funding, which made my Ph.D. experience both productive and stimulating. Thanks for giving me all the freedom and trust in doing my research. Thanks a lot for helping me out of questions and barriers of my research. I never forget many times in your office, we had more than 4 hours discussion till you have to go home. Thanks a lot for your accompany with me on the way to be independent and confident scientific researcher. Your rigorous approach to the research prompts me to be skilling in safety report, doing quantification. Ph.D. research is full of challenges. Your encouragement and trust motivated me to move ahead with my research, especially during my toughest times in Delft. Thanks for your compliment, "She (Yixiao) is smart", at the beginning of my Ph.D. Thanks for giving me many opportunities to be involved in extensive scientific discussions with people outside Delft. I enjoyed every time at international conferences together with you. Besides as a supervisor for my research, you are also a mentor in my life. You trigger me to think about my life direction. Thanks a lot for the beautiful time working with you.

Endless thanks go out to my promotor, prof. dr. Freek Kapteijn. Freek, thanks for offering me the opportunity to work in the Catalysis Engineering group. Your questions and comments on my work always reshaped my thoughts, triggering me to go deeper and broader in my scientific work. Thanks for guiding me into the world of modelling. Thanks for the time you spent together with me to check the details in calculations and reading literature. Thank you for the help you provided in improving the quality of my thesis. I am proud to be your Ph.D. student and a member of our CE group.

Particular thanks I want to convey to my daily guest supervisor, Jorrit Posthuma de Boer. Jorrit, I enjoyed the time we spent together in the big and clean TAP room, where you introduced me to and guided me in the TAP world. You are different from other supervisors. You firstly let me realise how challenging the TAP is. You started to teach me using Excel to deal with the massive amounts of data coming from the TAP experiments. Although, you spent whole weeks with me, I did not even finish the first series of TAP data. I spent days and nights to analyse the data, while I was still not able to catch up with the data being produced by the TAP equipment. You rescued me by programming automated data handling after I was almost drawn in a sea of data, around two months after me starting on the TAP. I will never forget your patience during your teaching. I was completely unable to follow the relationship between irreversible adsorption, reversible adsorption, and the shape of the TAP response. You connected my hobby (shopping) with the TAP response, helping me to understand it. Besides being a teacher, you are also a good friend for me. You convinced me that I am a qualified Ph.D. student in Delft, not just because of my luck. Thanks for being patient with me, when I was handicapped by my spoken English in the beginning. You helped me to pass the toughest time in Delft. Thanks for sharing my happiness, sorrow, failure, and success. All the memory will be my treasure.

Bart (van der Linden), now I finally found a place to express my sincere and genuine thanks to you. Thanks for all your support and assistance with my lab work. Thanks for your quick responses and immediate help. You were our M-O (Microbe-Obliterator) on the planet of the CE group, from the movie of 'WALL-E', as your mission was to keep our CE planet clean, no contamination. However, you were more a friend than a technician to me. The coffee break time with you was the most relaxing time during the day. Thanks for inviting me to the Flower Parade in your village; it was a great evening with you and your family. I would like to express my thanks to Harrie Jansma, Liliana Baron, and Willy Rook. Harrie, thanks for your support. One afternoon of my 2nd day in Delft, you knocked on my office door, and told me I can approach you for help if I had a question or problem. Your kind words greatly comforted me and eased my nerves. Willy, thank you so much for all your support in the BET experiments. Liliana, welcome to our CE group. Great to meet you during my last several months in Delft.

Thanks to my dear friends Sonia and Maxim. I miss you so much. Both of you left suddenly after my holiday in China. I missed so much the time we were together in my office, discussing scientific work or life. Maxim, you are a serious man in science but a funny guy in life. Sonia, besides being an outstanding chemist, you are also a good chief. I still missed your Spanish seafood. It was always a great time with you. Anastasiya, thank you for being my language teacher and for teaching me how to express my anger. My sincere gratitude went out to Anahid. We always had long and pleasant conversations in the coffee corner. You were a good listener and you shared my anxiety. Riming, Meixia, Xiaohui, Xinlei, Xuerui, and Guanna, thank you so much in all the help and support. Eduardo, thank you for providing so much fun to our CE group. You are a very creative person in making life full of joy, and you are a party boy. Tim, you set a good example to me in how to be confident. Alexey, Thanks for all the nice office talk with you, and all your kind help for all the different matters. Thanks to Adrian, Alma, Lide, Beatriz, Maria, Robert, Jara, Dmitrii, Irina, Ágnes, Constantino, and Ina. I am grateful to our group's secretaries in Delft, Els and Caroline. Thanks for all the administrative assistance, keeping us organized. Finally, thanks to the entire Catalysis Engineering group for all your uncited contributions.

I would like to acknowledge my LO students in Delft, Walter Starmans, Tim Ofman, Chris Hoekman, Sophie Winkenius, Jurre Keizers, and Mark van der Linde. Thanks for your interesting in working with me in the CE group. By teaching you, I develop my teaching skill. A lot thanks to my mater students, Rohan Godse and Daniël van den Berg. Thanks a lot for your contribution in the Di-Air deNO_x system.

I would also like to thank Wim Buijs (3ME,Delft). Wim, thanks a lot for your time in helping me to do the DFT calculations. I enjoyed the time with you. And a lot thanks for sharing your travelling story and photos with me.

I would also like to acknowledge the people from Utrecht university in the group of Inorganic Chemistry and Catalysis. Prof. dr. ir. B.M. Weckhuysen, Bert, thanks for the opportunity to do and your support during my Raman experiments in your group. Your recognition of my work had been an invaluable encouragement. A lot of thanks goes to Ramon Oord. Ramon, I very much appreciated your kind help during my work in Utrecht.

I am also thankful for the people from Fudan University. Professor Hualong Xu and Wei Shen, nice to meet you both in Shanghai and Delft. You are easy-going professors. I enjoyed every opportunity to talk with you. Many thanks for all your suggestions and instructions regarding my work and future career. I also would like to acknowledge Zhen Huang and Liang Huang for the great time at Fudan university. Zhen Huang, thanks for your beautiful ceria sample you provided for the Drift experiments. Liang Huang, you gave me a wonderful time in Fudan, and I very much appreciated your enthusiasm. Thanks for giving me a nickname, 'cactus'. It is so special to me. Pei Zhao, I would also like to thank you, giving me a great time in shopping from Shanghai to Suzhou.

Thanks to my dearest housemates, Yueting, Long, Jie and Yao. I am lucky to have spent my private time with you. You saw me dressed down and you saw my embarrasment. Expecially, I would like to thank Yueting. You are a *big* brother in our Delft family, not because you are oldest. As said by Jie, you are guading and protecting our Delft family members. Thanks you for helping washing the dishes these four years. And most importantly, thank you for all our discussion in investment, life, and artificial intellegence, which enlarge my eyes as well as my knowledge. Thanks also to the Delft Chinese Community, Fei, Anqi, Xinyu, Daijie, and Sixin.

I would like to thank my family for all their love and encouragements. I probably would not have been able to get an education if it was not for my grandmother. You raised me up and gave me a complete and joyful childhood. You spent all your time with me until you became old and vulnerable. Thanks to my parents. Thanks for all your hard work to support our family. Thanks for giving me all the possibility to freely grow up and became the person I am today. I would like to thank my dear sister (xiaojun) and my brother (weiqing). Thanks for all the support from your side.

I gratefully acknowledged the funding I received from the Chinese Scholarship Council (CSC), that made my Ph.D. work in Delft possible.

About the Author

Yixiao Wang, was born on the 8^{th} of January 1987 in Fuzhou, China. From 2005 to 2009, she studied at the department of Environmental Engineering in Beijing University of Chemistry and Technology (China), where she did her BSc project under the supervision of Prof. Xiujin Chen with the research topic of gas anaerobic digestion performance of the straw. She obtained the Bachelor degree in 2009. After graduation, she moved to Xiamen University (China) in 2010 to start her MSc education in Materials under the supervision of Prof. Zhang Qiqing and Hou Zhenqing. Her MSc thesis research was entitled: "controllable synthesis of metal oxides microcrystals". She obtained her MSc degree in 2013. In September of the same year, she started her PhD, on the topic of NO_x abatement for lean burn Engine of automotive, under the supervision of Prof.dr.ir. Michiel Makkee and Prof.dr. Freek Kapteijn, in the section of Catalysis Engineering, TU Delft. During her PhD, she joined a cooperation project with Fudan university for the topic of NO_x reduction using ceria catalyst in 2015. From 2016.6 to 2016.12, she was a guest researcher in Utrecht University (The Netherlands), in the group of prof. dr. ir. B.M. (Bert) Weckhuysen, department of Inorganic Chemistry and Catalysis.

Since September 2017, Yixiao is working as postdoc in the section of Catalysis Engineering at the TU Delft. From January 2018, she will start working as postdoc at Idaho National Laboratory, USA.